Parametric excitation of the quantum vacuum in nonlinear optical resonators

Dissertation
zur
Erlangung des Doktorgrades (Dr. rer. nat.)
der
Mathematisch-Naturwissenschaftlichen Fakultät
der
Rheinischen Friedrich-Wilhelms-Universität Bonn

von
Thorsten Friedrich Langerfeld
aus
Hückeswagen

Bonn, 11.10.2021

Angefertigt mit Genehmigung der Mathematisch-Naturwissenschaftlichen Fakultät der Rheinischen Friedrich-Wilhelms-Universität Bonn

1. Gutachter:	Prof. Dr. Michael Köhl
2. Gutachter:	Prof. Dr. Sebastian Hofferberth
Tag der Promotion:	22.02.2022
Erscheinungsjahr:	2022

Abstract

In this thesis, I present the generation of correlated photon pairs in high-finesse nonlinear optical micro-resonators. In a first attempt, we utilize the third-order nonlinear material polarization of the dielectric mirror coatings to generate correlated photon pairs via spontaneous four-wave mixing. Two pump photons are annihilated and a pair of signal and idler photons is created, a process where the cavity pump mode couples to adjacent cavity modes. We observe the photon pairs in the first spectral order, i.e. the frequencies are shifted by one free spectral range up- and downwards with respect to the pump mode, driven on the experimentally determined dispersion-compensated cavity resonance. We measure a photon-pair production rate of $\Gamma_{\mathrm{exp}} = (0.22 \pm 0.01)\,\mathrm{s}^{-1}\,\mathrm{W}^{-2}$ with respect to the intra-cavity power. The experiment demonstrates the fast response of the dielectric polarization to the rapidly oscillating standing wave inside the cavity and determines the magnitude of the nonlinearity of the dielectric coating stack.

Even though the size of the nonlinear material is restricted to sub-wavelength scales, i.e. the penetration depth of the electromagnetic wave into the dielectric mirror coating, a measurable amount of photon pairs is generated. In order to increase the stream of photon pairs, we filled a resonator with silicone oil to extend the interaction region to the whole cavity length. We observe a photon-pair production rate of $\Gamma_{\mathrm{exp}} = (330 \pm 30)\,\mathrm{s}^{-1}\,\mathrm{W}^{-2}$, which is an increase of more than three orders of magnitude as compared to the empty cavity. The spectral brightness is $(44 \pm 8)\,\mathrm{mW}^{-2}\,\mathrm{s}^{-1}\,\mathrm{MHz}^{-1}$, showing the narrow-band properties of the photon-pair source. Furthermore, we demonstrate the possible tunability of the photon frequencies by changing the spectral separation of the signal and idler mode to the pump mode. This is achieved by using pairs of longitudinal cavity modes shifted by multiples of the free spectral range.

These experiments show a formal equivalence to the dynamical Casimir effect where a time-dependent boundary condition to the electromagnetic field, e.g. an oscillating cavity length, gives rise to the excitation of photon pairs out of the vacuum. Both experiments can thereby be interpreted as the periodic modulation of the refractive index and, hence, the effective cavity length. By changing the pump geometry, we modulate the refractive index in the dielectric mirror coating of a micro-cavity with two dissimilar high-intensity lasers incident from the side of the resonator. The refractive index is then modified at the difference frequency of both lasers, adjusted to be twice the cavity resonance frequency. The modulation couples to the unoccupied cavity mode and gives rise to the creation of correlated photon pairs out of the vacuum state via parametric excitation. The underlying process is distinctive to the former spontaneous four-wave mixing, since one higher frequency pump photon is annihilated and a lower frequency pump photon is generated with the excess creating the photon pair on the unoccupied cavity mode. We measure a correlation signal outstanding almost four standard deviations from the mean accidental coincidence background. We exclude thermal radiation as origin for the observation by reference measurements and estimate the probability of a random appearence of the signal to be less than 0.01 %.

List of publications

Parts of this thesis have been published in

- **Thorsten F. Langerfeld**, Hendrik M. Meyer and Michael Köhl, *Correlated photon-pair emission from a cw-pumped Fabry-Perot microcavity* Phys. Rev. A **97** (2 2018) 023822, https://doi.org/10.1103/PhysRevA.97.023822
- Felix Rönchen, **Thorsten F. Langerfeld*** and Michael Köhl, *Correlated photon-pair generation in a liquid-filled microcavity*, New Journal of Physics **21**(12) (2019) 123037, https://doi.org/10.1088/1367-2630/ab5daa
  * Corresponding author

Contents

CHAPTER 1

Introduction

Among physicists, the name Max Planck is famous for leading physics from the classical to the quantum era, and initiating one of the most successful, but strangest theories of nature. In those days, one of the big questions was the explanation of the emission spectrum of a blackbody radiator. The Rayleigh-Jeans distribution can explain the characteristics for small, i.e. far infrared frequencies, but the energy density diverges at large frequencies. Planck solved this ultraviolet catastrophe by discretizing the energy portions a radiator can emit [1]. In his way of counting the possible ways indistinguishable energy packets can be distributed among radiators, he found the correct formula for the spectral energy density of thermal radiation. A rather unknown consequence from Planck's theory is the appearance of zero-point energy, even though he did not use any quantization procedures of modern quantum physics and only assumed energy to be emitted in discrete quanta [2, 3]. No experimental significance was attributed to this concept at first, but the idea attracted rising attention and is a well established and studied fact nowadays.

In modern quantum mechanics, the ground state energy of a harmonic oscillator is half of the excitation energy $\hbar\omega$, the exact same value appearing in Planck's (semi-) classical theory. Every mode of the electromagnetic field is described as a harmonic oscillator in second quantization. Consequently, the ground state of the total electromagnetic field contains an infinite amount of energy, which does not contradict fundamental laws of physics, since only energy differences between excited states and the ground state are accessible in measurements. Even though the infinite amount of energy can be removed due to renormalization, the impact of the vacuum field on nature is present. Together with the Heisenberg uncertainty principle, zero-point energy has remarkable consequences; we can borrow some energy to create a pair of particles, which annihilate in a glimpse of time. Therefore, the quantum vacuum state is not empty, but contains virtual particles floating in and out of existence. These vacuum fluctuations have measurable effects like lifting the degeneracy of the $^2S_{1/2}$ and $^2P_{1/2}$ level in hydrogen, known as Lamb shift [4], or van der Waals forces between non-polar molecules or atoms [3].

Furthermore, spontaneous emission can be interpreted in terms of stimulated emission by a virtual photon [5, 6], such that the vacuum field serves as a seed for the decay process. A similar interpretation is applicable for the generation of photon pairs in spontaneous parametric down-conversion (SPDC) and spontaneous four-wave mixing (SFWM). Both mechanisms rely on a driven nonlinear dielectric polarization in media due to interaction of applied electromagnetic radiation by the second- (SPDC) or third-order (SFWM) nonlinear response. In both processes, a pair of signal and idler photons is

created after the annihilation of one (SPDC) or two (SFWM) pump photons, respectively [7]. These mechanisms are the quantum counter-parts of the classical nonlinear processes difference-frequency generation and four-wave mixing, where two, respective three input fields generate a third and a fourth field. Likewise for spontaneous emission, vacuum fluctuations provide the seed fields for the two nonlinear quantum effects, where only pairs of virtual photons satisfying energy and momentum conservation are efficiently converted into real photons. For the free electromagnetic field, many pairs of signal and idler modes fulfil these criteria and the generated emission spectrum is on the order of up to several THz [8, 9]. In order to reduce the bandwidth, nonlinear media are often placed in optical cavities [10–12]. Resonators are wavelength selective devices due to the boundary conditions imposed on the electromagnetic field. Therefore, cavities strongly suppress most of the free field modes and greatly enhance the density of modes for resonant frequencies. As a consequence of enhancing the density of modes for cavity resonances, excited emitters embedded in a resonator are more likely to spontaneously emit a photon into the cavity, if the cavity is resonant for the transition frequency, known as Purcell effect. In a similar way, the cavity enhances above nonlinear effects in addition to the increase of the pump field strength.

Narrow-band photon-pair sources provide non-classical states of light, and are, thus, of special interest in fundamental tests of quantum physics [13, 14], quantum key distribution [15] and quantum information [16]. In the interconnection of remote quantum nodes with the purpose of creating networks [17], hybrid quantum systems need to be coupled by bridging wavelength gaps between dissimilar emitters [18, 19]. Therefore, tunable photon-pair sources with the capability of tailoring the signal and idler frequencies to the respective atomic or solid-state transitions are desirable. Cavities not only limit the feasible output channels, but imprint their linewidth on the photon pair. This is beneficial due to the narrow bandwidth of absorption of possible network nodes on the order of 10 MHz–1 GHz.

However, the resonator does not only affect the electromagnetic field, but the field impacts the cavity as well. The exclusion of free space modes in a resonator leads to a back-action onto the cavity mirrors, due to an imbalance between the amount of vacuum modes in between the mirrors and outside. The cavity mirrors exhibit an attractive force due to a mismatch of radiation pressure from virtual photons in the outer and the inner region, pushing the mirrors together. This effect is known as Casimir effect and has been experimentally observed for two conducting plates by Lamoreaux [20]. An interesting phenomenon is postulated if the boundary condition is modified, for instance, due to an oscillating cavity length [21] or, more general, a single mirror moving nonuniformly through space-time [22]. The mechanical oscillation energy is converted into a pair of photons, where the sum frequency of the pair matches the frequency of the oscillation. At relativistic velocities of the modulation, field modes cannot adapt to the changing boundary and the quantum vacuum is excited nonadiabatically [23], by virtue of a temporal mismatch of cavity modes [24], rather than a spatial mismatch as in the Casimir effect. Vacuum fluctuations impose a radiation pressure onto the mirror, damping its movement and, consequently, yielding the dissipation of energy in form of photon pairs. The effect is called dynamical Casimir effect (DCE).

Mechanical oscillation frequencies, however, are limited to values below 100 MHz reported in cavity optomechanical experiments [25]. These frequencies are infeasible for the detection of DCE radiation. Thus, efforts have been invested in proposing and conducting analogue experiments, where a system parameter determining the properties of the electromagnetic field is driven. By modulating the inductance of a superconducting quantum interference device at GHz frequencies, the effective length of a microwave transmission line has been modified, emitting electromagnetic radiation in a

broad bandwidth around half of the modulation frequency [23]. The effective length of a low Q-factor microwave resonator has been modulated in a similar manner by inserting a Josephson-metamaterial, giving rise to electromagnetic radiation on cavity modes [26]. In order to generate DCE-like radiation at optical frequencies, experiments have been proposed, where the second- or third-order nonlinear polarization of a material embedded in a cavity is driven by continuous-wave or pulsed lasers [27, 28]. The modulated polarization leads to a varying refractive index which is proportional to the applied electric field in second order (Pockels effect), and proportional to the intensity in third order (Kerr effect). Consequently, the oscillating refractive index leads to an oscillating effective cavity length. Hence, some SPDC and SFWM experiments can be interpreted in terms of optical analogues to the DCE and are formally equivalent [29]. Both, changes of the physical, or the effective resonator length, after all, alter the fundamental resonance of the cavity and can be explained as a parametric excitation of the unoccupied electromagnetic field modes. The DCE can, therefore, be generalized from the mechanically changing boundary condition to a modulation of a system parameter determining the properties of the electromagnetic field [30, 31]. Whether the generalization is in fact an unification, because of a mutual microscopic process, is open to question. Due to the limitations of mechanical oscillation frequencies, however, only analogue experiments can gain insights of the underlying mechanism.

In this thesis, three experiments on the creation of photon pairs via the parametric excitation of vacuum modes in optical micro-resonators are presented. In the first experiment, we utilize the third-order nonlinearity in the dielectric mirror coatings of a high-finesse micro-cavity to generate photon pairs on adjacent, unoccupied signal and idler modes (chapter 3). Two of the pump photons are annihilated and a photon pair on the neighboring cavity modes is created via spontaneous four-wave mixing. We use a miniaturized fiber Fabry-Pérot resonator to reduce the mode volume and increase the nonlinear effects. The experiment clarifies whether the nonlinear response of the material is fast enough to follow the rapidly oscillating electromagnetic field at twice the pump frequency, i.e. on femtosecond time scales.

In order to increase the photon-pair production rate, we fill a micro-cavity with a synthetic silicone oil (Tetramethyl-tetraphenyl-trisiloxane, DC704), extending the nonlinearity from sub-wavelength scales to the whole cavity length (chapter 4). Due to the enhanced nonlinearity, we expect a drastic increase of the photon-pair production rate as compared to the empty cavity experiment. Additionally, we measure photon pairs on several spectral orders of longitudinal signal and idler modes, demonstrating the possible tunability of the output frequencies. The observations show that the third-order nonlinear polarization in liquids is also fast enough to follow the changing intensity at optical frequencies.

In a third experiment, we change the pumping scheme from the standing wave inside the cavity driving the nonlinear polarization, to two distinct high-intensity continuous-wave lasers (chapter 5). The lasers are superimposed and modulate the refractive index of the dielectric coating of one mirror of a high-finesse cavity via the Kerr effect. The effective cavity length is, thus, driven at the difference frequency of the pump lasers forming a travelling intensity pattern. The cavity resonance is matched to half the modulation frequency, thus the unoccupied cavity mode is parametrically excited out of its vacuum state. The underlying process on a single photon level is the annihilation of a higher frequency pump photon, and the stimulated emission of a lower frequency pump photon, with the excess creating a photon pair on the cavity mode. Therefore, the process is different from the spontaneous four-wave mixing observed in the other two experiments and serves as an analogue experiment for the dynamical Casimir effect.

CHAPTER 2

Fiber Fabry-Pérot cavities as nonlinear resonators

Fabry-Pérot cavities have a vast field of application in optics. They consist of two mirrors, or reflective surfaces, facing each other. In general, due to interference of successive reflections of the incoming light, the resonator confines and stores light, and has wavelength selective properties. The most prominent use is in lasers, where the cavity contains a gain medium and imprints its spectral, e.g. frequency and linewidth, and geometric characteristics, e.g. spatial distribution, onto the beam. Furthermore, cavities are used for stabilization of lasers to a single frequency. Especially, in quantum metrology, where Hz–mHz-transitions are spectroscopically analyzed, high-finesse resonators, i.e. cavities with a narrow linewidth, are essential for reducing the linewidth of lasers to this level [32]. Due to their high precision, resonators are also used for fundamental tests of quantum electrodynamics, e.g. for probing the birefringence of the quantum vacuum [33]. Moreover, cavities are used in quantum information as an efficient light matter interface, where they increase the probability of collecting the photon emitted by a qubit, if the transition and cavity resonance coincide [34–36]. This is due to the higher mode density for modes of the electromagnetic field, resonant with the cavity. Optical resonators are furthermore applied in nonlinear optics, where their capabilities of storing light increases electric field strengths, in order to improve the conversion efficiency in e.g. second-harmonic generation or four-wave mixing processes. Nonlinearities in resonators are used for bistable operation in optical switches [37]. In spontaneous parametric down-conversion and spontaneous four-wave mixing experiments, cavities are used to tailor the frequencies and bandwidth of the generated photon pairs [10–12].

In this chapter I discuss fundamental properties of Fabry-Pérot resonators in subsection 2.1.1, the miniaturization of cavities by use of laser-machined optical fiber end facets as mirrors in subsection 2.1.2, and the physics of dielectric coatings for use in high-finesse cavities. Furthermore, I present the nonlinear polarization in materials in subsection 2.2.3 and discuss bistable operation of resonators containing nonlinear media. Finally, I calculate the photon-pair generation rate due to the third-order nonlinear polarization in an optical cavity in subsection 2.2.3 as a reference for later experiments.

2.1 Fiber Fabry-Pérot cavities

A Fabry-Pérot cavity or interferometer consists of two parallel reflecting surfaces separated by a fixed distance that lead to a wavelength-dependent transmission of the whole system. Especially for high reflectivities, the cavity acts as a wavelength selective device, drastically enhancing field strengths of resonant wavelengths inside the resonator, while almost completely suppressing waves not fulfilling the resonance condition. In the following I show the fundamental properties of optical resonators in subsection 2.1.1 (following [38]), describe the micro-machining of mirrors on fiber end facets in subsection 2.1.2 and discuss multilayer optical systems for high reflective dielectric mirror coatings in subsection 2.1.3.

2.1.1 Optical resonators

For two parallel mirrors separated by length l, a monochromatic wave with wavevector $k = \omega/c$, where ω is the angular velocity and c is the speed of light within the medium, acquires a phase of $2\phi = k \cdot 2l$ for each roundtrip inside the cavity. In order to constructively interfere with the incident wave and thus form a standing wave, the phase shift for the reflected wave has to be an integer multiple of 2π. From this requirement the frequencies of resonant modes are

$$\omega = 2\pi \cdot q \frac{c}{2l}\,, \tag{2.1}$$

for q being a positive integer. The free spectral range $\Delta\nu_{\mathrm{fsr}} = c/2l$ is the spectral distance between two adjacent resonant modes and the reciprocal of this quantity intuitively is the round-trip time τ_{rt}. The resonant longitudinal modes of the cavity are therefore determined by $\Delta\nu_{\mathrm{fsr}}$.

For perfect mirrors with a power reflectivity $\mathcal{R} = 1$ the standing wave can only build up at the precise resonance frequencies. However, in real systems the reflectivity is not unity, and mirrors have non-vanishing transmission $\mathcal{T} \neq 0$ and losses $\mathcal{L} \neq 0$ due to absorption and scattering, where $\mathcal{R} = 1 - \mathcal{T} - \mathcal{L}$ because of energy conservation. Consequently, the complex amplitude a_n for a wave after n roundtrips is lower than the initial amplitude a_0, thus a finite amount of power inside the resonator can build up for frequencies close to the resonance frequencies. The amplitude of a wave entering the resonator is $a_0 = t_1 \cdot a_{\mathrm{in}}$, where t_1 denotes the amplitude transmission coefficient of the first mirror and a_{in} is the complex amplitude of the incident wave (see Figure 2.1). During one round trip the wave acquires the phase $\phi = 2\pi l/\lambda$[1], where λ is the wavelength. The amplitude for a wave after a number of n roundtrips is thus

$$a_n = a_{n-1} \cdot r_1 r_2 e^{-i2\phi} = a_0 \cdot (r_1 r_2 e^{-i2\phi})^n\,, \tag{2.2}$$

where r_1 and r_2 are the amplitude reflection coefficients of the first and second mirror, respectively. In order to acquire the amplitude a_{circ} of the wave circulating inside the resonator, we have to sum over all partial waves, therefore

$$a_{\mathrm{circ}} = a_0 \sum_n (r_1 r_2 e^{-i2\phi})^n = a_0 \frac{1}{1 - r_1 r_2 e^{-i2\phi}}\,, \tag{2.3}$$

[1] This is valid for normal incidence of the radiation. At non-normal incidence a additional factor of $\cos(\theta)$ is added, where θ is the angle of incidence with respect to the optical axis.

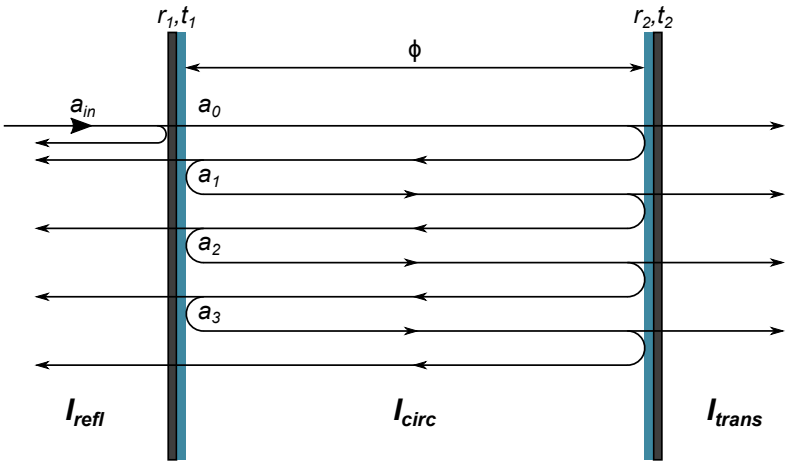

Figure 2.1: *Illustration of the multiple beam interference inside a Fabry-Pérot resonator, due to successive reflection at the mirrors or bounding interfaces with amplitude reflection and transmission coefficients r and t.*

where we used the closed form of the geometric series. The intensity inside the resonator is proportional to the square of the absolute value of the complex amplitude and can be expressed as

$$I_{\mathrm{circ}}(\nu) = \frac{I_{\max}}{1 + \left(\frac{2\mathcal{F}}{\pi} \sin\left(\pi \frac{\nu}{\Delta\nu_{\mathrm{fsr}}}\right)\right)^2} \,. \tag{2.4}$$

$I_{\max} = \mathcal{T}_1/(1 - \sqrt{\mathcal{R}_1\mathcal{R}_2})^2 \cdot I_{\mathrm{in}}$ is the maximum intensity for an incident intensity I_{in}. The quantity

$$\mathcal{F} = \frac{\pi(\mathcal{R}_1\mathcal{R}_2)^{\frac{1}{4}}}{1 - (\mathcal{R}_1\mathcal{R}_2)^{\frac{1}{2}}} \tag{2.5}$$

is the finesse of the resonator. Equation 2.4 demonstrates the strong suppression of non-resonant modes and high amplification of resonant modes, especially for high-reflective mirrors $\mathcal{R} \approx 1$, and, thus, a high finesse $\mathcal{F} \gg 1$. In this case the maximum intensity is approximately $I_{\max} \approx \mathcal{F}/\pi \cdot I_{\mathrm{in}}$ and the full width at half maximum or cavity linewidth is given by[2] $\delta\nu = \Delta\nu_{\mathrm{fsr}}/\mathcal{F}$. Intuitively, the factor $\mathcal{F}/\pi$ is the average number of roundtrips a single photon undergoes before leaving the resonator. In order to acquire the transmitted field, Equation 2.4 has to be multiplied by $\mathcal{T}_2(1 - \mathcal{L}_2)$.

The line shape given by the Airy function in Equation 2.4 can be approximated in the limit of high finesse for a single resonance frequency ω_0 as a Lorentzian [39] with

$$I_{\mathrm{circ}}(\omega) = I_{\max} \frac{\kappa^2}{\kappa^2 + (\omega - \omega_0)^2} \,. \tag{2.6}$$

The linewidth κ is characteristic for the decay rate of the internal field. If the cavity is not continuously pumped with the incident field, the internal intensity is reduced by $(\mathcal{T}_1 + \mathcal{L}_1 + \mathcal{T}_2 + \mathcal{L}_2) \cdot I_{\mathrm{circ}}$ on

[2] This expression follows from calculating $I_{\mathrm{circ}}(\nu + \delta\nu/2) = 1/2$ for a resonant frequency mode $\nu = q \cdot \Delta\nu_{\mathrm{fsr}}$.

each roundtrip. Consequently the temporal dynamics are described by the differential equation $\dot{I}(t) = -(\mathcal{T}_1 + \mathcal{L}_1 + \mathcal{T}_2 + \mathcal{L}_2)/\tau_{\mathrm{rt}} \cdot I(t) = -2\kappa \cdot I(t)$ which is solved by the exponential decay

$$I(t) = I(0)e^{-2\kappa t} \qquad \text{with} \qquad 2\kappa = \frac{1}{\tau_{\mathrm{rd}}} = 2\pi \cdot \delta\nu\,, \tag{2.7}$$

where we used the expression $\mathcal{F} \approx 2\pi/(\mathcal{T}_1 + \mathcal{L}_1 + \mathcal{T}_2 + \mathcal{L}_2)$ which is valid in the limit of high finesse [40].

So far, we discussed fundamental properties of Fabry-Pérot cavities stemming from the boundary conditions both mirrors imply in the longitudinal direction and did not take the geometry of the resonator, or the transversal direction into account. If both mirrors are planar, the cavity is very sensitive to misalignment of the incident light rays and the mirrors have to be perfectly parallel, otherwise the beams wander out of the resonator due to displacements from every reflection. Using spherical instead of planar mirrors increases the stability under certain conditions, since the light is confined due to focusing by the mirror curvature. A spherical resonator is composed of two mirrors with radii of curvature of R_1 and R_2, respectively. Using the transfer matrix method for paraxial rays, the condition

$$0 \leq g_1 g_2 \leq 1 \qquad \text{with} \qquad g_{\mathrm{i}} = 1 - \frac{l}{R_{\mathrm{i}}} \tag{2.8}$$

for a stable operation is obtained. From this inequality, various combinations of planar ($R = \infty$), concave ($R < 0$), and convex ($R > 0$) mirrors can be derived that serve as a stable resonator. Throughout this thesis, plano-concave resonators are used (see subsection 3.2.1, subsection 4.2.1 and subsection 5.2.2). For this configuration, the stability criterion requires the radius of curvature to be at most equal to the total resonator length.

In order to acquire the intensity distribution of the modes in transversal direction, the paraxial Helmholtz equation with boundary conditions imposed by the (spherical) mirrors on the electric field needs to be solved. It can be shown that (Hermite-) Gaussian beams are solutions to the spherical resonator [41]. The complex amplitude of the fundamental TEM_{00} mode is given by

$$E(\rho, z) = E_0 \frac{w_0}{w(z)} \exp\left(-\frac{\rho^2}{w^2(z)}\right) \exp\left(-ikz - ik\frac{\rho^2}{2R(z)} + i\zeta(z)\right)\,, \tag{2.9}$$

with $w(z) = w_0(1 + (z/z_{\mathrm{r}})^2)^{\frac{1}{2}}$ being the waist at position z, $R(z) = z(1 + (z_{\mathrm{r}}/z)^2)$ the wavefront curvature, $\zeta = \arctan(z/z_{\mathrm{r}})$ the Gouy phase, $z_{\mathrm{r}} = \pi w_0^2/\lambda$ the Rayleigh range, and ρ being the transversal distance from the center. For a TEM_{ij}-wave, both electric, and magnetic fields are perpendicular to the direction of propagation and the indices denote the number of nodes along the two transversal directions, respectively.

Intuitively, a Gaussian beam retraces itself after the reflection from one of the cavity mirrors, if its wavefront curvature is equal to the curvature of the mirror. The geometry of the resonator consequently determines the beam parameters such as waist w_0 and Rayleigh range z_{r}. For the plano-concave resonator, the spot sizes on both mirrors are [41]

$$w_0 = \sqrt{\frac{l\lambda}{\pi}}\left(\frac{R}{l} - 1\right)^{\frac{1}{4}} \qquad \text{and} \qquad w_{\mathrm{m}} = w_0\sqrt{\frac{R}{R-l}}\,, \tag{2.10}$$

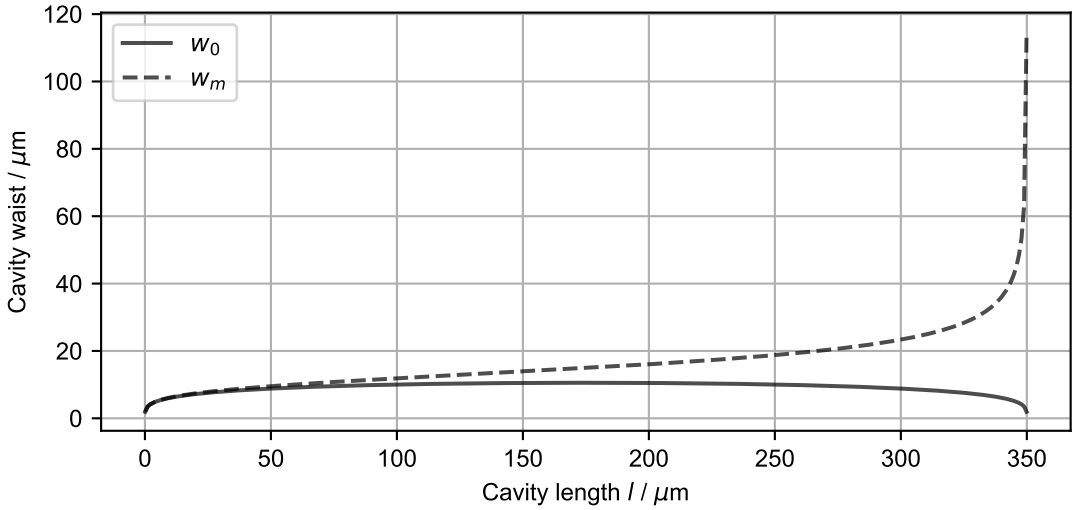

Figure 2.2: *Cavity waists for a plano-concave resonator for a mirror radius of curvature of 350 µm and a wavelength of 2 µm. The mode size on the planar mirror is maximal at a cavity length of half the radius of curvature and, while it goes to zero for the hemispherical configuration, the mode size on the curved mirror diverges.*

where w_0 is the waist on the planar mirror and w_m on the curved mirror, respectively. Figure 2.2 exemplarily shows the dependency of the cavity waists on the cavity length for a mirror radius of curvature of 350 µm and a wavelength of 2 µm. The waist on the planar mirror is maximal at a cavity length of half the radius of curvature and goes to zero for the cavity length approaching the radius of curvature, e.g. the hemispherical configuration. The waist on the curved mirror, however, diverges for this arrangement.

The intensity of the TEM_{00} mode is normally distributed in radial direction and extends infinitely. We will see in the next section that finite mirror sizes introduce additional losses by clipping of the mode, where especially for long fiber cavities, clipping losses become severe and limit the resonator length.

2.1.2 Micro-resonators with optical fibers

Fiber cavities enable miniaturization and scalability of optical systems. The small size features higher optical access and smaller mode volumes which are, for instance, necessary for efficient light-matter coupling in cavity quantum electrodynamics experiments [34–36]. Besides loss, due to the absorption in the dielectric mirror coatings, scattering of an uneven mirror surface reduces the resonator's finesse. Laser-machining of end facets of optical fibers yields ultralow roughness micro-mirrors, enabling miniature optical resonators with small bandwidth, i.e. high finesse [42]. Using a single-mode fiber for incoupling strongly suppresses higher-order modes and favors coupling to the fundamental TEM_{00} mode. The fibers used for the cavities constructed in chapter 3 and chapter 4 were fabricated by Hendrik-Marten Meyer and Matthias Steiner in Jacob Reichelt's group in Paris. The fibers used in the experiment described in chapter 5 were manufactured by Pia Fürtjes in the collaborative fiber laboratory at the university of Bonn.

In the previous chapter we saw that a concave structure is beneficial in constructing a stable cavity with high finesse. Therefore, in order to use fibers for optical resonators, the end facet has to be machined to become refocusing. Since fibers consist of glass which shows high absorption in the mid infrared regime, this is done via laser ablation with a pulsed CO_2-laser [42]. Even though fiber cavities provide above advantages and additionally direct coupling, the mode-matching efficiency is limited by the core size and depends on the radius of curvature of the incoupling mirror. Via the spatial overlap integral between cavity mode, and fiber mode the coupling efficiency can be calculated as [42]

$$\eta = 4\left(\left(\frac{w_\mathrm{f}}{w_\mathrm{m}} + \frac{w_\mathrm{m}}{w_\mathrm{f}}\right)^2 + \left(\frac{\pi n_\mathrm{f} w_\mathrm{f} w_\mathrm{m}}{\lambda R}\right)^2\right)^{-1}, \tag{2.11}$$

where w_f and w_m are the mode radii of the fiber and cavity, respectively, and n_f is the fiber's refractive index. Misalignment between mirror and fiber axis is not accounted for, which is caused by off-centered or non-normal incident laser pulses in production and non-zero cleave angles. The same equation is used for calculating the extraction efficiency for a photon out of the cavity. Figure 2.3 shows mode-matching for a mode field diameter of 13 µm of the single-mode fiber (Thorlabs SM2000) in a plano-concave cavity with mirror radius of curvature of 350 µm. Additionally, the total incoupling including the coating properties (see Figure 5.6) is shown. We observe the maximum coupling at a cavity waist matching the fiber mode radius (see Figure 2.2), and a strong decrease in coupling efficiency for longer cavity lengths. Due to the fixed mode geometry in a single-mode fiber, assemblies composed of a combination of a graded index (GRIN) and multi-mode fiber attached to the tip of the single-mode fiber are in development [43]. The transversal refractive index change of the GRIN-fiber forms a lens for refocusing the light, in order to match the input to the cavity mode and maximize their overlap.

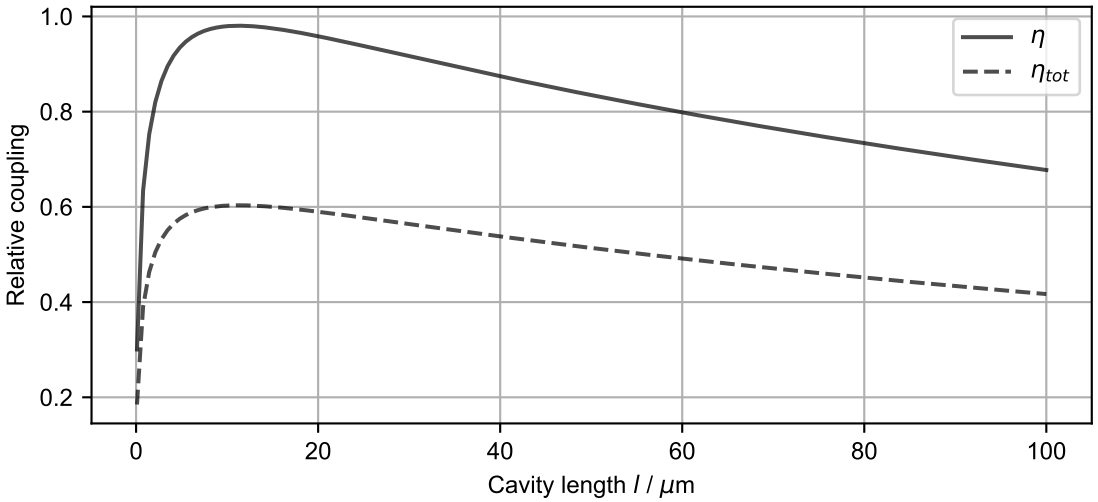

Figure 2.3: *Mode-matching efficiency η in a fiber cavity for a plano-concave resonator with radius of curvature of 350 µm and at an incident wave with wavelength of 2 µm dependent on the cavity length. The dashed line includes the limited coupling due to the coating properties for the total incoupling.*

Typical cavity lengths and radii of curvature are on the order of several hundred micrometer. The resulting waists are a few to tens of micrometer, depending on cavity length, mirror radii and wavelength as given by Equation 2.10 and illustrated in Figure 2.2. The concave structures imprinted by the ablation process, however, have a finite usable area, thus additional losses arise on each round trip due to clipping of the mode. The 'spillover' per reflection at a mirror of finite diameter D is [42]

$$\mathcal{L}_{\mathrm{cl}} = \exp\left(-2\left(\frac{D}{2w_{\mathrm{m}}}\right)^2\right) . \tag{2.12}$$

Equation 2.10 demonstrates that the waists of the cavity modes grow with increasing resonator length and larger wavelength, finally resulting in higher clipping losses. Consequently, the usable size of the imprinted concave structure greatly determines the possible cavity length. The shape induced by the ablation process equals the intensity distribution of the laser pulses to first order. Therefore, a gaussian height profile is imprinted into the fiber tip, where the central part can be approximated by a parabola (see Figure 2.4). The deviation from the actual surface profile determines the usable size of the mirror and, thereby, clipping losses and possible cavity length. A good measure for the mirror size is the radius at which the parabolic approximation and the actual shape differ by a quarter of the wavelength the cavity is operated at. This deviation induces a phase shift of π for the outer partial rays with respect to the central ones, which, thus, do not contribute to the mode anymore. Moreover, due to the deviation from the parabola, the curved wavefront and the curvature of the mirror do not coincide, wherefore parts of the mode are not refocused and, consequently, are scattered out of the resonator. Figure 2.5 shows the strong influence of the clipping losses on the possible maximum cavity length for a plano-concave resonator at a wavelength of about 2 µm and the coating properties are given by Figure 5.5.

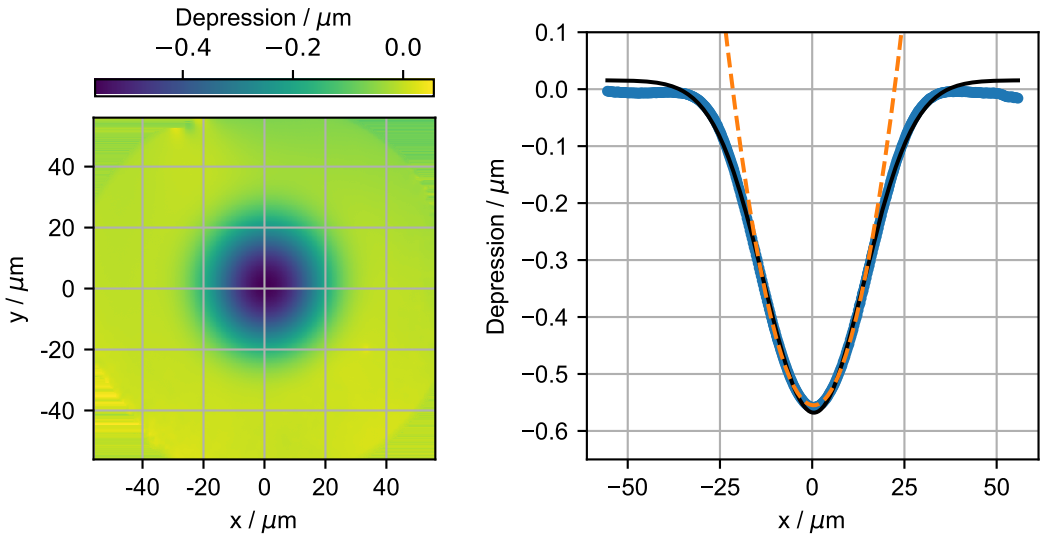

Figure 2.4: *Exemplary surface profile of a concave mirror structure imprinted on the end facet of a single-mode fiber due to ablation with a pulsed CO_2 laser. The usable mirror diameter is determined by the mismatch between a parabolic fit (dashed) to the center and the imprinted gaussian structure (solid).*

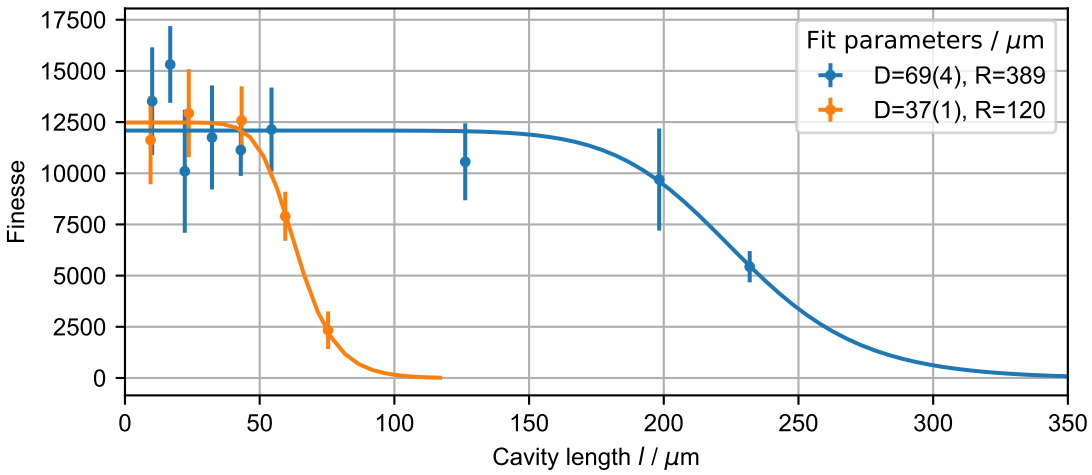

Figure 2.5: *Cavity finesse measurements dependent on the resonator length for plano-concave cavity geometries with different mirror sizes. The wavelength is about 2 µm and the dielectric coating properties are given by Figure 5.5. The solid lines are fits to the data including the additional losses due to clipping (see Equation 2.12), in order to extract the radius of curvature and the mirror diameter.*

2.1.3 Multilayer dielectric coatings

In order to reach a high cavity finesse, mirrors need to have a reflectivity close to unity and thus an almost vanishing transmission coefficient and ideally vanishing losses. This is not possible to achieve with metallic mirrors, since the reflectivity saturates at around 95 % with increasing layer thickness in the visible regime. While the transmission further decreases for thicker metallic films, losses from mainly absorption are around a few percent [44]. The problem can be solved by using stacks of different low absorptive dielectric layers with alternating high and low refractive index, called Bragg gratings [38]. Silicon dioxide (SiO_2) is usually chosen as a low refractive index material due to its low absorption, and e.g. niobium pentoxide (Nb_2O_5) or tantalum pentoxide (Ta_2O_5) as high index materials. Each layer itself only reflects a fraction of light, but if the layer thicknesses are chosen accordingly, the stack can have the properties required for high-finesse cavities. In such an arrangement, reflectivity and transmission depend on the phases partial beams acquire, which need to be tailored such that the reflected beams interfere constructively, while transmitted beams interfere destructively. The amplitude reflection and transmission coefficients for an electromagnetic wave passing an interface between media of refractive index n_1 and n_2 under an angle of incidence θ_1 are given by the Fresnel equations [38]

$$r_{12}^{(\mathrm{s})} = \frac{n_1\cos(\theta_1) - n_2\cos(\theta_2)}{n_1\cos(\theta_1) + n_2\cos(\theta_2)} \qquad t_{12}^{(\mathrm{s})} = \frac{2n_1\cos(\theta_1)}{n_1\cos(\theta_1) + n_2\cos(\theta_2)} \tag{2.13}$$

$$r_{12}^{(\mathrm{p})} = \frac{n_1\cos(\theta_2) - n_2\cos(\theta_1)}{n_1\cos(\theta_2) + n_2\cos(\theta_1)} \qquad t_{12}^{(\mathrm{p})} = \frac{2n_1\cos(\theta_2)}{n_1\cos(\theta_2) + n_2\cos(\theta_1)}\,. \tag{2.14}$$

The angle of propagation inside the second medium θ_2 is given by Snell's law and the superscripts (s) and (p) denote the polarization of the electromagnetic wave. Coatings are commonly designed such that the substrate is SiO_2 and the ambient medium is air or vacuum. Therefore, the reflection coefficient for the first layer is negative and, hence, the reflected beam acquires a phase of π relative to the incident beam, regardless whether the first layer has the high or low refractive index. In order to constructively interfere on the reflection side, all partially reflected beams need to experience the same phase shift, or an uneven integer multiple of π. Thus, the layers should have a thickness of $\lambda/4$, since a reflected beam passes the layer twice and, consequently, collects a phase shift of π, where $\lambda = \lambda_0/n$ is the wavelength in the respective medium. Commonly, the first layer is chosen to be the low refractive index material SiO_2. If, in this case, the first layer has a thickness of $\lambda/4$, the resulting phase shift for the beam reflected from the interface to the second layer is 2π, since the wave collects π from the path travelled, and π due to the reflection from the high refractive index material. Therefore, the first layer is supposed to have a thickness of $\lambda/2$, if it consists of the low refractive index material. The reflection and transmission coefficients of such a stack highly depend on the wavelength of the incoming beam, the angle of incidence, the refractive indices of the materials, and the number of layers and their thickness. The design and fabrication of such coatings is commonly done by professional companies, who tailor the stack parameters to the desired properties, where above considerations for the thicknesses are a rule of thumb.

In the following, we want to discuss the formalism used to determine the properties of arbitrary stacks, since we are interested in the intensity distribution inside the dielectric coating. In principle, an easy approach to find the reflection and transmission properties was already done in subsection 2.1.1, where we tracked every single reflected and transmitted beam in the system. However, extending this formalism to an arbitrary number of interfaces is tedious. A simpler approach is done with the wave-transfer matrix method and we follow the definitions in [38]. Every layer comprises a forwards and a backwards travelling wave with amplitudes $U_{\mathrm{i}}^{(+)}$ and $U_{\mathrm{i}}^{(-)}$, which are connected to the next layer via a 2×2 matrix M

$$\begin{pmatrix} U_{\mathrm{i+1}}^{(+)} \\ U_{\mathrm{i+1}}^{(-)} \end{pmatrix} = \begin{pmatrix} A & B \\ C & D \end{pmatrix} \begin{pmatrix} U_{\mathrm{i}}^{(+)} \\ U_{\mathrm{i}}^{(-)} \end{pmatrix} , \tag{2.15}$$

where the coefficients A, B, C and D contain the respective properties of the i-th and following layer. The transmission and reflection properties of the whole stack can thus be calculated by multiplying the wave-transfer matrices of each layer, such that the dielectric stack can be described via a single matrix

$$M = M_{\mathrm{N}} \dots M_2 M_1 . \tag{2.16}$$

The matrix for each layer consists of a propagation matrix handling the phase ϕ acquired along the path through the material, and a matrix for the transfer to the next layer

$$M_{\mathrm{i}} = \begin{pmatrix} e^{-i\phi} & 0 \\ 0 & e^{i\phi} \end{pmatrix} \frac{1}{t_{\mathrm{i+1,i}}} \begin{pmatrix} t_{\mathrm{i,i+1}} t_{\mathrm{i+1,i}} - r_{\mathrm{i,i+1}} r_{\mathrm{i+1,i}} & r_{\mathrm{i+1,i}} \\ -r_{\mathrm{i,i+1}} & 1 \end{pmatrix} \quad \text{with} \quad \phi = \frac{2\pi n_{\mathrm{i}}}{\lambda_0} d_{\mathrm{i}} \cos(\theta_{\mathrm{i}}) , \tag{2.17}$$

where r and t are the amplitude reflection and transmission coefficients for the respective interface and d is the layer thickness. The bounding layers, which are the ambient medium on the reflection side and the substrate on the transmission side, are taken to be infinitely thick, thus only the interface term is taken into account and not the propagation. The expression for the phase ϕ may be surprising

at first sight, since the path inside the layer is longer by a factor of $\cos(\theta_i)^{-1}$ at oblique incidence. However, the phase refers to the phase acquired in the direction of propagation, wherefore it is equal to the projection of the wavevector onto this axis, multiplied by the pathlength in this direction.

After determining the total transfer matrix M the reflection and transmission coefficients of the stack can be determined with the scattering matrix, which connects the outgoing waves of the system with the incoming ones. The four coefficients in this matrix denote the forward reflection r_{12} and transmission t_{12} coefficients, as well as the backward coefficients r_{21} and t_{21}. The wave-transfer matrix M and the scattering matrix S are connected by

$$S = \begin{pmatrix} t_{12} & r_{21} \\ r_{12} & t_{21} \end{pmatrix} = \frac{1}{D} \begin{pmatrix} AD - BC & B \\ -C & 1 \end{pmatrix}, \tag{2.18}$$

where the four coefficients A, B, C and D are given by Equation 2.15. Even though, the above method is easy to implement in a script, the calculations were mostly done with the python module `tmm` by S. J. Byrnes presented in [45].

The transmission spectrum of a sample coating designed for a wavelength of 1 100 nm consisting of 25 layers of SiO_2 and Nb_2O_5 with the layer arrangement described above, can be seen in Figure 2.6 a). With such a simple stack design, a high reflective mirror with low losses can be achieved. Interestingly, the stack is again highly reflective for a wavelength around 400 nm, which is expectable, since a wave with one third of the wavelength acquires the same phases as the design wavelength, if dispersion is neglected. For the shorter wavelength, the layer sizes are $3\lambda/4$ and, correspondingly, the stack is high-reflective as well. The intensity distribution of the electromagnetic wave for the design

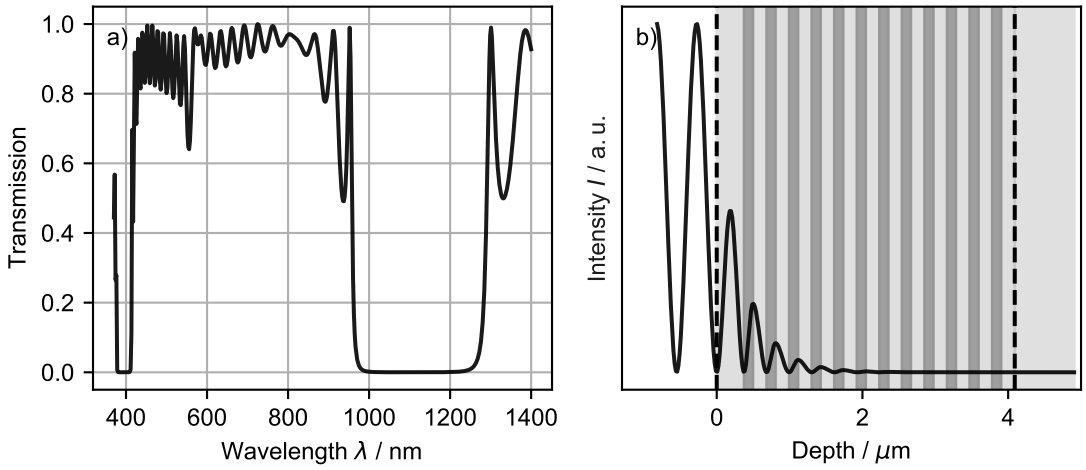

Figure 2.6: *Example dielectric high reflective coating consisting of 24 layers with alternating high and low refractive index (Nb_2O_5 and SiO_2) of thickness $\lambda/4 \cdot n$, and a protective layer out of SiO_2 with a thickness of $\lambda/2 \cdot n$. The design wavelength is 1 100 nm. The transmission spectrum a) indicates the high reflection coefficient at the design wavelength, as well as a second high-reflective interval at shorter wavelengths at around 400 nm. The intensity distribution of an incident electromagnetic wave at 1 100 nm is shown in b), demonstrating the exponential decay of the incident wave inside the dielectric coating.*

wavelength inside the coating is of special interest and can be seen in Figure 2.6 b). An exponential decay of the intensity over approximately one micrometer can be observed. The intensity in the first layer is highest and with the combination of a small cavity waist and high finesse, intensities on the order of $1 \times 10^{11}\,\mathrm{W\,m^{-1}}$ can easily be reached. The SiO_2 layer acts as a protective layer for the stack, since the extinction coefficient is lower than for Nb_2O_5 or Ta_2O_5 [46].

With knowledge of the intensity distribution inside the dielectric coating, we estimate the nonlinear response of the coating material, which will be used in chapter 3 in order to generate photon pairs due to spontaneous four-wave mixing. Furthermore, we will need the intensity distribution of the cavity mode inside the dielectric coating in chapter 5 to determine the coupling of an external pump field to the cavity mode. In this chapter, the second high-reflective region in the spectrum of the dielectric coating is used for stabilization of the cavity length, while the cavity mode at the signal frequency is kept unoccupied.

2.2 Nonlinearities in high-finesse cavities

In the previous section, we discussed the properties of optical resonators and the requirements for achieving a high finesse. Using micromachined and high-reflective coated end facets of fibers, leads to small mode volumes and, therefore, small mode waists on the resonator mirrors. Due to the resonant amplification of the cavity field, intensities of about $1 \times 10^{11}\,\mathrm{W\,m^{-2}}$ on the cavity mirrors are easily reached, even at low incoupled powers of a few hundred micro- or a few milliwatt. Such high intensities cause nonlinear polarization and thermal effects, which are studied in subsection 2.2.1. Nonlinearities in a cavity lead to optical bistability, where the cavity resonance shifts with the amount of light entering the resonator, which is analyzed in subsection 2.2.2. Finally, the coupling of different cavity modes via a third-order nonlinearity of the material polarization is investigated in subsection 2.2.3, where I derive an equation estimating the number of photon pairs produced by spontaneous four-wave mixing inside the cavity.

2.2.1 Nonlinear polarization

The refractive index of a material stems from the dielectric polarization an electromagnetic wave induces in the material. In a simple picture, the electrons inside the medium linearly follow the electric field out of their equilibrium position at low field strengths. The microscopically induced dipole moments are thus proportional to the electric field strength. Hence, the macroscopic polarization of the material, as the sum of all dipole moments induced, is proportional to the field strength as well. The total field inside the material is the displacement field D, which is the superposition of the incident electric field and the induced dielectric polarization, given by [44]

$$\mathbf{D} = \epsilon_0 \mathbf{E} + \mathbf{P}\,, \tag{2.19}$$

which is in general a vector quantity, depending on the polarization of the incident electromagnetic field and the orientation of the material polarization. The medium responds to the electric field linearly with $\mathbf{P} = \epsilon_0 \chi^{(1)} \mathbf{E}$, as long as the electric field strength is much smaller than the characteristic atomic field strength $E_{\mathrm{at}} \approx 5 \times 10^{11}\,\mathrm{V\,m^{-1}}$ [47]. In order to account for higher order effects, the polarization

can be written as a power series in the electric field as

$$P(t) = \epsilon_0(\chi^{(1)}E(t) + \chi^{(2)}E(t)^2 + \chi^{(3)}E(t)^3 + \ldots)\,, \tag{2.20}$$

where χ is the optical susceptibility. For simplicity the vector notation is dropped for now, ordinarily χ is a tensor with increasing rank, accounting for the geometry of different crystal lattices.

In general, the electric field is a superposition of all the applied input fields. Suppose the electric field consists of two electromagnetic waves with frequencies ω_1 and ω_2. The electric field for each wave is a sum of a positive frequency and a negative frequency term $E(\omega) = {}^{E_0}/_2(\exp(i\omega(z/c - t)) + \text{c.c.})$. The quadratic term in the second-order polarization mixes all of the frequency components of the electric field, such that the polarization contains terms with the sum and the difference frequency $\omega_1 \pm \omega_2$, as well as terms with twice the frequency $2\omega_{1/2}$ and time-independent terms. These expressions can act as source terms for new electromagnetic waves, leading to sum and difference frequency generation and electrostriction [47].

The second-order susceptibility $\chi^{(2)}$ is only present in materials without inversion symmetry, which can be seen by the quadratic dependence of the second-order polarization on the electric field [47]. Within this thesis, however, isotropic centrosymmetric materials such as glasses and liquids are studied, which posses inversion symmetry and, thus, a vanishing second-order nonlinearity. Therefore, the analysis is focused on the third-order nonlinearity in the following. Analogue to the second-order nonlinearity, the third order couples three waves. For only one incident frequency the total polarization is given by

$$P = \epsilon_0 \left(\left(\chi^{(1)} + \frac{3}{4}\chi^{(3)}|E|^2 \right) E(\omega) + \frac{1}{4}\chi^{(3)}E(3\omega) \right)\,, \tag{2.21}$$

where in addition to the linear response to the incident radiation, a term proportional to the absolute value of the electric field is present and a term oscillating with thrice the frequency. Using

$$n_2 = \frac{3\chi^{(3)}}{4n_0^2\epsilon_0 c_0} \quad \text{and} \quad I = 2n_0\epsilon_0 c_0|E|^2\,, \tag{2.22}$$

where I is the intensity of the incident radiation, we can define the nonlinear refractive index n_2 via

$$n = n_0 + n_2 \cdot I\,. \tag{2.23}$$

The refractive index thus changes with the intensity of the electric field applied, which is called Kerr effect. The nonlinear refractive index n_2 for SiO_2 is $3 \times 10^{-20}\,\mathrm{m^2\,W^{-1}}$, while it is about one order of magnitude larger for Ta_2O_5 and Nb_2O_5 [48]. It becomes evident that third-order effects appear only at high intensity radiation, which are achievable with lasers.

The intensity of a laser beam is defined generally as the temporal average over many optical periods, which is meaningful, since time scales are usually much longer than optical periods. However, the response of electrons in solid-state systems, liquids and gasses to the oscillating electric field is almost instantaneous, or at most about 100 attoseconds for solids [49], and a few femtoseconds in liquids and gasses [50, 51]. These time scales are far below, or comparable to a period of optical frequencies (1–10 fs), wherefore the refractive index can follow rapid oscillations or changes of the intensity. The refractive index of materials changes due to several processes besides the Kerr effect, which a

nonlinear refractive index can be attributed to. This contains thermal effects, as well as the alignment of anisotropic molecules with the incident electric field in liquids and gasses. While the electronic response of the system is quasi-instantaneous but weak, the other effects are stronger, but occur on longer time scales [52]. The refractive index changes with temperature on time scales of milliseconds and the corresponding nonlinear refractive index n_2^{th} is on the order of $1 \times 10^{-10}\,\text{m}^2\,\text{W}^{-1}$ [47]. Since the thermal nonlinearity depends on absorption of incident radiation in the material, the response time of the entire system can be as long as seconds, due to heat conduction and dissipation. Contributions in liquids including diffusive reorientation of induced dipoles, molecular libration, collisions and vibrations, however, occur on time scales of hundreds of femto- to picoseconds [47, 51] and, thus, do not or barely contribute to refractive index changes at optical periods.

So far, we neglected the general vector properties of the electric field, and the spatial properties of the medium the nonlinearity is studied in. Due to different lattice constants in the x, y and z direction, the susceptibility varies depending on the polarization of the field. In third order, the susceptibility is a tensor of fourth rank that couples three electric input fields to the material polarization. Suppose the total electric field consist of three different frequency components

$$\mathbf{E}(\mathbf{r},t) = \mathbf{E}_1 e^{i(\mathbf{k}_1\cdot\mathbf{r}-\omega_1 t)} + \mathbf{E}_2 e^{i(\mathbf{k}_2\cdot\mathbf{r}-\omega_2 t)} + \mathbf{E}_3 e^{i(\mathbf{k}_3\cdot\mathbf{r}-\omega_3 t)} + \text{c.c.}\,. \tag{2.24}$$

Then the i-th component of the nonlinear polarization is given by

$$P_i(\omega_p) = \sum_{j,k,l}\sum_{(mno)} \chi^{(3)}_{ijkl}(\omega_p;\omega_m,\omega_n,\omega_o)E_j(\omega_m)E_k(\omega_n)E_l(\omega_o)\,, \tag{2.25}$$

where the sum of the single frequencies $\omega_p = \omega_m + \omega_n + \omega_o$ is kept fixed and runs over positive and negative frequencies, and the indices i, j, k, l denote the spatial coordinates x, y, z [47]. The time dependence of the polarization is determined by the frequencies ω_p. Analogue to the second-order nonlinearity, the third order mixes the frequencies of all the electromagnetic waves. As a consequence, the total polarization contains 2×22 different frequency terms, with every possible mixture of the input frequencies $\omega_m \pm \omega_n \pm \omega_o$ with $m, n, o \in 1, 2, 3$ and the respective negative frequency terms.

Similar to the second-order nonlinear polarization, the time-dependent polarization contributions result in source terms leading to four-wave mixing. In this process, the coupling of three incident electromagnetic waves, due to the third-order susceptibility, gives rise to a fourth wave with a frequency according to the oscillation frequency ω_p of the polarization. The susceptibility, thereby, depends on the material geometry and determines the coupling between the different waves. For isotropic, centrosymmetric materials like glasses and liquids, only two entries in the susceptibility tensor are independent and $3\chi^{(3)}_{iiii} = \chi^{(3)}_{jkkj} = \chi^{(3)}_{jkjk}$ [50]. The coupling via the third-order nonlinearity expresses itself in various effects, such as self-focusing [53], self-phase and cross-phase modulation [54, 55] and self-trapping of light [56, 57], which are processes stemming from time-independent mixing terms. Furthermore, the intensity dependence of the refractive index leads to a bistable operation of cavities containing a nonlinear medium, which we will analyze in the next subsection 2.2.2. Four-wave mixing processes are third harmonic generation [58, 59], as given by the corresponding term in Equation 2.21, Raman scattering processes, where e.g. vibrational levels of molecules are investigated [60, 61], and electromagnetically induced transparency [62, 63].

If one of the three incident electromagnetic waves is a vacuum mode, the nonlinear polarization leads to the production of correlated photon pairs. This process is called spontaneous four-wave mixing,

where two of the incident pump photons are annihilated and a photon pair is created. Compared to the effects mentioned and studied in this subsection, this process cannot be explained classically and demands a quantum mechanical treatment. We will investigate this further in subsection 2.2.3, where we calculate the coupling of a pumped cavity mode to neighboring signal and idler modes via the third-order nonlinear polarization.

2.2.2 Optical bistability in high-finesse cavities

As seen in the previous chapter, high intensities can lead to nonlinear effects that alter the refractive index of a medium. Especially thermal effects are of interest, since they can be several orders of magnitude larger than electronic and molecular responses, and play an important role while operating a high-finesse cavity. Thermal effects can influence both the mechanical cavity length due to thermal expansion and the optical cavity length via the temperature dependence of the refractive index. The optical path length $l_{\mathrm{opt}} = n \cdot l$ is, thus, temperature-dependent and the total differential is

$$\mathrm{d}l_{\mathrm{opt}} = n\frac{\partial l}{\partial T}\mathrm{d}T + l\frac{\partial n}{\partial T}\mathrm{d}T + l\frac{\partial n}{\partial I}\mathrm{d}I\,, \tag{2.26}$$

where T is the temperature and I is the incident intensity. The first term refers to thermal expansion and is negative, since the expanding material shrinks the resonator's length. The second term corresponds to the thermo-optic response and increases the optical cavity length with rising temperature for most materials. The last term refers to the electronic contribution of the medium and can be neglected, since the thermo-optic and thermal expansion coefficients are several orders of magnitude larger than the intensity dependence of the refractive index. All of the temperature-dependent terms depend on the intensity as well, since the change in temperature is induced by absorption of the incident light. If the length of an optical resonator containing an absorptive medium is scanned over a cavity resonance, the intensity inside the resonator increases and, thus, the optical length changes in addition to the mechanical scan. With changing length, the free spectral range is changed as well, shifting the cavity resonance with increasing intra-cavity power. Consequently, the resonance frequency is shifted by $\Delta\nu_{\mathrm{res}}$ according to

$$\tilde{\nu}_{\mathrm{res}} = q\frac{c}{2(l+\Delta l)} \approx \nu_{\mathrm{res}}\left(1 - \frac{\Delta l}{l}\right) \quad \Rightarrow \quad \Delta\nu_{\mathrm{res}} \approx -\nu_{\mathrm{res}}\frac{\Delta l}{l}\,. \tag{2.27}$$

The result is a bistable operation altering the characteristic Lorentzian line shape (see Equation 2.6) to an asymmetric and tilted Lorentzian, due to a power hysteresis curve [64].

A self-consistent equation for the altered line shape can be acquired by inserting the additional detuning in the Lorentzian in Equation 2.6. We find the relation given by [64]

$$\frac{P_{\mathrm{out}}}{P_{\mathrm{in}}} = \frac{1}{1 + (\Delta - \beta)^2}\,, \tag{2.28}$$

where $\Delta = (\nu - \nu_0)/\delta\nu$ is the detuning of the incident radiation to the resonance in terms of half the resonator linewidth $\delta\nu$, and $\beta \approx -\frac{\nu_{\mathrm{res}}}{\delta\nu}\frac{\Delta l}{l}$ is the additional power dependent shift from thermal effects. If the cavity length is scanned over a resonance of the incident laser frequency, the scan direction, e.g. from blue to red detuned or vice versa, determines the acquired line shape, since the respective response of the nonlinearity is unidirectional for rising intensity. The scan velocity, thereby, needs to

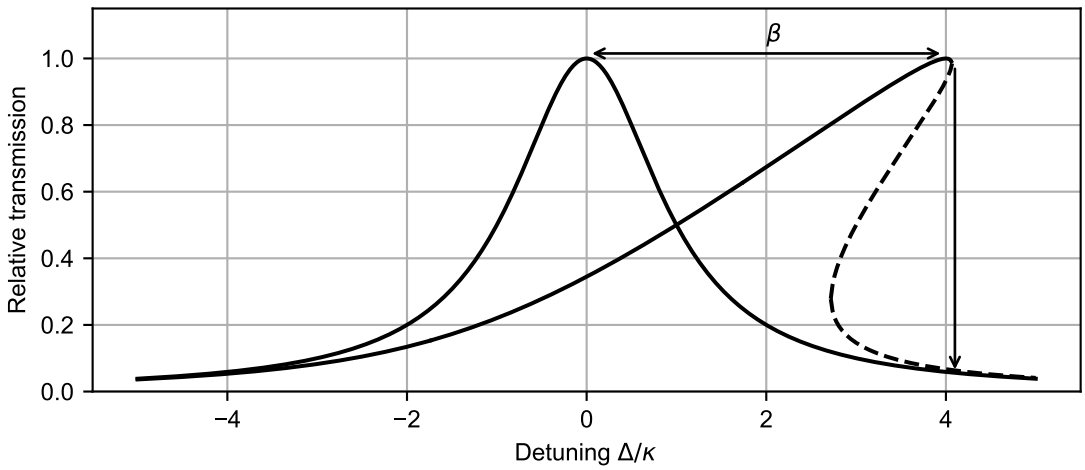

Figure 2.7: *The asymmetric and tilted Lorentzian line shape in comparison to an unaltered cavity resonance. The altered curve is a solution to the self-consistent Equation 2.28 solved analytically for $\beta = 4$, which is defined as the spectral distance between the two maximum values normalized to half the cavity linewidth. The solid lines refer to stable solutions of the equation, while the dashed lines belong to unstable solutions. Therefore, the intensity in the resonator abruptly falls of two zero, when the maximum is surpassed, indicated by the vertical arrow.*

be in the adiabatic limit, such that the material response is faster than the scan over the resonance [64]. Assuming, exemplarily, solely thermal expansion, the scan velocity is increased when the cavity is scanned from blue to red detuned, since the expanding cavity mirrors counteract the increasing length due to the applied scan. Consequently, the resonance line shape is broadened, leading to a slower increase in intra-cavity power, and an abrupt collapse of the intra-cavity power, when the resonance is surpassed. This behavior is illustrated in Figure 2.7 for a lineshift of $\beta = 4$ via the smoother increase and the almost instantaneous decrease, indicated by the vertical arrow. The collapse is caused by the cooling of the cavity after the resonance is surpassed, yielding a strongly increased scan velocity. For the scan direction from red to blue, e.g. decreasing cavity length, the scan velocity is increased before the resonance, leading to a steeper rise of the intra-cavity power. When the resonance is surpassed, the power decays more slowly, since the scan velocity is decreased due to the material contraction by cooling.

The line shapes of the shifted and tilted resonance curves are described in terms of thermal expansion, e.g. the first term in Equation 2.26, however, similar explanations hold for the thermo-optic effect. If the thermo-optic coefficient is positive—as it is for most glasses in room temperature—the effects are complementary, since the optical path length increases with rising refractive index.

We will observe bistability in chapter 3, where predominantly the thermal expansion of the dielectric coating and mirror substrates lead to the shifting resonance. In chapter 4 the bistable operation is primarily due to the thermo-optic effect of the liquid filling the cavity. Furthermore, thermal effects will be a reference in the alignment of the external pump lasers with respect to the cavity mode in chapter 5.

2.2.3 Photon-pair generation by parametric excitation of cavity modes

In subsection 2.2.2 we studied the nonlinear effects inside high-finesse cavities arising due to thermal expansion of the cavity mirrors, and the change of the refractive index by temperature changes of the medium filling the cavity. We neglected the contribution to the varying refractive index by the intense laser radiation, since thermal effects govern the dynamics on the time scales observed. In the following we want to study the influence of the electronic response on the dynamics of a cavity containing a third-order nonlinear medium, i.e. we want to investigate the coupling of a strongly pumped cavity mode E_p to neighboring, and unoccupied signal E_s and idler E_i modes. This process is known as spontaneous four-wave mixing (SFWM), where two pump photons are annihilated and a signal and idler photon pair is generated [65, 66]. The emitted photon pair is thereby correlated and the vacuum state is squeezed [67–69].

In order to determine the rate of photons generated by the SFWM process, we need to calculate and examine the Hamiltonian of the system. The pump mode will be described classically, since it is in a coherent state with a large number of photons. Both signal and idler modes, however, are described quantum mechanically. The electromagnetic energy for a non-magnetic medium is [70]

$$H = \frac{1}{2}\int_V \mathrm{d}^3 r \, \frac{1}{\mu_0}\mathbf{B}\cdot\mathbf{B} + \mathbf{E}\cdot\mathbf{D}\,, \tag{2.29}$$

where V is the quantization volume of the cavity mode, μ_0 is the vacuum permeability, $\mathbf{B}$ the magnetic field, $\mathbf{E}$ the electric field and $\mathbf{D}$ is the displacement field as defined in Equation 2.19. For simplicity, we drop the vector notation in the following, by assuming that all fields are equally linearly polarized. Inserting the definition for the displacement field into the electromagnetic energy in Equation 2.29, we find the nonlinear term

$$H_\mathrm{nl} = \frac{1}{2}\int_V \mathrm{d}^3 r \, \epsilon_0 \chi^{(3)} E^4\,, \tag{2.30}$$

where the integration volume denotes the volume of the nonlinear medium inside the cavity. A free classical electromagnetic wave travelling in z-direction is described by a superposition of positive and negative frequency solutions of the Helmholtz equation and reads

$$E = E^{(+)} + E^{(-)} = \frac{1}{2}\tilde{E}(e^{i(kz-\omega t)} + \mathrm{c.c.})\,, \tag{2.31}$$

where $\tilde{E} = \tilde{E}(x, y)$ is the amplitude containing the transverse spatial profile, k is the wave vector and ω is the frequency. The cavity mode, however, is a standing wave, which is given as the sum of two counter propagating plane waves, where the reflected wave is phase shifted by π (see subsection 2.1.1). Thus, the cavity mode is given by

$$E_\mathrm{p} = E(k) - E(-k) = 2\tilde{E}\sin(kz)\cos(\omega t)\,. \tag{2.32}$$

In second quantization of the electromagnetic field, each frequency mode is described as a harmonic oscillator, where a single excitation of the mode corresponds to a photon. The positive and negative frequency modes in Equation 2.31 thus can be attributed to the annihilation and creation operators, respectively [3, 70, 71]. The operator for a free electric field mode travelling in z-direction in the

Schrödinger picture is [70]

$$\hat{E} = -i\sqrt{\frac{\hbar\omega}{2\epsilon_0 V}}g(x,y)(\hat{a}e^{ikz} - \hat{a}^\dagger e^{-ikz}) \quad , \tag{2.33}$$

where V is the quantization volume of the field mode, $g(x,y)$ the transversal mode profile and $\hat{a}$ and $\hat{a}^\dagger$ are the destruction and annihilation operators for a photon of frequency ω. Analogous to the classical case, the operator for a cavity mode can be given as [28]

$$\hat{E} = -\sqrt{\frac{2\hbar\omega}{\epsilon_0 V}}\sin(kz)g(x,y)(\hat{a} - \hat{a}^\dagger)\,. \tag{2.34}$$

Assuming a gaussian transversal mode profile $g(x,y) = \exp(-(x^2+y^2)/\sigma^2)$ and a cavity of length l, the quantization volume is $V = \pi\sigma^2 l$.

The total electric field is a superposition of all three cavity modes, which are the classical pump mode E_p, and the two initially unoccupied quantized signal $\hat{E}_\mathrm{s}$ and idler modes $\hat{E}_\mathrm{i}$. Evaluating the fourth power of the electric field in the nonlinear Hamiltonian, reveals following terms

$$\begin{aligned} E^4 &= (E_\mathrm{p} + \hat{E}_\mathrm{s} + \hat{E}_\mathrm{i})^4 \\ &= E_\mathrm{p}^4 + (\hat{E}_\mathrm{s} + \hat{E}_\mathrm{i})^4 + 4(E_\mathrm{p}^3(\hat{E}_\mathrm{s} + \hat{E}_\mathrm{i}) + E_\mathrm{p}(\hat{E}_\mathrm{s} + \hat{E}_\mathrm{i})^3) + 6E_\mathrm{p}^2(\hat{E}_\mathrm{s} + \hat{E}_\mathrm{i})^2 \\ &\simeq E_\mathrm{p}^4 + 4E_\mathrm{p}^3(\hat{E}_\mathrm{s} + \hat{E}_\mathrm{i}) + 6E_\mathrm{p}^2(\hat{E}_\mathrm{s}^2 + \hat{E}_\mathrm{i}^2 + 2\hat{E}_\mathrm{s}\hat{E}_\mathrm{i})\,, \end{aligned} \tag{2.35}$$

where only terms are kept which are at least in second order of the pump mode E_p, since in comparison, the terms are suppressed by the amplitude of the pump beam, or the amplitude squared. The amplitude is proportional to the square root of the photon flux, which is around 10^{18} photons per second for a beam with a power on the order of watt. We want to understand the physical processes behind the terms contained in above equation. Terms to the power of four are the mixing of a single electric field mode with itself. Using the expression for the quantized, not classical[3], field mode, we get in total 16 combinations of the annihilation and creation operators, where each term contains four operators, respectively. This mixing happens for every mode, wherefore the indices are dropped for now. In principle, there are four types of mixtures of the operators, corresponding to four photon absorption $\hat{a}^4$ and emission $(\hat{a}^\dagger)^4$, three photon absorption and emission of one photon $(\hat{a}^\dagger)^3\hat{a}$, as well as the reverse process $\hat{a}^3\hat{a}^\dagger$ and, finally, two photon emission and absorption $(\hat{a}^\dagger)^2\hat{a}^2$, with every permutation of the terms. The last term corresponds to the Kerr effect [71, 72] slightly shifting the cavity resonance, while the other terms do not couple to real resonant, only virtual levels and can, thus, be neglected. The different multi-photon absorption and emission processes are described pictorially in Figure 2.8. Terms mixing different field modes describe similar multiphoton absorption and emission processes, coupling to different virtual levels, since the frequencies are not equal. The last expression, mixing the pump mode with the signal or idler mode, contains in addition to the multiphoton transition terms, Kerr terms for a mixture of two modes like $\hat{a}_1^\dagger\hat{a}_2^\dagger\hat{a}_1\hat{a}_2$ [71].

Spontaneous four-wave mixing terms, where two of the pump photons are annihilated and two

[3] As well as we can attribute the photon annihilation and creation operators to the positive and negative frequency terms of an electromagnetic wave, we can do the opposite. For the sake of clarity, we discuss the different mixtures of the field in terms of operators, not fields.

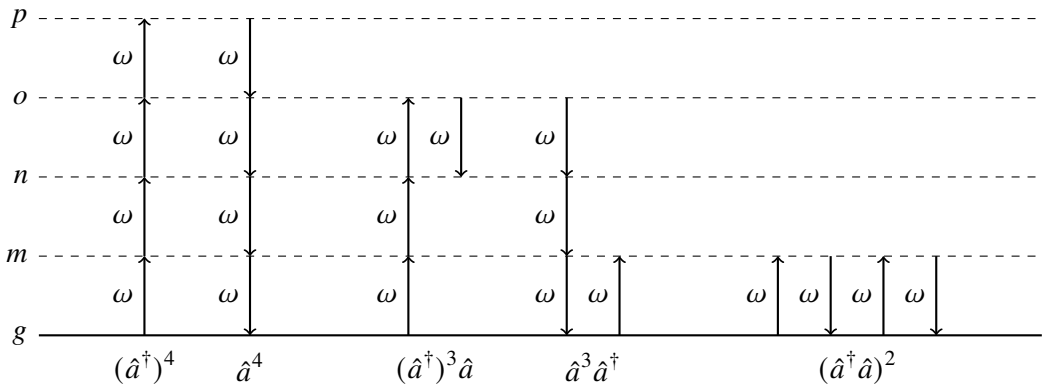

Figure 2.8: *Energy diagrams representing the multi-photon absorption and emission processes, coupling different virtual levels. The processes are described by the nonlinear Hamiltonian in Equation 2.30, but refer to only one component of the electromagnetic field. The last term describes the Kerr effect, effectively shifting the cavity resonance.*

signal, or two idler photons are created, are present as well. Terms for the reverse processes are also involved, however, since we assume the frequencies of the signal and idler modes to be shifted by one or more free spectral ranges with respect to the pump mode, these terms cannot be on resonance. Thus, for the spontaneous four-wave mixing process only the last term is considered, which is $E_\mathrm{p}^2\hat{E}_\mathrm{s}\hat{E}_\mathrm{i}$ and all other terms will be neglected. Notice, that this term still contains off-resonant terms, like creation of two pump photons, and one signal and idler photon, which will be eliminated later. The Kerr terms do not contribute to the dynamics of the system, but slightly shift the energy levels, i.e. the cavity resonance frequencies, and will, therefore, be neglected for simplicity. We can write the nonlinear part of the Hamiltonian as

$$\hat{H}_\mathrm{nl} = \int_V \mathrm{d}^3 r\, \epsilon_0 \chi^{(3)} (6E_\mathrm{p}^2\hat{E}_\mathrm{s}\hat{E}_\mathrm{i}) \propto \frac{\hbar}{\pi\sigma^2 l}\sqrt{\frac{\omega_\mathrm{i}\omega_\mathrm{s}}{\epsilon_\mathrm{i}\epsilon_\mathrm{s}}} n_0 n_2 I \cos^2(\omega_\mathrm{p} t)\eta_\perp\eta_\parallel(\hat{a}_\mathrm{s} - \hat{a}_\mathrm{s}^\dagger)(\hat{a}_\mathrm{i} - \hat{a}_\mathrm{i}^\dagger)\,, \quad (2.36)$$

where $\eta_\perp$ and $\eta_\parallel$ are the couplings stemming from the integration over the spatial mode profiles and are given by

$$\eta_\perp = \int_{-\infty}^{+\infty}\int_{-\infty}^{+\infty} \mathrm{d}x\mathrm{d}y\, g_\mathrm{p}(x,y)^2 g_\mathrm{s}(x,y) g_\mathrm{i}(x,y) = \frac{\pi\sigma^2}{4}\,, \quad (2.37)$$

assuming the same waist σ for all three modes, and

$$\tilde{\eta}_\parallel = \int_{-l_\mathrm{nl}/2}^{l_\mathrm{nl}/2} \mathrm{d}z\, \sin^2(k_\mathrm{p} z)\sin(k_\mathrm{s} z)\sin(k_\mathrm{i} z) \quad (2.38)$$

$$\propto \int_{-l_\mathrm{nl}/2}^{l_\mathrm{nl}/2} \mathrm{d}z\, (e^{i(2k_\mathrm{p}+k_\mathrm{s}+k_\mathrm{i})z} - e^{i(2k_\mathrm{p}-k_\mathrm{s}+k_\mathrm{i})z} - e^{i(2k_\mathrm{p}+k_\mathrm{s}-k_\mathrm{i})z} + e^{i(2k_\mathrm{p}-k_\mathrm{s}-k_\mathrm{i})z} \quad (2.39)$$

$$- 2(e^{i(k_\mathrm{s}+k_\mathrm{i})z} - e^{i(k_\mathrm{s}-k_\mathrm{i})z}) + \mathrm{c.c.})\,. \quad (2.40)$$

$\eta_\parallel$ contains the momentum conservation and phase-matching condition for an effective generation

of the photon pairs at the signal and idler frequencies, which becomes clearer if the length of the nonlinear medium l_{nl} is extended to infinity. In this case, the integral over each exponential function gives the δ-function with the respective sum of wave vectors as argument. Intuitively, the terms contain the different mixing of momenta in the photon-pair generation processes. Since every mode is a standing wave inside the cavity, we have forward- and backward-travelling photons with respect to the cavity axis z, which is evident by the plus and minus signs in the wave vector sums. Equation 2.38, therefore, contains every possible way to add up the momenta $k_{\mathrm{p}} \pm k_{\mathrm{p}} \pm k_{\mathrm{s}} \pm k_{\mathrm{i}}$. It is clear, that only those terms have a significant contribution to the generation of photon pairs, where the sum of the wavevectors is (close to) zero, since these fulfill the phase-matching condition known from classical nonlinear optics [47]. Solving the integral for a particular sum of wavevectors, e.g. $\Delta k = 2k_{\mathrm{p}} - k_{\mathrm{s}} - k_{\mathrm{i}}$, and taking a pre-factor of $2/l_{\mathrm{nl}}$ into account, gives the characteristic sinc-function

$$\eta_{\mathrm{PM}} = \frac{\sin(\frac{\Delta k \cdot l_{\mathrm{nl}}}{2})}{\frac{\Delta k \cdot l_{\mathrm{nl}}}{2}} \tag{2.41}$$

for the coherent build-up of the output mode across the nonlinear medium in the classical case. Figure 2.9 shows the phase-matching quality dependent on the wavevector mismatch for different lengths of the nonlinear medium. In the case of perfect phase matching $\Delta k = 0$, the coupling between the modes does not depend on the length of the medium and the nonlinear process is not suppressed. With rising length of the nonlinear medium, the phase matching is much more important for an efficient coupling between the modes and the allowed wavevector mismatch becomes smaller. We can define the maximum wavevector mismatch in dependence of the length of the nonlinear medium as $\Delta k \leq 1/l$ [47]. In the classical case, the phase matching is the coherent build-up of output radiation

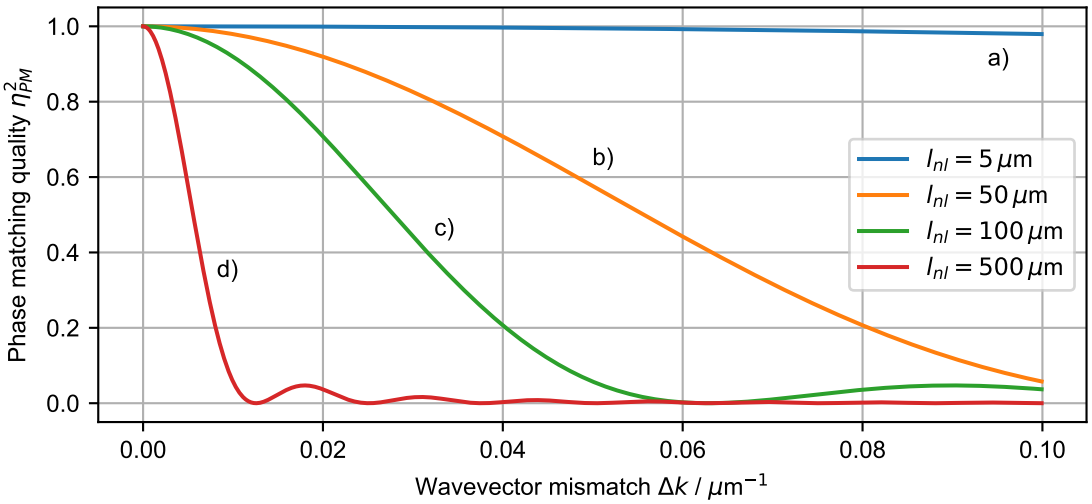

Figure 2.9: *Phase matching η^2_{PM} (see Equation 2.41) for different lengths of the nonlinear medium in dependence of the wavevector mismatch Δk. With increasing length, the allowed wavevector mismatch gets smaller, since the radiation cannot coherently build up along the whole nonlinear medium and the waves dephase. For a short length, the allowed wavevector mismatch is much larger than for longer nonlinear media.*

along the nonlinear medium. Out of phase partial waves do not interfere constructively and no output wave can be generated. Since we are interested in the creation of single photons, this perspective does not apply. The phase matching is here rather an overlap integral determining the coupling of the pump mode to the vacuum modes. If the waves are out of phase, the coupling is reduced, since the vacuum modes do not "see" the driving of the nonlinear polarization, and cannot be excited efficiently.

So far, we treated the problem in the Schrödinger picture, where the entire time dependence is contained in the wavefunction and operators do not change in time. In the following, we want to transform the nonlinear Hamiltonian to the interaction picture, where the time evolution is split between the operators and the wavefunction. The operators evolve according to the free Hamiltonian H_0, while the wavefunction contains the evolution due to the total Hamiltonian $H = H_0 + \hat{H}_{\mathrm{nl}}$. The transformation for an operator $\hat{A}$ to the interaction picture is given by the Baker-Hausdorff theorem [73]

$$\hat{A}_{\mathrm{I}} = e^{\frac{i}{\hbar}\hat{H}_0 t}\,\hat{A}\,e^{-\frac{i}{\hbar}\hat{H}_0 t} \tag{2.42}$$

$$= \hat{A} + \frac{it}{\hbar}[\hat{H}_0, \hat{A}] + \frac{1}{2!}\left(\frac{it}{\hbar}\right)^2 [\hat{H}_0, [\hat{H}_0, \hat{A}]] + \frac{1}{3!}\left(\frac{it}{\hbar}\right)^3 [\hat{H}_0, [\hat{H}_0, [\hat{H}_0, \hat{A}]]] + \dots\,. \tag{2.43}$$

Here the free Hamiltonian is simply the energy in each of the unoccupied signal and idler modes

$$\hat{H}_0 = \hbar\omega_{\mathrm{s}}\hat{a}_{\mathrm{s}}^{\dagger}\hat{a}_{\mathrm{s}} + \hbar\omega_{\mathrm{i}}\hat{a}_{\mathrm{i}}^{\dagger}\hat{a}_{\mathrm{i}}\,. \tag{2.44}$$

The destruction operator, thus, transforms like $\hat{a}_{\mathrm{I}}(t) = \hat{a}e^{-i\omega t}$. We observe that the creation and annihilation operators evolve with the respective frequency of their modes, while they can be related to the negative and positive frequency solution of a classical mode function. Transforming the Hamiltonian to the interaction picture, we find several products of the signal and idler creation and annihilation operators, oscillating with the sum or difference frequency, respectively. Taking the temporal evolution of the pump into account, we find terms with $\omega_{\mathrm{p}} \pm \omega_{\mathrm{p}} \pm \omega_{\mathrm{s}} \pm \omega_{\mathrm{i}}$, and the corresponding negative frequency terms. We assume the signal and idler frequencies to be shifted by an integer multiple of the free spectral range up- and downwards with respect to the pump frequency. Thus only the two terms $2\omega_{\mathrm{p}} - \omega_{\mathrm{s}} - \omega_{\mathrm{i}}$, and its negative counterpart can be on resonance and give a significant contribution to the dynamics of the system. Therefore, we only consider terms with a time dependence close or equal to zero, which is the rotating wave approximation (RWA) [74]. From this perspective it is clear why we can neglect the multi-photon absorption and emission terms, since these oscillate at very high frequencies and average out. Finally, the Hamiltonian in the interaction picture is

$$\hat{H}_{\mathrm{int}}(t) = \frac{\hbar}{l}\epsilon_0\sqrt{\frac{\omega_{\mathrm{i}}\omega_{\mathrm{s}}}{\epsilon_{\mathrm{i}}\epsilon_{\mathrm{s}}}}n_0 n_2 I\eta_{\parallel}(\hat{a}_{\mathrm{s}}\hat{a}_{\mathrm{i}}e^{i(2\omega_{\mathrm{p}}-\omega_{\mathrm{s}}-\omega_{\mathrm{i}})t} + \hat{a}_{\mathrm{s}}^{\dagger}\hat{a}_{\mathrm{i}}^{\dagger}e^{-i(2\omega_{\mathrm{p}}-\omega_{\mathrm{s}}-\omega_{\mathrm{i}})t})\,. \tag{2.45}$$

For simplicity, the pump mode is treated classically, however, we could describe it as a coherent state and do similar calculations as above, in order to get the Hamiltonian in a full quantum treatment of the three coupled cavity modes. The Hamiltonian in the interaction picture is then

$$\hat{H}_{\mathrm{int}}(t) \propto ((\hat{a}_{\mathrm{p}}^{\dagger})^2\hat{a}_{\mathrm{s}}\hat{a}_{\mathrm{i}}e^{i(2\omega_{\mathrm{p}}-\omega_{\mathrm{s}}-\omega_{\mathrm{i}})t} + (\hat{a}_{\mathrm{p}})^2\hat{a}_{\mathrm{s}}^{\dagger}\hat{a}_{\mathrm{i}}^{\dagger}e^{-i(2\omega_{\mathrm{p}}-\omega_{\mathrm{s}}-\omega_{\mathrm{i}})t})\,, \tag{2.46}$$

which shows the characteristic terms for spontaneous four-wave mixing, where two pump photons are annihilated and a pair of signal and idler photons is created $(\hat{a}_{\mathrm{p}})^2\hat{a}_{\mathrm{s}}^{\dagger}\hat{a}_{\mathrm{i}}^{\dagger}$.

Before we continue to calculate the photon pair generation rate, we want to have a closer look at the Hamiltonian and the corresponding state. Initially, our wavefunction is simply in the vacuum state, i.e. it does not contain any photons $|\Psi_S\rangle = |0\rangle$. Due to the nonlinearity, however, the vacuum is squeezed, since it actually contains real photons, as we will see in the following. On resonance, the Hamiltonian is time-independent, i.e. $2\omega_c - \omega_s - \omega_i = 0$, and the time evolution of the wavefunction $|\Psi\rangle$ is

$$|\Psi_I(t)\rangle = \hat{U}(t, t_0)\,|\Psi_S(t)\rangle = e^{i\hat{H}_0 t/\hbar} e^{-i(\hat{H}_0+\hat{H}_{nl})t/\hbar}\,|\Psi_S\rangle\ . \tag{2.47}$$

The time evolution following the free Hamiltonian $\hat{H}_0$ does not change the vacuum state, but the nonlinear term does, because of the two creation operators for the signal and idler modes. With application of the time evolution due to the full Hamiltonian H, the new Schrödinger picture state $|\Psi_S(t)\rangle$ is

$$|\Psi_S(t)\rangle = e^{-i(\hat{H}_0+\hat{H}_{nl})t/\hbar}\,|0\rangle = \sum_k \left(-\frac{it}{\hbar}\right)^k \frac{1}{k!}(\hat{H}_0 + \hat{H}_{nl})^k\,|0\rangle\ . \tag{2.48}$$

We see that with successive application of the nonlinear Hamiltonian, the state becomes a superposition of number states containing even numbers of photons. To first order—since the coupling constant is very weak—the resulting state has the form

$$|\Psi_S(t)\rangle = c_0\,|0,0\rangle + c_1\,|1,1\rangle \quad \text{with} \quad c_i \in \mathbb{C},\ \text{and}\ |c_0|^2 + |c_1|^2 = 1\,, \tag{2.49}$$

where the state $|1,1\rangle$ contains one signal and idler photon, respectively. This state is called a squeezed vacuum state [75] and demonstrates the creation of pairs of photon pairs due to the third-order nonlinearity.

Calculating the photon-pair rate via the density matrix After we calculated the Hamiltonian describing the dynamics of our system, we want to determine the generation rate of signal and idler photons. This can be done by calculating the expectation value of the photon number operator for the signal, or idler mode $\langle \hat{a}_s^\dagger \hat{a}_s\rangle = \langle \hat{a}_i^\dagger \hat{a}_i\rangle$. We can achieve this by solving the master equation for the system's density matrix $\hat{\rho} = |\Psi\rangle\langle\Psi|$ [76]

$$\dot{\hat{\rho}} = -\frac{i}{\hbar}[\hat{H}_{int}, \hat{\rho}] + \mathcal{L}(\hat{\rho})\,, \tag{2.50}$$

where $|\Psi\rangle$ is the wavefunction of the system and $\mathcal{L}$ is the Lindblad super-operator containing the dissipation of the system to the surrounding environment. The operator is given in a diagonal form as [76]

$$\mathcal{L}(\hat{\rho}) = \sum_{j=1}^{N^2-1} \gamma_j \left(\hat{L}_j \hat{\rho} \hat{L}_j^\dagger - \frac{1}{2}\left\{\hat{L}_j^\dagger \hat{L}_j, \hat{\rho}\right\}\right)\,. \tag{2.51}$$

Here, the operators $\hat{L}_j$ are the system's ladder operators $\hat{a}_j$, the curly brackets denote the anticommutator and γ_j is the dissipation rate of each mode given by the cavity decay rate κ.

We want to express the wavefunction $|\Psi\rangle$ as a superposition of Fock states, i.e. photon number

states $|n_1\rangle \otimes |n_2\rangle \otimes \ldots \otimes |n_N\rangle = |n_1, n_2, \ldots, n_N\rangle$. In general, each mode can be occupied by infinitely many photons, which leads to a density matrix with infinitely many entries. Additionally, without specifying the signal and idler mode, there are, in principle, infinitely many modes the pump mode can couple to, as long as energy conservation is fulfilled. This is ensured by the RWA and the time dependence in the exponential function ($\exp(\pm i\Delta t)$ with $\Delta = 2\omega_p - \omega_s - \omega_i$). We want to restrict the following calculations to two modes, which are shifted by an integer multiple of the free spectral range up- and downwards with respect to the pump mode. The restriction to two modes is a valid simplification, since the spectral distance between modes is not necessarily equal due to dispersion, which is studied in section 3.4. Furthermore, we restrict the states to contain at most one signal and idler photon each, which is reasonable, since we expect the cavity decay rate to be much larger than the photon-pair generation rate, and the coupling from the pump to the vacuum modes is weak ($\eta \ll \kappa$). We define the wavefunction of the system

$$|\Psi\rangle = c_{00}\,|0,0\rangle + c_{10}\,|1,0\rangle + c_{01}\,|0,1\rangle + c_{11}\,|1,1\rangle := c_0\,|0\rangle + c_1\,|1\rangle + c_2\,|2\rangle + c_3\,|3\rangle \ . \tag{2.52}$$

Each ket-state can be expressed as a four row vector and consequently the density matrix is a 4×4 matrix. We can calculate it as

$$\hat{\rho} = \sum_{mn} \rho_{mn}\,|m\rangle\langle n| \quad \text{with} \quad \rho_{mn} := c_m c_n^* \,, \tag{2.53}$$

where m and n run from 0 to 3. Inserting Equation 2.53 in the master equation Equation 2.50, we find at zero detuning $\Delta = 0$ an expression for the commutator

$$-\frac{i}{\hbar}[\hat{H}_{\text{int}}, \hat{\rho}] = -i\eta \begin{pmatrix} \rho_{30} - \rho_{03} & \rho_{31} & \rho_{32} & \rho_{33} - \rho_{11} \\ -\rho_{13} & 0 & 0 & \rho_{10} \\ -\rho_{23} & 0 & 0 & \rho_{20} \\ -(\rho_{33} - \rho_{11}) & -\rho_{01} & -\rho_{02} & \rho_{03} - \rho_{30} \end{pmatrix}. \tag{2.54}$$

The matrix nicely demonstrates the coupling between the two-photon state and the vacuum state, given by the entries on the diagonal. For the dissipation to the environment via the Lindblad term we find

$$\mathcal{L}(\hat{\rho}) = \frac{\kappa}{2} \begin{pmatrix} 2(\rho_{11} + \rho_{22}) & 2\rho_{23} - \rho_{01} & 2\rho_{13} - \rho_{02} & -2\rho_{03} \\ 2\rho_{32} - \rho_{10} & 2(\rho_{33} - \rho_{11}) & -2\rho_{12} & 2\rho_{13} \\ 2\rho_{31} - \rho_{20} & -2\rho_{21} & 2(\rho_{33} - \rho_{22}) & -2\rho_{23} \\ -2\rho_{30} & 2\rho_{31} & -2\rho_{32} & -4\rho_{33} \end{pmatrix}. \tag{2.55}$$

This term shows the coupling between the different number states on the diagonal by stepwise reduction of the photon number, due to the loss via the the cavity decay.

In total, the master equation contains 16 differential equations, which can easily be solved analytically in the steady state ($\dot{\hat{\rho}} = 0$). Using $\text{tr}(\hat{\rho}) = 1$ [76], we find

$$\hat{\rho} = -\frac{1}{2\eta^2 + \kappa^2} \begin{pmatrix} \eta^2 - \kappa^2 & 0 & 0 & i\eta\kappa \\ 0 & -\eta^2 & 0 & 0 \\ 0 & 0 & -\eta^2 & 0 \\ -i\eta\kappa & 0 & 0 & -\eta^2 \end{pmatrix}. \tag{2.56}$$

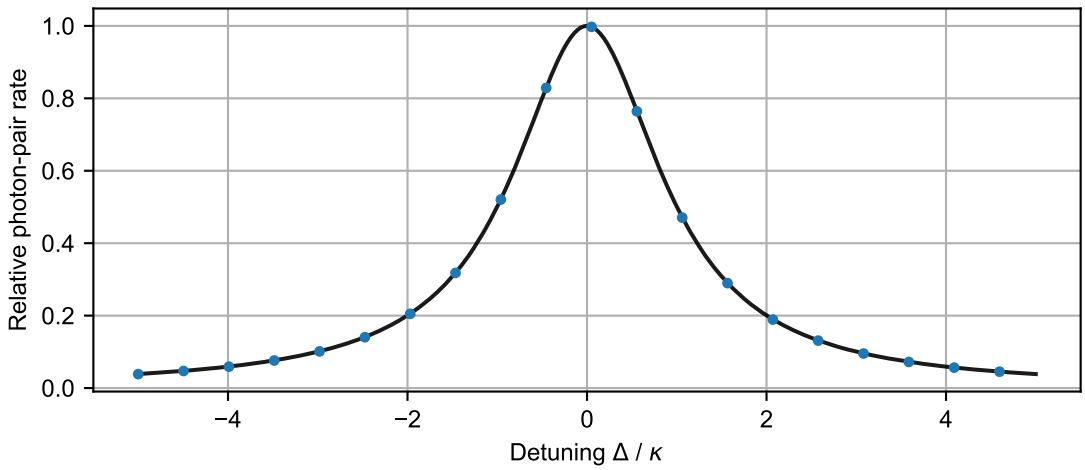

Figure 2.10: *Relative photon-pair rate depending on the spectral difference of up- and downwards shifted modes to the pump mode. The spectral width is equal to the cavity linewidth as confirmed by the overlaid data points calculated from a Lorentzian with half width at half maximum κ.*

The expectation value of an operator A can be calculated with the density matrix as $\langle \hat{A} \rangle = \mathrm{tr}(\hat{\rho}\hat{A})$ [76], from which we can calculate the photon-pair rate per sideband emitted by the cavity

$$\Gamma = \kappa \langle \hat{a}_\mathrm{s}^\dagger \hat{a}_\mathrm{s} \rangle = 2\frac{\kappa\eta^2}{2\eta^2 + \kappa^2} \approx \frac{2\eta^2}{\kappa} = \frac{F\Delta\omega_\mathrm{fsr}}{\pi^2}(k_\mathrm{c} n_2 I \eta_\parallel)^2 \,, \tag{2.57}$$

where I is the resonantly enhanced intensity of the pump mode inside the cavity and the decay rate is much larger than the coupling rate ($\eta \ll \kappa$). The expression shows the enhancement of the process due to the cavity by scaling with the resonator finesse. It further shows a quadratic dependence on the pump intensity characteristic for SFWM [65, 77, 78].

Above expression for the expected photon-pair rate is valid under ideal experimental circumstances, since it has been calculated for a vanishing detuning between the pump, signal, and idler modes. Due to dispersion, the spectral distance towards neighboring modes varies, such that the resonance condition is not necessarily fulfilled. Therefore, we want to estimate the effect of the detuning on the photon-pair rate, which will be a suitable reference for the required precision on the frequencies in the experiments. Even though, it is possible to solve above set of differential equations analytically in the time-dependent case, we simply solve it numerically[4]. Figure 2.10 shows the normalized photon-pair rate depending on the detuning Δ. A Lorentzian line shape with half width at half maximum of the cavity decay rate κ can be seen, which is confirmed by the overlaid data points calculated from a Lorentzian of corresponding width. Consequently, the cavity infers the necessary precision on the frequencies. We can intuitively understand this by reminding the origin of the cavity linewidth. Due to the non-unity reflection coefficients of the cavity, frequencies close to resonance are already supported by the resonator, since partial waves do not completely destructively interfere and, hence, a fraction of

[4] I use the `NDSolve` method from *Wolfram Mathematica*.

the incident light can be stored in the cavity. The nonlinear process efficiently couples to every pair of modes that conserves energy ($\Delta \approx 0$), whereas only the coupling to the modes that are in resonance with the cavity is supported. Therefore, the detuning needs to be less than half of the cavity linewidth, because otherwise, the nonlinearity couples to frequencies which are suppressed by the cavity.

2.2.4 Photon statistics and correlations

Before we investigate the experiments in the next chapters, we need to discuss how to analyze and detect the photon pairs generated in the spontaneous four-wave mixing process. From the derivation of the nonlinear Hamiltonian and the estimation of the wavefunction in subsection 2.2.3, we expect photons being simultaneously produced on cavity modes adjacent to the pump mode. If we spectrally separate the signal and idler photons from the coherent pump mode, and detect single photon events time resolved, we can analyze the properties of the photon source via extracting the time delay between photon arrival times on the detectors. Due to the simultaneous generation of the photon pair, an excess of coincidence events at zero time delay is expected in the measured coincidence distribution. The corresponding normalized quantity, characterizing the photon statistics of a photon source, is the second-order correlation function $g^{(2)}$. For a classical field, it is defined by [79]

$$g^{(2)}(r_1, t_1, r_2, t_2) = \frac{\langle E^*(r_1, t_1) E^*(r_2, t_2) E(r_2, t_2) E(r_1, t_1) \rangle}{\langle |E(r_1, t_1)|^2 \rangle \langle |E(r_2, t_2)|^2 \rangle}, \tag{2.58}$$

where $\langle \ldots \rangle$ denotes the time average. Above definition can be rewritten in terms of the field intensity at position r_i and time t_i and, thus, the $g^{(2)}$ function contains information about the energy dynamics, i.e. photon arrival times, at different places [79].

Depending on the studied light source, the correlation function has different properties. For a classical thermal light source, photons are said to arrive in bunches, i.e. there is an excess of coincidence events between the detectors at zero or short time delays over large temporal separations. The light is chaotic, and considering the time distribution of the photons, one can calculate $g^{(2)}(\tau) = 1$ for time delays larger than the coherence time ($\tau \gg \tau_c$), and in particular $g^{(2)}(0) = 2$ [70]. The lineshape of the coincidence distribution depends on the distribution of the frequencies and the coherence time [79].

The correlation function can be generalized to quantum states by exchanging the fields with the appropriate positive and negative frequency parts of the electric field operator (see Equation 2.33), likewise in the derivation of the nonlinear Hamiltonian in the previous subsection 2.2.3. For a single mode quantum field, the second-order correlation function is given by [79]

$$g_2(\tau) = \frac{\langle \hat{a}^\dagger(t) \hat{a}^\dagger(t+\tau) \hat{a}(t+\tau) \hat{a}(t) \rangle}{\langle \hat{a}^\dagger(t) \hat{a}(t) \rangle^2}. \tag{2.59}$$

Interestingly, the second-order correlation function can be smaller than 1 for quantum fields, which is found in the emission of single atomic, or solid state emitters [80, 81]. This behavior is expected, as only one photon is released in the transition from the excited to the ground state, and another excitation needs to happen before an additional photon can be emitted. Photons, consequently, arrive separately, and hence, antibunched. For a coherent light source, such as a laser, the correlation function is constant, i.e. $g^{(2)}(\tau)$ equals 1, since photons randomly arrive with no explicit time relation [70]. In

both measurements, coincidences between the two output ports of a beamsplitter are studied.

However, we are interested in the cross-correlation between two modes, which can be obtained by generalizing Equation 2.59 by [70]

$$g_{\mathrm{si}}^{(2)}(\tau) = \frac{\langle \hat{a}_{\mathrm{s}}^{\dagger}(t)\hat{a}_{\mathrm{i}}^{\dagger}(t+\tau)\hat{a}_{\mathrm{i}}(t+\tau)\hat{a}_{\mathrm{s}}(t)\rangle}{\langle \hat{a}_{\mathrm{i}}^{\dagger}(t)\hat{a}_{\mathrm{i}}(t)\rangle\langle \hat{a}_{\mathrm{s}}^{\dagger}(t)\hat{a}_{\mathrm{s}}(t)\rangle}\,. \tag{2.60}$$

This quantity is, in general, not limited to 2 at zero time delay like the correlation function of a classical, thermal photon source. This makes the photon-pair source distinguishable from the classical source and shows the quantum nature of the underlying process. The numerator in this expression is proportional to the probability of finding a coincidence event [82]. The denominator is proportional to the probability of finding a random coincidence and gives the background of accidental coincidence events (cf. Equation 3.7). For time delays between photon arrival times larger than the correlation time, $g_{\mathrm{si}}^{(2)}$ is 1. In the coincidence measurements, the obtained distribution of counting time differences between photon arrival times is proportional to $g_{\mathrm{si}}^{(2)}$, and equal if it is normalized to the accidental coincidence background [82].

CHAPTER 3

Spontaneous four-wave mixing in an empty optical cavity

Correlated photon-pair sources are an important tool for testing fundamental effects in quantum mechanics like antibunching of indistinguishable photons [13] or teleportation of polarization states [14]. Furthermore, the interconnection of remote [17], or dissimilar quantum systems [18, 19] relies on photon pairs bridging frequency gaps between the respective energy levels. This task requires a broad tunability of the associated wavelengths, in addition with a narrow linewidth, in order to match the properties of the respective network node. Common techniques for the generation of correlated photon pairs are spontaneous parametric down-conversion (SPDC) and spontaneous four-wave mixing (SFWM). These effects are based on a nonlinear response of the material polarization and create a pair of signal and idler photons in excess of the annihilation of one (SPDC) or two (SFWM) pump photons. The creation of a pair of photons is triggered by vacuum fluctuations on the unoccupied electromagnetic modes and only those virtual photons are converted to real photons that fulfill energy and momentum conservation.

Both processes employ high intensity pump laser pulses propagating through crystals [83] or fibers [9, 84], where requirements on phase matching between the dissimilar wavelengths determine the bandwidth of the photon-pair emission spectrum. Without filtering, the bandwidth can be up to several THz [8, 9], while the linewidth of atomic or solid-state emitter transitions is on the order of 10 MHz–1 GHz. In narrow-band photon-pair sources, therefore, phase matching needs to be tailored precisely and additional filtering is needed to match the bandwidths of source and sample [85]. Commonly, the nonlinear medium is placed inside an optical resonator, in order to adjust the bandwidth and enhance the nonlinearity due to resonant amplification in the cavity [10–12].

In this chapter, I present an experiment utilizing the third-order nonlinearity in the dielectric mirror coating of a high-finesse cavity, with purpose of generating correlated photon pairs on cavity modes adjacent to the pump mode. The signal and idler frequencies are shifted by one free spectral range up- and downwards with respect to the pump mode. In subsection 2.2.2, we analyzed the influence of high intensities on the dynamics of optical resonators and discovered a bistable behavior due to thermal and thermo-optic nonlinearities. We further encountered in subsection 2.2.3 that in a resonator containing a nonlinear medium, cavity modes can couple to each other and photon pairs are generated via spontaneous four-wave mixing. The Kerr nonlinearity in dielectric mirror coatings has experimentally been studied in [86], where the reflection and transmission coefficients of the stack

are altered due to the intensity-dependent refractive index of the coating layers. Furthermore, third harmonic generation in dielectric mirror coatings has been reported in [58]. Both studies employ high-intensity pulse lasers driving the nonlinearity, whereas we use a continuous-wave laser to pump the cavity.

The expected photon-pair production rate is estimated in section 3.1, where the properties of the dielectric coating are computed, by virtue of calculating the intensity distribution of the cavity mode driving the nonlinearity. The experimental setup is described in section 3.2 and characteristics of the high finesse cavity are analyzed. Bistable operation due to high intensities and, thus, thermal effects in the dielectric coating are studied in section 3.3. In section 3.4 measurements of correlated photon pairs are presented and analyzed, in order to find the photon-pair production rate and bandwidth. The results have been published in [87].

3.1 Spontaneous four-wave mixing in dielectric coatings

In the following, we want to use Equation 2.57, with purpose of estimating the photon-pair production rate stemming from the nonlinearity inside the dielectric coating. We use the wave transfer-matrix formalism described in subsection 2.1.3 to determine the transmission properties and the intensity distribution of the coating (see Figure 3.1). The high refractive index material is niobium pentoxide (Nb_2O_5, dark grey) and the low refractive index material is silicon dioxide (SiO_2, light grey). The nominal transmission of the coating is $T = 180\,\text{ppm}$ at a wavelength of 790 nm, where it will be operated at in the experiment. The intensity distribution inside the coating is shown for the same wavelength and used to numerically integrate Equation 2.57, which can be written as

$$\Gamma = 4\frac{F\Delta\omega_{\text{fsr}}}{\pi^2}\left(\int \mathrm{d}z\, k(z)n_2(z)I(z)\eta\right)^2 . \tag{3.1}$$

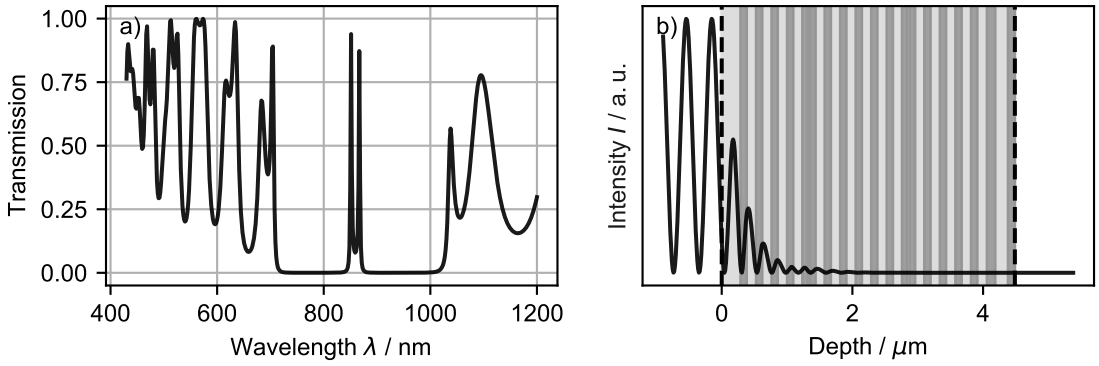

Figure 3.1: *Transmission spectrum a) and axial intensity distribution b) for a normally incident beam with wavelength 790 nm of the dielectric mirror coating. Light grey depicts the low refractive index material SiO_2 and dark grey depicts the high refractive index material Nb_2O_5.*

The integral goes over the whole stack of dielectric layers, k and n_2 differ in each layer due to the alternating media, I is the intensity distribution as shown in Figure 3.1, and η is the coupling of the pump wave to the signal and idler wave. The coupling is approximated by $I(z)/\tilde{I}$, where $\tilde{I}$ is the norm of the intensity distribution.

In subsection 2.2.3 we encountered the different mixing mechanisms of the wavevectors of the pump, signal, and idler waves. The nonlinear driving of the material polarization excites the neighboring vacuum modes parametrically, with the consequence of creating real photons on the signal and idler modes. The direction in which the photons leave the cavity is random, whereby four scenarios are possible; both photons leave in the transmission or reflection direction, or each photon leaves to the respective other side. Since we will only collect the photons transmitted by the cavity, the factor of four in Equation 3.1 vanishes.

The nonlinear refractive indices of the coating materials are $n_2(Nb_2O_5) = 3.2 \times 10^{-19}\,m^2\,W^{-1}$, and $n_2(SiO_2) = 2.7 \times 10^{-20}\,m^2\,W^{-1}$ [48]. Since the nonlinear refractive index of Nb_2O_5 is an order of magnitude larger than for SiO_2, the main contribution to the photon-pair production rate stems from the second layer in the dielectric coating. With a finesse of $F = 4500$, free spectral range of $\Delta\omega_{fsr} = 2\pi \times 4.5\,THz$ and $I = 2P/\pi\sigma^2$ with $\sigma = 4\,\mu m$ (cf. subsection 3.2.1), we can estimate the photon-pair rate to be $\Gamma_{theo} = 0.4\,s^{-1}\,W^{-2}$. Notice that both mirrors of the cavity need to be taken into account, thus a factor of two in the integral for the single mirror gives a global factor of 4.

The photon-pair production rate is limited by the sub-micrometer scale nonlinear medium and demands a high stability of the experimental setup, since measurements have to be performed over several hours in order to collect enough samples for a statistically representative observation.

3.2 Experimental apparatus

We started the construction of this experiment in the context of my master thesis [88], however, we achieved the results in the first half year in the beginning of my PhD, which have been published in [87]. For the sake of completeness, the experimental setup will be described, even though it has not been part of my PhD, but my master thesis.

3.2.1 Resonator construction and characterization

The cavity is a combination of a macroscopic planar mirror and a micromachined and coated end facet of an optical single-mode fiber. Both, mirror and fiber, have the identical coating (see Figure 3.1), which is optimized for 780 nm and 935 nm. Both are attached to a bulk monolithic aluminum block, standing on four Viton balls inside an ultra-high vacuum chamber. The Viton provides mechanical isolation and the vacuum additionally isolates the cavity from temperature, humidity and pressure fluctuations. The macroscopic mirror is mounted on a v-groove, screwed to a translation stage (Elliot Scientific Martock MDE261, vacuum compatible), making the cavity length adjustable. The fiber is glued (LOCTITE STYCAST 2850FT with LOCTITE CAT 9) onto a shear plate actuator (Noliac CSAP03) providing precise length adjustment, necessary for tuning the cavity and stabilizing its length to an incident laser. The actuator itself is encapsulated between to alumina plates for electrical isolation.

Before the gluing process the fiber is aligned with a five axis translation stage, in order to adjust the position in front of the mirror, the length of the cavity and the angle, whereby the fiber should be

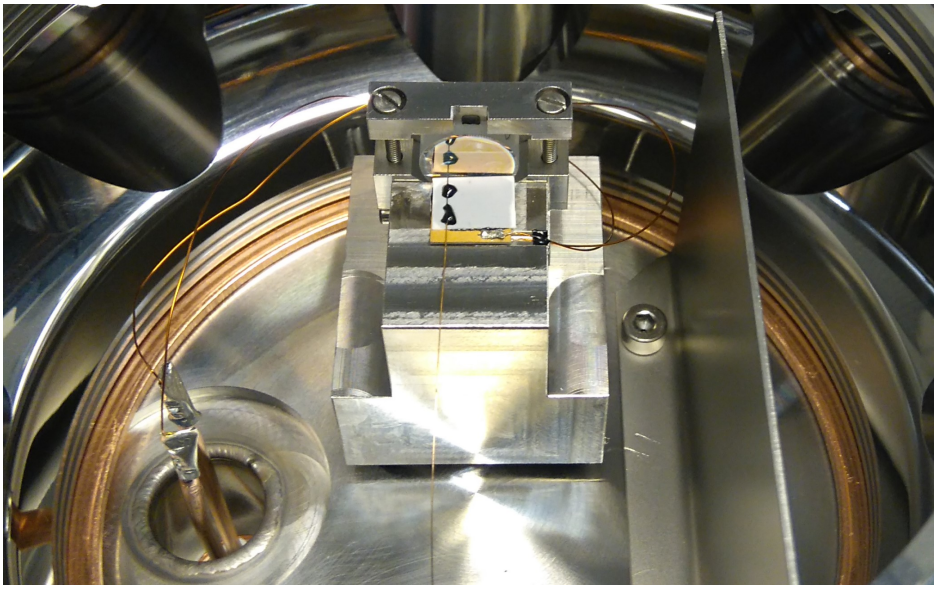

Figure 3.2: *Picture of the final assembled cavity inside the vacuum chamber. The feed through for electrical wiring is seen on the lower left. A stainless steel shielding is seen on the right, protecting the cavity mirrors from a titanium sublimation pump.*

perpendicular to the mirror surface[1]. For simplification, the fiber is observed via two microscope cameras from above and the side, with purpose of a raw alignment. Optimizing the resonator configuration is done via maximizing the incoupling of an incident laser into the cavity. For this purpose, the cavity length is scanned by a piezo-electric element implemented in the translation stage and the reflection signal is observed with an oscilloscope.

A picture of the final assembled cavity inside the vacuum chamber can be seen in Figure 3.2. The feed through for the electrical wiring of the piezo actuator is visible in the lower left corner. A vertically mounted stainless steel shielding on the right protects the cavity from the atom flow of a titanium sublimation pump attached to the vacuum system. The single-mode fiber is fed through the bottom flange, which is not seen in the picture. After evacuating the chamber with a pre-pump and a turbo nuclear pump and baking out the system at 100 °C for a week, the vacuum is maintained by an ion pump (Gamma Vacuum 45S-CV-2V-SC-N-N) at a pressure of 1×10^{-11} mbar.

Resonator characterization The free spectral range of the cavity is measured to be $\Delta\nu_{\mathrm{fsr}} = 4.5\,\mathrm{THz}$ by overlapping the reflection dips of two grating-stabilized external cavity diode lasers on an oscilloscope. In the process, the frequency of one laser is tuned, while keeping the reference laser frequency fixed, until the next longitudinal mode can again be overlapped with the reference laser. The length estimated with a microscope picture gives a good reference and starting point. The frequencies are determined by a wavelength meter (Highfinesse WS7-60) with an absolute accuracy of 60 MHz, whereas the relative accuracy is 4 MHz as stated by the manufacturer. From the free spectral range, the cavity length is computed to $l = 33\,\mu\mathrm{m}$ with negligible error. By applying sidebands to the incident

[1] If the end facet does show imperfections like a tilted cleave or an off-center mirror structure, the ideal fiber alignment can deviate from the mirror surface normal.

laser via an electro-optic modulator (iXblue NIR-MPX800-LN-05), serving as precise frequency references, the linewidth is measured by fitting an overlap of three Lorentzian line shape functions to the reflection signal. The linewidth is $\delta\nu = 1\,\mathrm{GHz}$ from which the cavity finesse is calculated to be $F = 4500 \pm 60$. The nominal coating transmission is $T = 180\,\mathrm{ppm}$ at a wavelength of 790 nm, corresponding to losses of $L = 520\,\mathrm{ppm}$ per mirror. The radius of curvature of the fiber mirror is $R = 170\,\mu\mathrm{m}$, leading to a mode waist of $w_0 = 4\,\mu\mathrm{m}$ on the planar mirror, and a waist of $w_\mathrm{m} = 5\,\mu\mathrm{m}$ on the fiber tip (see Equation 2.10). The highly curved fiber mirror and the short cavity length, thus, provide a small mode volume that enhances the desired nonlinear effects in the mirror coatings. The total incoupling from the fiber into the cavity is 40 %, including the possible incoupling from the coating characteristics and the overlap of the cavity and fiber modes (cf. subsection 2.1.2). The total transmission is measured to 7 ‰. It has to be mentioned that during the measurements, the cavity finesse decreased from its initial value of 10000 to the value stated above, which we attribute to increased losses inside the coating due to weak optical damage from the high intra-cavity powers. Therefore, the initial losses per mirror have been 130 ppm.

Dispersion compensation For an efficient conversion of two pump photons into neighboring signal and idler cavity modes, momentum and energy need to be conserved. In theory, resonant frequencies are equidistantly spaced, and hence, both requirements are fulfilled automatically. However, due to dispersion of the coating materials this is not necessarily given. We calculated the coupling constant of the spontaneous four-wave mixing process in subsection 2.2.3 and found an expression for the phase matching (see Equation 2.38 and Equation 2.41). For the corresponding coupling factor, the product of the longitudinal mode profiles of the involved fields is integrated over the length of the nonlinearity. The value is reduced with rising wavevector mismatch ($2k_\mathrm{p} \neq k_\mathrm{s} + k_\mathrm{i}$) (see Figure 2.9). However, by virtue of the sub-wavelength thick nonlinear medium, the requirements for the phase matching are weak $\Delta k = 1/l \approx 1\,\mu\mathrm{m}^{-1}$. Furthermore, we encountered a decrease of the photon-pair production rate due to a detuning of the pump to signal and idler frequencies ($2\omega_\mathrm{p} \neq \omega_\mathrm{s} + \omega_\mathrm{i}$). From the numerical estimation we have found that the photon-pair production rate follows a Lorentzian line shape function with full width at half maximum of twice the cavity decay rate κ (see Figure 2.10). Correspondingly, the detuning needs to be smaller than this value. We can connect the wavevector mismatch to the detuning via $\Delta k = \Delta\omega/c \approx 2 \times 10^{-5}\,\mu\mathrm{m}^{-1}$. Consequently, if we match the detuning of the signal and idler modes with respect to the pump mode, the phase-matching condition is already ensured. Since the restriction on energy matching is much more severe due to the narrow cavity linewidth, than the restriction on phase matching because of the material thickness, matching the frequencies of the pump, signal, and idler modes ensures an efficient conversion process. We select the signal and idler modes to be spectrally shifted from the pump resonance by one free spectral range up- and downwards. However, due to dispersion the spectral distances between the modes are not necessarily equal. Hence, we need to find a pump wavelength, where the frequency differences of the upper and lower mode with respect to the pump frequency are equal. This ensures energy and momentum conservation.

With purpose of finding the dispersion zero-point, the pump laser resonance is overlapped with a second probe laser, which is tuned for several free spectral ranges relative to the fixed pump laser frequency ω'. From this measurement we can determine the spectral mismatch between neighboring first-order shifted modes for several center frequencies $\omega_\mathrm{n} = \omega' + \delta\omega_\mathrm{n}$ by calculating the detuning Δ

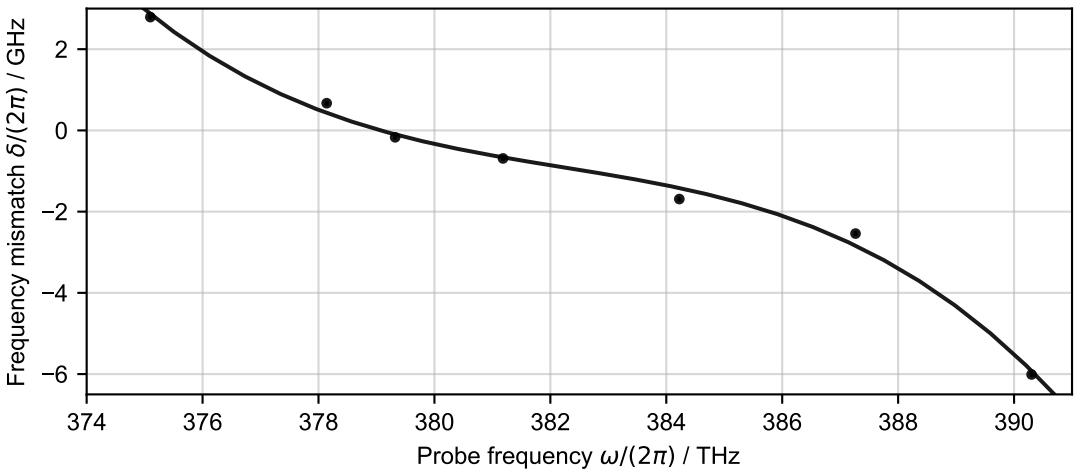

Figure 3.3: *Dispersion curve of the dielectric coating. The dispersion compensation point is roughly at a frequency of 379 THz, given by the zero-crossing of the extrapolation of the measured data by a third-order polynomial.*

for the adjacent modes of the respective order n via

$$\delta = (\omega' + \delta\omega_{\text{n-1}}) + (\omega' + \delta\omega_{\text{n+1}}) - 2(\omega' + \delta\omega_{\text{n}}) = \delta\omega_{\text{n-1}} + \delta\omega_{\text{n+1}} - 2\delta\omega_{\text{n}}\,. \tag{3.2}$$

From the spectral mismatch of the free spectral ranges with respect to the center frequency, we can find the dispersion-compensated pump frequency by extrapolating the data with a third-order polynomial as seen in Figure 3.3. The zero-crossing of the polynomial gives a reference frequency from which the dispersion zero-point is experimentally determined. For this, the pump laser frequency is tuned and the free spectral ranges to the next and previous modes is determined. The optimized pump frequency is 379.3 THz at which the neighboring first-order modes agree to within 170 MHz, which is smaller than the cavity decay rate $\kappa = 2\pi \times 500$ MHz and accurately enough to fulfill the energy and momentum conservation.

Since the nonlinearity is given by the dielectric coatings, the cavity can in principle be as short as possible, which increases the photon-pair rate. Nevertheless, the free spectral range can get so large that the signal and idler mode do not lie inside the high reflective bandwidth of the mirror coating, which decreases the photon-pair production rate due to a lower finesse at the respective wavelengths, or a dispersion compensation point may not be found.

3.2.2 Laser pumping setup, spectrometer and detection setup

A simplified scheme of the optical setup can be found in Figure 3.4. Two grating-stabilized external cavity diode lasers are combined via a 50:50 beamsplitter to be coupled into the cavity fiber. The far tunable probe laser (Toptica DL Pro) with an integrated optical isolator is used for the dispersion compensation measurements, while the second laser is home-build and used for pumping the cavity. The pump laser passes a faraday isolator and is spectrally filtered by a holographic diffraction grating,

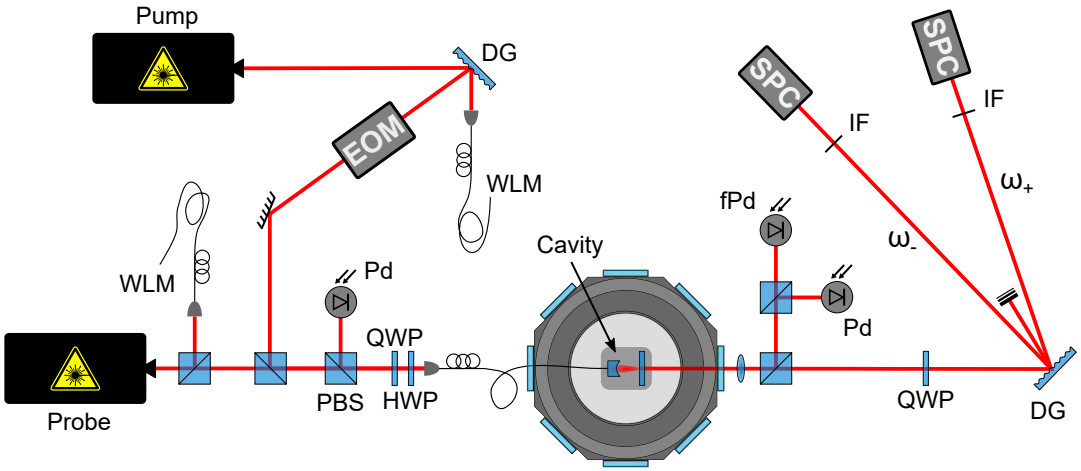

Figure 3.4: *Optical setup including laser pumping scheme, employing two lasers for pumping and probing, with purpose of finding the dispersion compensation point, the experiment cavity with stabilization photodiodes, and the home-build spectrometer with single photon counters (SPC), and narrow-band filtering (IF). Abbreviations: diffraction grating (DG), wavelength meter (WLM), quarter-wave retardation plate (QWP), half-wave retardation plate (HWP), (fast) photodiode ((f)Pd), electro-optic modulator (EOM)*

in order to suppress the background of the laser diode. The zeroth order of the diffraction pattern is send via a polarization maintaining optical fiber to the wavelength meter and the first order is used for pumping the cavity. The phase is modulated via a home-build electro-optic modulator, in order to apply sidebands at 60 MHz to the laser frequency, with the purpose of stabilizing the cavity length to the laser frequency. The light is coupled into the cavity single-mode fiber. To avoid unwanted polarization rotations due to temperature fluctuations, mechanical stress, etc., the fiber is fixed to the optical table. The table itself is temperature stabilized and the fiber phase retardation is adjusted to 0 or π through applying mechanical stress. The polarization of the light is set with a quarter-wave retardation plate (QWP) to be circularly polarized by maximizing the light entering the photodiode in the reflection branch of a polarizing beamsplitter.

The cavity is stabilized by a Pound-Drever-Hall lock to the pump laser [89], which itself is locked via subsequently measuring the frequency from the wavelength meter and adjusting the frequency fluctuations to the reference frequency. The fluctuations are compensated by tuning the piezo-electric element attached to the holographic grating inside the pump laser, through applying voltages from an analog output of a digital data acquisition card (NI 6229). The frequency measurement, and thus the stabilization, happens on a Hz level and is accurate to within 4 MHz, given by the relative accuracy of the wavelength meter itself. The cavity lock is analog and operates on a kHz scale, which can thus follow the frequency fluctuations and changes of the pump laser, which are much smaller than the cavity linewidth. While the lock laser is free running in between adjustments, the stabilization of the pump frequency via the wavelength meter is sufficient for compensating long-term drifts. In order to reduce fluctuations of the voltage supplied to the cavity piezo actuator, a low noise battery box[2] is

[2] The battery box has been designed and build by Dr. Akos Hoffmann.

used, which contains twenty 9 V batteries connected in series and the output voltage can be adjusted in steps of 18 V from −198 V to 198 V.

A fraction of the light transmitted by the cavity is send via a beamsplitter to the stabilization diodes for the Pound-Drever-Hall lock and 90 % are directed onto a holographic diffraction grating (Thorlabs GH25-18V), separating the pump light from the signal and idler modes. The light passes a QWP before the grating, in order to change the polarization orthogonal to the grating lines (p) for optimized diffraction efficiency. The pump light is captured in a beam dumb, while the signal and idler mode are each send to a single photon counter (Excelitas SPCM-AQRH) after being spectrally filtered with narrow-line interference filters (Semrock LL01-785-12.5 and Semrock LL01-808-12.5). The line filters have a linewidth of 3 nm and are tilted to transmit light at the respective detection wavelength (781 nm and 799 nm). The spectrometer has a resolution of $\lambda/\delta\lambda = 6000$ and detection efficiencies of the signal and idler path are measured to be $\eta_1 = 36\,\%$ and $\eta_2 = 40\,\%$, taking into account the diffraction efficiency of the grating, the transmission of the interference filters, and the beamsplitter transmission $\eta_{\mathrm{bs}} = 0.9$. With the purpose of reducing stray light, the whole spectrometer setup is surrounded by a light-impermeable box.

The timing jitter of the photon counting modules is 350 ps. A time-to-digital converter (Cronologic HPTDC8-PCI) with a resolution of 45 ps records the photon counter signals to generate a list of arrival times. In between the counters and the time-to-digital converter, the TTL pulses are converted to NIM pulses. From the photon arrival times on the detectors, a correlation analysis is done by calculating the time differences between detection events on both counters. For each entry on channel one, a coincidence event is recorded, if the time difference to an entry on channel two lies in the time window of 40 ns. The resulting distribution of time delays between arriving photons on both detectors is proportional to the $g^{(2)}$ or intensity-intensity correlation [90] (see subsection 2.2.4).

3.3 Optical bistability

In subsection 2.2.2, we encountered that high-finesse cavities experience optical bistability, an effect leading to a broadening or narrowing of the cavity resonance, depending on the scan direction of the cavity length. It is caused by thermal expansion of the cavity mirrors, shrinking the cavity length, and a change in the refractive index of the mirror coatings due to a thermo-optic response. Equation 2.26 shows the different mechanisms, whereby only the first term is relevant for the system at hand, since the change in refractive index is only present in the first layers of the dielectric coating (see Figure 3.1), whereas we can assume the material contributing to the thermal expansion to be several orders of magnitude longer than the exponential decay of the cavity field inside the coating.

Figure 3.5 shows the characteristic bistable resonance line shapes at several intra-cavity powers and for both scan directions of the cavity length. Already at relatively low powers, a slight tilt in the Lorentzian is observable (see a and d). A narrowing of the curve with at decreasing cavity length can be seen (d), e.g. a steeper rise and a slower decay, and a slower rise and steeper decay for the other scan direction (a). With rising intra-cavity power these characteristics become much more prominent as seen in the other subfigures (b, c, e, and f). For the increasing cavity length (b, c), the rising flank gets more gradual before the resonance, since the thermal expansion counters the mirror movement and slows the scan velocity. The falling flank gets much steeper due to the increased scan velocity, by virtue of the contraction of the material due to cooling. The opposite is happening for the decreasing cavity length (e, f). On the red detuned side, the scan velocity is increased because of the thermal

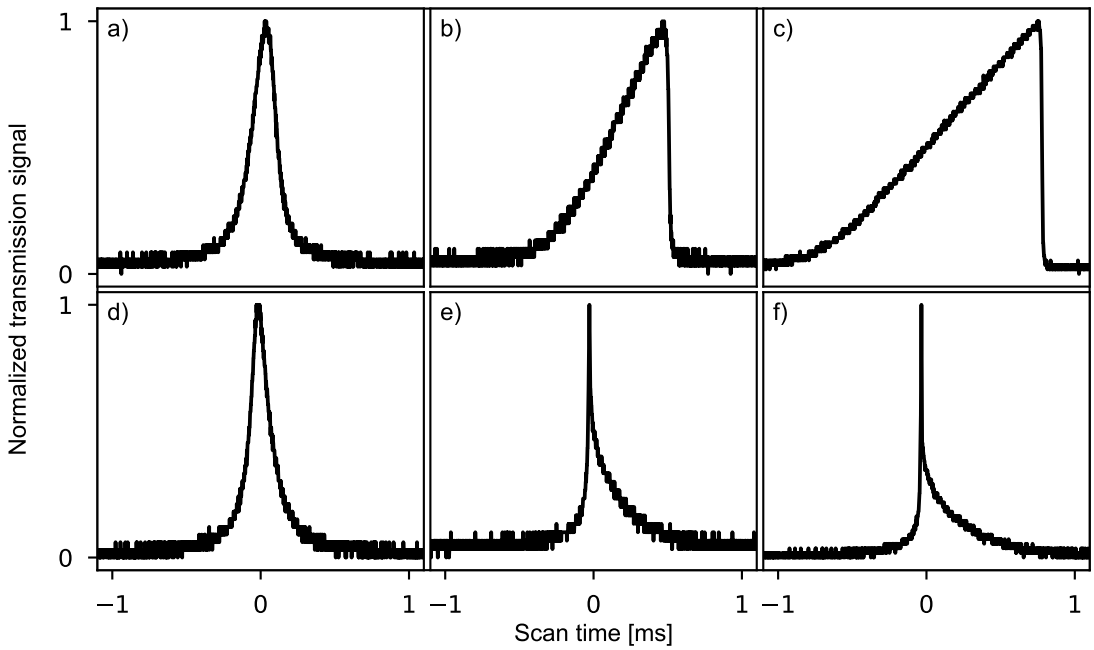

Figure 3.5: *Bistable cavity resonances for a decreasing (a) to c)) and increasing cavity length (d) to f)) at various intra-cavity powers of 50 mW (a, d), 500 mW (b, e) and 1 W (c, f). Even at relatively low intra-cavity powers, a slight tilt in the Lorentzian line shape can be observed (see a, d), whereby with increasing power the resonance is broadened for decreasing and narrowed for increasing cavity length.*

expansion of the material acting in the same direction as the mirror movement, leading to a steeper rise. On the blue detuned side, however, the material contracts and, therefore, counters the mirror movement, slowing down the scan velocity.

We can extract the lineshift β from the measurements of decreasing cavity length by calibrating the x-axis in terms of the linewidth of the unperturbed Lorentzian, and find a shift of 3 GHz and 6 GHz for the measurements in Figure 3.5 b) and c), respectively. Following [64], we can calculate the temperature increase via

$$\Delta T = \frac{C_0 P_\mathrm{i} A}{\pi l \kappa}\,, \tag{3.3}$$

where C_0 is a dimensionless factor[3], depending on the geometry of the mirror, P_i is the intra-cavity power, A is the absorption in the coating, assumed to be equal to the total cavity losses, l is the cavity length, and κ is the thermal conductivity. We find a temperature increase of 5 K for the measurement

[3] It is calculated by solving the integral

$$C_0 = \frac{1}{2}\int_0^\infty \mathrm{d}q\, \exp(-w^2 q^2/4l^2)\frac{\cosh(q)-1}{q\cosh(q)}\,, \tag{3.4}$$

where w is the cavity waist, and l the cavity length [64]. It has to be mentioned that the coating thickness is assumed to be much smaller than the cavity waist, which is not fulfilled in this case, where both are on the same order.

at a intra-cavity power of 500 mW, and an increase of 10 K for a power of 1 W. In combination with the lineshift β, the material depth l_{pen}, contributing to the thermal expansion, is estimated to be 20 µm, whereby the cavity length is approximately changed by 120 pm b), and 240 pm c), respectively. This is estimated by $\Delta l = 2\alpha l_{\mathrm{pen}}\Delta T$, where $\alpha \approx 6 \times 10^{-7}\,\mathrm{m\,K^{-1}}$ is the thermal expansion coefficient for fused silica [91].

In [64], a maximal temperature increase of 1 K is reported, even though the intra-cavity intensity is almost two orders of magnitude larger. There are three primary reasons for the different behavior. First, the temperature increase is calculated assuming the total losses stem from absorption, neglecting contributions from scattering. The calculated temperature increase can thus be seen as an upper limit. Second, one of the cavity mirrors is a single-mode fiber which has a much lower thermal mass than a macroscopic mirror substrate. We can, therefore, expect the main contribution to the thermal expansion from the fiber, whereas we treated both, fiber and macroscopic mirror, equally. Lastly, the cavity is under vacuum, restricting heat dissipation mainly to thermal radiation, instead of heat exchange with the surrounding air.

In conclusion, the characteristic bistability in high-finesse cavities due to thermal expansion of the dielectric mirror coatings and substrates as postulated in subsection 2.2.2 is shown and analyzed. A maximum lineshift of 6 GHz is measured due to a temperature increase of about 10 K, yielding a decrease in cavity length of 240 pm. These values are upper limits for the thermal effects in the cavity, while the thermo-optic properties were neglected.

3.4 Correlation measurements

In order to measure the photon-pair production rate, we perform correlation measurements between the signal and idler branches in the spectrometer for multiple pump powers. For a single measurement, we lock the pump laser to the dispersion-compensated pump frequency and the cavity to the laser frequency, as described above. We collect timestamps from the TDC for several hours with purpose of performing a coincidence analysis on the acquired data. We expect a flat background of accidental coincidences, excessed by a peak near zero time delay. From the peak distribution we extract the height, temporal width, and total number of coincidences measured within the measurement time. Before we discuss the results from the measurements, we need to investigate the expected correlation signal.

Expected signal distribution In the coincidence measurement, we measure the correlation of the intensity on two separate detectors, which is a second-order or intensity-intensity correlation [70] (see subsection 2.2.4). For a coherent state such as a laser, the arrival times between two incident photons is Poisson distributed, yielding a constant number of coincidences with respect to the time delay between the photon detections [92]. The expected uniform background is caused by uncorrelated counts on the detectors, either by stray light from the laser and other sources, or detector dark counts. Since the two photons are created simultaneously, they have a definite time relation and cause coincidences at a fixed time delay. Consequently, we expect a peak surpassing the constant value of accidental background coincidences. Thermal light sources, however, emit photons in bunches, leading to a peak in the respective correlation function[4], similar to the signal we expect to observe. However, the

[4] If the correlation function is normalized to the offset, the expected peak height is 2.

occupation of cavity modes due to thermal excitation is greatly suppressed, because the photon energy is much larger than the thermal energy at room temperature ($\hbar\omega \gg k_B T$) and, therefore, we can be expected no significant contribution to the coincidence measurement.

The peak distribution is determined by two separate processes which are the cavity ring-down dynamics and the timing jitter of the single photon counting modules. The latter is governed by a normal distribution with a standard deviation of the detector timing jitter $\tau_{\mathrm{jit}} = 350\,\mathrm{ps}$, while the former depends on the cavity ring-down time τ_{rd}. In subsection 2.1.1 we found the cavity ring-down to be an exponential decay. The corresponding probability density for a single photon to be found in the cavity at time t after entering the cavity at $t_0 = 0$ is $f(t) = {}^1/_{\tau_{\mathrm{rd}}} \exp(-t/\tau_{\mathrm{rd}})$ for $t \geq 0$. We are interested in the probability density of the joint probability of finding an idler photon at the time difference $\tau \geq 0$ after the detection of a signal photon. The probability of detecting a signal photon in an infinitesimal time window $\mathrm{d}t'$ at time t' after its creation is $f(t')\mathrm{d}t$, and the probability for an idler photon to be found on the detector in the time interval $t' + \tau$ is $f(t' + \tau)$. We want to determine the probability of finding an idler photon τ after the detection of a signal photon, therefore we need to integrate the product of both probabilities over all signal arrival times t' and we find

$$\int_0^\infty f(t')f(t'+\tau)\mathrm{d}t' \propto \exp\left(-\frac{\tau}{\tau_{\mathrm{rd}}}\right), \tag{3.5}$$

where the limits of integration are taken to be positive, since the photon pair is assumed to be produced at $t_0 = 0$. The normalized joint probability density for the detection of a photon pair with an arrival time difference of τ is thus

$$g(\tau) = \frac{1}{2\tau_{\mathrm{rd}}} \exp\left(-\frac{|\tau|}{\tau_{\mathrm{rd}}}\right), \tag{3.6}$$

which itself is an exponential distribution. Hence, time differences at the two detectors are distributed like the arrival times of the single photons. Notice that the probability density is allowed for negative arguments, due to the dependence on the absolute value of the time difference τ. In the derivation we assumed the signal photon to arrive at first by the restriction of τ being positive, which is only true in half of the cases. The derivation can be repeated for negative time differences, where we find the same result as in Equation 3.5 for $\tau \to -\tau$. Hence, both cases can be combined by the absolute value as used in Equation 3.6.

The form of the coincidence peak depends on the ratio of the cavity ring-down time constant and the timing jitter of the single photon counting modules. The process can be qualitatively simulated by drawing from an exponential distribution with decay constant τ_{rd} and adding the timing jitter by drawing from a normal distribution with width τ_{jit}. The simulation for time differences in arrival times on the two detectors is shown in Figure 3.6 a) without, and b) with timing jitter, respectively. The dashed and solid lines are exponential and gaussian fits to the data, clearly indicating that the timing jitter dominates the distribution of coincidences, resulting in a gaussian line shape of the coincidence peak. The decay constant extracted from the exponential fit in Figure 3.6 a) is the cavity ring-down time as expected from above derivation of the joint probability density function. If the cavity ring-down time is much smaller than the timing jitter of the single photon counting modules $\tau_{\mathrm{rd}} \ll \tau_{\mathrm{jit}}$, the coincidence distribution is a gaussian with width $\sqrt{2}\tau_{\mathrm{jit}}$, which simply follows from gaussian error propagation, since each detector has a standard deviation of τ_{jit} in the photon arrival time. The temporal resolution of the time-to-digital converter leads, in principle, to a gaussian broadening as

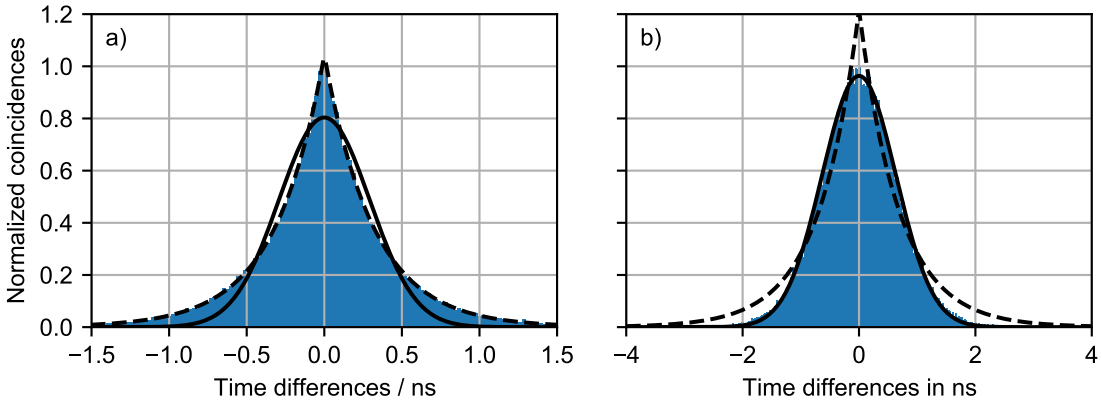

Figure 3.6: *Simulation of the line shape of the coincidence peak without a), and with timing jitter b) for a cavity ring-down time of* $\tau_{rd} = 160\,\text{ps}$ *and a timing jitter of the single photon counting modules of* $\tau_{jit} = 350\,\text{ps}$*. The dashed and solid lines are exponential and gaussian fits, showing that the line shape of the experimental data will be dominated by the timing jitter of the detectors and not by the cavity decay dynamics.*

well, but can be neglected by virtue of the much larger detector timing jitter and cavity ring-down time.

Results For an intra-cavity power of approximately 1.3 W and an integration time of almost 12 h, a sample histogram of time differences between the two channels is shown in Figure 3.7. A clear peak close to zero time delay excessing the constant background of random coincidences can be observed. A Gaussian line shape function is fitted to the data, in order to determine the peak width and height, and the accidental coincidence rates by adding a constant offset. The time delay arises due to slightly dissimilar travel path lengths in the spectrometer setup and different signal travel times in the electronic readout. The constant background has several origins, which are dark counts of the detector modules, stray light from the environment, the background of the pump laser diode, and spontaneous Raman scattering in the single-mode fiber and in the cavity itself. The dark counts of the detector modules are at most $50\,\text{s}^{-1}$ as stated by the manufacturer and stray light is suppressed by at least four orders of magnitude due to the narrow-band line filters. The background from the pump laser diode is suppressed by the additional holographic diffraction grating in front of the coupling to the cavity fiber (see Figure 3.4), which is evident by a decrease of a factor of one hundred in the count rates on the detectors. Spontaneous Raman scattering generates single photons by virtue of photons scattering from phonons and, hence, depends linearly on the pump intensity. The scattering and photons from stray light, etc. therefore produce accidental coincidences with no definite time correlation in contrast to the spontaneous four-wave mixing process, where two photons are concurrently generated and arrive within a time delay determined by the cavity ring-down time (see Equation 3.6). Because of the low intensity inside the fiber and the short nonlinear medium inside the cavity, Raman scattering, however, does not significantly contribute to the background counts on the detectors, which are dominated by the other uncorrelated photon sources.

The dependence of the bare count rates relative to the intra-cavity pump power P is shown in Figure 3.8 a), from which we find the linear relationship $R_\text{i} = \gamma_\text{i} \cdot P$. The rates incident on the respective detector depending on the pump power are extracted to $\gamma_1 = (4\,300 \pm 70)\,\text{W}^{-1}\,\text{s}^{-1}$ and

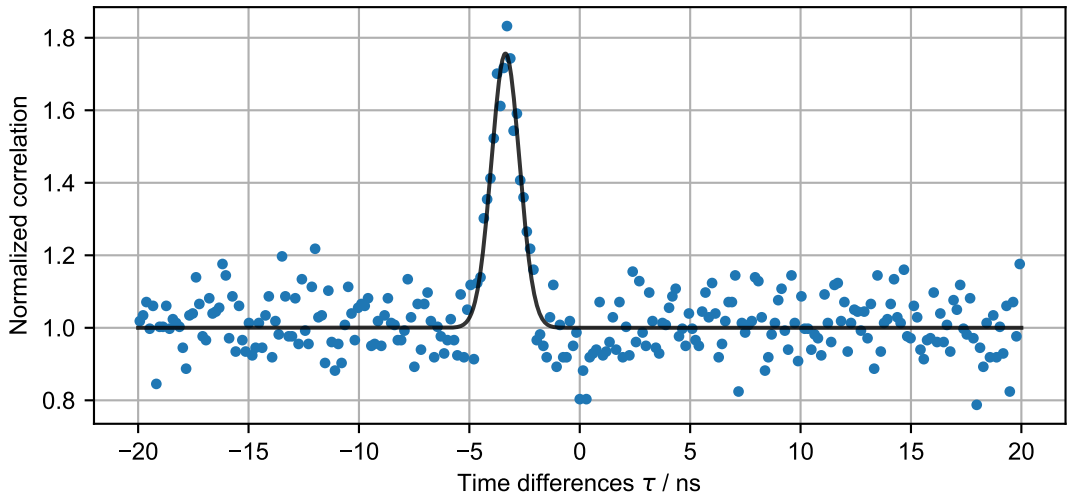

Figure 3.7: *Sample histogram of time differences between arrival times of photons on the two detector branches with a bin size of 150 ps. The measurement time is 12 h at an intra-cavity power of 1.3 W. A clear peak at approximately zero time delay on top of a constant background of random accidental coincidences can be observed. The black line is a Gaussian fit to the data. The coincidence to accidental ratio is 1.74.*

$\gamma_2 = (4\,000 \pm 70)\,\mathrm{W}^{-1}\,\mathrm{s}^{-1}$. From this, the expected accidental coincidence rate per bin can be calculated via[5]

$$\Gamma_{\mathrm{acc}} = \gamma_1 \gamma_2 \tau_\Delta \cdot P^2\,, \tag{3.7}$$

where τ_Δ is the bin size of the histogram bars and P is the pump power inside the cavity. The relationship between accidental coincidences and intra-cavity pump power is shown in Figure 3.8 b), where the quadratic curve shows the rate expected from Equation 3.7 and the data points are the extracted accidental rates from the experimental data. The theoretically expected accidental rates fit to the experimentally determined rates, extracted from the histograms by fitting a Gaussian function with constant offset. Taking into account that the intensity throughout the measurements is not stabilized, the expected and measured accidental coincidence rates are in very good agreement.

From the coincidence measurements, the number of coincidences need to be determined, in order to acquire the photon-pair production rate. The amount of photon pairs is supposed to be independent of the binning in the histograms, whereas the fit amplitude and offset depend on the binning. If the number of bins is doubled, the height is halved, thus we cannot simply integrate the fitted function, but need to relate the integral to the binning time. In principle, the number of coincidences N is the

[5] This expression can be found by considering the probability of finding a photon on detector i in a time interval of the bin size τ_Δ, as given by $p_i = \gamma_i \tau_\Delta P$. The probability of finding a coincidence is then $p_{12} = p_1 p_2$, which divided by the bin size τ_Δ yields the accidental coincidence rate.

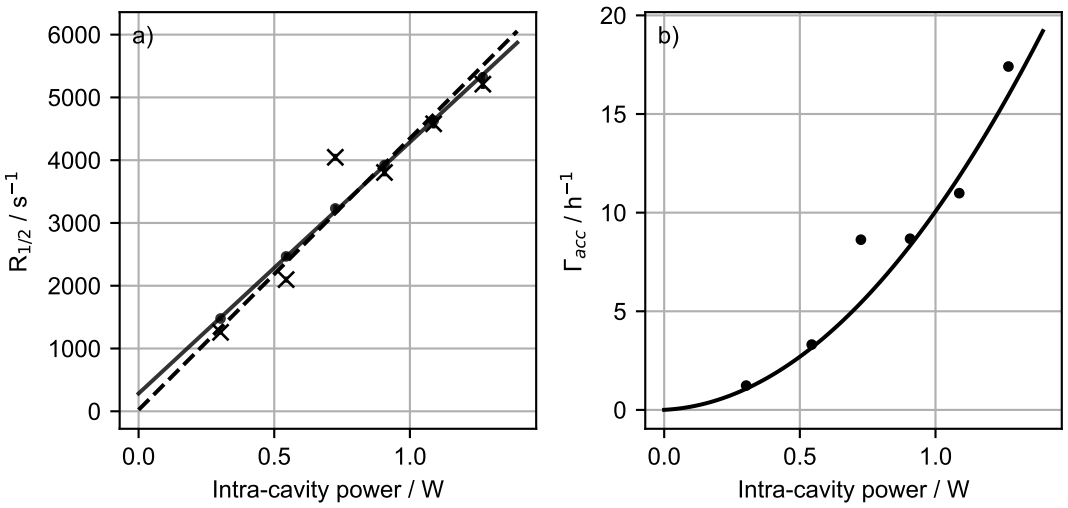

Figure 3.8: *Count rates of the channels relative to the intra-cavity power in a). We find a linear relationship from the fits with constant slopes* $\gamma_1 = (4\,300 \pm 70)\,\mathrm{W}^{-1}\,\mathrm{s}^{-1}$ *(dashed line, crosses) and* $\gamma_2 = (4\,000 \pm 70)\,\mathrm{W}^{-1}\,\mathrm{s}^{-1}$ *(solid line, dots). With the background rates, the expected accidental coincidences can be calculated via Equation 3.7. b) shows the expected rate (solid curve) and experimental determined accidental coincidence rates for a bin size of 150 ps. A nice agreement can be observed, taking into account that the intensity during the measurements is not stabilized and may drift during the long measurement time.*

sum over all bins h_i subtracted by the offset, which we can relate to the Gaussian fit via

$$N \cdot \tau_\Delta = \sum_i h_i \cdot \tau_\Delta = \int_{-\infty}^{+\infty} A e^{-\frac{\tau^2}{2\sigma^2}} \mathrm{d}\tau \quad \Rightarrow \quad N = \sqrt{2\pi}\frac{\sigma}{\tau_\Delta} A\,. \tag{3.8}$$

The extracted coincidence rates per hour R_{12} in dependence of the intra-cavity pump power P are shown in Figure 3.9. For a spontaneous four-wave mixing process we expect a quadratic dependence (cf. Equation 3.1). Therefore, we fit a quadratic function $R_{12} = \Gamma P^2$ to the data, from which we determine the experimental photon-pair generation rate $\tilde{\Gamma}_{\mathrm{exp}} = (2.6 \pm 0.1) \times 10^{-2}\,\mathrm{s}^{-1}\,\mathrm{W}^{-2}$. Taking the efficiencies into account, the theoretically achievable rate in the transmission direction is $\Gamma_{\mathrm{exp}} = \tilde{\Gamma}_{\mathrm{exp}}/(\eta_1\eta_2\eta_{\mathrm{bs}}^2(1-L)^2) = (0.22 \pm 0.01)\,\mathrm{s}^{-1}\,\mathrm{W}^{-2}$, where L are the losses per mirror as stated in subsection 3.2.1. Each photon needs to be transmitted by the cavity and is lost with the probability of $1 - L$, while, additionally, every tenth photon is reflected by the beamsplitter, and photons are detected with a probability of η_{i} per branch. Comparing this value to the rate estimated in section 3.1, we find an agreement to within less than a factor of 2. The discrepancy can have multiple causes. On the one hand, the theory does not take the fast, but finite response time of the medium to the oscillating intensity into account, which reduces the response of the system. The assumed value is measured with picosecond laser pulses [48], which are about three orders of magnitude slower than the period of the intensity oscillation studied here. Therefore, in addition to the electronic response to the intensity variation, the nuclear response increases the nonlinear refractive index in comparison to this experiment. On the other hand, throughout the long measurements of several hours, instabilities in the experimental setup, especially drifts of the wavelength meter, can cause a drift in the pump

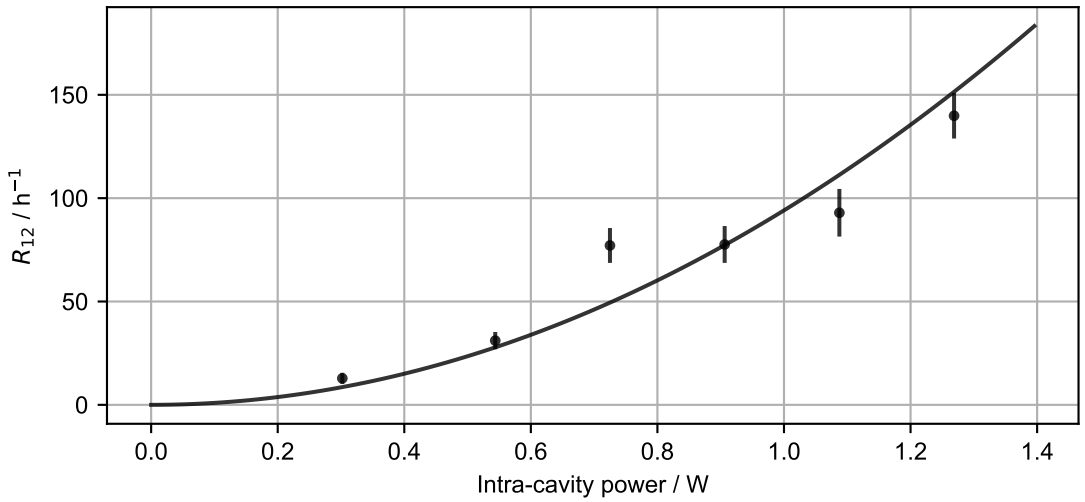

Figure 3.9: *Photon-pair correlation rate per hour R in relation to the pump power. The solid line is a quadratic fit to the data from which the photon-pair generation rate is extracted to* $\Gamma_{exp} = (2.6 \pm 0.1) \times 10^{-2}\,\mathrm{s}^{-1}\,\mathrm{W}^{-2}$.

frequency away from the optimized dispersion zero point. In addition, the spectral distances between signal and pump mode, and idler and pump mode only agree to within 170 MHz, leading to a small reduction of the photon-pair rate by 10 % (see Figure 2.10).

From the fitted Gaussian functions, we extract the width of the correlation peaks at different pump powers, which is shown in Figure 3.10 a). The black dashed line denotes the mean value and the grey shaded area depicts one standard deviation. With the measured cavity linewidth and the known detector timing jitter, we can approximate the expected peak width as $\tau_{\mathrm{exp}} = \sqrt{2\tau_{\mathrm{jit}}^2 + \tau_{\mathrm{FWHM}}^2} = 0.66\,\mathrm{ns}$, which is in excellent agreement with the mean width $\bar{\tau} = (0.64 \pm 0.07)$ ns, and the width extracted from above simulation $\tau_{\mathrm{sim}} = 0.63\,\mathrm{ns}$ using the experiment parameters. $\tau_{\mathrm{FWHM}} = 2\ln(2)\tau_{\mathrm{rd}}$ is the full width at half maximum of the exponential decay [93].

Of special interest is the ratio of real coincidences to accidental coincidences (CAR), which is the height of the coincidence peak divided by the constant offset. Figure 3.10 b) shows the CAR for measurements at different pump powers, where the black dashed line denotes the mean value of $\overline{\mathrm{CAR}} = 1.86 \pm 0.16$ and the grey shaded area indicates one standard deviation. Except for the measurement at 300 mW intra-cavity power all CAR values are below 2, which, in principle, can be exceeded by a nonclassical photon-pair source. The ratio of optical to thermal energy in this frequency regime at room temperature is $\hbar\omega / k_{\mathrm{B}}T \approx 390$, which shows that the thermal occupation of cavity modes can be neglected, and coincidences from the thermal source are irrelevant. We can calculate the expected CAR from the measured photon-pair production rate and the expected accidental coincidence

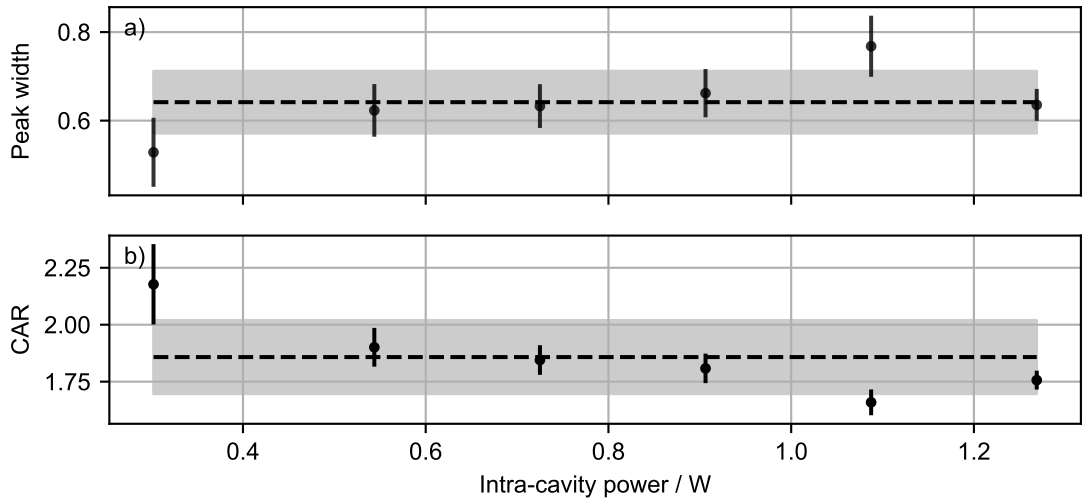

Figure 3.10: *Peak width a) and CAR b) extracted from the measurements at different intra-cavity pump powers. The dashed black line is the respective mean and the shaded area denotes one standard deviation. One can observe that the low power measurement slightly deviates from the other measurements in peak width and CAR. This can be caused by slightly higher intra-cavity losses due to weak optical damage in the mirror coating.*

rate (see Equation 3.7) via[6]

$$\mathrm{CAR}_{\mathrm{theo}} = 1 + \frac{\Gamma}{\sqrt{2\pi}\sigma\gamma_1\gamma_2}\,, \tag{3.10}$$

to 1.92 ± 0.11, which is in good agreement with the mean value. This derivation shows that we are limited by the accidental coincidence rate caused by the mechanisms stated above. Further filtering in the spectrometer could reduce the background rates and, consequently, increase the coincidence to accidental coincidence ratio. However, since the detection efficiencies in both spectrometer branches would decrease as well, the necessary measurement time for gaining enough statistics for each measurement would also increase. We observe that the peak width and CAR values for the measurements at 300 mW and 1.1 W intra-cavity power deviate from the mean values and see an anticorrelation between these two quantities. The lower peak width for the first measurement may be attributed to a larger cavity linewidth due to the weak optical damage in the mirror coatings. Due to the lower peak width, the CAR increases, and decreases for the measurement at higher power.

Influence of the binning onto the measurements So far, we fixed the binning time in the analysis of the correlation data to 150 ps, which is a reasonable time interval, since the TDC temporal resolution

[6] This equation can be derived from the accidental coincidence rate and the amplitude A of the coincidence peak, which is related to the photon-pair production rate by $A = \tau_\Delta \Gamma P^2/\sqrt{2\pi}\sigma$. We find

$$\mathrm{CAR}_{\mathrm{theo}} = 1 + \frac{A}{\Gamma_{\mathrm{acc}}} = 1 + \frac{\tau_\Delta \Gamma P^2}{\sqrt{2\pi\sigma^2}} \frac{1}{\gamma_1\gamma_2 P^2 \tau_\Delta} = 1 + \frac{\Gamma}{\sqrt{2\pi}\sigma\gamma_1\gamma_2}\,. \tag{3.9}$$

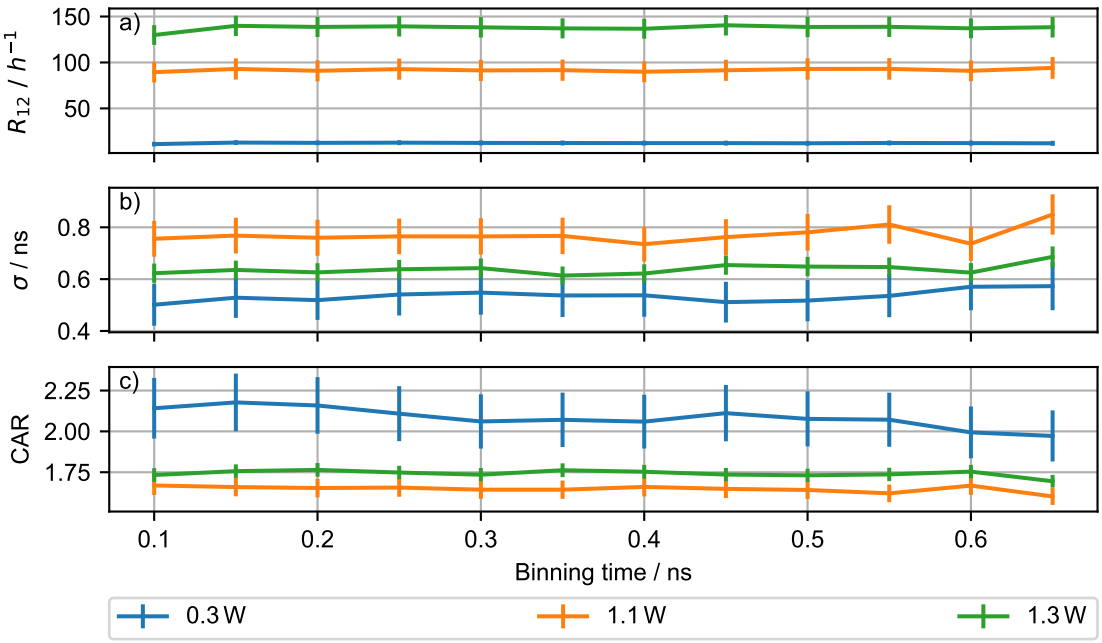

Figure 3.11: *Influence of bin width on the data analysis ranging from 0.1 ns to 0.65 ns. For the sake of clarity, a collection of measurements is shown, while the same behavior is observed for the other measurements. The experimentally determined coincidence rate per hour is shown in a) and constant over the entire range. Coincidence peak width b) and coincidence to accidental coincidence ratio c) are constant within the error margins, in which a slight anticorrelation between these quantities can be observed. Consequently, the analysis is independent of the binning, which is expectable and required. The drifts of the width and CAR for the measurement at lowest power of 0.3 W is caused by the lower amount of coincidence events in comparison to the other datasets, which increases fluctuations and error bars of the histogram bins.*

is 45 ps and lowering the binning time to 90 ps or less leads to artefacts from the measurement. A lower binning time is desirable, since the fitting of the Gaussian functions is then done with more data points, however, especially for measurements with a smaller dataset, error bars and noise in the histograms become larger. We, therefore, want to investigate the influence of the bin size on the peak width, CAR, and the photon-pair production rate. Figure 3.11 shows these quantities in relation to the binning times ranging from 0.1 ns to 0.65 ns, while for the sake of clarity only a collection of datasets is shown. The upper limit of bin widths is chosen because of the expected peak width stated above. At larger bin widths, only a few data points lie in the coincidence peak, making the fit more sensitive to fluctuations in the random distribution of coincidence events over the peak. The rate of coincidences per hour is constant over the entire range of binning times for every measurement, demonstrating that the analysis is independent of the bin width. For the width and CAR, slight variations within the error margins can be observed, leading to larger deviations for longer binning times. This behavior is expectable since the fitting is then done with only a few data points. The amount of photon pairs is not affected by this, since it is proportional to the product of the peak amplitude and width, which cancels variations in both quantities that arise by changing the binning time. Width and CAR values for the

measurement at the lowest intra-cavity pump power of 0.3 W show a drift in comparison to the other measurements, which can be explained by the less amount of coincidence events in the dataset due to smaller rates. Nevertheless, the analysis of the experimental data is independent of the binning time, indicating the robustness of the results.

3.5 Summary

In summary, I presented an experiment where the third-order nonlinear polarization of the dielectric coating in a high-finesse micro-cavity is used to generate correlated photon pairs via spontaneous four-wave mixing. The leakage of the electric field of the standing wave into the dielectric mirror coating leads to a modulation of the material polarization at twice the pump wavelength. Resultingly, two photons from the pump wave are annihilated and a pair of signal and idler photons on neighboring cavity modes, shifted by one free spectral range up- and downwards, is created.

The theoretically possible coincidence rate is estimated via numerically integrating the calculated intensity distribution inside the dielectric coating, following the theoretical model established in subsection 2.2.3. The theoretical rate $\Gamma_{\text{theo}} = 0.4\,\text{s}^{-1}\,\text{W}^{-2}$ and the experimentally determined rate $\Gamma_{\text{exp}} = (0.22 \pm 0.01)\,\text{s}^{-1}\,\text{W}^{-2}$ are found to be in fair agreement, considering possible drifts throughout the measurement time of several hours, imperfections in the dispersion compensation of the pump frequency, and a possibly lower nonlinear refractive index, due to a longer response time of the medium.

It has been shown that the data evaluation is independent of the bandwidth of the correlation analysis by varying the binning time. The ratio of real coincidences to accidental coincidences is found to be smaller than two, such that the nonclassical nature of the experiment was not entirely verified. This is due to a limitation by the detector background rates, since the theoretical possible ratio is found to be $\text{CAR}_{\text{theo}} = 1.92 \pm 0.11$, which is in agreement with the experimentally determined mean value of $\text{CAR}_{\text{exp}} = 1.86 \pm 0.16$. It has been further verified by simulation and experiment that the correlation time of the coincidence peaks is broadened by the timing jitter of the single photon counting modules. The experiment demonstrates that, in principle, every cavity featuring dielectric mirror coatings can act as a photon-pair source, even though the cavity does not contain an additional nonlinear medium. Moreover, it shows that the material response of the third-order dielectric polarization can follow the driving field at optical frequencies, i.e. on a femtosecond time scale.

There are two ways of tuning the frequencies of the generated photons in order to tailor the system to e.g. bridge wavelength gaps in hybrid quantum systems. By using cavity modes of higher order, i.e. a frequency separation of several free spectral ranges, the frequencies of the output photons are changed, while the pump frequency needs to be adjusted for dispersion compensation. A second possibility is to change the cavity length in order to change the mode separation. In addition to the tunability, the system features an easy use because of its self-alignment and the avoidance of fulfilling an explicit phase-matching condition, due to the sub-wavelength thick nonlinear medium. By increasing the photon-pair generation rate, the dielectric coating can be designed such that the intensity is increased in a specific layer with a high nonlinear refractive index. From the simulations it is evident that mainly the second layer out of Nb_2O_5 contributes to the nonlinearity, and the dielectric coating can be optimized to have a large reflectivity and high intensity in a thicker Nb_2O_5 layer.

With the present experiment, the quantum nature of the spontaneous four-wave mixing process has not be shown, since the amount of background coincidences in comparison with the rate of real

coincidences is too large. In order to increase the photon-pair production rate, a larger nonlinearity or a longer interaction region is desirable. In the next chapter we will see that filling the resonator with a liquid extends the nonlinear interaction range to the whole cavity length and increases the photon-pair rate by several orders of magnitude.

CHAPTER 4

Spontaneous four-wave mixing in a liquid-filled cavity

In the last chapter, I introduced and motivated the necessity of tunable photon-pair sources for interconnecting hybrid quantum systems and to bridge wavelength gaps between dissimilar emitters with the final goal of building a quantum network. I demonstrated a novel approach for utilizing the third-order nonlinear dielectric polarization inside the high-reflective coatings of a high-finesse optical micro-resonator with purpose of generating correlated photon pairs on cavity modes adjacent to the pump mode. The approach benefits from a simple, self-aligned setup with intrinsic phase matching due to the sub-wavelength thick nonlinear medium. The photon-pair frequencies can, in principle, be tuned by changing the cavity length, or generating signal and idler photons on cavity modes shifted by multiple free spectral ranges from the pump mode. The micro-cavity increases the desired nonlinear effects and the photon-pair bandwidth is determined by the cavity linewidth.

However, in order to increase the photon-pair generation rate, an extension of the nonlinear medium to the complete cavity length is desirable. From the discussion of the phase matching in subsection 2.2.3, we see that this can be ensured for even longer media than the sub-wavelength thick material in the previous chapter 3. In this experiment, we fill a micro-cavity with a liquid, to increase the length of the nonlinear medium to the entire cavity length. Correlated photon pairs have been produced in liquid-filled photonic crystal fibers [94], but this experiment is the first realization of spontaneous four-wave mixing in a liquid-filled high-finesse micro-cavity and the results have been published in [95]. The experiment was conducted in the context of the master thesis of Felix Rönchen [96].

First in this chapter, I discuss the choice of liquid in terms of nonlinear response and experimental difficulties, like potential health hazards, flammable vapors, etc. (section 4.1). Then, I briefly describe the construction of the cavity with focus on the liquid filling, and point out differences and extensions to the previous setup in section 4.2. With the increase of nonlinear effects, the bistable operation is much more severe as compared to the empty cavity, which I discuss in section 4.3. Finally, I present and analyze correlation measurements performed for second- and third-order adjacent longitudinal modes in section 4.4.

4.1 Choice of nonlinear medium and photon-pair rate estimation

Due to the highly curved wavefronts in a micro Fabry-Pérot cavity, crystals are not suitable for extending the interaction length, since interfaces lead to scattering of photons out of the cavity mode, increasing losses and, thus, decreasing the finesse. Gases would completely fill the space between the mirrors without imposing an additional boundary, however, the third-order nonlinearity is several orders of magnitude lower than for solids, even at pressures on the order of several hundred bar [97]. Liquids have similar electronic nonlinear responses like solids (see subsection 2.2.1) without imposing additional interfaces inside the cavity. Therefore, by filling the resonator with a synthetic silicone oil, we extend the nonlinearity to the complete cavity length and drastically increase the photon-pair generation rate. From the discussion of nonlinear electronic and molecular responses of liquids in subsection 2.2.1, it is evident that solely the electronic response can contribute to the desired spontaneous four-wave mixing process in the liquid. The choice of the nonlinear medium requires attention to several aspects such as low absorption, high nonlinear response, simple handling, and a high light-induced damage threshold. A low absorption coefficient is mandatory to maintain the finesse of the resonator.

Carbon disulfide (CS_2) is a reference for nonlinear optical liquids, since it has one of the largest electronic nonlinear responses of $n_2 = 1.5 \times 10^{-19}\,\mathrm{m^2\,W^{-1}}$ [98], which is almost the same as for niobium pentoxide (Nb_2O_5) and tantalum pentoxide (Ta_2O_5), and about one order of magnitude larger than for silicon dioxide (SiO_2). Benzene derivatives show nonlinear electronic responses lower by a factor of two compared to CS_2, while the responses of alcohols, acetone, and water are about the response of SiO_2 [51]. Regarding the nonlinear response, CS_2 would be the proper choice, however, the handling is not simple, since it is inflammable, irritant, and shows other health hazards [99]. Benzene derivatives like nitrobenzene and toluene show high nonlinear responses as well [100], while health hazards such as acute toxicity, flammable liquids and vapors, skin irritations, etc. [101, 102], limit the suitability for a proof of principle experiment, since engineering a stable, reliable, and safe experimental setup is required. Due to these limitations and restrictions a synthetic silicone oil (Tetramethyl-tetraphenyl-trisiloxane) is used, which has high optical transparency. Silicone oils have a vast range of applications in the industry and are used as lubricants in vacuum pumps, for instance. It features a low vapor pressure [103], which is necessary for a reliable and stable operation without the need of refilling the liquid.

However, the instantaneous nonlinear refractive index is not stated in literature, only the low-frequency value [104], thus we assume the coefficient of acetone ($n_2 = 4 \times 10^{-20}\,\mathrm{m^2\,W^{-1}}$ [105]) for the estimation of the photon-pair rate. We further assume similar cavity properties and experimental conditions as in the previous experiment. Suppose a cavity finesse of $F = 10000$ and a length of $l = 33\,\mu\mathrm{m}$ similar to the cavity reported on in chapter 3. Taking the refractive index of the silicone oil of $n = 1.556$ into account [106], the free spectral range is about $\Delta\omega_{\mathrm{fsr}} = 2\pi \times 3\,\mathrm{THz}$. As a result, the expected photon-pair production rate is $\Gamma_{\mathrm{theo}} = 140\,\mathrm{W^{-2}\,s^{-1}}$, where in contrast to the previous experiment the phase matching between the pump, and signal and idler modes is relevant and given by Equation 2.38. We have discussed the phase matching in subsection 2.2.3 and have seen that a medium of the length considered here still allows a larger wavevector mismatch and the requirements on phase matching are not very difficult to fulfill. In the last chapter, furthermore, we have seen that the energy matching between the pump, and signal and idler modes already ensures phase matching. The pump frequency has been adjusted such that the spectral distance between pump and signal, and pump and idler mode is similar. Because of dispersion of the material this is not necessarily satisfied.

Nevertheless, we expect an increase in the generation rate by filling the cavity with the nonlinear liquid of almost three orders of magnitude, as compared to the rate due to solely the nonlinearity in the dielectric mirror.

4.2 Liquid-filled cavity construction and experimental apparatus

The experimental setup is analogous to the generation of photon pairs in the empty cavity (cf. chapter 3), however, using a liquid as (additional) nonlinear medium, demands some changes regarding the apparatus, which shall be briefly presented in this section. First the construction and characterization of the cavity before and after the insertion of the liquid is described in subsection 4.2.1. Then, additions to the optical setup and the spectrometer with respect to the previous experiment are mentioned in subsection 4.2.2.

4.2.1 Cavity construction and liquid filling

The cavity is formed by a micro-machined and high-reflective coated end facet of an optical single-mode fiber as one mirror, and a planar macroscopic mirror with the same coating as the second mirror. The coating properties can be seen in section 3.1 and the specifications are a transmission of 100 ppm and losses are about 150 ppm per mirror. An illustration showing the cavity inside an aluminum housing for isolation from sound waves and dust protection can be observed in Figure 4.1. The fiber is glued onto a piezo-electric shear plate actuator (Noliac CSAP02), electrically isolated with alumina plates,

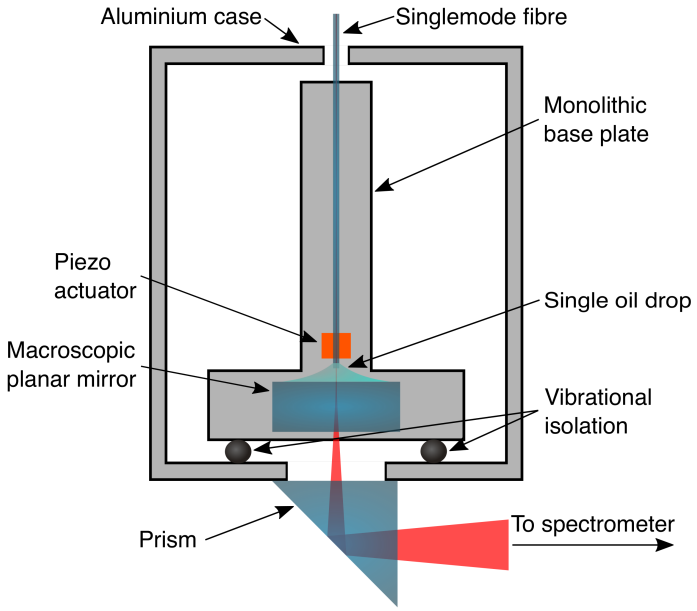

Figure 4.1: *Scheme of the cavity setup [95]. The cavity is composed of a high-reflective coated and micro-machined end facet of a single-mode fiber, and a macroscopic mirror arranged on a monolithic mount for an increased stability. The mount is fixed on Viton balls for isolation from mechanical oscillations, while the aluminum enclosure shields the system against acoustic vibrations and dust. A single oil drop is inserted into the cavity in order to increase third-order nonlinear effects.*

attached to an aluminum base. The macroscopic mirror is mounted in a v-groove on the aluminum base, establishing a monolithic setup for reducing the impact of mechanical oscillations and vibrations on the stability of the high-finesse cavity. The alignment of the fiber is done with a five axis translation stage, observed via two microscope cameras directed onto the fiber tip from above and the side. During the alignment the cavity is scanned with a piezo-electric element inside the translation stage and the incoupling into the cavity of an incident laser via the single-mode fiber is optimized. Viton balls are used for further vibrational isolation improving the stability of the cavity lock. The mount is clamped perpendicular to the ground such that a single oil drop can be placed onto the macroscopic mirror, while the transmitted light is redirected by a right angle prism with appropriate antireflection coating on its legs (Thorlabs PS910-B). The mechanical cavity length is 38.4 µm and the cavity finesse is $F = 12500 \pm 500$. The radius of curvature of the fiber mirror is $R = 200\,\mu\text{m}$ leading to a mode waist of $w_0 = 4.4\,\mu\text{m}$ on the planar mirror and a waist of $w_\text{m} = 5.5\,\mu\text{m}$ on the fiber mirror, calculated via Equation 2.10. The small volume of the cavity mode increases the desired nonlinear effects, but also thermo-optic responses leading to bistable behavior (see section 4.3).

The resonator is filled with the synthetic silicone oil (Tetramethyl-tetraphenyl-trisiloxane, DC704). For this purpose, a syringe filled with the oil is moved close to the fiber tip with a three axis translation stage. The cavity is observed with microscope cameras from two sides, since the fiber could easily break when touched and the mirror could be scratched. When the syringe is close to the fiber, its piston is pushed with a micrometer screw, in order to cautiously place a single oil drop on the macroscopic mirror. The oil changes the properties of the cavity, since it increases the optical path length by a factor of its refractive index. Consequently, the free spectral range is changed from (3.901 ± 0.001) THz to (2.507 ± 0.002) THz. The refractive index of the silicone oil can be determined from the ratio of the free spectral ranges to be $n = 1.556$, which is in excellent agreement with the literature value [106]. The medium does not decrease the cavity finesse, instead the linewidth is reduced from its initial value of 313 MHz to 200 MHz, which implies a high optical quality of the oil. Here, the ratio of the linewidths is again the refractive index of the oil and the finesse stays constant within the precision of the measurement. The oil slightly alters the reflection properties of the dielectric mirror coatings, since these are designed to use in air or vacuum. Therefore, the first interface is different due to the changed ambient medium and the transmission coefficient increases from its initial value of 100 ppm to 190 ppm at a wavelength of 780 nm. Since the finesse stays constant, we can conclude that the losses decrease by the same amount the transmission increases. We attribute this to the smoothening of the mirror surface due to the refractive index matching between the medium inside the cavity and the SiO_2 layer. Both refractive indices are very similar, wherefore the first layer of the coating effectively vanishes and losses due to scattering of the uneven surface are reduced. From the change in cavity losses, we can estimate the absorption of the oil. We assume the remaining losses to stem solely from absorption in the medium and can calculate the absorption coefficient α via rearranging the Lambert-Beer law to

$$\alpha = -\frac{1}{l}\ln(1 - \mathcal{A})\,, \tag{4.1}$$

where $\mathcal{A} = 60\,\text{ppm}$ are the absorption losses extracted from the finesse measurement and l is the cavity length. The upper limit for the absorption coefficient is thus $\alpha = 1.6\,\text{m}^{-1}$, indicating a high optical quality at near infrared wavelengths.

4.2.2 Laser and detection setup

The laser and detection setup is analogous to the setup described in subsection 3.2.2, but is briefly summarized in the following and changes, e.g. additional components, are pointed out. For comparison see the scheme of the optical setup in Figure 3.4. Another far tunable probe laser (Toptica DL Pro) is used in order to quickly determine the dispersion compensation point of the cavity, which is essential for an efficient generation of correlated photon pairs (cf. subsection 3.2.1). Since the cavity linewidth is much smaller than in the previous experiment, a precise determination of the dispersion compensated pump frequency is much more important. The pump laser is spectrally filtered with a holographic diffraction grating and the zeroth order is send to a wavelength meter. The first order is modulated with a home-built electro-optic modulator, in order to apply sidebands with a beat frequency of 60 MHz. Sidebands are used to stabilize the cavity length to the pump laser frequency via a Pound-Drever-Hall lock [89]. The two reference lasers are overlaid via a 50:50 beamsplitter and the combined beams are then overlapped with the pump laser to be simultaneously coupled into the cavity fiber. The fiber is fixed to the table and the polarization of the incident light is adjusted by a combination of half-waveplate and quarter-waveplate (QWP) to be circularly polarized in combination with the retardation induced by the glass fiber. This is done by maximizing the cavity reflection signal on the reflection path of a polarizing beamsplitter.

The light transmitted by the cavity is split by a beamsplitter, where 10 % are send to two photodiodes for observing the polarization state of the cavity transmission signal. 90 % are send to the spectrometer. The polarization of the light is changed to horizontal via a QWP, in order to reach the highest efficiency of the following diffraction grating (Thorlabs GH50-18V) spectrally dispersing the incident light. The zeroth order of the diffraction grating is send to a fast photodiode providing the error signal for the Pound-Drever-Hall stabilization. The spectrometer has a resolution of $\lambda/\delta\lambda = 6000$. While the pump light is dumped, the separated cavity modes are send to single photon counters. In each branch, the light is further filtered by narrow line filters (Semrock LL01-785-12.5 and Semrock LL01-808-12.5) with a bandwidth of 3 nm and additional pinholes, leading to a suppression of stray light of at least four orders of magnitude. The quantum efficiencies of both paths , are 9.9 % and 7.2 %, respectively, including beamsplitter coupling, diffraction efficiency, spectral filtering, and detection efficiencies of the single photon counters (SPCM, Excelitas SPCM-AQRH).

The output of the single photon counters is recorded with a time-to-digital converter (TDC, Cronologic HPTDC8-PCI), where the TTL pulses from the SPCM are converted to NIM pulses in between. The timing jitter of the SPCM is 350 ps and the resolution of the TDC is 45 ps. From the list of arrival times, we perform a correlation analysis between the two channels with adjustable bandwidth. For every entry on the list on channel one, time differences to counts on channel two are extracted, if the time difference is in a certain time window, e.g. 40 ns.

4.3 Optical bistability

In the last chapter, we observed the bistable operation of the cavity at high pump powers (cf. section 3.3), due to the thermo-optic nonlinearity in the dielectric coating and mainly the thermal expansion of the cavity mirrors, inducing an additional intensity-dependent phase shift. The result is a broadened or narrowed Lorentzian line shape (see subsection 2.2.2), depending on the scan direction of the piezo-electric element. Even though the nonlinearity is restricted to a few micrometers in the dielectric coating and the mirror substrates, the change in mechanical and optical length leads to lineshifts on

the order of several GHz. We expect a much larger nonlinearity due to thermo-optic processes in the experiment at hand, since the nonlinearity is extended to the complete cavity length.

Figure 4.2 a) shows the characteristic bistable lineshape for both scan directions, where the broadened curve corresponds to a decreasing cavity scan, i.e. a scan from red to blue detuned. The thermo-optic dynamics oppose the decreasing cavity length due to the increase of optical path length by virtue of the rising refractive index. When the resonance is passed, however, the power reduces much more rapidly due to the decreasing refractive index by cooling. The lineshift depends on the total power incident on the cavity and we find a linear relationship between the lineshift β and the power transmitted by the cavity (see Figure 4.2 b)). From the lineshift we can calculate the temperature increase of the oil. We thereby assume the scan time to be much slower than the thermal response time, such that the cavity is scanned adiabatically and reaches thermal equilibrium during the scan. We further assume that the lineshift solely originates in the thermo-optic response and neglect the thermal expansion of the cavity mirrors. This is a reasonable assumption, since the lineshifts observed in the previous experiment are one order of magnitude smaller, at roughly three times higher intra-cavity power. From Equation 2.26 and Equation 2.28 we find the relation

$$\beta \approx Q \frac{\kappa}{n} \Delta T \,, \tag{4.2}$$

where $Q = 2 \times 10^6$ is the quality factor of the resonator, and κ is the thermo-optic coefficient, which is about $3 \times 10^{-4}\,\mathrm{K}^{-1}$ for various silicone oils [107]. The resulting temperature increase for a lineshift of $\beta = 70$ is $\Delta T = 0.2\,\mathrm{K}$. The low value may surprise at first, however, in liquids heat is not only dissipated by conduction, but additionally by convection. Compared to the reported values in [64], the temperature increase is about one order of magnitude smaller and two orders of magnitude smaller than the temperature increase obtained for the empty cavity in vacuum (cf. section 3.3).

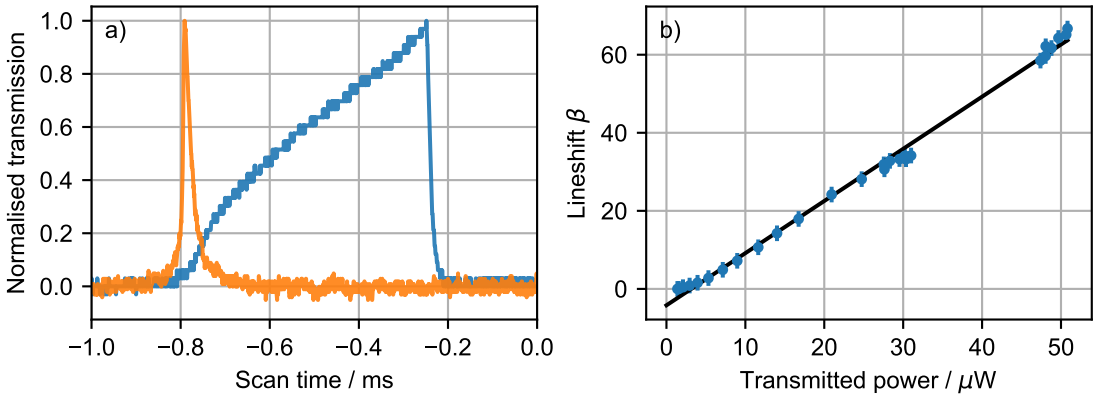

Figure 4.2: *Bistable dynamics of the liquid-filled micro-resonator. a) shows the characteristic bistable lineshapes due to the effectively reduced or increased scan velocity by the intensity dependent thermo-optic response of the liquid. The broadened line refers to a decreasing cavity length. b) shows the lineshift extracted from the broadened lineshape with respect to the transmitted cavity power (cf. Figure 2.7).*

4.4 Correlation measurements

Before every measurement the dispersion compensation point is determined by overlapping both probe laser resonances with the pump laser resonance, and successively tuning the pump frequency, until the spectral distance between the pump laser and the respective signal and idler frequency are similar (cf. subsection 3.2.1). We notice small shifts in the dispersion zero-point due to changing ambient temperature, pressure and humidity, which the cavity is not protected against, in comparison to the previous cavity in vacuum. The large nonlinear bistability leads to an additional shift of the dispersion compensation point such that the measurement needs to be performed at the corresponding pump power. The dispersion compensation point additionally depends on the order m of longitudinal mode, i.e. the number of free spectral ranges the signal and idler modes are shifted up- and downwards with respect to the pump mode. After finding the optimal frequency, we stabilize the pump laser to this value with a wavelength meter and lock the cavity to the pump laser frequency with a Pound-Drever-Hall locking scheme. The correlation data is acquired by reading out the TDC for several tens of minutes and perform a correlation analysis on the list of timestamps between the detectors in the respective spectrometer branches.

In first order, only a flat background of accidental coincidences can be observed. This is due to high background rates on the photon counters by virtue of spontaneous Raman scattering inside the oil. This process, in general, generates photons on lower (Stokes) and higher (anti-Stokes) frequencies by photon-phonon scattering, where either phonons are created (Stokes) or annihilated (anti-Stokes). Raman scattering creates single photons with no time correlation, wherefore they contribute to accidental coincidences and, consequently, generate an uniform correlation signal. With background rates on the order of $1 \times 10^5\,\mathrm{s}^{-1}$, an accidental coincidence rate of about $1\,000\,\mathrm{s}^{-1}$ can be expected (see Equation 3.7). Taking the detection efficiencies into account, a coincidence rate on the order of $1\,\mathrm{s}^{-1}$ is anticipated. The signal-to-noise ratio is thus dominated by the background and the coincidence peak cannot be observed.

In second order, however, the background from spontaneous Raman scattering is reduced due to the higher separation of the signal and idler mode from the pump mode. Additionally, spatial filtering by inserting iris diaphragms in the signal and idler path behind the diffraction grating further reduces the background rates. In Figure 4.3, a sample histogram of time differences with a bin width of 0.25 ns acquired in 30 minutes at an intra-cavity power of 0.58 W can be seen. The respective signal and idler frequencies are $\omega_{2,-} = 2\pi \times 377.155\,\mathrm{THz}$ and $\omega_{2,+} = 2\pi \times 387.155\,\mathrm{THz}$ at a pump frequency of $\omega_0 = 2\pi \times 382.155\,\mathrm{THz}$. A constant background of accidental coincidences exceeded by a clear peak at about −12 ns time delay can be observed. The delay stems from slightly different path lengths of the two spectrometer branches and mainly from the different cable lengths in the electronic readout circuit. An additional cable is inserted in order to intentionally shift the coincidence peak by 10 ns from the zero delay. The solid curve is a Lorentzian[1] fit to the data with constant background, from which we determine the coincidence rate and bandwidth of the photon pairs. The full width at

[1] We assume a Lorentzian line shape here, since the correlation distribution is neither dominated by the cavity characteristics, nor by the timing jitter of the detection setup. Consequently, the exponential distribution overestimates the photon number and the gaussian distribution underestimates it. In principle, the convolution of the exponential decay from the cavity dynamics and the gaussian broadening due to the timing jitter should be the correct distribution. However, this function employs error functions and does not e.g. recover the expected timing jitter, which may be due to the limited number of coincidence events in the datasets. Therefore, for simplicity, a Lorentzian is assumed, since it fits better to the given distribution than the exponential or gaussian distribution and, thus, quantities like the number of coincidences and the correlation time can be extracted more accurately.

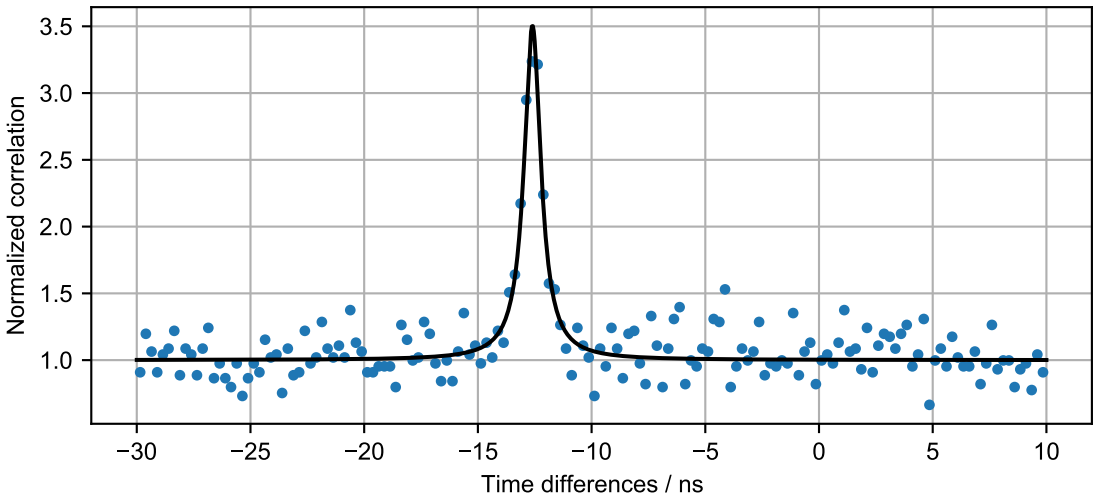

Figure 4.3: *Normalized coincidence measurement in second order at an intra-cavity power of 0.58 W, for a measurement time of 30 minutes, and a bin width of 0.25 ns. A clear peak exceeding the constant background is visible at about −12 ns. The shifted peak position stems from different lengths of the spectrometer branches and mainly from different cable lengths in the electronic readout circuit. The solid line is a Lorentzian fit to the data.*

half maximum is (1.06 ± 0.08) ns, corresponding to a linewidth of (328 ± 19) MHz. The increased linewidth is attributed to lower reflectivities of the dielectric mirror coating at the signal or idler frequency. The coincidence-to-accidental ratio (CAR) given by the peak height relative to the uniform background can be extracted to be 3.5 ± 0.2, which, in contrast to the previous experiment, exceeds the classical limit of 2 and shows the quantum nature of the photon-pair source [92].

The total number of coincidence events is the area under the Lorentzian line shape function, which is determined by integrating the distribution. The integral is dependent on the bin width, since the fit parameters change with varying binning times. In order to account for the variations and make the result independent of the histogram parameters, we divide the area under the Lorentzian by the bin width τ_Δ and find

$$N = \frac{\pi\tau}{2\tau_\Delta} A\,, \tag{4.3}$$

for the total number of coincidences[2] in dependence of the fit amplitude A and full-width-half-maximum τ. We perform the correlation measurement at additional pump powers and observe the characteristic quadratic dependence of the coincidence rate on pump power as shown in Figure 4.4. The solid line is a quadratic fit of the form $R_{12} = \Gamma \cdot P^2$, yielding a photon-pair generation rate of $\Gamma_{\text{exp}} = (1.89 \pm 0.15)\,\text{s}^{-1}\,\text{W}^{-2}$. Considering the efficiencies in the detection branches, we find a total experimental rate of $\Gamma_{\text{exp}} = (330 \pm 30)\,\text{s}^{-1}\,\text{W}^{-2}$. From this experimentally determined rate and Equation 2.57, we can compute the nonlinear refractive index of the oil to be $n_2 = (5.6 \pm 0.3) \times 10^{-20}\,\text{m}^2\,\text{W}^{-1}$, in which the phase matching is accounted for (see Equation 2.38). The

[2] The derivation of the equation is analogue to the calculation in Equation 3.8.

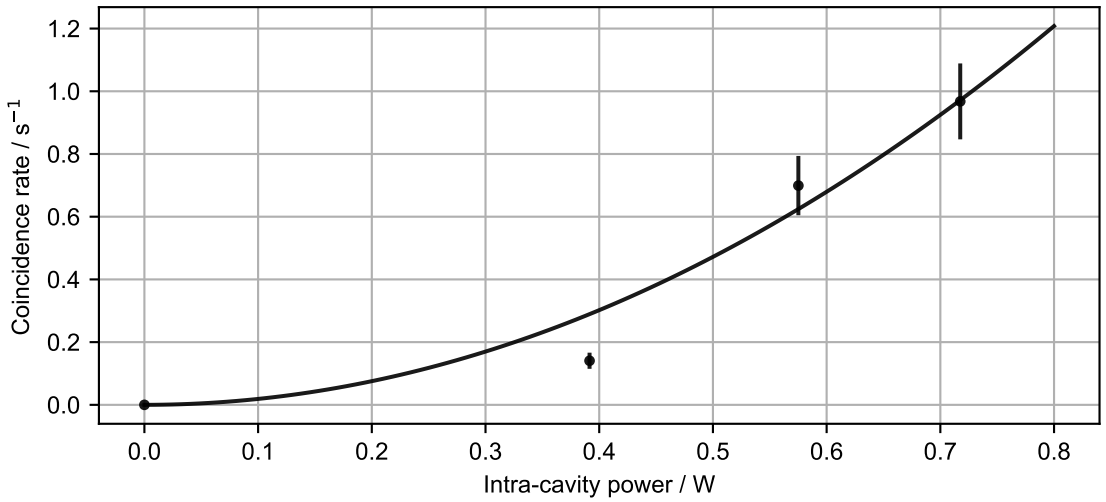

Figure 4.4: *Coincidence rate dependent on intra cavity pump power. The solid line is a quadratic fit to the data, showing the characteristic relationship for a spontaneous four-wave mixing process. The coincidence generation rate is determined from the fit to be* $\Gamma_{\mathrm{exp}} = (1.89 \pm 0.15)\,\mathrm{s}^{-1}\,\mathrm{W}^{-2}$.

electronic nonlinearity is slightly larger than the coefficient of acetone and around the nonlinear response of nitrobenzene [105].

The uniform backgrounds in the correlation measurements give the accidental coincidence rate per pump power. From the raw counts on the detector for each measurement, we can extract the count rate per pump power for the respective detection branch in the spectrometer by fitting the linear function $R_i = \gamma_i \cdot P$ (see Figure 4.5 a)). We find $\gamma_1 = (37\,000 \pm 2\,200)\,\mathrm{W}^{-1}\,\mathrm{s}^{-1}$ and $\gamma_2 = (15\,000 \pm 900)\,\mathrm{W}^{-1}\,\mathrm{s}^{-1}$. Inserting these values and above bin width into Equation 3.7, the accidental coincidence rate can be calculated. Figure 4.5 b) shows the expected accidental coincidence rates per pump power (solid line) and the measured rates extracted from the fitted distributions. Considering potential intensity drifts throughout the measurement, both expectation and measured accidental coincidence rate are in good agreement. The detector count rates and the accidental coincidence rate are about one order of magnitude larger as compared to the previous experiment (cf. Figure 3.8). Furthermore, the count rate on the detector in the lower frequency branch of the spectrometer is larger than for the higher frequency branch, although the detector efficiencies are similar. This is expected from spontaneous Raman scattering, since the Stokes process excites vibrational states in the material, while the anti-Stokes process reduces the vibrational energy in the system. Consequently, the lower frequency branch in the spectrometer shows a higher count rate due to the different population of vibrational states in thermal equilibrium [47]. The ratio of the anti-Stokes to the Stokes intensity is given by [108]

$$\frac{I_{\mathrm{AS}}}{I_{\mathrm{S}}} = \left(\frac{\omega + \omega_{\mathrm{v}}}{\omega - \omega_{\mathrm{v}}}\right)^4 \exp\left(-\frac{\hbar\omega_{\mathrm{v}}}{k_{\mathrm{B}}T}\right), \tag{4.4}$$

where ω is the excitation laser frequency, ω_{v} is the vibrational energy, T is the temperature, and k_{B} is Boltzmann's constant. Using the spectral distance between the pump and the signal modes as the

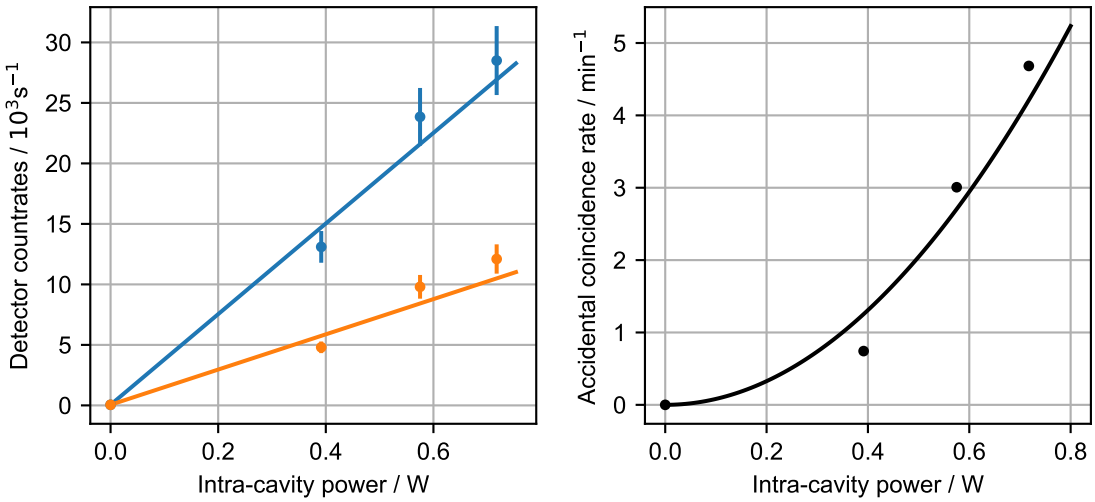

Figure 4.5: *Raw count rates per pump power in the respective detection branch a) and the corresponding expected and measured accidental coincidence rate b).*

vibrational energy, assuming room temperature (300 K), and inserting the pump frequency, we expect a ratio of 0.50. Considering above detector count rates and the corresponding detection efficiencies gives a measured ratio of 0.56 ± 0.07. Both values are in very good agreement, which confirms spontaneous Raman scattering being the origin of the larger count rates as compared to the previous experiment and the main contribution to the accidental coincidence rate.

Averaging the extracted temporal widths gives the mean full-width-half-maximum value $\overline{\tau} = (0.94 \pm 0.06)$ ns (see Figure 4.6 a)), resulting in the mean spectral bandwidth (340 ± 20) MHz. This value indicates a lower finesse of $7\,400 \pm 500$ due to weak optical damage and different coating properties at the signal or idler modes. If we refer the photon-pair generation rate to the pump power incident on the cavity, we find a total rate of $\tilde{\Gamma}_{\mathrm{exp}} = (14\,500 \pm 2\,400)\ \mathrm{mW}^{-2}\,\mathrm{s}^{-1}$, with a resulting spectral brightness of $(44 \pm 8)\ \mathrm{mW}^{-2}\,\mathrm{s}^{-1}\,\mathrm{MHz}^{-1}$. This quantity demonstrates the narrow-band operation of the photon-pair source. The CARs extracted from the measurements are shown in Figure 4.6 b) and yield a mean value of 3.1 ± 0.1. We can calculate the expected CAR by[3]

$$\mathrm{CAR}_{\mathrm{theo}} = 1 + \frac{2\Gamma}{\pi\tau\gamma_1\gamma_2}\,. \tag{4.6}$$

Taking above values, we find a value of 3.35 ± 0.31, which is in good agreement with the measured ratio.

In order to investigate the dependence of the analysis on the bin width, we determine above

[3] This equation can be derived from the accidental coincidence rate Γ_{acc}, which determines the uniform background in the histograms, and the peak amplitude, which is related to the photon-pair production rate as $A = 2\Gamma\tau_\Delta P^2/\pi\tau$. We find

$$\mathrm{CAR}_{\mathrm{theo}} = 1 + \frac{A}{\Gamma_{\mathrm{acc}}} = 1 + \frac{2\Gamma\tau_\Delta P^2}{\pi\tau}\,\frac{1}{\gamma_1\gamma_2\tau_\Delta P^2} = 1 + \frac{2\Gamma}{\pi\tau\gamma_1\gamma_2} \tag{4.5}$$

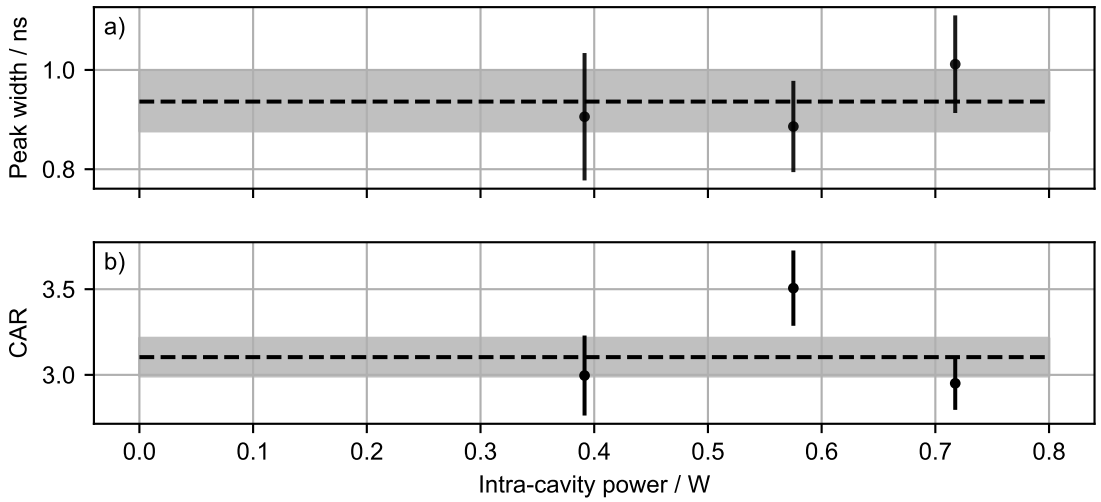

Figure 4.6: *Full-width-half-maximum a) and coincidence-to-accidental ratio b) obtained from the fitted histograms at different pump powers. The dashed lines and the grey shaded area indicate the mean value and one standard deviation, respectively.*

representative quantities, i.e. correlation width, CAR and photon-pair rate for several binning times (see Figure 4.7). All quantities are constant within the error margins for bin widths between 0.1 ns and 0.5 ns. The lower limit is chosen because of the 45 ps timing resolution of the TDC and the higher limit is determined by the peak width of 1 ns. Smaller bin widths lead to artifacts due to the finite temporal resolution and larger bin widths cause unstable fits because of a small amount of data points in the coincidence distribution. The analysis shows the independence on the bin width, especially for the determined photon-pair rates. There is an anti-correlation between the full-width-half-maximum and CAR, which is due to the correlation between amplitude and peak width in the fitted Lorentzian lineshape function. This does not affect the photon-pair production rate, since this quantity is proportional to the product of both values, such that fluctuations in the fitted parameters cancel.

We also investigate the generation of photon pairs in third order, i.e. the signal and idler modes are shifted by three free spectral ranges from the pump frequency. In principle, neglecting slight variations in the phase matching, the expected rate of generated photon pairs is independent of the spectral separation of the signal and idler frequencies to the pump frequency. Limits are imposed by the coating properties, since the rate depends on the finesse of the target frequencies. We need to search a new dispersion compensation point and find the pump, and signal and idler frequencies $\omega_0 = 2\pi \times 382.410\,\mathrm{THz}$, $\omega_{3,+} = 2\pi \times 389.988\,\mathrm{THz}$, and $\omega_{3,+} = 2\pi \times 374.831\,\mathrm{THz}$. The measured photon-pair generation rate in third order is $(0.58 \pm 0.22)\,\mathrm{W}^{-2}\,\mathrm{s}^{-1}$, which is about a factor of three smaller than the value obtained in the second-order measurements. The coupling coefficient in third order is a factor of two larger than for the second order, neglecting dispersion. Therefore, we attribute the deviation to weak optical damage from the high intensity measurements in second order and, moreover, to the lower reflectivity of the high reflective coatings for one of the signal or idler frequencies.

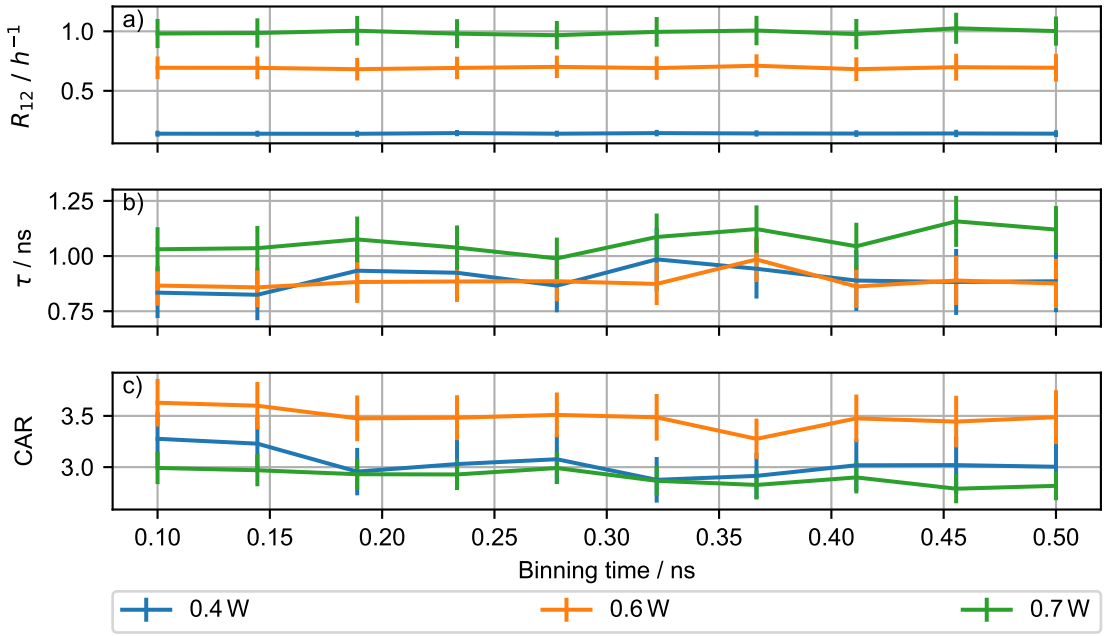

Figure 4.7: *Analysis of the characteristic quantities photon-pair rate a), correlation width b), and CAR c) in dependence of the bin width ranging from 0.1 ns to 0.5 ns. Within the error margins all quantities are constant and therefore independent of the binning. There is an anti-correlation between width and CAR, which is due to the correlation between the amplitude and width in the fitted Lorentzian lineshape function.*

4.5 Summary

In this chapter, I have presented an experiment generating correlated photon pairs in a liquid-filled cavity. The region of interaction has been extended from the sub-wavelength thick dielectric mirror coating utilized in the previous chapter 3 to the whole cavity length by inserting the liquid. I have discussed the choice of silicone oil as the nonlinear medium in the context of experimental difficulties such as health hazards, explosive vapors, etc., imposed by using benzene derivatives or carbon disulfide with known high third-order nonlinearities. We have observed a much stronger bistable behavior as compared to the previous experiment stemming from thermo-optic effects, rather than thermal expansion. The liquid exhibits a very low absorption coefficient and does not reduce the finesse of the resonator.

We have studied the generation of correlated photon pairs in the micro-cavity due to spontaneous four-wave mixing, in which two photons from the pump mode are scattered into neighboring longitudinal modes shifted by multiples of the free spectral range up- and downwards with respect to the pump mode. In second order, we have found a rate of $\Gamma_{\mathrm{exp}} = (330 \pm 30)\,\mathrm{s}^{-1}\,\mathrm{W}^{-2}$ with respect to the intra-cavity power and the total rate of $\tilde{\Gamma}_{\mathrm{exp}} = (14\,500 \pm 2\,400)\,\mathrm{mW}^{-2}\,\mathrm{s}^{-1}$ referring to the incident power. This shows another benefit of the high finesse cavity besides imposing its spectral characteristics onto the photon pair: due to the large resonant amplification of the cavity mode, a simple diode laser with a few milliwatt of pump power is sufficient to reach power levels for the generation of an adequate

stream of correlated photon pairs. The spectral bandwidth of the source is (340 ± 20) MHz, yielding a spectral brightness of $(44 \pm 8)\,\mathrm{mW^{-2}\,s^{-1}\,MHz^{-1}}$, demonstrating the narrow-band operation of the photon-pair source. The mean coincidence-to-accidental ratio is 3.1 ± 0.1 in agreement with the theoretically expected value of 3.35 ± 0.31 determined from experimental parameters. The CAR exceeds the limit of 2 given for a classical, thermal photon source, revealing the quantum nature of the underlying process. The ratio is limited by the background radiation mainly caused by spontaneous Raman scattering in the oil. This has been confirmed by the ratio of the count rates on the detectors in the signal and idler branch of the spectrometer. We furthermore observed the generation of correlated photon pairs in third order, where the rate is reduced due to weak optical damage in the mirror coatings by virtue of the high intensities employed in the second-order measurements, and a lower coating reflectivity at the signal or idler mode.

The frequencies of the signal and idler photons can, in principle, be tuned by changing the cavity length, in order to alter the spectral distance to the pump mode. With choosing a liquid as the nonlinear medium, a continuous change of the cavity length is possible. Another way to modify the output wavelengths is the generation of photon pairs on higher order modes, as has been demonstrated in the experiment. This approach does not only change the frequencies of the signal and idler photons, but the spectral spacing in between the photon pair. The generation rate can be further increased by using carbon disulfide as the nonlinear liquid, which would increase the coincidence rate by a factor of ten at least, while accidental coincidences due to Raman scattering would stay constant.

In principle, by increasing the cavity length, the nonlinear medium is further extended and the photon-pair generation rate can be improved. From Equation 2.57, a linear relationship between rate and cavity length can be extracted, however, phase-matching requirements in combination with dispersion and a larger mode volume for longer cavities limit the gain in increasing the cavity length. By changing the properties of the dielectric mirror coating to also be high reflective in the visible and the infrared spectrum at a telecom wavelength, photon pairs with a photon on a matter qubit transition and a flying qubit on the telecom band for long-range communication between network nodes can be generated without the need of photon conversion schemes. A further interesting extension of the experiment is a possible multiplexed operation where the dispersion is not only compensated for one pair of cavity modes, but multiple [15]. Driving this system above the parametric threshold could lead to the generation of a Kerr frequency comb [109, 110], where the comb teeth are generated on cavity modes via four-wave mixing processes between the pump and consecutively populated cavity modes. Within these systems, optical solitons play an important role, which lift dispersion due to the intensity-dependent refractive index and enabling coupling between multiple modes [111]. In this context, the system dynamics become very complicated due to potential chaotic behavior [112] and further research is necessary to outline possible experiments.

CHAPTER 5

Optical analogue of the Dynamical Casimir Effect

So far, we encountered two experiments where the third-order nonlinearities in high-finesse cavities lead to spontaneous four-wave mixing, a process which annihilates two pump photons and creates a correlated photon pair of signal and idler photons. Inside the cavity, the signal and idler mode are shifted in frequency by integer multiples of the free spectral range up- and downwards with respect to the pump frequency. Besides from the perspective of spontaneous four-wave mixing, the process can be interpreted as a sinusoidal oscillation of the fundamental resonator frequency mode, due to the modulation of the refractive index via the Kerr effect. The standing wave intensity pattern inside the dielectric mirror coating or the liquid oscillates at twice the pump frequency, resulting in a modulation of the refractive index and thus a variation of the free spectral range at the same frequency. A change in the free spectral range can be attributed to a change of the effective cavity length. In 1970 Gerald T. Moore showed that moving mirrors of a cavity excite photons out of the quantum vacuum, while the number of generated photons becomes significant under relativistic velocities and continuous mirror trajectories [21]. The creation of photons from the electromagnetic vacuum was later generalized by Fulling and Davies to a single mirror oscillating in space time [22].

In general, the phenomenon of generation of particles due to changes of the mode structure of a quantum field, by virtue of a boundary undergoing relativistic motion, or the change of material properties of the medium containing the field, is called dynamical Casimir effect [31]. Hereby, the system parameter needs to be modulated nonuniformly [29] and photons are emitted pairwise. Hence, spontaneous four-wave mixing experiments can be interpreted as such, since the oscillation of the intensity—and thus the refractive index—at twice the pump frequency gives rise to emission of photons on the signal and idler modes. Both, modulation of the effective or optical cavity length, and oscillation of the physical cavity length are formally equivalent [29]. The spontaneous four-wave mixing process can be seen as the scattering of two pump photons into the signal and idler mode mediated by the third-order nonlinearity [66]. In the dynamical Casimir effect in cavities, the modulation of the fundamental frequency leads to the emission of photon pairs. In the experiments conducted so far, both interpretations apply, since either two pump photons are converted into a pair of signal and idler photons, or the refractive index is modulated and, consequently, the fundamental frequency.

Mechanical oscillation frequencies reported in optomechanical experiments are at most 100 MHz [25], yielding observation of the dynamical Casimir effect infeasible. Therefore experiments focus on the modulation of system parameters like the optical path length. For a microwave transmission line terminated by a superconducting quantum interference device (SQUID), the dynamical Casimir effect

has been observed by modulating the inductance of the SQUID at GHz frequencies [23]. This leads to an effective oscillation of the length of the transmission line at a few percent of the speed of light. However, the effect has not been observed on a single photon level. With a Josephson metamaterial embedded into a low Q-factor microwave resonator, the dynamical Casimir effect has been detected for cavities as well [26]. Similar experiments have been proposed which employ a modulation of the material polarization at optical frequencies in cavities [27, 28], or modulation of the skin-depth of a semiconductor [30, 113]. Photon pairs have been generated in a dispersion oscillating fiber by the spatial and temporal modulation of the refractive index with high-intensity laser pulses mediated by the $\chi^{(3)}$ nonlinearity of the fiber [114]. However, the generation of photon pairs in tapered waveguides is also interpreted in terms of spontaneous four-wave mixing [115].

In this chapter an experiment is presented where the refractive index of the dielectric mirror coating of an empty cavity is modulated by a travelling intensity pattern, formed by the superposition of two dissimilar pump beams. The lasers are incident under a finite angle with respect to the cavity axis, in order to exclude the scattering of two pump photons into the unoccupied cavity mode as a mechanism for the creation of photon pairs. In section 5.1, the dynamical Casimir effect is further investigated and its formal equivalence to spontaneous four-wave mixing is pointed out. In addition, experimental considerations regarding the outline of the experiment with an estimation of the photon-pair generation rate are discussed. In section 5.2, the construction of the cavity, the setup of the laser pumping system and efforts to an automated measurement are described, which is necessary due to long measurement times. Finally, correlation measurements are shown in section 5.3 with an analysis of the thermal background and an estimation of the likelihood for a random occurrence of the observed signal.

5.1 Introduction to the Dynamical Casimir Effect and experimental considerations

In this chapter, I first discuss the dynamical Casimir effect in more detail and observe the formal equivalence to spontaneous four-wave mixing, and the parametric excitation of vacuum modes in subsection 5.1.1. Furthermore, I introduce an experiment where the optical path length of a cavity is modulated not by the pump light inside the resonator, but by two superimposed high-intensity continuous-wave lasers that form a travelling intensity pattern. The geometry of the arrangement excludes the annihilation of two pump photons and creation of a photon pair on the unoccupied cavity mode, such that the process is distinctive from the spontaneous four-wave mixing mechanism utilized in the former experiments. For this experiment, a dielectric coating is optimized which is highly transmissive at the pump frequencies, but highly reflective for the expected signal frequency of the photon pair (see subsection 5.1.2). Moreover, I calculate the photon-pair generation rate analytically and numerically in subsection 5.1.3, in order to have a reference on the necessary pump power levels and accuracies in the experimental outline.

5.1.1 The Dynamical Casimir Effect and experiment proposal

In second quantization of the electromagnetic field, every field mode ω is described by a quantum harmonic oscillator, which has a finite energy of $\hbar\omega/2$ in the ground state. Consequently, the ground state energy of the free electromagnetic field is infinite, which is not a problem, since measurements, after all, are measurements of the energy difference between an excited state and the ground state

of the system. The zero-point energy leads to quantum fluctuations; the expectation values of the electric and magnetic field components vanish for the electromagnetic field in the ground, i.e. vacuum state and all other stationary states ($\langle \mathbf{E}(\mathbf{r},t)\rangle = \langle \mathbf{B}(\mathbf{r},t)\rangle = 0$), while the expectation values of the squared quantities are finite ($\langle \mathbf{E}^2(\mathbf{r},t)\rangle = \langle \mathbf{B}^2(\mathbf{r},t)\rangle \neq 0$) [3]. This indicates that the electric and magnetic fields in the vacuum state are statistically fluctuating around their expectation value of zero. Furthermore, the square of the electric field is proportional to the intensity, which itself is a measure for the number of photons in the field mode. Consequently, the non-vanishing expectation value for the squared electric field yields the interpretation of fluctuating particle numbers, i.e. the occupation of the vacuum state by virtual photons.

Even though the vacuum energy can be eliminated by rescaling the system Hamiltonian with the zero-point energy, it has measurable effects, such as the Lamb shift, van der Waals forces between non-polar molecules or atoms, and the Casimir effect. The latter is the attractive force between two opposing dielectric or conducting metal plates, as both impose boundary conditions onto the electromagnetic vacuum, altering the density of modes in the cavity. Due to a mismatch of allowed modes inside and outside the cavity, the radiation pressure stemming from vacuum fluctuations is larger in the outer region, causing an effective inwards directed force onto the mirrors. This effect has been observed by Lamoreaux in 1997 [20]. An even more direct consequence of vacuum fluctuations is the dynamical Casimir effect, proposed by Moore [21] for a resonator with oscillating length. Fulling and Davies generalized this effect to a single mirror moving through space-time [22]. Both predict the dissipation of photon pairs due to a damping of the oscillation by radiation pressure from vacuum fluctuations opposing the mirror movement. The dissipative force is anti-proportional to the squared speed of light c, and scales with the third-order derivative of the mirror position, indicating a significant effect at only relativistic velocities and for nonuniform accelerations [116]. The mechanical energy is herein converted into a pair of real photons due to presence of virtual photons. The oscillating mirror changes the boundary conditions for the electromagnetic field and in the case of the cavity the free spectral range of the resonator. For velocities much smaller than the speed of light, the field modes can adapt adiabatically to the changing boundary. However, for modulations on relativistic time scales, the field is excited nonadiabatically out of the vacuum [23], due to a temporal mismatch of virtual modes in the cavity [24]. The generated photon-pair flux is proportional to the squared ratio of the peak velocity and the speed of light [23, 116], demonstrating the relativistic nature of the effect.

Modulating the mirror position alters the mode structure inside the cavity and, consequently, the free spectral range and the resonance frequencies become time-dependent. The corresponding effective Hamiltonian in terms of annihilation and creation operators for a single cavity mode with time-dependent resonance frequency ω reads [74]

$$\hat{H} = \hbar\omega(t)\hat{a}^\dagger\hat{a} - i\hbar\frac{1}{4\omega(t)}\frac{\mathrm{d}\omega}{\mathrm{d}t}(\hat{a}-\hat{a}^\dagger)^2\,. \tag{5.1}$$

For small amplitudes Δl and a sinusoidal acceleration of the cavity length $l(t) = l_0 + \Delta l\sin(\Omega t)$ at frequency Ω, the free spectral range is approximately

$$\omega_{\mathrm{fsr}} \approx \frac{c}{2l_0}\left(1 - \frac{\Delta l}{l_0}\sin(\Omega t)\right)\,. \tag{5.2}$$

Inserting this expression into above Hamiltonian, yields the nonlinear term

$$\hat{H}_{\mathrm{nl}} = i\hbar\Omega\frac{\Delta l}{4l_0}\cos(\Omega t)(\hat{a} - \hat{a}^{\dagger})^2\,, \tag{5.3}$$

which demonstrates the coupling from the mechanical oscillation of the resonator length to a single cavity mode $\hat{a}$. This Hamiltonian is quadratic in the order of creation and annihilation operators, leading to pairwise creation of photons on a single cavity mode with $\Omega = 2\omega$ on resonance. This demonstrates the underlying parametric excitation of the vacuum mode due to the mechanical modulation, rather than the driven material polarization we discussed in subsection 2.2.3 and studied in the last two chapters experimentally. Furthermore, a comparison of the nonlinear Hamiltonian for the mechanical modulation of the cavity length with the nonlinear Hamiltonian for the spontaneous four-wave mixing process shows the same formalism (see Equation 2.36). We can see the similarity, if we write the free spectral range in terms of the optical path length $l_{\mathrm{opt}} = nl_0$, where n is the refractive index of the medium the cavity mode is contained in. Assuming a similar modulation of the refractive index as for the mechanical cavity length $n(t) = n_0 + n_2 I\sin(\Omega t)$, where I is the amplitude of the intensity modulation and n_2 is the nonlinear refractive index, yields the nonlinear Hamiltonian

$$\hat{H}_{\mathrm{nl}} = i\hbar\Omega\frac{n_2}{4n_0}I\cos(\Omega t)(\hat{a} - \hat{a}^{\dagger})^2\,. \tag{5.4}$$

Both nonlinear terms for the oscillation of the mechanical and the optical length have a similar form, resulting from the temporal dependence of the resonance frequency, which leads to creation of photon pairs. Moreover, if we compare Equation 5.4 and the nonlinear Hamiltonian in Equation 2.36, calculated from the parametrically driven polarization, we observe a similar time dependence and coupling constant.

In the previous experiments, the modulation of the refractive index stems from the standing wave oscillating at twice the pump frequency either in the dielectric mirror coating or the liquid. The nonlinearity driven by the cavity pump modes couples to neighboring unoccupied cavity modes, if energy and momentum conservation for the process are fulfilled. We want to change the pumping scheme, such that the effective cavity length is not modulated by light in the cavity but from the outside. Furthermore, we want to exclude the scattering of two pump photons into the unoccupied cavity mode as the underlying process. A standing wave serves as an infinite momentum reservoir [117], such that, in principle, photon pairs orthogonal to the cavity axis can be observed. A travelling wave, on the other hand, carries momentum which is depleted to the photon pair. If we overlap two distinct laser frequencies like a green (g) and an infrared (ir) laser, a time-dependent intensity pattern is formed with sum and difference frequency and wavevector components. The intensity pattern is given by the interference term of the corresponding electric fields

$$E_{\mathrm{g}}E_{\mathrm{ir}} = \frac{1}{4}E_{0,\mathrm{g}}E_{0,\mathrm{ir}}(e^{i((\mathbf{k}_{\mathrm{g}}+\mathbf{k}_{\mathrm{ir}})\mathbf{r}-(\omega_{\mathrm{g}}+\omega_{\mathrm{ir}})t)} + e^{i((\mathbf{k}_{\mathrm{g}}-\mathbf{k}_{\mathrm{ir}})\mathbf{r}-(\omega_{\mathrm{g}}-\omega_{\mathrm{ir}})t)} + \mathrm{c.c.})\,, \tag{5.5}$$

where the choice of angles of incidence of the two pump lasers determines the geometry of the intensity wave[1]. In comparison to a standing wave, the spatial and temporal dependences do not separate into

[1] The complete pattern also contains time-independent terms and frequency components of two times the respective pump frequency, which are neglected here, but relevant when we numerically estimate the modulation of the refractive index in a thin dielectric slab (see subsection 5.1.2).

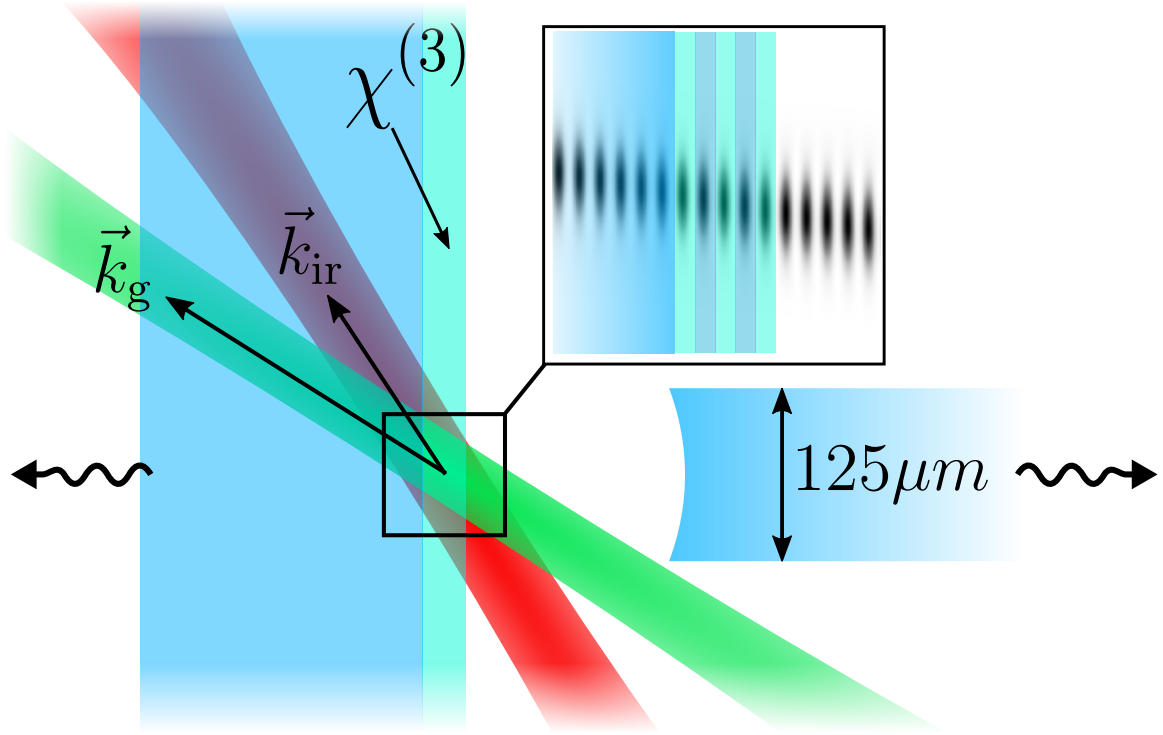

Figure 5.1: *Experiment scheme for modulating the optical path length of a high-finesse cavity by superimposing two distinct high-power continuous-wave laser beams. A cavity composed of a macroscopic mirror and a high-reflective coated fiber end facet is beneficial for short a cavity length and a small mode volume. The laser frequencies are chosen to have a difference frequency of twice the cavity resonance. Consequently, the unoccupied cavity mode is parametrically excited, due to the intensity pattern moving through the dielectric mirror coating, leading to the creation of photon pairs.*

the arguments of two trigonometric functions. Consequently, the intensity pattern moves along the direction determined by the sum and difference wavevector terms and, hence, carries momentum. If the laser beams are arranged such that the intensity pattern is parallel to the macroscopic mirror in a plano-concave cavity, the refractive index in the mirror coating[2] is modulated and, thus, the effective cavity length (see Figure 5.1). In this configuration, the difference frequency determines the temporal modulation and the difference wavevector affects the geometry of the intensity pattern, e.g. the spacing between intensity maxima. Since the pump beams are not collinear with the cavity axis, the generated photon pair cannot stem from the annihilation of two of the pump photons—the scattering of two pump photons into the unoccupied signal and idler modes is impossible due to momentum conservation. Moreover, with this pumping scheme the cavity is not necessary for the generation of photon pairs, but enhances the process for resonant frequencies and, consequently, increases the photon-pair generation rate.

In the oscillation of the mechanical length, the photon pair is generated via annihilation of a phonon and simultaneous creation of the photon pair, where the sum of the photon frequencies equals the

[2] The refractive index of any medium in the overlapping region is modulated, including the air in front of the mirror. Due to its low third-order susceptibility, however, the contribution to the modulation is negligible.

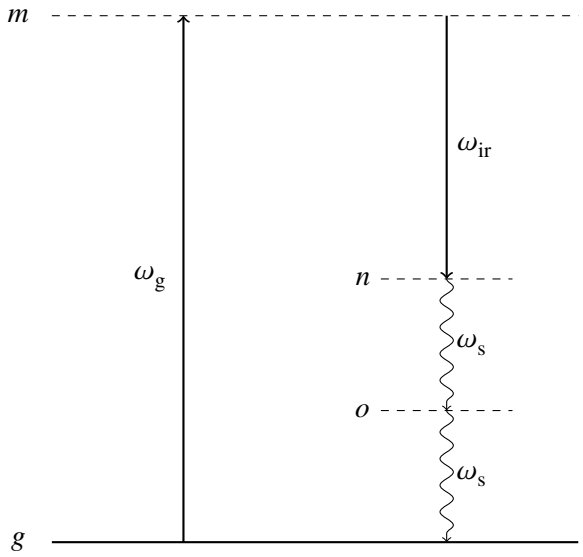

Figure 5.2: *Energy level scheme for the creation of a photon pair due to the modulation of the refractive index with the difference frequency of the superimposed green and infrared pump lasers. After the excitation to a virtual level via the annihilation of a green pump photon, an infrared pump photon does stimulated emission on the virtual level and a photon pair is generated at the signal frequency.*

frequency of the phonon [116]. How does the proposed process of the modulation of the refractive index by the superimposed pump laser beams conserve energy? The situation becomes clear if we look at the corresponding nonlinear Hamiltonian and the nature of the underlying process modulating the optical cavity length. The oscillation of the intensity at the difference frequency of the two pump lasers is obtained by mixing of the positive frequency component of one laser and the negative frequency component of the other. The coupling to the unoccupied cavity mode $\hat{a}_c$ via the third-order nonlinear polarization is then given by

$$\hat{H}_{nl} \propto \chi^{(3)}(E_g^{(-)}E_{ir}^{(+)} + E_g^{(+)}E_{ir}^{(-)})(\hat{a}_c^\dagger - \hat{a}_c)^2 \,. \tag{5.6}$$

From the derivation of the nonlinear Hamiltonian for the coupling of the pump mode to the signal and idler modes in subsection 2.2.3, we know that the creation and annihilation operators in the interaction picture evolve according to the positive and negative frequency ω_c and, consequently, the squared operators evolve with twice the frequency. The time dependence of the pump field is given by the difference frequency, which we choose to be equal to twice the cavity resonance. Hence, after performing the rotating wave approximation, only terms like $E_g^{(-)}E_{ir}^{(+)}(\hat{a}_c^\dagger)^2$ and the Hermitian conjugate contribute to the nonlinear Hamiltonian. We can associate the negative frequency components $E_g^{(-)}$ with the destruction of a green pump photon and the positive frequency components $E_{ir}^{(+)}$ with the creation of an infrared photon. The underlying process in the single photon picture is therefore the transition to a virtual level, by virtue of annihilation of a green photon, followed by the creation of an infrared pump photon and the photon pair on the cavity mode (see Figure 5.2). The presence of the intense infrared pump laser stimulates the creation of an infrared photon, which is similar to difference frequency mixing in a second-order nonlinear medium, where two pump lasers

with a higher and a lower frequency give rise to the generation of a third wave. In this process the smaller pump frequency is amplified due to stimulated emission on the virtual level [47], which is comparable to the third-order process studied here.

From the energy level diagram and the corresponding nonlinear Hamiltonian, we clearly see the difference to the spontaneous four-wave mixing process in the previous experiments[3]. Anyways, the process at hand can be referred to the class of spontaneous four-wave mixing experiments as well, even though these are commonly reported as the elastic scattering of two pump photons into the signal and idler modes [7, 66]. Here, three photons are created out of one incident pump photon, which rather refers to an inelastic scattering. However, the interpretation in the context of scattering may be due to historic reasons. Four-wave mixing in general is a classical effect and can be explained by the coupling of three input waves to a time-dependent material polarization acting as a source for a fourth field. In the spontaneous case, where two photons are generated, only two input fields are given and the unoccupied vacuum modes trigger the interaction by acting as a seed for the third input field. However, it is a pure quantum effect and not explainable in the context of classical four-wave mixing. Therefore, by considering the nonlinear Hamiltonian, the interpretation as a parametric excitation of vacuum modes may be more precise.

In order to conclude the discussion of the dynamical Casimir effect and the introduction to the analogue experiment, I want to briefly summarize above considerations. The dynamical Casimir effect is the creation of photon pairs due to a modulation of a system parameter changing the boundary conditions imposed onto the electromagnetic field. If the change is fast enough, the vacuum field cannot adapt adiabatically to the variation and, consequently, energy is dissipated via the creation of a pair of photons. The effect was historically approached from the mechanical change of a cavity length and later generalized to the change of the optical length, due to the similarity of the formal description. We can therefore interpret the effect of spontaneous four-wave mixing on the macroscopic level as the modulation of the refractive index of the nonlinear medium and, hence, as a change of the boundary conditions. On a microscopic level, however, the effect can be interpreted as the annihilation of two pump photons and the simultaneous creation of a pair of signal and idler photons, triggered by vacuum fluctuations and mediated by the third-order nonlinearity. The mechanical oscillation of the mirror in the macroscopic picture is the modulation of the boundary condition likewise the interpretation of the spontaneous four-wave mixing on a macroscopic level. But what happens on the microscopic level? A single oscillating atom as the microscopic model for the (mechanical) dynamical Casimir effect is expected to parametrically excite photon pairs if it is driven below its transition frequency [118]. It is caused by the interplay between unoccupied vacuum modes and the atomic polarizability [119]. Extending the single atom approach to a collection of atoms oscillating in phase, the microscopic description hints towards photon-pair emission due to the time-dependent material polarization on a macroscopic level. Therefore, since both effects have the same formal description, similar microscopic and macroscopic interpretations in terms of the parametric excitation of vacuum modes, they may have the same origin and may be two sides of one medal. A differentiation may be only due to distinctive historic approaches, however, a more detailed analysis is beyond the scope of this thesis.

In the experiment introduced in this section, an unoccupied mode of an optical cavity is driven by a time-dependent intensity pattern generated by superposition of two distinct continuous-wave

[3] Furthermore, the term-scheme reminds of a Raman process, where a molecule is excited to rotational or vibrational levels by absorption of a higher frequency photon and stimulated emission on the excited level by a lower frequency photon. However, the process at hand is coherent and therefore no virtual level is populated, but the annihilation and creation of the photons happens simultaneously.

high-intensity lasers. The cavity enhances the mode density at certain resonance frequencies and therefore amplifies the generation of photon pairs, while on a macroscopic level, the optical cavity length is modulated by a time-dependent refractive index in the dielectric mirror coating. On a microscopic level, however, the process can be understood in terms of spontaneous four-wave mixing. Here, the creation of the photon pair is triggered by stimulated emission of the lower frequency pump photon on a virtual level after a higher energy pump photon is annihilated. Therefore, the interpretation of elastic scattering of two pump photons into a pair of signal and idler modes is not applicable, but the process can be interpreted in terms of inelastic scattering.

In the experiment, we will use pump laser frequencies of $\nu_g = 581.85\,\mathrm{THz}$ (ALS fiber laser, 10 W, 515 nm) and $\nu_{ir} = 281.65\,\mathrm{THz}$ (Coherent Mephisto Mopa, CW-DPSS-Laser, 55 W, 1 064 nm) giving rise to a signal frequency of 150.1 THz, corresponding to a wavelength of about 2 µm. The signal frequency is thus in the short wave infrared regime, where the choice of pump frequencies is, more or less, arbitrary and determined by the lasers already available in the laboratory. However, the spectral distance between the two pump laser frequencies needs to be so large that the signal photons can still be detected and the lasers need to provide a high output power.

5.1.2 Intensity oscillation of superimposed laser beams

We want to estimate the modulation of the refractive index dependent on the angles of incidence of the two pump lasers. Intuitively, we can expect that the contrast, i.e. the amplitude of the oscillation to the intensity offset is highest, if the intensity pattern is parallel to the mirror surface. In order to achieve this, the angles of incidence need to be chosen such that the wavevector component orthogonal to the cavity axis vanishes. Calling the direction of the cavity axis x, and the orthogonal direction y, while neglecting the z axis due to rotational symmetry, $k_{\mathrm{g}}^{(y)} - k_{\mathrm{ir}}^{(y)} = 0$ is required. Measuring the angles of incidence with respect to the cavity axis, we find the relation for the inter-medium angles

$$\theta_{\mathrm{ir}} = \arcsin\left(\frac{\nu_{\mathrm{g}}}{\nu_{\mathrm{ir}}}\frac{n_{\mathrm{g}}}{n_{\mathrm{ir}}}\sin\theta_{\mathrm{g}}\right), \tag{5.7}$$

which can be transferred to the angles of incidence via Snell's law. The refractive indices appear due to the material dispersion. Taking the frequencies to be $\nu_{\mathrm{g}} = 581.85\,\mathrm{THz}$ and $\nu_{\mathrm{ir}} = 281.65\,\mathrm{THz}$ with refractive indices of $n_{\mathrm{g}} = 2.1529$ and $n_{\mathrm{ir}} = 2.0760$ for Ta_2O_5 [46], Figure 5.3 shows the relation between the pump laser angles.

Equation 5.7 gives the requirement for an intensity wave parallel to the mirror surface, however, the relationship does not take into account the potential reduction of modulation due to a decrease in the spatial period of the intensity pattern. With increasing angle of incidence, the x-component of the wavevectors decreases, where ultimately the difference wavevector increases, since the relationship between the angles is nonlinear and the IR laser needs to come in much steeper in order to have the same y-component as the green laser. As a result, the distance between the intensity maxima is reduced. Correspondingly, more spatial periods fit into a dielectric slab, decreasing the contrast of the intensity modulation amplitude to the offset. Therefore, we want to simulate the modulation of the refractive index in a slab of Ta_2O_5 with a width of about 500 nm. The width stems from the fact that the first layer of a dielectric coating usually has a thickness of half a wavelength in the respective material, while the coating is designed for the signal wavelength of approximately 2 µm. With the simulation, we do not only gain information about the modulation amplitude, but can estimate the

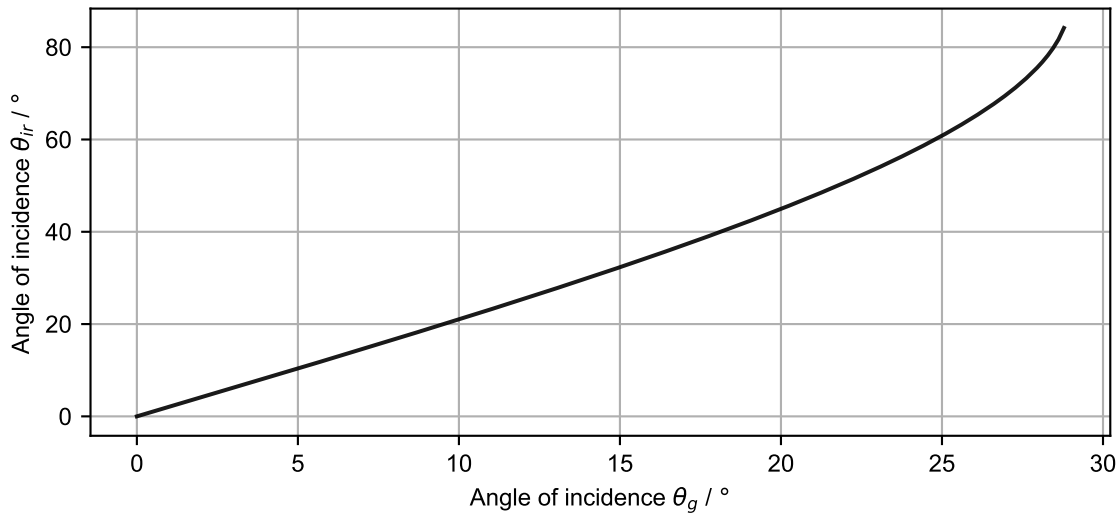

Figure 5.3: *Angle of incidence of the infrared laser depending on the angle of incidence for the green pump laser for an intensity pattern parallel to the cavity mirror surface, i.e. a vanishing y-component of the difference wavevector.*

necessary precision on the alignment of the pump lasers in the experiment.

In order to simulate the modulation, we assume the slab to be infinitely extended in the y-direction, and the pump lasers and cavity mode to be gaussian beams with waists of 10 µm (see Equation 2.9). In order to include the coupling to the cavity mode, the electric field of the cavity mode at normal incidence is once calculated and its absolute value squared is computed. For a pair of angles of incidence, the respective electric fields of the pump modes are calculated, superimposed, and the absolute value squared of the total pump field is computed as well. By multiplying both intensity patterns, the coupling to the cavity mode in the dielectric slab is accounted for. The product of both patterns is then integrated over the entire slab, in order to get a reference value for the total intensity inside the dielectric. This is repeated for one entire optical period of the difference frequency wave, such that we acquire the total intensity inside the slab dependent on time, while the cavity mode is taken to be static. The pattern has several different frequency contributions due to the possible mixtures of the electric fields, which are the sum and difference components of the two pump beams, and the self-mixing of the respective pump, resulting in a time-independent term and a term oscillating at twice the frequency. Fitting an offset and four sine functions with amplitude, frequency and phase as free parameters, we can verify the oscillation frequency and get the amplitude of the intensity oscillation, which is the measure for the modulation of the refractive index. Repeating the procedure for every pair of angles of incidence, we can estimate the modulation amplitude and determine the optimal angle pair.

The simulation shows the amplitude of the difference frequency component normalized to the intensity offset at normal incidence (see Figure 5.4). We can observe a strong dependence of the intensity modulation on the angles of incidence, where above intuitive calculated relation is recovered as the ideal choice of angles. However, we can observe the amplitude to rapidly decline for angles of incidence larger than approximately 18° for the green laser beam and 40° for the infrared laser. As

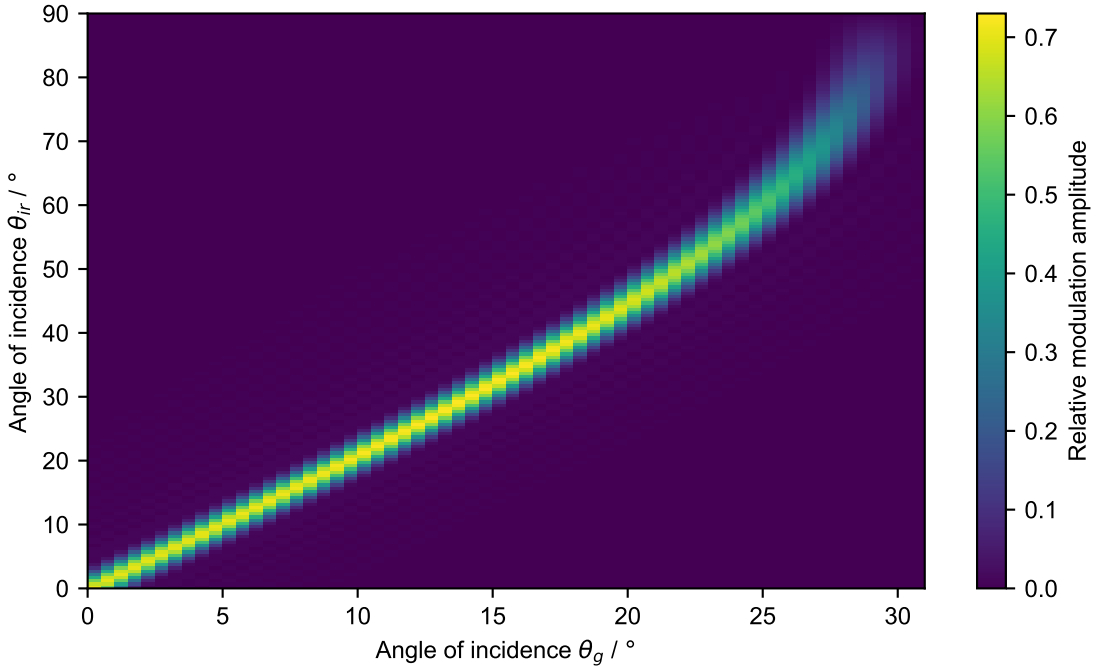

Figure 5.4: *Simulation of the modulation of the refractive index in an approximately 500 nm thick slab of Ta_2O_5 due to interference of two pump lasers in dependence of their angle of incidence. The modulation is normalized to the intensity offset at normal incidence of both pump lasers and takes the coupling to the cavity mode into account.*

expected, this is due to the reduced spacing between intensity antinodes. Furthermore, the requirements on precision in the alignment of the pump lasers regarding the ideal angle relation can be extracted from the simulation. Keeping the angle of incidence for the green laser fixed, the modulation decreases about 50 % for the infrared laser deviating by about 3° from the optimal angle. Vice versa, a deviation of 1.5° for the green laser from the optimal angle, while keeping the angle of incidence for the infrared laser fixed, leads to a decline of about 50 % in the oscillation of the refractive index. Hence, the angles need to be adjusted on a level to one degree. The amplitude is normalized to the offset and, thus, for the ideal choice of angles more than 70 % of the incident intensity contribute to the modulation. This is obviously less than for the modulation with the standing wave, where the intensity, in fact, oscillates between zero and four times the single wave intensity, yielding the full contrast of the amplitude with respect to the offset. But, anyways, we notice that at the right combination of angles, a high modulation of the refractive index can be achieved.

An interesting connection can be drawn between the amplitude of the refractive index modulation for the ideal combination of pump laser angles and the phase matching in the system. We observe the highest intensity modulation inside the dielectric slab for a normal incidence of the two pump lasers, which decreases for steeper incidence of the pump beams. For small angles, the wavelength of the intensity pattern is largest and, hence, one antinode fits into the slab. Therefore, the contrast of the intensity inside the slab is highest when the maximum or the minimum is in its center, since the cavity mode has nodes at the boundaries imposed by the slab. With increasing angles of incidence,

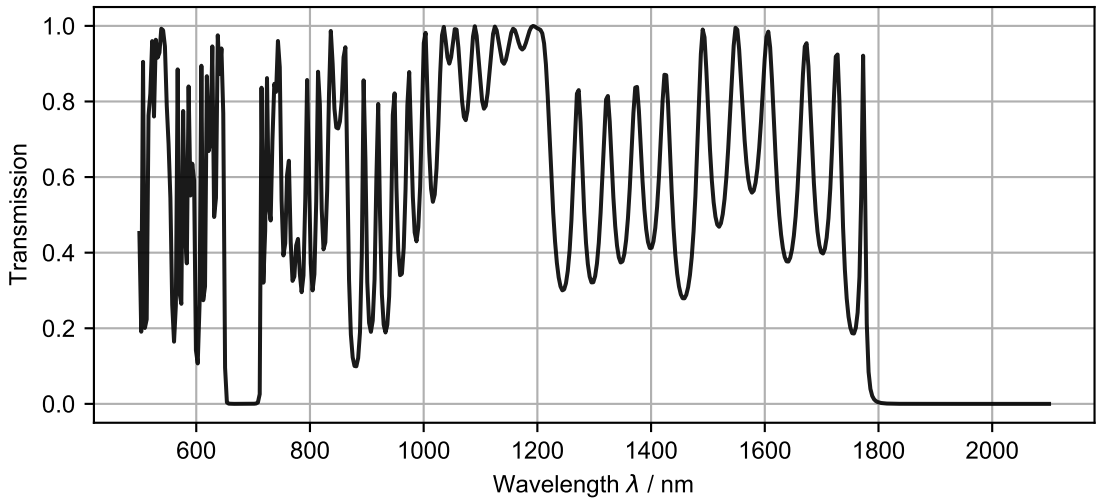

Figure 5.5: *Simulation of the transmission spectrum of the dielectric coating at normal angle of incidence. The coating is designed for high reflection at a wavelength of about 2 µm, wherefore it is also highly reflective at wavelengths around 670 nm. This resonance is used for length stabilization of the cavity in the experiment.*

the spacing between the intensity maxima becomes shorter and, consequently, more antinodes move through the slab, decreasing the intensity contrast along one temporal period. In the case of phase matching, the difference wavevector of the pump waves and the wavevectors of the photon pair, matches perfectly for normal incidence, when dispersion is neglected. The travelling wave thus provides the momentum necessary for the creation of the photon pair. With increasing angles of incidence, the difference wavevector gets actually larger than two times the signal wavevector and there is a momentum excess. Similar arguments hold for non-ideal angles of incidence, where phase matching cannot be ensured on the one hand, and the refractive index modulation, on the other hand, vanishes by virtue of the intensity pattern tilted with respect to the slab surface. Notice, that we are actually numerically computing the integral in Equation 2.36 for the present electric fields and, in principle, determine the coupling constant of the non-linear Hamiltonian.

Optimized dielectric coating From above computations, we choose the angles of incidence of the two pump lasers to be 18° for the green laser beam and 40° for the infrared laser, respectively. The coating is supposed to be highly reflective for the signal wavelength at 2 µm, but transmissive for the pump lasers. Otherwise, the refractive index will not only be modulated at the difference frequency of the pump lasers, but additionally at twice the respective pump frequency due to standing wave components. Furthermore, the incident waves interfere with the reflected waves yielding additional sum and difference frequency modulations that reduce the amplitude of the refractive index oscillation. The coating is designed by Laser Optik and a simulation of the transmission spectrum for normal incidence can be seen in Figure 5.5. It is highly reflective for wavelengths of about 2 µm, as well as for wavelengths around 670 nm, since the coating layers have thicknesses of approximately $3\lambda/4$ in this spectral regime, yielding similar phase shifts as for the design wavelength and consequently a high reflection (cf. subsection 2.1.3). Therefore, the cavity has two regimes where it can be operated and

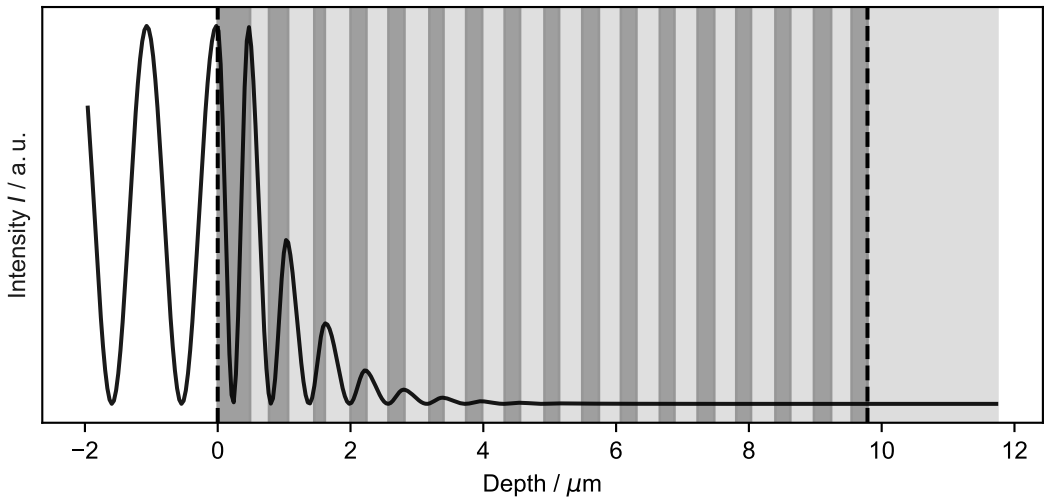

Figure 5.6: *Intensity distribution of the cavity mode in the dielectric coating at the signal wavelength of 2 µm. The light grey shaded layers refer to SiO_2, while the darker layers refer to Ta_2O_5. Notice that the first layer is the high index material and the stack is designed such that the coupling from the pump field to the cavity mode is increased compared to the coatings used in the previous experiments (see Figure 3.1).*

the resonance at the shorter wavelength is used for length stabilization of the resonator. The coating is highly transmissive for the infrared and green laser at angles of incidence of 40° and 18°, which are chosen[4] according to the simulation shown in Figure 5.4. Since the pump lasers need to pass the single-mode fiber of the cavity, the angles, especially for the green laser, need to be as large as possible, while maximizing the modulation of the refractive index. The transmission of the pump lasers at the corresponding angles are measured to be larger than 95 %, as stated by the manufacturer.

5.1.3 Estimation of the photon-pair generation rate

With the outline of the experiment parameters done, we want to estimate the expected photon-pair generation rate analytically and numerically. In the calculation of the modulation of the refractive index of the dielectric slab in the previous subsection, we only estimated the modulation inside the first layer of the dielectric mirror coating and have not taken the complete stack into account. In order to include this, the intensity distribution of the cavity mode and the pump lasers inside the dielectric coating need to be computed, which is done via the transfer-matrix method (see subsection 2.1.3). The intensity distribution of the cavity mode is shown in Figure 5.6. The grey shaded areas refer to the high and low refractive index materials, Ta_2O_5 and SiO_2, respectively. For this coating, the first layer is a $\lambda/2$ thick slab of the high index material, since it has the larger nonlinear refractive

[4] In principle, a choice of larger angles of incidence would have been possible as well, since the decrease in modulation from changing the green laser angle from 18° to e.g. 25° is not very large. However, initial computations have been done with a dielectric slab out of silicon dioxide which is commonly used as the first layer in a dielectric coating (see subsection 2.1.3). Due to the larger refractive index of Ta_2O_5, the angles of incidence inside the coating are smaller as compared to SiO_2 and, hence, the spacing and, consequently, the modulation amplitude do not decline as fast for larger angles of incidence.

index, wherefore the nonlinearity is increased compared to the previous experiments. Furthermore, the coating is designed such that the typical exponential decay of the intensity begins with the second layer, in order to increase the coupling of the cavity mode to the nonlinearity.

An analytical expression for the photon-pair rate can be found in a similar way as in subsection 2.2.3 and we want to briefly observe the differences. A more detailed derivation is shown in Appendix A. The nonlinear driving is done via the modulation of the third-order polarization of the medium by the two superimposed pump beams, which couple to a single cavity mode. From the experimental considerations in subsection 5.1.1, we already know the dominant mechanism, which is the mixing of the positive and negative frequency components of the pump lasers, interacting with the unoccupied cavity mode. Therefore, we neglect every other mixing term of the applied fields (cf. Equation 2.35) and only consider the corresponding Hamiltonian

$$H_{\mathrm{nl}} = 6 \int_V \mathrm{d}^3 r \, \epsilon_0 \chi^{(3)} (E_{\mathrm{g}}^{(-)} E_{\mathrm{ir}}^{(+)} + E_{\mathrm{g}}^{(-)} E_{\mathrm{ir}}^{(+)}) E_{\mathrm{c}}^2 \tag{5.8}$$

$$= 6\chi^{(3)} E_{0,\mathrm{g}} E_{0,\mathrm{ir}} \frac{2\hbar\omega_{\mathrm{c}}}{\pi\sigma_{\mathrm{c}}^2 l} \eta_\perp \int_0^\infty \mathrm{d}z \, \cos(\Delta k z - \Delta\omega t) \sin^2(k_{\mathrm{c}} z) e^{-\frac{2z}{z_{\mathrm{l}}}} (\hat{a}_{\mathrm{c}} - \hat{a}_{\mathrm{c}}^\dagger)^2 \,, \tag{5.9}$$

where we included the exponential decay of the cavity mode $\hat{a}_{\mathrm{c}}$ inside the coating with decay constant z_{l}. $\eta_\perp$ is the coupling due to the gaussian envelopes of the pump beams to the cavity mode (see Equation 2.37), σ_{c} is the cavity mode waist and l is the cavity length.

The Hamiltonian can be transformed into the interaction picture and after applying the rotating wave approximation, we find the Hamiltonian determining the system dynamics

$$H_{\mathrm{int}}(t) = \hbar\eta(\beta(\hat{a}^\dagger)^2 e^{-i\Delta t} + \beta^* \hat{a}^2 e^{i\Delta t}) \,, \tag{5.10}$$

where Δ is the detuning between driving field and cavity mode. η is a coupling constant given by

$$\eta = \frac{\omega_{\mathrm{c}}}{\pi\sigma_{\mathrm{c}}^2 l} z_{\mathrm{l}} \eta_\perp \frac{n_0^2 n_2}{\sqrt{n_{0,\mathrm{g}} n_{0,\mathrm{ir}}}} \sqrt{I_{\mathrm{g}} I_{\mathrm{ir}}} \,, \tag{5.11}$$

and β is a dimensionless factor

$$\beta = \frac{2i}{2i + z_{\mathrm{l}}\Delta k} + \frac{i}{2i + (\Delta k - 2k_{\mathrm{c}}) z_{\mathrm{l}}} + \frac{i}{2i + (\Delta k + 2k_{\mathrm{c}}) z_{\mathrm{l}}} \,, \tag{5.12}$$

describing the possible ways to mix the wavevectors. Since the momentum of the pump wave is finite, only the directions of the momenta of the photon pair change, in contrast to the coupling between cavity modes (cf. Equation 2.38), which are composed out of forward and backward travelling waves. Naturally, the sum of the momenta invokes the phase matching and maximizes the coupling if it vanishes. However, due to the small interaction length given by the exponential decay constant z_{l}, the requirements for the phase matching are weak (cf. Figure 2.9).

The Hamiltonian is very similar to the parametric amplifier in spontaneous parametric down-conversion [71], when the pump wave is described classically. Moreover, if we compare the coupling constant η and the time dependence in the nonlinear Hamiltonian from the modulated polarization with the Hamiltonian obtained from the time-dependent resonance frequency (cf. Equation 5.4), we find a similar scaling and time dependence. Following the procedure in subsection 2.2.3 by solving

the master equation in the steady state and calculating the expectation value of the photon number, we find the photon-pair generation rate

$$\Gamma = \kappa \langle \hat{a}^\dagger \hat{a} \rangle \approx 16 \frac{F \omega_{\mathrm{fsr}}}{\pi^2} \left(k_c z_1 n_0 n_2 \sqrt{I_g I_{ir}} |\beta| \frac{\eta_\perp}{\pi \sigma_c^2} \right)^2 . \tag{5.13}$$

We assume parameters identical to the experiment conditions, e.g. a finesse $F = 9000$, free spectral range $\omega_{\mathrm{fsr}} = 2\pi \times 0.79\,\mathrm{THz}$, i.e. a cavity length of $l = 190\,\mu\mathrm{m}$ and a cavity waist of $\sigma_c = 10\,\mu\mathrm{m}$. For the pump lasers we assume powers of $P_g = 3\,\mathrm{W}$ and $P_{ir} = 20\,\mathrm{W}$ with waists of $\sigma_g = 11\,\mu\mathrm{m}$ and $\sigma_{ir} = 24\,\mu\mathrm{m}$, respectively. For the nonlinear refractive index n_2 of Ta_2O_5 different values can be found in literature [48, 109, 120–122], where we take the mean value of approximately $\overline{n}_2 \approx 5 \times 10^{-19}\,\mathrm{m^2\,W^{-1}}$. For above parameters, the predicted photon-pair generation rate is computed to be $\Gamma_{\mathrm{theo,ana}} = 1.6\,\mathrm{s^{-1}}$.

In above analytic estimation of the generation rate, we did not take the intensity distribution of the pump lasers inside the dielectric coating into account, but assumed a cosine dependence due to the interference term of the squared absolute value of the total electric field. The cavity mode is described via a sine wave squared and an exponential decay inside the mirror coating. We can determine the rate numerically by simulating the electric field distribution of both pump lasers inside the coating. The coupling to the cavity mode is done via multiplying the total electric field with the intensity distribution of the cavity mode, similar to the estimation of the photon-pair rate in section 3.1. Consequently, we numerically solve the integral in Equation 5.8 and use Equation 5.13. We find a rate of $\Gamma_{\mathrm{theo,num}} = 0.9\,\mathrm{s^{-1}}$ for above parameters. The slight discrepancy certainly stems from the different spatial intensity profile of the pump beams inside the dielectric coating, i.e. the intensity pattern differs from the ideal cosine, due to the layer structure and interference with reflected partial waves.

Both estimations, however, imply a possibly measurable effect. We will see, that due to limited detection efficiencies, much lower in comparison to the former experiments performed in the visible regime, the realization of the experiment is much more complicated. A total detection efficiency on the order of 1×10^{-4}, leads to a expected experimental rate of about one photon pair per hour.

5.2 Experimental apparatus

In contrast to the previous experiments, where the third-order nonlinearity in the coating and the liquid, is driven by the light coupled into the cavity, the system at hand is not self-aligned regarding the overlap of pump lasers and cavity mode. Furthermore, in the former experiments, the cavity is stabilized to the pump laser, hence fluctuations in the pump frequency are compensated by a change in the resonator length, keeping the resonance condition for the photon-pair generation fulfilled, as long as the center frequency does not drift out of the dispersion compensation point by more than half the cavity linewidth (see Figure 2.10). The same condition is required for the frequency stabilization of the pump frequency, i.e. the difference frequency of both pump lasers with respect to the lock frequency to which the cavity is stabilized. In order to reach maximum modulation of the refractive index, the angles of incidence of the pump lasers need to be precisely adjusted to the calculated optimum values and, moreover, need to be accurately overlapped with the cavity mode.

The experimental setup is thus more complex than for the experiments previously shown, since, besides the cavity, locking and detection setup, it involves the two continuous-wave pump lasers

with the requirement of precise alignment and a stabilized frequency dependence. Due to the low photon-pair generation rate, the experiment requires a reliable operation for days to gain enough coincidence events, which refers to the length stabilization of the cavity, as well as the frequency stabilization of the pump and lock lasers, and the operation of the superconducting nanowire single photon counters necessary for the detection of the short-wave infrared (SWIR) signal photons. Due to the need for precise angle adjustment of the pump lasers, the alignment needs to be done carefully and accurately to fulfil the requirements estimated in the former section 5.1. The demand for an acute angle of incidence of one of the pump lasers requires grinding of the cavity fiber, in order to gain optical access.

The process of grinding of the cavity mirror fiber is presented in subsection 5.2.1, the design, construction and characterization, as well as the length stabilization of the cavity is described in subsection 5.2.2. The pumping laser setup, frequency stabilization, and the alignment procedure of the pump beams are shown in subsection 5.2.3. In subsection 5.2.4 the detection setup is described, where the superconducting nanowire detectors are characterized and efforts to an automated measurement are presented.

5.2.1 Grinding of cavity mirror fiber for gaining optical access

In section 5.1, we encountered the angular dependence of the intensity modulation due to the superimposed pump lasers and found the intensity amplitude drastically decreasing for angles of incidence of the green pump beam larger than 18° with respect to the cavity axis. The necessity of the acute angle leads to challenging experimental considerations. The expected rate of generated photon pairs for the case of the nonlinear dielectric coating scales proportionally to the free spectral range and, hence, inversely to the cavity length (see Equation 5.13). Thus, a short cavity is beneficial, however, by virtue of the acute angle of incidence for the green pump laser, a longer cavity is necessary, since otherwise the path to the location of the cavity mode on the macroscopic resonator mirror is blocked by the fiber. Partial blocking or clipping of the beam leads to less power at the location of the cavity mode, as well as to larger and distorted focus profiles reducing the pump intensity and, finally, heating of the cavity fiber with potential damage of the mirror coating. Therefore, a longer cavity length is demanded. A longer cavity on the other hand, reduces the coupling between fiber and cavity mode (see Figure 2.2) and requires larger mirror structures on the fiber end facet in order to prevent additional intra-cavity losses reducing the finesse (see Figure 2.5) and, consequently, the photon-pair rate. A short cavity length is therefore beneficial for several reasons, since it enhances the collection of photons due to the fiber, prevents reduction of the finesse, and increases the photon-pair rate.

A simple geometric calculation for a beam waist of 10 µm, angle of incidence of 18° and the standard single-mode fiber diameter of 125 µm yields a minimal cavity length of 225 µm, where the shortest distance between the pump beam axis and the fiber edge is the waist. In this arrangement, the fiber is subject to a high amount of laser radiation, that at least leads to an unstable operation or, worse, a damaged cavity. In order to combine a shorter cavity length by virtue of less light incident on the fiber tip, the edges of the fiber are ground on two opposite sides within the plane of the pump lasers. The edges are ground under an angle of 17° with respect to the cavity axis, accounting for the incoming green pump beam angle. Even though the coating is nominally transparent for the green pump, the macroscopic cavity mirror still reflects a non-negligible amount of light, wherefore both sides are polished. The grinding is done after the fibers have been coated, requiring a process protecting the mirror coating from scratches, the fragile fiber from breaking, and the complete removal

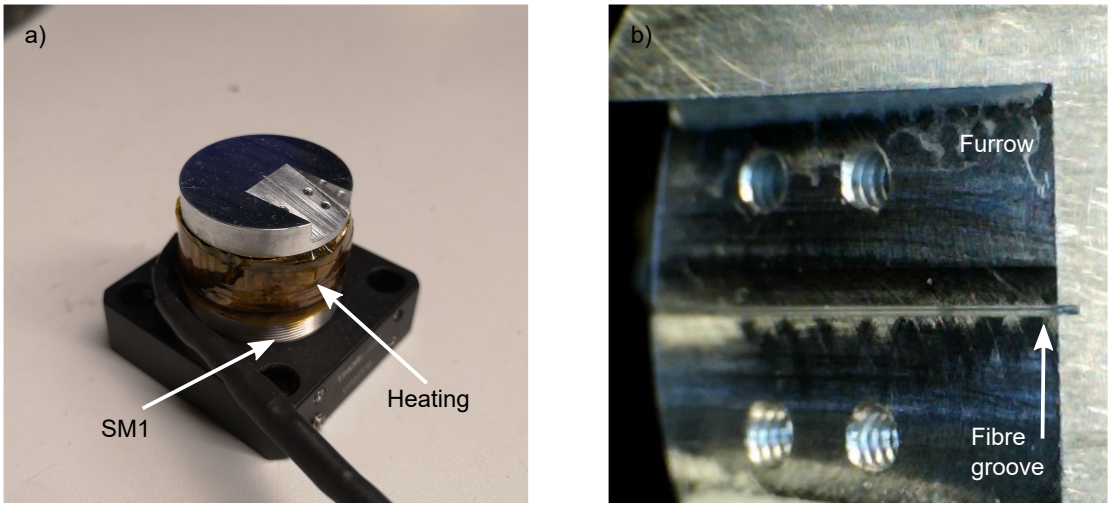

Figure 5.7: *Mount for grinding of the cavity fiber.*

of the substance which is used for fixing the fiber in the respective grinding mount. Solid waxes are commonly used in the process of polishing and grinding, in order to temporarily attach the workpiece to the respective mount during the machining. These waxes are soluble by solvents, alkali detergents or even hot water and can be removed entirely, which is mandatory to prevent absorption losses in the resonator from the grinding process. They melt at temperatures above 60° lubricating the sample and attaching it to the polishing mount after cooling to room temperature.

Figure 5.7 shows the mount designed for the grinding process. It is a cylindrical aluminum block with a SM1 thread on one side to connect it to a Thorlabs cage system for further mounting and handling purpose. On the top side, used for the polishing, a large furrow at the desired angle with respect to the top base is milled out from the lateral surface to the center of the top base. In the center of the furrow, a groove 300 µm wide and 200 µm deep is milled out by virtue of mounting the fiber in the grinding process. Furthermore, on the lateral surface from close above the bottom base to roughly two thirds to the top base, the diameter of the cylinder is reduced with a lathe by a few millimeters, with purpose of attaching a heating wire.

Before grinding, the fiber has to be positioned in the small groove of the polishing mount, which is done by observing the end of the groove towards the polishing surface with two microscope cameras from above and the side. The groove is mounted such that the furrow is parallel to the table surface and the fiber is precisely aligned with a five axis translation stage. With the camera viewing the alignment from the side, the distance of the fiber sticking out of the groove can be adjusted and, hence, the amount which is ground off. In principle, the material up to the cavity mirror can be removed. After alignment, the grinding mount is heated and small pieces of solid wax are put onto the fiber, enclosing the fiber inside the groove. In order to reduce pressure onto the fiber tip during grinding, wax is put on the polishing surface as well. The grinding is done on lapping sheets (Thorlabs LF3D), until the wax on the surface is completely removed. Afterwards, the wax is dissolved with isopropanol and the fiber is rotated by 180° to polish the opposite side as well by repeating above process.

With knowledge of the angles and amount of polished material, the power illuminating the fiber can

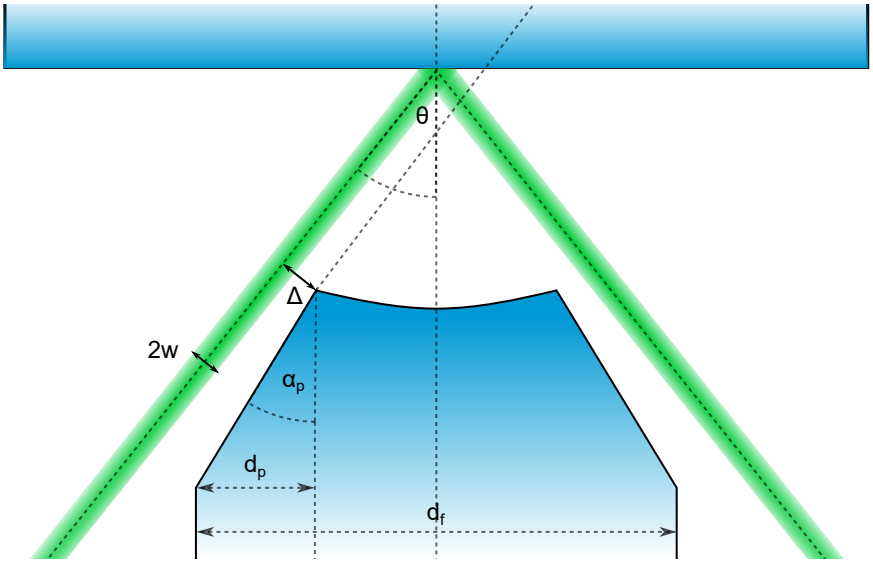

Figure 5.8: *Sketch of a ground fiber passed by a pump beam for determination of the shortest distance between fiber edge and pump center.*

be calculated from simple geometric considerations (see Figure 5.8). The closest distance from the pump laser axis to the edge of the polished cavity fiber is

$$\Delta = l \sin(\theta) - \left(\frac{d_\mathrm{f}}{2} - d_\mathrm{p}\right) \cos(\theta)\,, \tag{5.14}$$

where l is the cavity length, d_f is the fiber diameter, d_p is the distance from the former fiber edge to the new edge on the fiber tip. Here, the polishing angle α_p is required to be smaller or equal to the angle of incidence of the pump beam θ_g. If the polishing angle is larger than the angle of incidence, the distance is calculated via

$$\Delta = \left(l - \frac{d_\mathrm{f}}{2\tan(\gamma)}\right) \sin(\theta) - \frac{d_\mathrm{f}}{2} \cos(\theta) \quad \text{with} \quad \gamma = \arctan\left(\frac{2d_\mathrm{p}}{d_\mathrm{f} \tan(\alpha_\mathrm{p})}\right). \tag{5.15}$$

Assuming a gaussian beam profile centered at $(0, 0)$, the distance between fiber edge and the beam axis defines the position from where the beam is clipped, such that the power incident on the cavity fiber can be approximated by integrating the transversal beam profile from Δ to infinity.

The final ground fiber used for the high-finesse cavity can be seen in Figure 5.9. From the picture, the angle and depth of the grinding can be extracted to be 24° and 29 µm for the one side and 20° and 15 µm for the other side. The deviation of the grinding angles from the angle of 17° aimed for, stems from a misalignment of the fiber while the wax is cured. Using Equation 5.15, we can estimate the relative amount of light incident on the fiber with respect to the cavity length, in order to determine the ideal cavity length. Only the green pump beam is considered, due to its acute angle of incidence. Figure 5.10 shows the computed relative power incident on the fiber dependent on the cavity length for the incoming and reflected green pump beam. In the calculations, the reflection coefficient of the coating of about 5 % is accounted for, while the reduction of power due to the clipping of the

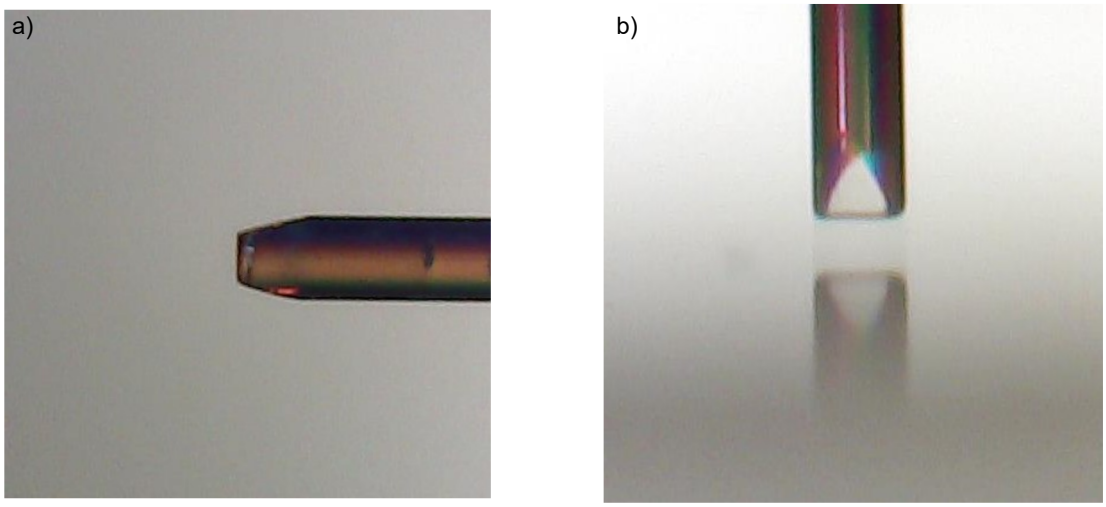

Figure 5.9: *Image of the final ground mirror fiber from the top a) and the side b). From the top view, the grinding angles and depths can be extracted to be 24° and 29 µm, and for the one side and 20° and 15 µm.*

incident beam is not considered. At short cavity lengths around 100 µm, the fiber completely blocks the incoming beam and even at 160 µm, 1 % of the incident light illuminates the fiber, which is a lot considering pump powers on the order of several watt. Therefore the cavity length is set to 190 µm, which is a compromise of low illumination and short cavity length. Comparing the curves for the incoming and reflected beam shows that the angle at which the fiber is ground influences the amount of light incident on the fiber much more than the grinding depth.

5.2.2 Cavity construction, characterization and locking scheme

The cavity is formed out of the dielectric coated end facet of the ground fiber reported in the previous subsection and a macroscopic mirror with the same coating. A picture of the final assembled resonator is shown in Figure 5.11. The mirror is mounted on a v-groove attached to a linear translation stage (Elliot Scientific Martock MDE261, vacuum compatible), which can move the mirror perpendicular to the cavity axis, in order to restore the resonator finesse, if the coating is damaged by the intense pump lasers (cf. subsection 3.2.1). The fiber is glued on a T-shaped aluminum block, which itself is attached to a linear translation stage (Elliot Scientific Martock MDE261, vacuum compatible), used for adjusting the cavity length. Both translation stages are screwed on a baseplate out of aluminum.

Before gluing, the fiber is aligned with a five axis translation stage, by maximizing the light coupled into the cavity, while keeping the fiber centered with respect to the macroscopic mirror. In the process, the mirror translation stage is in its center position. The alignment process is observed with two microscope cameras, whereas the fiber needs to be rotated such that the ground edges are in the horizontal plane. The fiber is glued (LOCTITE STYCAST 2850FT with LOCTITE CAT 9) onto a shear plate actuator (Noliac CSAP03) encapsulated by two alumina plates for electrical isolation, with purpose of precise adjustment of the cavity length. Further alumina plates are used in order to extend the aluminum mount, and by virtue of stress release, the fiber is glued behind the splice between the short mirror fiber and the single-mode fiber, for feed through and incoupling of the laser radiation.

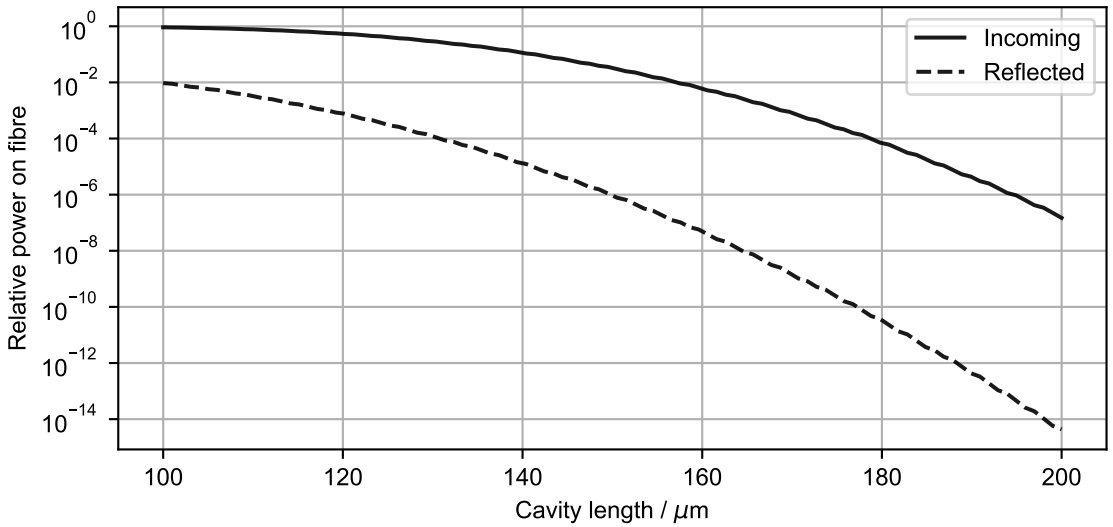

Figure 5.10: *Relative power incident on the ground cavity mirror fiber for the incoming and reflected green pump beam for the grinding angle and depth extracted from Figure 5.9. For the reflected side, the reflection coefficient of the mirror coating is taken into account, whereby the reduced power of the incident beam due to clipping by the fiber is not considered. At short cavity lengths, the fiber completely blocks the incoming beam, i.e. all power is incident on the fiber. From the calculation, the cavity length is set to 190 µm, since only 10 ppm of the incoming power are incident on the fiber at this length. The comparison between both curves shows that the polishing angle has a much larger impact on the amount of light clipped by the fiber than the depth of the grinding.*

The coating specifications shown in Figure 5.5 imply that the cavity can be operated at wavelengths larger than 1.9 µm and close to 670 nm. At the former the signal photons will be generated, while the latter is used for length stabilization of the cavity. Two lasers are coupled into the cavity simultaneously via a dispersive equilateral prism, which serves as a beam combiner and, additionally, for filtering the signal photons from the lock and pump laser light in the correlation measurements.

The resonator finesse is measured by determination of the free spectral range with a probe laser at around 670 nm, while scanning the cavity with the piezo actuator. The signal laser at a wavelength near 2 µm is kept constant in order to get a fixed reference for the cavity length. The probe laser frequency is then shifted, such that the next longitudinal mode can be overlapped with the signal laser resonance on an oscilloscope. From the frequency difference of the two probe laser resonances, the free spectral range is determined to be 0.79 THz, which corresponds to a cavity length of 190 µm. By locking the cavity to the probe laser resonance, the linewidth of the signal laser resonance is determined by scanning its frequency and measuring the light reflected (or transmitted) by the cavity. With fitting a Lorentzian lineshape function to the reflection signal, the linewidth is extracted to be (91 ± 8) MHz, resulting in a cavity finesse of 8600 ± 780 for laser frequencies of about 150.11 THz. The finesse is reduced from the nominal value of about 13000 by clipping losses on the fiber mirror due to the large cavity length. From the reflection signal, the incoupling is determined to be 40 %. At the probe frequency, the cavity finesse is 1500, measured by applying sidebands with an electro-optic modulator as frequency reference.

As in the previous experiments, the output of the PID-controller is combined with a constant

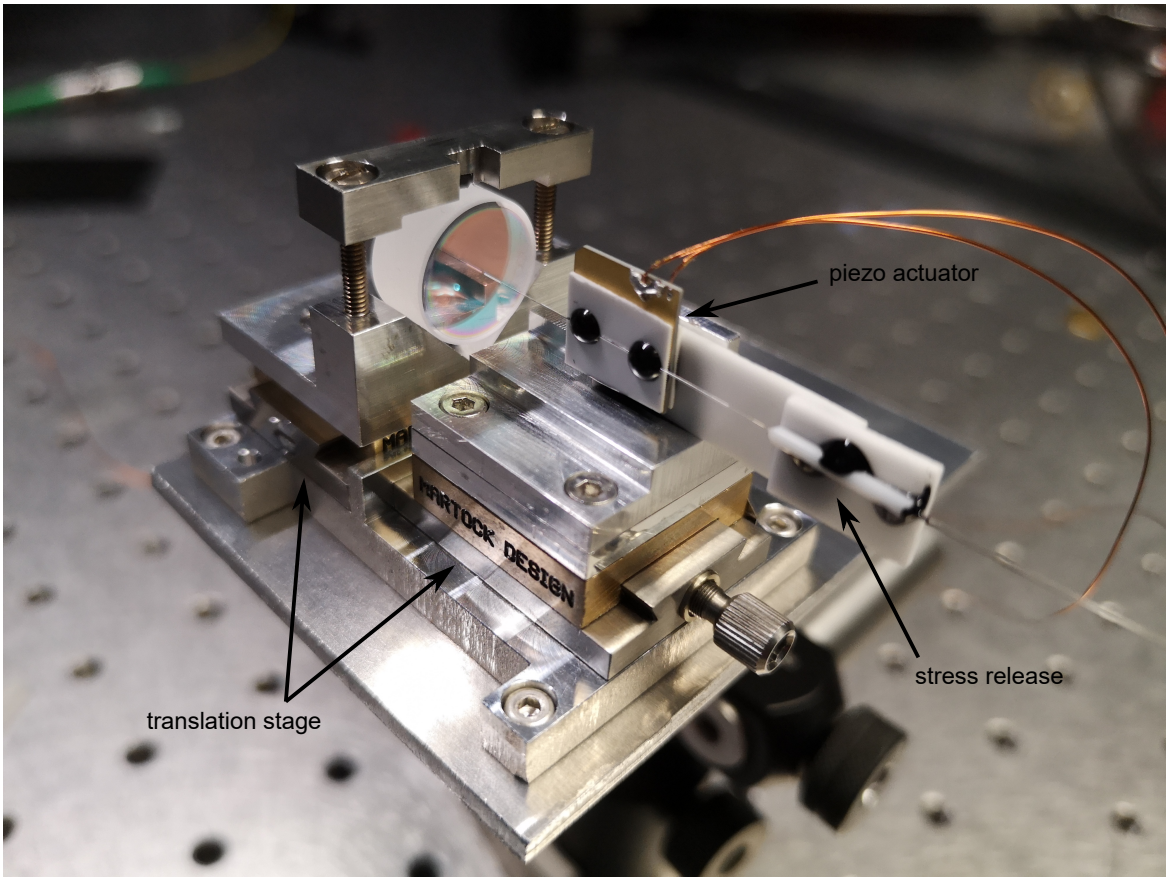

Figure 5.11: *Image of the final assembled cavity.*

voltage signal stemming from a low-noise battery box, expanding the tuning range accessible with the piezo actuator to about one micrometer. The constant voltage can be varied in steps of 18 V to a total range of ±216 V. While locking the cavity, the lock-point is drifting due to thermal effects in the resonator setup, which cannot be compensated by the PID-controller, due to its limited range of ±10.5 V. Therefore, the battery-box[5] is extended with digitally controllable relays, in order to switch to the next battery setting, whenever the output of the controller reaches a limit of 10 V or −10 V. A 1 µF capacitor guarantees a smooth transition to the new voltage setting, ensuring the stabilization can follow the changing offset voltage and the cavity stays in lock.

Fiber grinding induced birefringence The grinding of the cavity mirror fiber induces a birefringence of 330 MHz, much larger than the cavity linewidth. Both axes coincide with the laboratory polarizations s and p to within a few degree, due to the alignment of the ground edges in the horizontal plane. A common origin of birefringence in fiber cavities is an ellipticity of the mirror imprinted onto the fiber end facet. As discussed in subsection 2.1.1, the radius of curvature of the mirror determines the mode geometry and, consequently, the resonance frequency as well. The frequency splitting

[5] The battery-box was designed and built by Dr. Akos Hoffmann. We discussed the necessary extensions for the digitally controlled battery-box, which he realized.

between the two polarization modes for the radii of curvature R_i for the two respective axes and incident light with wavevector k is [123]

$$\Delta\nu_{\mathrm{HV}} = \frac{\nu_{\mathrm{fsr}}}{2\pi k}\frac{R_1 - R_2}{R_1 R_2}\,. \tag{5.16}$$

Due to the coating procedure, the coating films are under mechanical stress, typically on the order of several hundred MPa to GPa, which can deform the substrate the dielectric film is deposited on [124]. Assuming the grinding changes the mechanical stress in one direction such that the birefringence is induced due to a change of the radius of curvature in the direction the fiber is ground, we find for the altered radius of curvature $R_2 \approx 100\,\mu\mathrm{m}$. This is obviously not possible, since the cavity length is twice as large and the curvature must at least be equal to the cavity length due to the stability criterium for the plano-concave resonator (see subsection 2.1.1). Therefore, the birefringence cannot (solely) result from a change in the radius of curvature.

However, the refractive index of a material is changed by applying force, which changes the boundary conditions for the electric field inside the resonator in one axis. In the following, we want to estimate the shift in the refractive index causing the observed splitting, assuming the frequency shift is uniquely caused by the changed refractive index. A relation between the retardation Δs due to the changed optical path length along the distance d and the mechanical stress σ is given by [125]

$$\Delta s = K \cdot d \cdot \sigma\,, \tag{5.17}$$

where K is the stress-optical coefficient. Consequently, the refractive index change is related to the induced stress via $\Delta n = K \cdot \sigma$. The retardation varies the phase acquired along one round trip inside the resonator. From Equation 2.4, the phase is given by $\phi = \pi\nu/\nu_{\mathrm{fsr}}$, which results in a shift of the resonance frequency by

$$\Delta\nu = \nu\frac{\delta l}{l}\frac{\Delta n}{n}\,, \tag{5.18}$$

where l is the resonator length, $\delta l \approx 10\,\mu\mathrm{m}$ is the coating thickness and Δn is the change in refractive index. Inserting appropriate numbers yields a refractive index change of 1×10^{-4}. The mechanical stress changes by 40 MPa, assuming a typical value of the stress-optical coefficient of $K \approx 3 \times 10^{-6}\,\mathrm{MPa}^{-1}$ for glasses [125].

The change in the coating stress seems to be a reasonable number, however, the mode splitting can be a combination of a change in the radius of curvature and a variation of the refractive index and the computed stress gives an upper limit. The divergence of the boundary condition has a larger effect on the splitting than the variation in the radius of curvature and can be viewed as its main cause. After all, the calculations are estimations of the origin of the birefringence rather than a precise characterization.

5.2.3 Laser pumping scheme and frequency stabilization

Since the experiment was initially planned to be performed under vacuum, the setup is designed to fit into a 6 inch spherical octagon vacuum chamber (Kimball Physics), which leads to geometrical restrictions for the pump beams to be aligned with respect to the cavity mode, according to the requirements mentioned before (see section 5.1). Therefore, the setup is extended by an aluminum plate serving as a base for the cavity, a lens collecting the light outcoupled from the cavity (Thorlabs

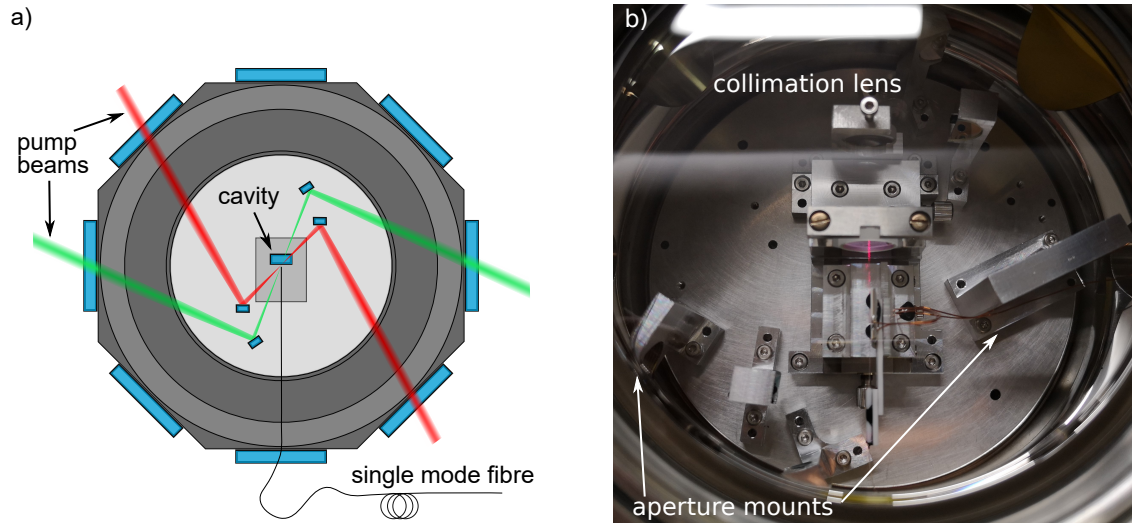

Figure 5.12: *Illustration of the interior of the vacuum chamber showing the paths of the pump beams a) and a picture of the final assembled setup b).*

AL2520) and fixed mirrors supposed to realign the incoming pump beams towards the cavity under the correct angle of incidence. An illustration, as well as a picture of the final assembled interior in the vacuum chamber, is shown in Figure 5.12. The base plate is sized to fit onto the CF 100 bottom flange of the vacuum chamber and it is standing on four Viton balls for mechanical isolation. The cavity and the other components are arranged on the base plate for the surface of the macroscopic mirror to be in the center of the chamber and the cavity fiber is supposed to be in the central horizontal plane. The mirror mounts are designed, placed, and rotated such that the respective pump beam entering the vacuum chamber through its specific port illuminates the cavity mirror under the correct angle. The chamber is closed with a CF 100 uncoated viewport (Vacom VPCF100B-L) on top, whereby the ports for the pump beams are sealed with appropriately coated CF 40 viewports (Thorlabs VC234A and VC234C). The cavity transmission exits the chamber through an uncoated fused silica window (Thorlabs VC234). The design of the interior setup already gives a pre-alignment of the pump beams, since the entering and exiting ports serve as apertures establishing a fixed path in combination with the mirrors (Thorlabs BBD05-E02 and BBD05-E03). In addition, mounts for holding iris diaphragms are attached to the bottom plate, specifying the respective laser paths.

A fraction of the light of both pump lasers is send to a wavelength meter via an optical fiber with the purpose of frequency stabilization. The amount of light send to the experiment is adjusted via a combination of half-wave plate (HWP) and polarizing beam splitter (PBS) for each pump laser. The PBS also cleans up the degree of polarization to over 99.9 %, which can then be adjusted via a further HWP. For a large modulation of the refractive index, the pump lasers need to be focused to spot sizes on the order of the cavity waist. Therefore, both lasers, respectively, are first enlarged and then focused by an achromat with a focal length of 200 mm (Thorlabs AC508-200-A and AC508-200-C) to waist radii of 11 µm for the green and 24 µm for the infrared laser. The spot sizes are limited by the viewport clear apertures, respectively. Similar achromats collect the light exiting the vacuum chamber, forming microscopes in combination with 500 mm achromats with a magnification of 2.5

for alignment purposes. The imaging is illustrated in Figure 5.14. Backside polished mirrors can be inserted to dump most of the power before reaching the respective cameras (Thorlabs DCC1545M) in the imaging planes. The spots can still be observed while increasing the pump power, even though the image is shifted and slightly defocused due to the tilted mirrors. Nevertheless, potential drifts in the pump beam positions can be observed.

Pump laser alignment The first step in aligning the pump lasers is making use of the pre-alignment given by the assembled interior components at low powers. The pump beams are shrunk by use of an iris diaphragm and the focusing lenses before the chamber are not inserted at first. The collimated beam illuminates the cavity such that the shadow of the fiber can be imaged. The microscopes are aligned to give a sharp image and the fiber position is marked, since knowledge of the exact position is crucial for further alignment. The correct angles in the horizontal plane are verified by placing a triangle ruler onto the top viewport and the beams are adjusted such that the height with respect to the base plate is constant between the two fixed internal mirrors. The weak reflection from the cavity mirror gives a reference for an orthogonal angle of incidence in the vertical plane.

The respective lens in front of the chamber is installed afterwards and mounted on a three axis translation stage (Elliot Martock MDE122) for fine alignment of the spot with respect to the marked fiber position. Since the microscope is set for a sharp image of the fiber shadow, the cavity mode on the macroscopic mirror is not in the imaging plane, because this is adjusted to the edge of the fiber. The position of the lens along the beam path is set such that the minimum spot size is visible on the camera, whereby the demands on accuracy are not very strict, since the Rayleigh ranges of the two focused pump laser beams are 0.74 mm and 1.7 mm. Therefore, the adjustment error due to the differing imaging plane is in principle negligible, but can be compensated with the translation stage.

The fine alignment in the transversal directions is done with the lens on the translation stage as well, since, to first order, the beam is displaced parallel to the optical axis and thus the angle of incidence with respect to the cavity mirror is not changed. The correct position of the spot on the camera of the respective imaging system can be calculated with Equation 5.14 or Equation 5.15, which gives the position relative to the initially marked cavity fiber. For a more accurate positioning of the pump beams, it would be desirable if the cavity mode on the mirror was observable. Therefore two more microscopes are installed, observing the cavity from the top and the side, collecting the stray light of the red lock laser from the mirror, as well as the stray light from the pump laser spots (see Figure 5.13). With the positions of the cavity mode and the pump laser spot visible on the same image, both can simply be overlapped. Even though achromats are used for the microscopes, the imaging planes for the lock laser and the infrared pump laser deviate, since there is a larger focal shift due to the large difference of the wavelengths. For viewing a sharp image of the infrared laser focus, the microscopes have to be realigned, shifting the position of the image on the camera. Therefore this method is only useful for the alignment of the green pump beam, since both spots, cavity mode and pump laser, can be observed simultaneously. For the vertical alignment, the lock light scattered by the fiber is much more intense than the stray light from the pump laser spot, making it difficult to properly align the beam in this direction. This cannot be observed in Figure 5.13, since for sake of clarity the intensity of the stray light has been reduced in the preparation of the figure.

So far, the alignment is only done with microscope images, however, a more precise alignment can be achieved with direct feedback from the system. Since the pump lasers heat up the cavity mirror and fiber, the resonator changes its characteristics due to the thermal effects discussed in subsection 2.2.2.

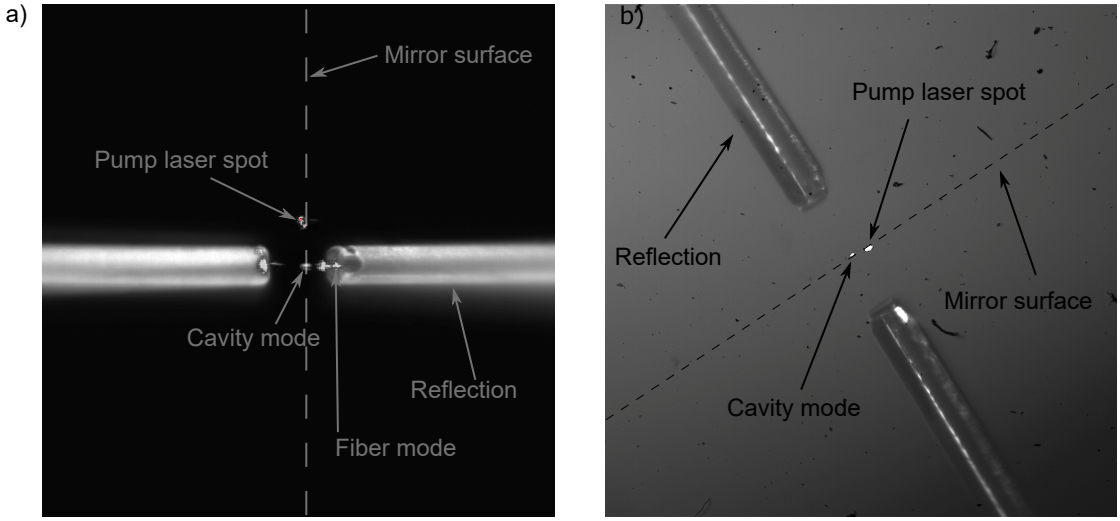

Figure 5.13: *Microscope images from the side (a) and the top (b), showing the fiber cavity and the stray light of the cavity mode on the macroscopic mirror, as well as the stray light from the green pump laser. The second fiber is the reflection in the macroscopic mirror. Even though the spot size of the pump laser is small, and the distance between the fiber and the beam's optical axis is larger than the beam waist, a large amount of light in the wings of the gaussian intensity distribution illuminates the fiber visible on the side image (a). The stray light leads to thermal effects.*

We can expect that the cavity expands most, if the pump laser spot and the cavity mode on the mirror are overlapped. This yields a change in the lock voltage applied to the piezo actuator for length stabilization. Since the laser frequency is constant, the changing lock voltage is a direct measure for the heating of the cavity mirror. The response relies on thermal effects, wherefore the timescales are on the order of seconds. The light illuminating the fiber thereby leads to heating as well and the system responds in the same manner as when the cavity mode on the mirror and the pump beam are overlapped. Furthermore, the fiber heats up more than the mirror due to its smaller thermal mass, which is why the alignment needs to be verified by the microscope images.

Another method of aligning the pump lasers on a much faster timescale is observing the number of collected stray photons from the cavity fiber with a single photon counting module. We can expect that the fiber collects the highest amount of photons if the pump beam is overlapped with the cavity mode, since the stray light is isotropically scattered and the fiber is directed onto this point, due to the cavity alignment. Moving the pump lasers across the cavity mode first shows an increase in collected stray photons, peaking when both spots overlap and decreasing when the pump beam is moved further. The response is similar for both the horizontal and the vertical direction.

For both methods, light in the wings of the gaussian intensity distribution illuminates the single-mode fiber, leading to a slight heating and a change in the lock voltage in the first case and pump light entering the fiber causing a rise in photon number in the second method. These effects are especially present for the green pump laser, since due to its acute angle of incidence the distance between its optical axis and the fiber is small, causing more light illuminating the fiber (see subsection 5.2.1). Additionally, the absorption of the green radiation is larger than for the infrared, leading to stronger thermal effects. However, the combination of microscope images and direct feedback of the cavity

makes it possible to find the correct location for the pump beams. Drifts in the pump beam positions were not observed, excluding the necessity of an active stabilization, e.g. with piezo actuator driven mirror mounts.

Frequency stabilization Besides the correct alignment of the pump beams with respect to the cavity mode, the stability of the pump frequency is crucial for a measurable photon-pair rate (see subsection 2.2.3). The lasers are stabilized via a wavelength meter (High Finesse WS7), which has an absolute resolution of 60 MHz and a relative accuracy of about 4 MHz, as stated by the manufacturer. For the experiment, only the frequency difference between the two pump lasers is relevant, wherefore the relative accuracy is the pertinent quantity. Of the two lasers, only the infrared laser is tunable, thus frequency drifts of the green pumping laser need to be compensated by adapting the infrared pump frequency. In a long-term measurement oscillations and drifts in the green pump laser frequency are observed, whereby the infrared laser is stable to within 20 MHz after an initial warm up time of approximately one hour. As an atomic reference the D2 line of ^{87}Rb is measured as well, showing no drifts of the wavelength meter. The difference frequency follows mainly the variations of the green pump laser, which are up to 200 MHz, much larger than the cavity linewidth. An active feedback is therefore mandatory.

The infrared laser frequency can be fine adjusted by ±65 MHz by changing the length of the internal etalon with a piezo-electric element and by 30 GHz via tuning the temperature of the seeding diode. Thus, the fine alignment is not sufficient to adapt to the frequency deviations and a combination of temperature regulation accounting for the long-term drifts, and etalon tuning countering the fast short term oscillations is used. The frequencies are read from the wavelength meter every second and the frequency discrepancy $\Delta\omega$ between the set signal frequency ω_s and the frequency difference of the pump lasers is calculated via

$$\Delta\omega = 2\omega_s - (\omega_g - \omega_{ir}) , \tag{5.19}$$

where ω_g and ω_{ir} are the measured pump frequencies, respectively. Both etalon and temperature can be adjusted by applying a constant voltage, yielding frequency tuning coefficients of $\eta_p = 1\,\mathrm{MHz\,V^{-1}}$ and $\eta_t = -3\,\mathrm{GHz\,V^{-1}}$. Due to the tuning bandwidth of 100 kHz, the piezo is adjusted every second, whereby the temperature is varied every twenty seconds because of the slow response. In order to keep the piezo voltage close to zero, the voltage applied to the temperature control accounts for the frequency shift due to the etalon. The variation of the infrared laser frequency accounts for the frequency drifts of the green pump laser and, resultingly, the difference frequency is stable to within 20 MHz.

5.2.4 Detection setup

In the former experiments, the transmitted light from the cavity has been send to a grating spectrometer, separating the signal and idler photons from the intense pump beam. The grating, therefore, has two purposes: spectrally decomposing the outcoupled light and suppressing background counts from the pump laser. In the experiment at hand, we correlate the photons in the reflection branch with the photons leaving the cavity in transmission. Furthermore, we expect the signal photons to be degenerate in frequency, since we do not search for a dispersion compensation point of the cavity, wherefore the creation of photon pairs on neighboring modes is restrained. Moreover, by virtue of the

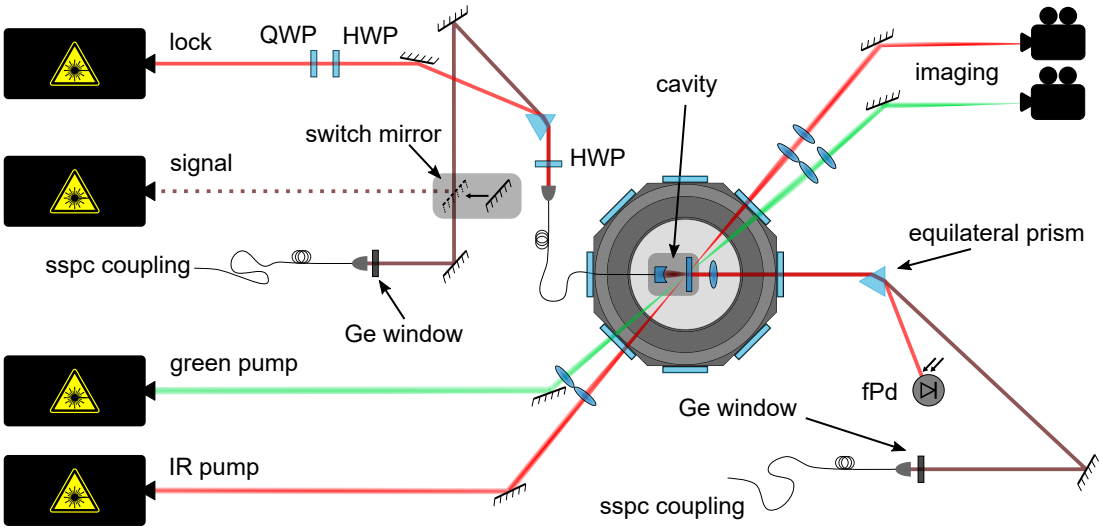

Figure 5.14: *Illustration of the optical detection setup (Abbreviations: quarter-wave retardation plate QWP, half-wave retardation plate HWP, fast photodiode fPd).*

distinct pumping scheme, degenerate photon pairs are actually observable, which is not the case in the previous experiments, where they cannot be filtered from the pump light.

Due to the large spectral separation of the signal photons to the pump and lock lasers, the frequencies can easily be decomposed by an equilateral dispersive prism with a resolution of $\delta\nu \approx 1.2\,\mathrm{THz}$, which is already in use for combining the signal and lock laser on the reflection side for simultaneous operation of the cavity (see Figure 5.14). In addition, the fiber couplings to the superconducting single photon counting modules (SSPC) act as spatial filtering. Further stray light is cleared by germanium windows (Thorlabs WG91050-C9), which have a transmission of about 90 % at the signal frequency and suppress the pump and lock lasers by four to eight orders of magnitude. The windows are attached in front of the fiber couplings to the single photon detectors in the transmission and reflection branch of the cavity[6], mainly suppressing the stray light from the lock laser. Additional background photons from Raman scattering are very unlikely due to the large spectral separation between the signal frequency and the other lasers, the low amount of lock light inside the fiber on the order of microwatt, and the short interaction region inside the coating. In order to probe the cavity with the signal laser, a D-shaped mirror in a rotation mount is placed before the prism in the reflection path ("switch mirror" in Figure 5.14). The mirror can be rotated with a stepper motor, such that the laser can be coupled into the cavity if needed, or photons exiting the cavity pass the mirror and are directed to the detector fiber coupling. The computer controlled switching is necessary for automation of the experiment, since during the measurements the cavity is probed with the signal laser, in order to determine the resonance frequency and account for possible drifts. The polarization of the lock and signal laser can be separately adjusted via half- (HWP) and quarter-wave retardation plates (QWP), with purpose of selecting the respective cavity polarization axis for each laser individually. In case of the lock laser,

[6] It is necessary to close every possible entrance point in between the fiber coupling lens and the fiber ferrule holder, as well as covering the fiber patch cable, since especially the infrared laser highly contributes to background photons undesired in the experiment. With covering the fiber cable and the coupler, the background rate is reduced at least by a factor of two.

the coupling to different transversal modes is adjusted by the polarization as well, since the cavity fiber is a rather multi-mode fiber for this wavelength and the respective fiber mode can be selected by changing the polarization. Phase retardation due to glass fibers are compensated by inducing stress by bending. A fast photodiode (fPd) in transmission of the cavity is used for stabilization of the resonator length.

Superconducting nanowire single photon counting modules For the detection of the signal photons at a wavelength of about 2 µm, superconducting nanowire single photon counting modules are used, which are operated with liquid helium in order to cool the wire below its critical temperature. Across the wire, a bias current close to the superconducting critical current is applied. Whenever a photon is incident on the wire, cooper pairs are broken, which locally reduces the critical current below the bias current. This results in a non-superconducting region, giving rise to a resistance [126]. Consequently, a voltage pulse is formed, which is amplified in order to have a measurable amplitude. After the current is shunted in the amplifier, the nanowire is cooled again, restoring its superconducting state.

The system at hand is fiber coupled and encapsulated in an approximately one meter long dipstick (Scontel), which is submerged into liquid helium contained in a Dewar (Wessington Cryogenics CH 120). Two channels are used, which are optimized for operation at the telecom O-band (CH II) and in the SWIR regime close to a wavelength of 2 µm (CH IV), respectively[7]. Inside the dipstick, the single-mode fibers of several meters length are winded up, in order to induce bending losses for wavelengths different from the signal wavelength for the reduction of dark counts. A scheme of the total detection setup consisting of the helium cycle and the electronic circuit is shown in Figure 5.15. Dewar and dipstick are each connected to a helium recuperation system via a control box for switching between direct connection of the dipstick to the reoccupation, and connection to the rotary vane pump (Agilent EM20) for cooling the detectors. There are check valves for preventing a backflow into the Dewar, which also lead to a rise in pressure during the pumping operation. Therefore a valve is installed to surpass the control box for a possible audited pressure release, before removing the dipstick from the tank. A squeezing valve is connected to the top of the Dewar in order to prevent helium loss through the Dewar neck, where the dipstick is inserted.

The cooling is done by successively inserting the dipstick further into the tank and pumping the cold helium vapors through the dipstick at first, and finally filling the bottom with liquid helium. A typical temperature and pressure curve is shown in Figure 5.16. Both quantities are read out by the electronic control box. Whenever the temperature is settling and the cooling rate is reduced, the dipstick is inserted further into the Dewar. This is done until the liquid helium is reached, which results in an increase in pressure, visible at around 2:10 in Figure 5.16. The final temperature is 2.1 K at a pressure of about 20 mbar and the total cooling process takes about 3.5 h.

The detectors are connected to the electronic control box via SMA-cables, for setting the bias current and acquiring the voltage pulses from the photon detection. After the first amplification stage within the box, the pulses have an amplitude of about 150 mV and are further amplified by 20 dB (Mini-Circuits PHA-13LN+) to an amplitude of 2 V, sufficient for TTL logic. The pulses are split (Mini-Circuits ZFSC-2-1-S+) and directed to a pulse counting module and the time-to-digital converter (HPTDC8 Cronologic), where the signal to the TDC is additionally converted to NIM logic.

[7] The system contains four detector channels in total, i.e. one further detector for each wavelength regime. However, with start of the measurements, only the two detectors stated here were functional.

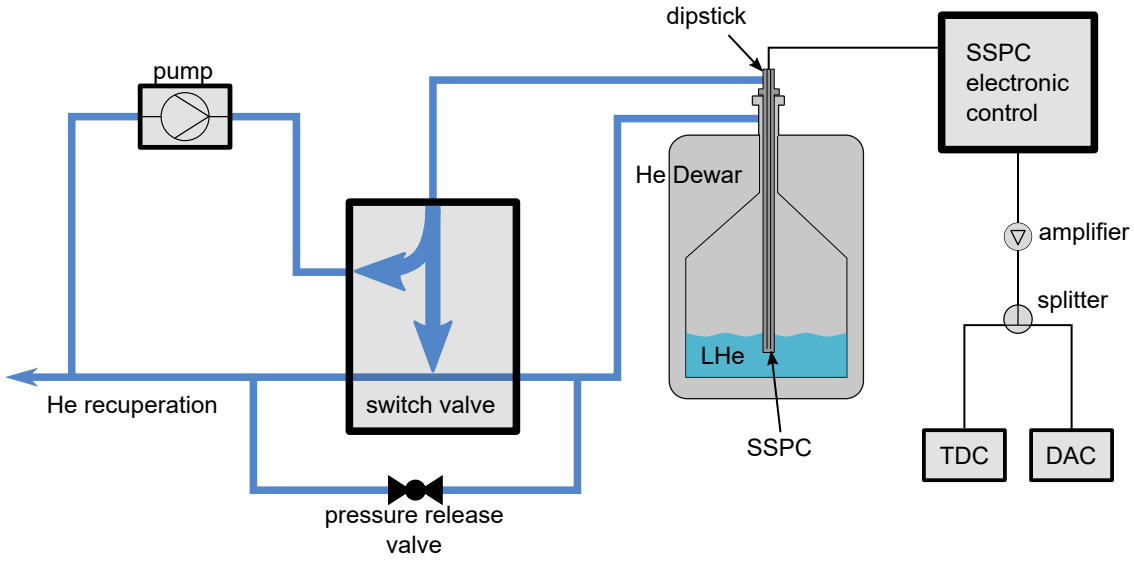

Figure 5.15: *Scheme of the complete detection hardware, consisting of the helium cycle with dipstick, Dewar, and helium retrieval system and the electronics part with control box for setting the bias currents and initial amplification of the voltage pulses, second amplification stage and signal detection by the time-to-digital converter (TDC) and pulse counting device (DAC).*

The bias currents are chosen to be negative, in order to invert the outgoing voltage pulses.

Detector calibration For optimized operation of the detector, the ideal bias current needs to be set, which is found by measuring the dark count rate and the quantum efficiency in dependence of the applied current, respectively. Typical calibration curves are shown in Figure 5.17. Applied bias currents differ for both modules and their quantum efficiency (a and b) and dark count rates (c and d) vary from day to day. By dividing the quantum efficiency by the dark count rate, the ideal bias current is determined from the maximum value of the ratio. Due to the changing detector performances, the ideal set value for the bias currents is determined before each correlation measurement.

From a measurement of the autocorrelation function for each channel, we can verify the dead time of the respective detector, which are shown in Figure 5.18. The data is obtained during a correlation measurement performed in the next section. Therefore the number of autocorrelation events for both detectors differ, due to varying background rates. A typical rise in correlation events can be observed and the corresponding times are about 35 ns (CH II) and 40 ns (CH IV), in which the detection efficiency is restored. This value is comparable to measurements in other systems [128]. In addition to the expected increase in autocorrelations, multiple peaks on the rising edge of the distribution are visible, exceeding the number of autocorrelation events by several orders of magnitude. We attribute these autocorrelation signals to reflections in the electronic circuit, or afterpulses from the amplifier or detector itself, as described in [127]. Releasing the cable connecting the temperature and pressure sensor from the dipstick decreases the number of autocorrelations, but does not completely prevent them. Nevertheless, these peaks are clearly a systematic error in the measurement process, wherefore an artificial dead time of 25 ns is imposed on the datasets in the correlation measurements. Hence, the

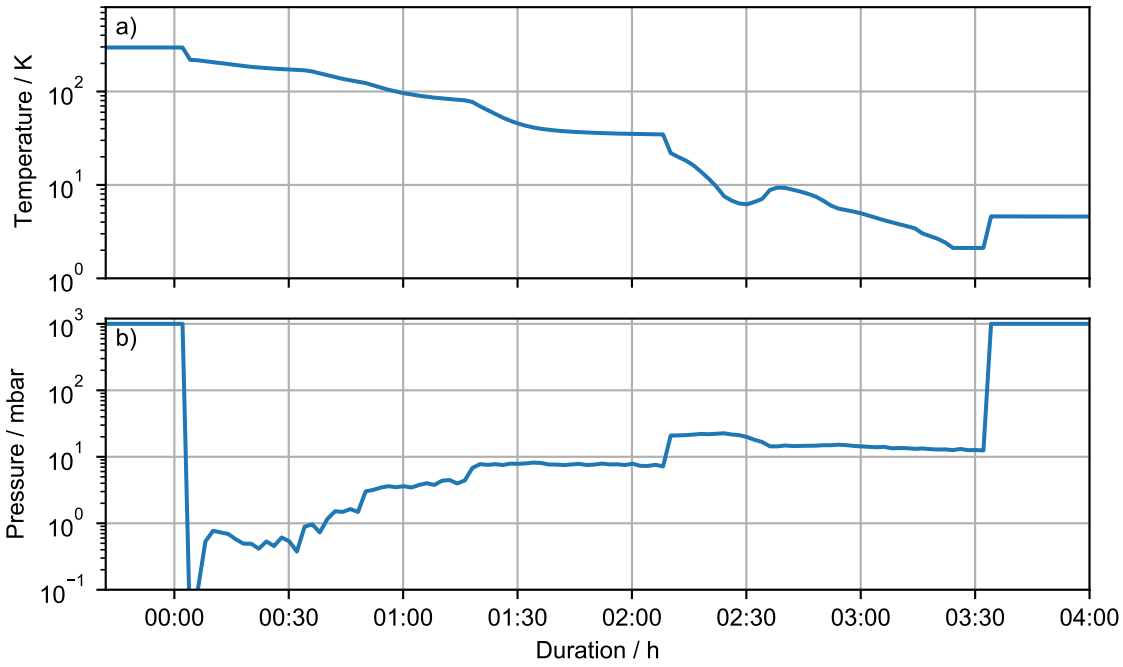

Figure 5.16: *Typical temperature and pressure curve measured close to the superconducting nanowire detectors. When the temperature is settling, the dipstick is inserted further into the liquid helium Dewar. The pressure is rising when the dipstick is submerged into the liquid helium. The final temperature is 2.1 K at a pressure of about 20 mbar. The total cooling process takes about 3.5 h.*

data is postprocessed by neglecting every timestamp following an detection event within this time interval on the respective detector. Otherwise, coincidence events may be counted twice with the time difference shifted by the peak positions in the autocorrelation measurements. Additionally, the rate of accidental coincidences increases, due to the increased number of counts. The peaks show a gaussian distribution due to the timing jitter of the detection setup, which can be determined by extracting the width of the peak (cf. section 3.4). From the fits (see inset in Figure 5.18), we measure mean values of $\tau_{\mathrm{jit,II}}(142 \pm 29)$ ps and $\tau_{\mathrm{jit,IV}}(182 \pm 18)$ ps, respectively. By integrating the gaussian distribution, the total number of autocorrelation events can be estimated, from which the probability for an autocorrelation event to occur is calculated to be approximately 3×10^{-4}.

The detector behavior reported on in this paragraph was observed in the evaluation of the correlation data described in the next subsection 5.3.2. For a characterization measurement, a coherent light source would be beneficial, due to its uniform photon statistics and larger intensity for increased number of autocorrelation events.

Detection efficiency and time delay Taking into account the transmission coefficients of the optics in the detection branches, outcoupling efficiency of the cavity into the fiber mode, fiber coupling efficiencies, and the detector efficiencies we get the total efficiency of about $\eta = 7 \times 10^{-4}$ for typical detector efficiencies of about 10 %.

By virtue of determining the position of the coincidence peak, the time delay between the detection

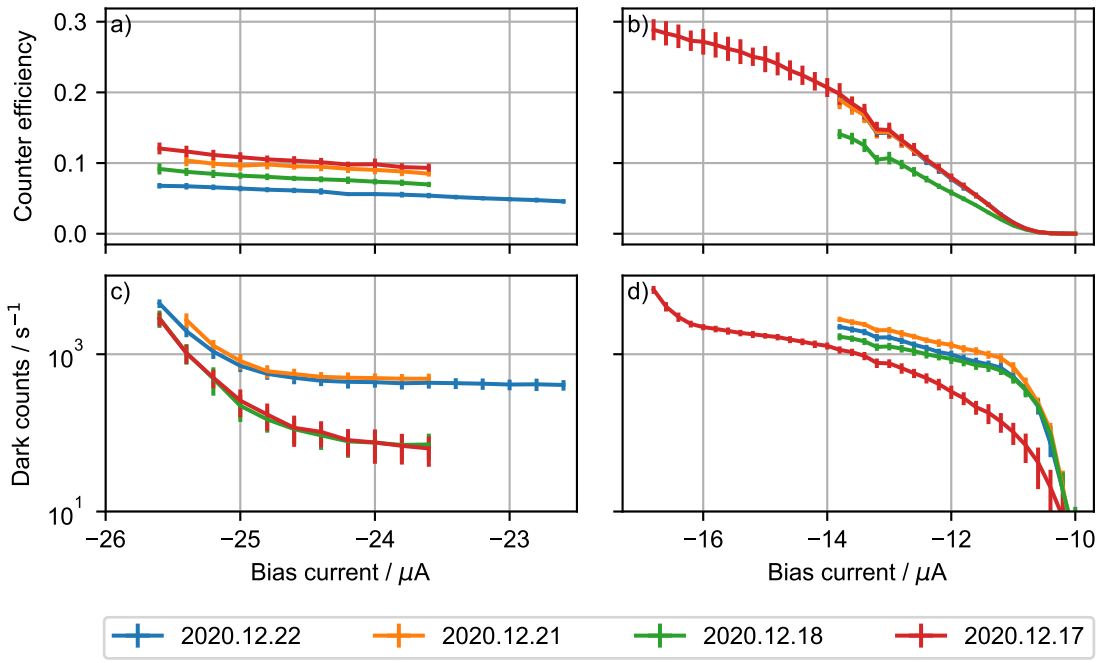

Figure 5.17: *Typical calibration curves for the quantum efficiency (a, b) and the dark counts (c, d) of the two detectors, respectively. The data shows a similar trend for every measurement, but slightly different parameters from day to day. Therefore, the calibration is done on a daily basis before measurements and the bias currents are adjusted accordingly.*

branches should be approximated. A potential delay in the electronic readout is estimated by simulating coincidence signals with a signal generator, yielding a delay of 4 ns for the transmission path over the reflection path, even though the cable lengths are similar. The main path length difference stems from the cavity single-mode fiber of approximately 4 m length, resulting in a travel time difference for photons in the reflection branch of 20 ns. Taking the small difference of 10 cm between the path lengths of the respective outcoupling lens to the detector fiber coupling and the length difference of the single-mode fibers inside the detectors of roughly 60 cm into account, the delay yields about –19 ns. However, a potential delay of the electronic control box and the detectors is not included in this estimation. Moreover, the delay due to the simulation of coincidences via the signal generator may underestimate the actual delay of real pulses, since these have a much shorter pulse-length on the order of ten picosecond. Hence, the group delay of the pulses is different, such that the true delay stemming from the electronic readout is certainly larger than 4 ns, shifting the time delay further to positive values. In order to precisely characterize this, the delay needs to be measured with a pulsed source, e.g. pulses generated by an electro-optic modulator. Furthermore, in this test setup, cross-talk between the detectors can be investigated. Due to the uncertain delays of some of the components and the unknown group delay, the value for the delay between the counters estimated here is more of an estimate for the order of magnitude, or rather a lower limit than an actual expectation.

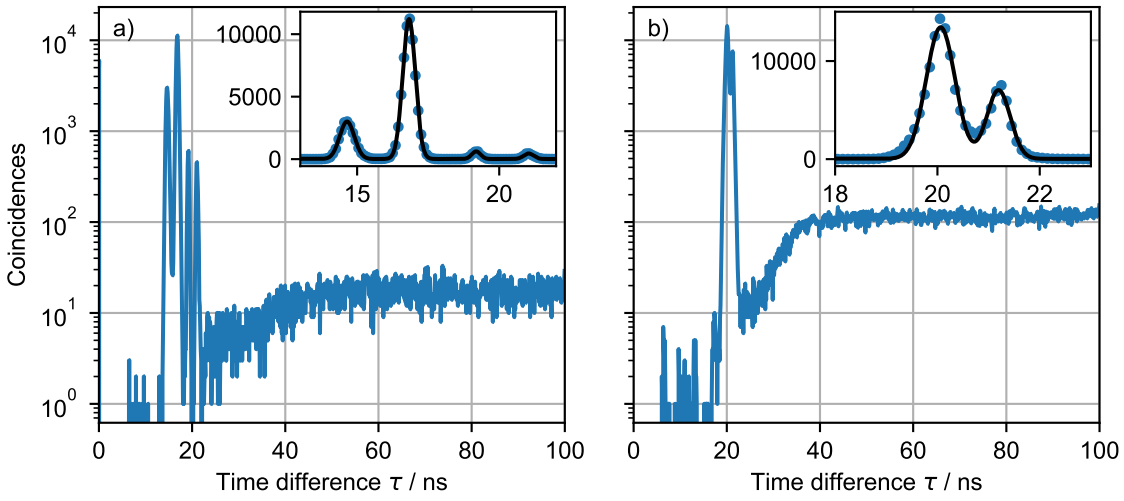

Figure 5.18: *Autocorrelation function with bin size 0.1 ns for CH II (a) and CH IV (b), obtained from correlation measurements performed in subsection 5.3.2. A typical rise in correlation events for increasing time difference between the incoming photons due to the finite dead time after a detection can be observed. In addition, for each detector multiple coincidence peaks on the rising edge at 14.6 ns, 16.9 ns, 19.2 ns and 21.0 ns, and 20.1 ns and 21.2 ns are visible, which stem from internal reflections of the electronic signal or afterpulses from the amplifier or the detector itself, as described in [127]. Therefore, an artificial deadtime of 25 ns is set, in order to exclude counting incident photons twice. The inset is a magnification of the interval where the respective autocorrelation peaks appear and additionally shows the gaussian fit for determination of the exact position and the timing jitter.*

Automated measurement Due to the small photon-pair rate, measurements have to be performed for several hours or even days. The experimental conditions, e.g. lock point of the cavity, frequency difference between pump lasers and length stabilization of the cavity, must not drift or fail during measurements. Therefore, the measurements are divided into sequences performed by a computer program, observing the experiment parameters and deciding, whether the conditions for a correct measurement are fulfilled or the recording of timestamps needs to be interrupted.

The measurement parameters are manually initialized, involving polarization of the signal and lock cavity mode, as well as the pump lasers, the pump powers and the laser frequencies. The frequency for the cavity lock laser is adjusted by overlapping the resonator reflection signals of both signal and lock lasers. Fine tuning of the overlap is done by stabilizing the cavity to the lock laser frequency and adjusting the signal laser temperature, in order to minimize its reflection signal. The lock laser frequency is stabilized to the adjusted wavelength via the wavelength meter and the signal laser frequency is set as the reference value for the frequency stabilization of the pump lasers (see subsection 5.2.3), which are also stabilized via the wavelength meter.

The client adjusting the laser frequencies sets a control flag on a server to false, whenever the detuning to the setpoint is larger than 20 MHz. Besides the necessity for the lasers to be on resonance, the cavity needs to stay in lock, which is monitored by measuring the voltage output of the PID-controller and determining the standard deviation of the last ten seconds. If the cavity is not stabilized, the standard deviation of the lock voltage is larger than the threshold value of 0.5 V, since the voltage

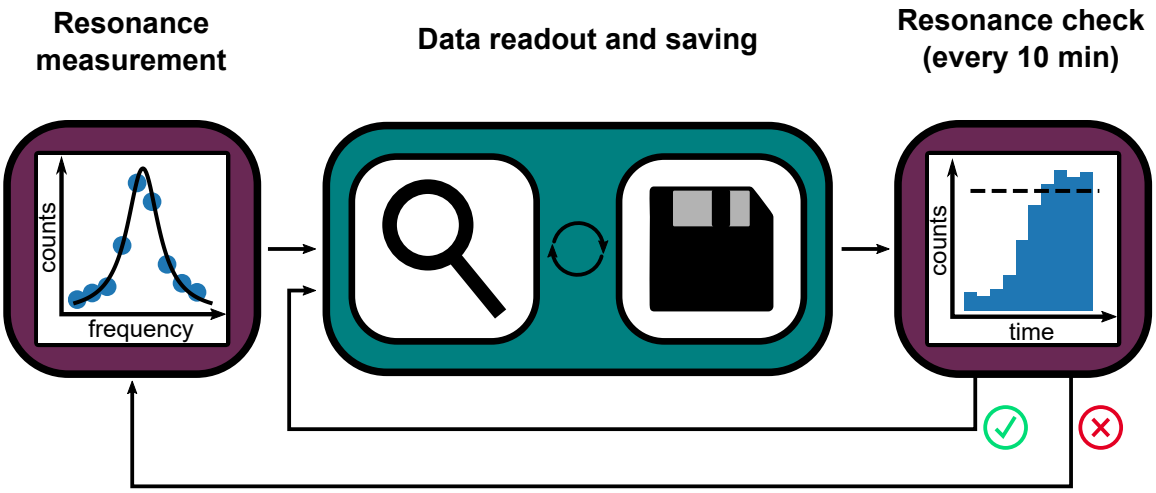

Figure 5.19: *Schematic illustration of a measurement sequence. First, the cavity resonance is probed by measuring the transmitted photons in dependence of the signal laser frequency and fitting a Lorentzian line shape function for extracting the resonance frequency. The measurement process is done by checking the parameters, i.e. cavity stabilization and frequency setpoints, and acquiring and saving the data. Every ten minutes the cavity is probed by the signal laser, in order to test the resonance. After a successful outcome the sequence returns to the measurement cycle and a failed outcome returns the sequence to the resonance measurement.*

applied to the piezo actuator is then ramped over the whole range of the PID-controller. A control flag is also set, if the condition is not met. Only if all of the control flags are set to true, the requirements for a successful measurement are given and timestamps are recorded.

With the manual setting of the parameters being complete, the automated measurement is initialized with measuring the amount of transmitted signal photons in order to have a reference value for the transmitted power at resonance. The signal laser is attenuated after the manual initialization, by virtue of not disabling the photon counter due to overexposing. A measurement sequence is shown schematically in Figure 5.19. First, the setup is switched into the probe mode by opening a shutter and setting the rotation mirror to couple the signal laser into the cavity. The resonance frequency is determined by measuring the transmitted counts in dependence of the signal laser frequency and fitting a Lorentzian to the data for extraction of the resonance frequency. This is set as reference value for the frequency stabilization of the pump lasers, if the fit is successful. Then, with the shutter being closed, and the rotation mirror switched to the transmission mode, the measurement cycle is started with checking the measurement parameters read from the control server, only acquiring and saving data, if the criteria for the measurement are given. Every ten minutes, the cavity is probed by the signal laser in order to measure the amount of transmitted photons. This value is compared to the initially determined photon flux on resonance. If the measured rate is higher than this threshold value, the sequence returns to the measurement cycle, or measures the cavity resonance again at an incorrect outcome. A complete sequence takes thirty minutes[8] in total.

[8] The time for a sequence and the interval in which the resonance is probed can be adjusted. The durations given in the text

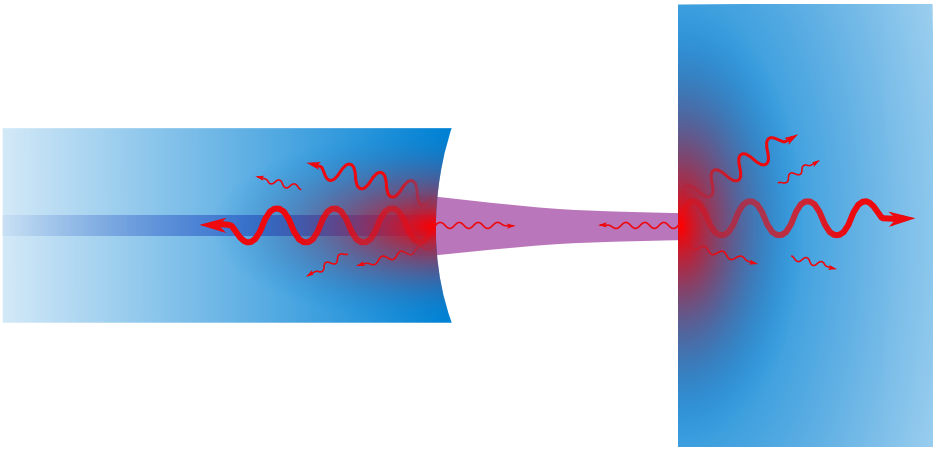

Figure 5.20: *Scheme of the thermal occupation of cavity modes. Both, mirror surface and fiber radiate thermal photons into the cavity and towards the detection branches. The cavity selects only those modes that are resonant, which is implied by the differences in photons radiated into the cavity and radiated from the cavity. Hence, the resonator suppresses coincidences from thermal bunching, because intensity correlations on both sides of the cavity are measured.*

5.3 Measurements and data analysis

In this section, correlation measurements are analyzed. First, the thermal occupation of cavity modes is evaluated in subsection 5.3.1 and a rate of coincidences from thermal radiation is estimated in terms of the temperature of the cavity. Then, correlation measurements are described in subsection 5.3.2, where two datasets with different adjustments of the pump laser polarizations are analyzed[9]. Afterwards, the likelihood for a random appearance of the observed correlation signal is estimated via a simulation in subsection 5.3.3.

5.3.1 Thermal occupation of cavity modes

Since the frequency of the signal photons is in the infrared regime, we need to estimate the background of thermal photons emitted by the cavity. Thermal photons show bunching, giving rise to correlation events in the same fashion as the signal we want to observe (see subsection 2.2.4). Therefore, we need to estimate the coincidence rate expected from the thermal occupation of the cavity modes for our system. Figure 5.20 shows a schematic representation of the resonator. The macroscopic mirror and the cavity fiber are heated by absorption of the pump light and isotropically emit photons due to thermal radiation. The cavity itself selects the amount of photons contributing to the thermal coincidence rate, since while the thermal emission is broadband, the resonator transmits only those modes fulfilling the resonance condition. Hence, we need to consider the spectral filtering imposed by the cavity and the equilateral prisms, as well as the spatial collection of radiated photons by the cavity.

were taken for possible post selection of data if the pump laser alignment drifts throughout a long-term measurement.

[9] After several hours of measurements for two settings of the polarizations of the pump lasers and the cavity mode, unfortunately, the resonator was permanently destroyed during the alignment process, i.e. the coating on the single-mode fiber was damaged by one of the pump beams, such that the cavity could not be locked anymore and therefore no more measurements could be performed.

The total spectral energy density of a blackbody with temperature T at thermal equilibrium absorbing at all frequencies ν is given by [3]

$$\rho(\nu) = \frac{8\pi\nu^2}{c^3}\frac{h\nu}{e^{h\nu/k_\mathrm{B}T} - 1}\,, \tag{5.20}$$

where k_B is Boltzmann's constant. This is connected to the spectral radiance by multiplying a factor of $c/4\pi$, giving the power radiated from a unit surface per unit frequency and unit angle. The differential number of photons per unit time is thus given by

$$\mathrm{d}\gamma(\nu, T) = \frac{c}{4\pi}\frac{\rho(\nu, T)}{h\nu}\mathrm{d}\nu\,\mathrm{d}\Omega\,\mathrm{d}A\,\cos(\theta)\,. \tag{5.21}$$

However, this will drastically overestimate the rate of thermal photons, since glass is not a blackbody in the frequency range observed here, but highly transparent. Hence, following Kirchhoff's law of thermal radiation, above equation needs to be multiplied by the emissivity of the material [129]. In thermal equilibrium the emissivity is equal to the absorption coefficient α, which we will assume to be equal to the cavity losses ($\approx 100\,\mathrm{ppm}$). The spatial integral can be approximated in the small-angle approximation by the factor $2\pi^2 w_0^2 w_\mathrm{m}^3/l^3$, where w_0 and w_m are the cavity waists on the macroscopic mirror and the fiber surface, and l is the cavity length. This factor is evaluated for the radiation emitted by the macroscopic mirror into the cavity, however, since $w_0 \lessapprox w_\mathrm{m} \ll l$, the result is in principle the same for the fiber, wherefore another factor of 2 will be added, in order to account for both mirrors[10]. Given the free spectral range $\Delta\nu_\mathrm{fsr} = 0.79\,\mathrm{THz}$ and the spectral resolution of the prism $\Delta\lambda = 1.2\,\mathrm{THz}$, only one cavity mode ν contributes to thermal coincidences and the rate can be calculated in dependence of the temperature with

$$\gamma_\nu(T) = \alpha\frac{8\pi^2 w_\mathrm{m}^2 w_0^3}{c^2 l^3}\Delta\nu_\mathrm{fsr}\frac{\nu^2}{\exp\left(\frac{h\nu}{k_\mathrm{B}T}\right) - 1}\,. \tag{5.22}$$

Figure 5.21 shows the expected thermal coincidence rate for the signal frequency $\nu = 150.1\,\mathrm{THz}$ and the system parameters with varying temperature. We observe, that without strong heating ($T < 350\,\mathrm{K}$) the expected rate is at least one order of magnitude less than the expected (real) coincidence rate determined in subsection 5.1.3.

In order to determine the rate of thermal coincidences, we need to estimate the temperature of the cavity. In the previous chapters we already observed severe nonlinear characteristics due to heating induced by high intensities inside the resonators. Besides a few hundred microwatt of circulating lock light, the cavity is empty, however, the pump lasers will lead to an increase of the resonator temperature, resulting in a drift of the cavity resonance. We won't observe the typical bistability as in the former experiments (cf. section 3.3 and section 4.3), since the heating is not related to the scan of the cavity length but steady, wherefore we cannot determine the lineshift, in order to estimate the temperature. Nonetheless, by comparing the relationship between the lock frequency to the signal frequency with, and without illumination by the pump lasers, we can calculate the respective temperature.

[10] In addition, we will assume fiber and mirror to have the same temperature, which is—strictly speaking—not correct, evident from the alignment process of the pump lasers.

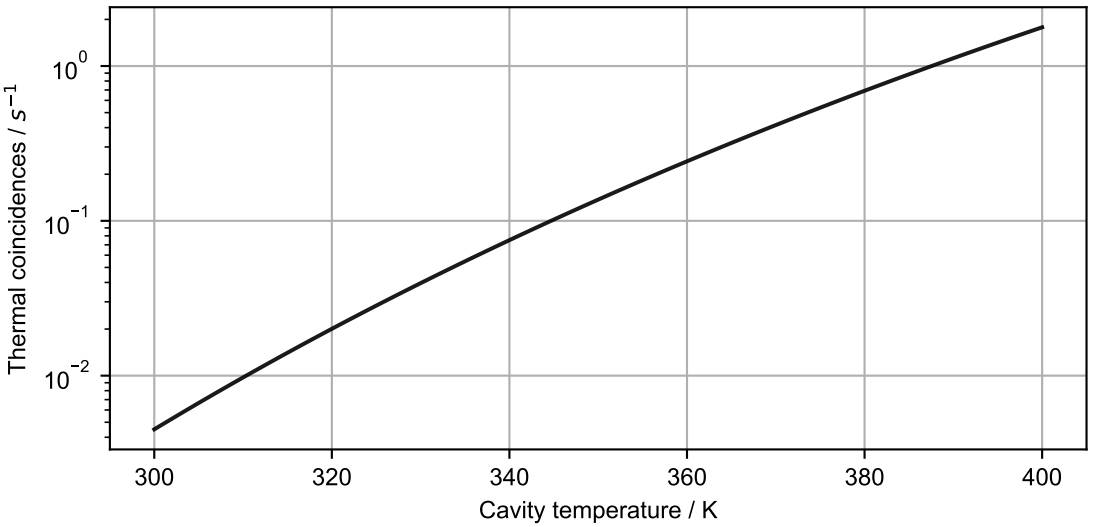

Figure 5.21: *Rate of thermal coincidences in dependence of the temperature of the cavity mirrors calculated with Equation 5.22.*

Figure 5.22 shows the dependence of the lock frequency on the signal frequency with, and without illumination of the pump lasers at 20 W infrared and 3 W green power, at which the measurements in the following section are conducted. We can observe a linear dependence for both datasets, but the lock resonances are shifted by 21 GHz for the heated cavity, which refers to 7 GHz for the signal frequencies. The cavity is heated due to the absorbed laser radiation and, hence, thermally expands and the refractive index in the coating changes due to the thermo-optic effect (cf. subsection 2.2.2). The resonance shift is caused by the variation in the free spectral range $\delta\nu_{\mathrm{fsr}}$ due to the temperature increase and is equal to the mode-number q times the variation. Assuming the difference in the free spectral range is entirely due to the change in the refractive index, we find for the temperature change

$$\Delta T = \frac{\delta\nu}{\nu}\frac{n}{n_2^{\mathrm{therm}}}\,, \tag{5.23}$$

which is approximately $\Delta T \approx 10\,\mathrm{K}$ for the thermo-optic coefficient $n_2^{\mathrm{therm}} \approx 1\times10^{-5}\,\mathrm{K}^{-1}$ [130] and the refractive index $n = 2.1$ for Ta_2O_5 at the lock frequency. Consequently, the expected coincidence rate due to the thermal occupation of the cavity modes is on the order of $1\times10^{-2}\,\mathrm{s}^{-1}$. In comparison to the expected photon-pair generation rate, this is more than one order of magnitude less, wherefore the main mechanism of photon bunching is the parametric excitation of cavity modes and not thermal radiation.

5.3.2 Correlation measurements

In order to perform a measurement, the pump lasers are aligned and system parameters are initialized as described in the previous section 5.2. Timestamps of photon detection events are collected for several hours and during the measurement the list of timestamps is analyzed for coincidences in a time-window of ±100 ns. From the list of timestamps, the algorithm searches for entries on the second

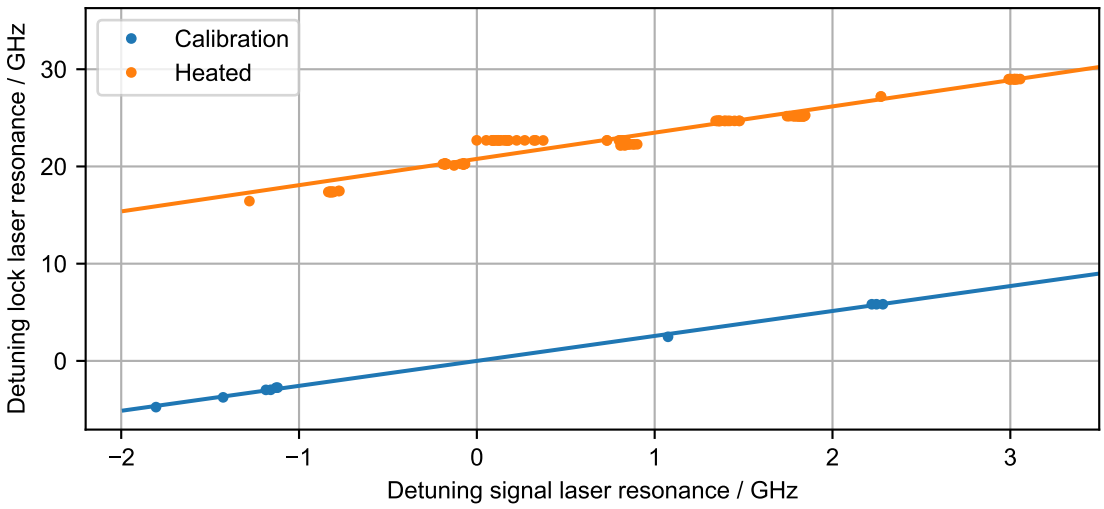

Figure 5.22: *Relation between lock and signal frequency with, and without illumination of the pump lasers at 20 W infrared and 3 W green power. The two datasets show a linear relationship between the two frequencies and the frequency shift due to the temperature change is extracted from the distance of the two lines to be 21 GHz and 7 GHz for the lock and signal laser, respectively. The x and y axes are shifted by 150.109 THz and 446.239 THz, respectively.*

channel in the specified time-window with respect to each entry on the first channel. Due to the already ordered list of photon arrival times, the data can be efficiently evaluated with a `for`-loop, simultaneously checking for prior and later arrived photons. The algorithm is also efficient for post-processing, even though several million entries need to be analyzed.

As mentioned in the introduction to this section, the amount of statistics obtained during the measurements is limited by virtue of the destruction of the resonator. Two datasets will be discussed, with integration times of 12 h and 13 h, respectively. Both have been measured at pump powers of 20 W infrared and 3 W green light. From the calculations for the expected photon-pair rate performed at the beginning of the chapter, we expect about 40 events under ideal circumstances, i.e. alignment and frequency stability. Therefore, before we analyze the data, we need to consider the distribution of coincidences, in order to calculate the optimal binning time in dependence of the accidental coincidence rate. In the previous chapters, we have observed that timing jitter of the electronic detection circuit alters the expected exponential distribution. However, since the cavity decay time $\tau_{\mathrm{rd}} \approx 1.7\,\mathrm{ns}$ is one order of magnitude larger than the timing jitter $\tau_{\mathrm{jit}} \approx 150\,\mathrm{ps}$ measured in subsection 5.2.4, we do not expect a change in the distribution, which is confirmed by a simulation (see Figure 5.23).

With knowledge about the expected distribution, the bin size in dependence of the relative number of correlation events a can be calculated. This is simply obtained by integrating the probability density function in Equation 3.6 over the bin size τ_Δ around the center. One finds the logarithmic dependence

$$\tau_\Delta = -2\tau_{\mathrm{rd}} \ln(1-a)\,. \tag{5.24}$$

The grey dashed lines in Figure 5.23 indicate the areas containing 50 %, 90 % and 99 % of the total coincidence events. While the relative amount and, consequently, the coincidence rate settles at a

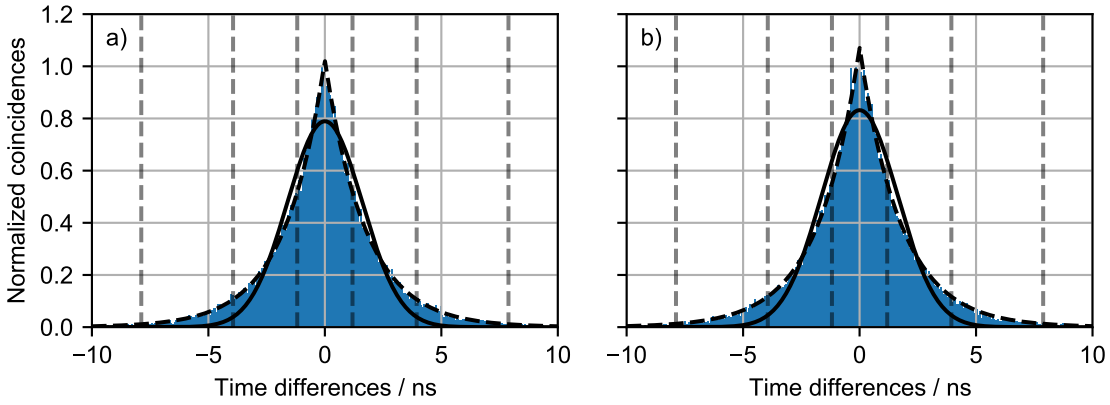

Figure 5.23: *Simulation of the expected correlation distribution for a cavity decay time of $\tau_{rd} \approx 1.7$ ns without a) and with b) timing jitter of $\tau_{jit} \approx 150$ ps taken into account. The jitter does not alter the lineshape of the exponential distribution of arrival time differences between the detectors. Grey dashed lines denote the regions of the peak containing 50 %, 90 % and 99 % of the total coincidence events. The black dashed (solid) lines are exponential (gaussian) fits to the simulated data, demonstrating that the jitter does not affect the exponential distribution of photon coincidences.*

finite value, the accidental coincidence rate increases linearly. Accordingly, the signal-to-noise is reduced with increasing bin size. The optimal bin size can be estimated by calculating the variance of a single bin depending on the binning time, which is expected to be a monotonically decreasing function. Time differences for the accidental coincidence rate are distributed uniformly over every bin with probability $p = \tau_\Delta / T$, where T is the total time-window under investigation. The standard deviation for one bin can be calculated via the binomial distribution, since a coincidence is either in the particular bin with probability p, or it is not with the complementary probability of $q = 1 - p$ [92]. The relative error per bin of mean height $\overline{k}$ is

$$\frac{\Delta k}{\overline{k}} = \sqrt{\frac{1-p}{p \cdot N}}, \tag{5.25}$$

where N is the sample size of coincidence events in time-window T. The optimal bin size is given by the maximum value of the ratio of signal-to-noise to the error on accidental coincidences. For the sample size of 6800 and an expected number of real coincidence events of 40, the optimal bin size is 4.6 ns (see Figure 5.26), with an accidental coincidence rate of 12.1 h^{-1}.

Figure 5.24 a) shows the coincidence rate per time difference at 20 W infrared and 3 W green pump laser power for a binning time of 4.6 ns. The polarizations of the pump lasers are adjusted to be perpendicular to the table surface, while the cavity is stabilized to the mode polarized parallel in the lab-frame. The measurement is a combination of several measurements with the same parameter settings and the data is acquired in a total time of about 12 h. The black line indicates the mean value of $(12.1 \pm 1.2)\,\mathrm{h}^{-1}$ and the grey shaded areas denote one and two standard deviations, respectively. The expected accidental coincidence rate of $(12.4 \pm 1.4)\,\mathrm{h}^{-1}$, calculated via Equation 3.7 from the detector count rates of $\gamma_{\mathrm{CH\,II}} = (1\,250 \pm 100)\,\mathrm{s}^{-1}$ and $\gamma_{\mathrm{CH\,IV}} = (600 \pm 50)\,\mathrm{s}^{-1}$ fits to the mean value. The detector efficiencies are $\eta_{\mathrm{CH\,II}} = 9\,\%$ and $\eta_{\mathrm{CH\,VI}} = 11\,\%$ at bias currents of $I_{\mathrm{CH\,II}} = -23.4\,\mu\mathrm{A}$

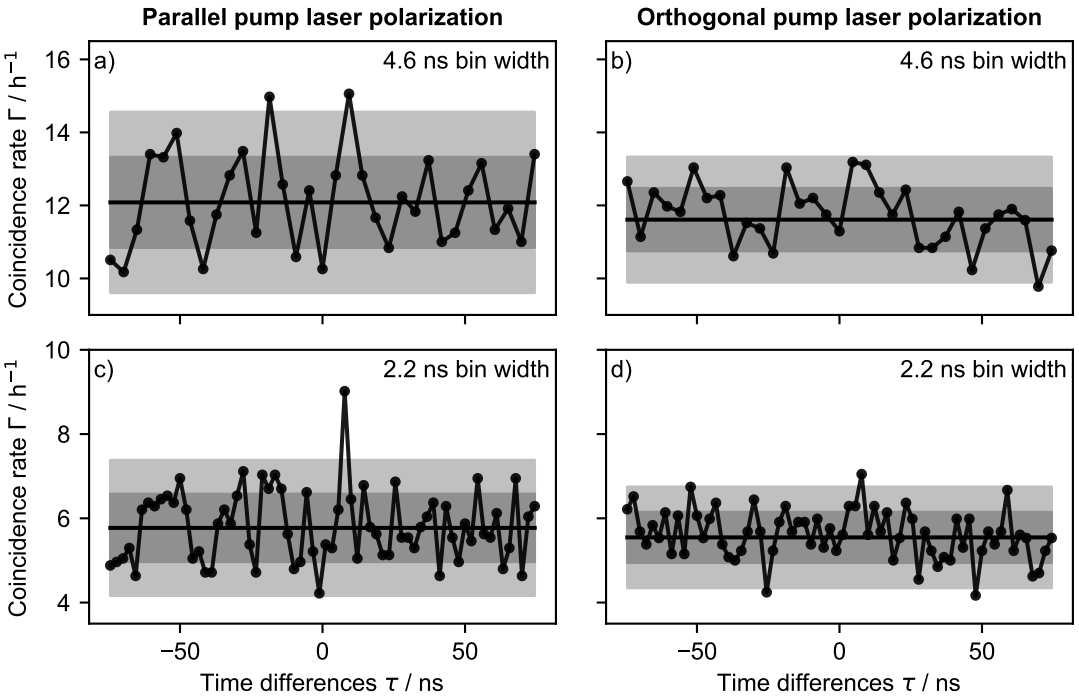

Figure 5.24: *Histograms of time differences per hour between arrival times on the two detectors in reflection and transmission of the cavity for two different binning times of 4.6 ns (a, b) and 2.2 ns (c, d). The black line is the mean value for each dataset and the grey shaded areas denote one and two standard deviations, respectively. In a) and c) both pump lasers are polarized parallel with respect to each other and orthogonal to the signal cavity mode, whereby the pump lasers are orthogonally polarized in b) and d). For the first measurement potential correlation signals can be observed, whereby the second measurement shows a flat correlation distribution, which is expected due to the birefringence of the cavity. The absence of a correlation signal in the second measurement excludes thermal radiation as a cause for the signal in the first measurement.*

and $I_{\mathrm{CH\,VI}} = -12.6\,\mu\mathrm{A}$. Two outlying data points of approximately equal height can be seen at about −20 ns and 8 ns, deviating from the mean background by more than two standard deviations, i.e. $2.4\,\sigma$ and $2.6\,\sigma$, respectively. Subtracting the mean from the more prominent peak, yields a possible coincidence rate of $3\,\mathrm{h}^{-1}$ which refers to a theoretical rate of $\Gamma_{\mathrm{theo}} = 1.3\,\mathrm{s}^{-1}$, taking the detection efficiency into account. This value is in fair agreement with the rates of $\Gamma_{\mathrm{theo,an}} = 1.6\,\mathrm{s}^{-1}$ calculated analytically and $\Gamma_{\mathrm{theo,sim}} = 0.9\,\mathrm{s}^{-1}$ estimated numerically.

After all, the small sample size prevents a definite comparison to the theoretical estimations and therefore the agreement between experiment and theory may be coincidence. Furthermore, the appearance of a potential second correlation peak needs to be investigated, whereas the position of one outlier at the approximated delay between the two branches of roughly −20 ns hints to a successful measurement. Decreasing the binning time may lead to a larger signal-to-noise, since the accidental coincidence rate scales linearly and real coincidences exponentially with binning time (see Equation 5.24 and Equation 3.7). Moreover, coincidence events are distributed according to an exponential distribution (see Equation 3.6 and Figure 5.23) and are randomly scattered over the bins. Thus, because of the small amount of events, the ideal bin width of 4.6 ns may be too large, since

it is calculated in the limit of an infinite number of events. Figure 5.24 c) shows the measurement for a binning time of 2.2 ns. The outlier at negative time delay vanishes, whereby a clear peak outstanding the flat background by almost four standard deviations at approximately 7 ns can be seen. The peak position deviates from the anticipated position by 26 ns. Nevertheless, as stated earlier, the estimated time delay between both detection branches is more of a lower limit rather than a precise characterization, wherefore the significance of the calculated delay should not be overestimated. Due to the small amount of statistics the distribution of the photon arrival times cannot be resolved, but we need to investigate whether the appearance of the correlation signal is due to thermal radiation, or a systematic error.

Comparison measurement with cross-polarized pump beams By changing measurement parameters such that no coincidences from the modulation of the refractive index are expected, we can test the origin of the observed coincidence signal. If correlations from the mechanism of the changing optical cavity length can be excluded, remaining coincidences must stem from thermal correlations, or possibly systematic errors, like cross-talk between the detectors. Naively, one could argue that due to orthogonal pump laser polarizations the refractive index is not modulated, because the pump beams do not interfere. Anyway, since the susceptibility is a tensor (see Equation 2.22 and Equation 2.25), there is still a modulation of the polarization of the medium present. Nevertheless, we would not expect a signal after all, because of the birefringence of the cavity. As observed in subsection 5.2.2, the splitting of the two polarization modes of the cavity is larger than the cavity linewidth, wherefore both modes are completely separated. For the two pump lasers being orthogonally polarized, the polarization of the expected photons need to be orthogonal as well, due to the symmetry of the susceptibility for centrosymmetric media (see subsection 2.2.1). Since only one polarization can be resonant with the cavity, the photon-pair generation process is highly suppressed. Consequently, no correlations from the modulation of the polarization are expected, and furthermore, a remaining coincidence signal must occur due to the thermal occupation of the resonator modes[11].

Figure 5.24 c) shows a measurement at the same pump powers as in the previous measurement for the optimal bin size of 4.6 ns, but crossed pump laser polarizations. The dataset has a comparable integration time of about 13 h and a similar accidental coincidence rate of $\Gamma_{\mathrm{acc}} = (11.6 \pm 0.9)\,\mathrm{h}^{-1}$. The bare detector count rates are $\gamma_{\mathrm{CH\,II}} = (820 \pm 80)\,\mathrm{s}^{-1}$ and $\gamma_{\mathrm{CH\,IV}} = (920 \pm 90)\,\mathrm{s}^{-1}$, which indicate an expected accidental coincidence rate of $\Gamma_{\mathrm{acc}} = (12.5 \pm 2.0)\,\mathrm{h}^{-1}$ which is in fair agreement to the measured value. Even though the count rates are similar, the detection efficiency for the reference measurement is approximately increased by a factor of two, due to the higher detector efficiencies of $\eta_{\mathrm{CH\,II}} = 11\,\%$ and $\eta_{\mathrm{CH\,IV}} = 17\,\%$ at bias currents of $I_{\mathrm{CH\,II}} = -24.4\,\mu\mathrm{A}$ and $I_{\mathrm{CH\,VI}} = -15.2\,\mu\mathrm{A}$, respectively. Comparing both datasets for the optimal binning time of 4.6 ns (see Figure 5.24 a) and c)), we observe two bins at the same positions of the outliers in the previous measurement, deviating from the mean bin height by almost two standard deviations. Nevertheless, if the bin size is reduced (see Figure 5.24 b) and d)) no peak is observable. Only a slight deviation from the mean by roughly two standard deviations a at around 7 ns is visible. A lasting signal can be attributed to the thermal occupation of cavity modes and a non-perfect coincidence between the laboratory polarization frame

[11] Since the axes of the cavity do not completely coincide with the polarization axes in the laboratory frame, a small contribution can be expected, because the cavity axes can be expressed as superpositions of the vectors spanning the laboratory polarization frame. Furthermore, the stress induced in the coating may lift the centrosymmetry of the material, giving rise to further components of the susceptibility tensor.

and the birefringence of the cavity. The comparison between reference and coincidence measurement indicates that the origin of the observed peak at a delay of about 7 ns stems from the modulation of the effective cavity length and thermal radiation has at least a minor contribution to the signal. Furthermore, the absence of similar outlying bins excludes a systematic error in the detection setup, since this should occur in both measurements independently of the pump laser polarization.

How can we ensure that the adjustment of the pump lasers is similar in both measurements? If the alignment is different, the cavity may not reach the same temperature and, thus, the rate of thermal coincidences would decrease (see Figure 5.21). We can verify the similarity of the alignment in both measurements by comparing the ratio of the lock frequency to the signal frequency. In subsection 5.3.1 we encountered the shift of the linear relationship between these parameters, by virtue of heating due to the illumination by the pump lasers. The ratio is determined by the slope constant plus the offset divided by the signal frequency, which is approximately constant over the range the frequencies are changed. This quantity, therefore, gives an unique identifier for the alignment, or rather the temperature of the cavity. After all, for the thermal coincidence rate, the precision of the overlap of the pump laser spots with the cavity mode, and the angular relations are not relevant since only the temperature determines the rate. For both measurements we find ratios of 2.972900 for the parallel polarized pump beams and 2.972904 for the orthogonal polarized pump beams. If the cavity is not illuminated, we find a ratio of 2.972762. The difference in the ratios stems from a change of the cavity polarization axis from p to s, which results in a shift in the ratio of 6.54×10^{-6} due to the birefringence. This does not explain the shift entirely, however, the measured value and the expected value differ by 3×10^{-6}, which refers to a frequency shift on the order of the linewidth, which is much smaller than the shift due to the temperature change. In addition, the ratio—as stated above—does slightly depend on the signal frequency, which deviates in both measurements by a few GHz. Consequently, both measurements can be seen as similar regarding the alignment and thermal bunching can be excluded as origin for the observed correlation signal at parallelly polarized pump beams.

5.3.3 Likelihood estimation for random correlation signals

With exclusion of systematic errors in the experiment and the thermal occupation of cavity modes as origin for the correlations, we want to estimate whether the appearance of the observed signal is coincidence. Due to the few correlation events, the lineshape of the distribution cannot be resolved and, so far, we only observed the data at two bin sizes. The bin size and position, however, determine the respective heights, wherefore the deviation from the mean may differ with varying bin size and outliers can occur out of coincidence. This behavior gets clear by investigating the relative error of the binomial distribution in Equation 5.25. With rising number of bins, the probability for a coincidence event to be sorted into a particular bin p decreases, such that the relative error, or the spreading of data points increases. In order to determine the randomness of the observed outliers, we want to compare their aberration from the mean bin height relative to the standard deviation to a simulation of random time differences. From the simulated data we want to generate the cumulative distribution function for finding the probability of a random occurrence of the observed peak.

First, we want to analyze the potential correlation signal at the optimal binning time of 4.6 ns calculated above. For comparison, the outlier at the expected time delay is also analyzed. In order to simulate a measurement of uncorrelated events on the two detectors, we generate random time differences with characteristics similar to the real measurements, e.g. sample size and time-window. Accidental coincidences result in a flat background—as for a coherent light source—since the

arrival times are random and independent, and therefore follow a Poisson distribution [90] (see subsection 2.2.4). We can simulate a measurement of an uncorrelated signal by drawing time differences from an uniform distribution in the range of the time-window we want to investigate. The time-window, however, determines the probability of finding an outlier, since, obviously, the more bins are under investigation, the higher the chance for a larger deviation from the mean bin height. This is evident from the relative error (see Equation 5.25): halving the time-window reduces the number of bins at constant bin width and increases the probability for an event being sorted into a particular bin by two. The smaller time-window, on the other hand, cuts the number of samples by two, yielding a reduction of the relative error like

$$\frac{\Delta k}{\overline{k}} = \sqrt{\frac{1-p}{pN} - (a-1)\frac{1}{N}}\,, \tag{5.26}$$

where a is the value by which the time-window is reduced ($a = 2$ in above example). Consequently, for a given time-window and corresponding dataset N, reducing the sample size by a factor of $1/a$, leads to a reduction of the relative error and, thus, a decrease of the probability of finding an outlier deviating from the mean bin height. Nevertheless, if the time-window under investigation is too large, the random occurrence of an outlier is overestimated. Therefore, we want to investigate several time-windows characteristic for time scales in the experiment. The distance between the two detector fiber couplings refers to roughly 20 ns travel time, wherefore we choose the smallest time-window to be ±20 ns. Taking the fibers to the nanowires into account, the travel-times from the cavity to the detectors are 40 ns and 60 ns, respectively, for which we choose the time-window accordingly.

We draw 6800 time differences from the uniform distribution in the range of ±100 ns, which refers to the number of events and time-window in above measurements. After the mean bin height and its standard deviation is calculated, the randomly generated dataset is reduced according to the time-window under investigation and the highest bin is selected. The relative aberration, e.g. the difference between the bin height and the mean value divided by the standard deviation is computed and serves as one measurement. The process is repeated one hundred thousand times in order to acquire the cumulative probability function for the occurrence of random outlying events. By virtue of sorting the computed aberrations into a histogram, the probability distribution is gained. This can be summed to a particular aberration and normalized by the total number of entries, with purpose of receiving the probability of finding a bin with the particular aberration or less. We are interested in the probability of finding a bin with a certain aberration or higher, wherefore we calculate the complementary probability. The cumulative probability functions for finding a peak with aberration σ or higher for the different time-windows is shown in Figure 5.25. We can observe the expected shift to higher aberrations with increasing time-window. For smaller time-windows, negative values are possible and more likely, since the mean value is taken over the complete dataset and not only the reduced part, likewise in the real measurements. To clarify, the cumulative probability distribution gives the probability for finding an outlier of aberration σ or higher, wherefore the probability is 1 for small or negative deviations from the mean value, even though they occur rarely in the simulation. For the complementary probability, obviously, the probability to find an outlier with a negative aberration is very low.

We can compare the deviation of the peaks encountered in the measurement with the simulated data and get the probability of a random occurrence by reading the value from the acquired cumulative probability distribution. For the two outliers in the dataset with parallel pump laser polarizations, we

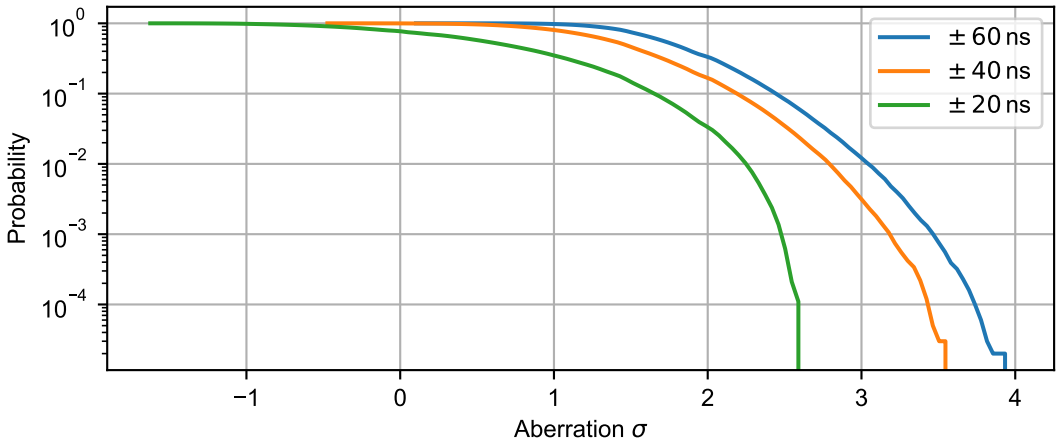

Figure 5.25: *Cumulative probability distributions of finding a peak with aberration σ or higher for the time-windows* ±20 ns, ±40 ns, *and* ±60 ns *characteristic for the experiment. The bin width in the evaluated histograms is 4.6 ns. Notice that the distribution can become negative since the mean value is extracted from the total time-window and not only the cropped region.*

Table 5.1: *Estimation of the probability for finding a random outlier of equal or higher aberration like the two potential correlation signals under investigation for different time-windows and a binning time of 4.6 ns.*

Peak properties		Probability per time-window		
Position	Aberration	±20 ns	±40 ns	±60 ns
−18.4 ns	2.35	5×10^{-3}	0.05	0.43
9.2 ns	2.61	$< 1 \times 10^{-5}$	0.02	0.2

find the aberrations with their corresponding probabilities summarized in Table 5.1. The probability of finding an outlier of the same or higher aberration rises with the size of the time-window observed. For the smallest time-window, the probability observing a random outlier with the observed aberration is less than one percent. Furthermore, for the peak at positive time delay the probability is less than 1×10^{-5}, since in one hundred thousand repetitions no peak of the same aberration or higher was recorded. While the probability at the second time-window is already on the order of a few percent, we can still deduce the observed signals being random is unlikely. However, at the largest time-window, the probabilities are on the order of several ten percent, indicating a larger likelihood for the outliers to be coincidence. Nevertheless, the largest time-window under investigation is in total 120 ns long, which is not a delay we would expect between the arrival times of photons. Therefore, the largest time-window seems to overestimate the likelihood for a random appearance. Furthermore, we observed the signal-to-noise to increase for the peak at positive time delay at lower binning times, which we want to analyze in the following.

Analysis with varying binning times In the histograms, the bin width and centration determine the bin height, by virtue of the random distribution of the correlation events over several nanoseconds.

Therefore, peaks may vanish and reappear with varying bin size, since the events become distributed over several bins at smaller bin widths, but may outstand the mean value if they coincide in one bin. This can also happen for a distribution of random accidental coincidence signals with a low amount of events. Even though the distribution is expected to be uniform, the relative error rises with decreasing number of events, and rising number of bins, increasing the probability for bins deviating from the mean value (see Equation 5.25).

We want to analyze how the peak height changes with altering bin size and determine the aberration from the mean in terms of standard deviations in dependence of the binning. First, we need to determine a lower limit for the bin size, while the upper limit is given by the optimal value of 4.6 ns obtained above. We calculate the signal-to-noise ratio for the measurement parameters and the error on the accidental coincidence rate with respect to the binning. From the fraction of the signal-to-noise ratio and the error, we can recover the upper limit on the bin size from the maximum of the curve. We choose 2 ns as the lower limit, since below this value the ratio is dominated by the noise on the background (see Figure 5.26).

In the previous analysis at fixed bin width, we simply read the bin heights at the corresponding positions from the histogram and calculate the aberration. With changing bin size, the dataset will be analyzed by sorting the time differences into a histogram at every bin width and extracting the maximum bin height, its position, as well as the mean bin height and its standard deviation in a small time-window around the specific outlier we want to analyze. From the list of aberrations we can calculate the weighted average, which serves as the reference value for comparison to the simulated data. In the analysis, the bin size is changed in steps of 50 ps, which is a rather arbitrary choice. The smaller time-window around the possible coincidence signal is necessary, in order to exclude arising

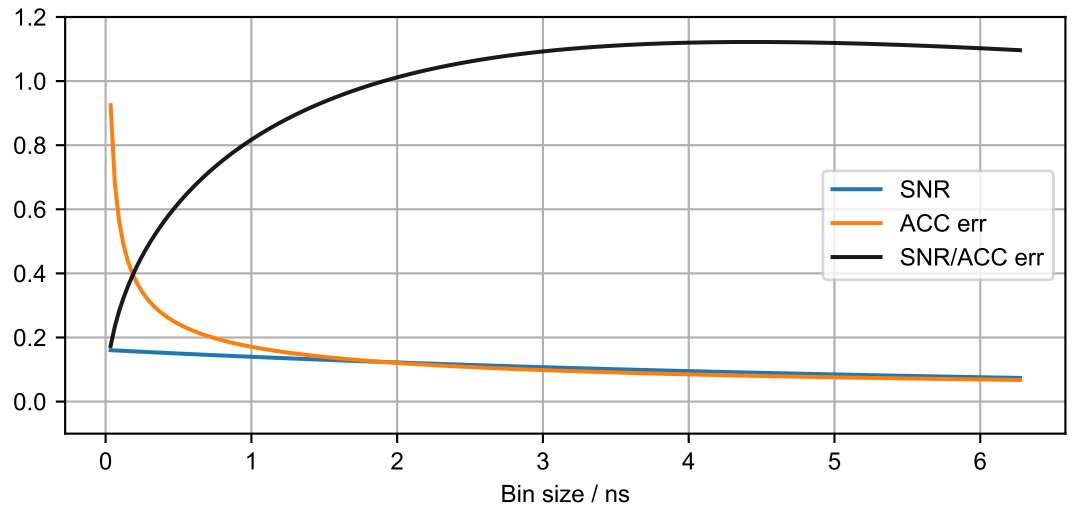

Figure 5.26: *Signal-to-noise (SNR) and accidental coincidence error (ACC) depending on the bin size for finding the optimal bin width for analyzing the data. The ratio between the quantities has a maximum at a bin width of 4.6 ns, which serves as the upper limit. At a bin size of about 2 ns, the ratio of the signal-to-noise to the error is one, which serves as the lower limit of bin sizes in the analyzation, since below this value the ratio is dominated by the noise of background coincidences.*

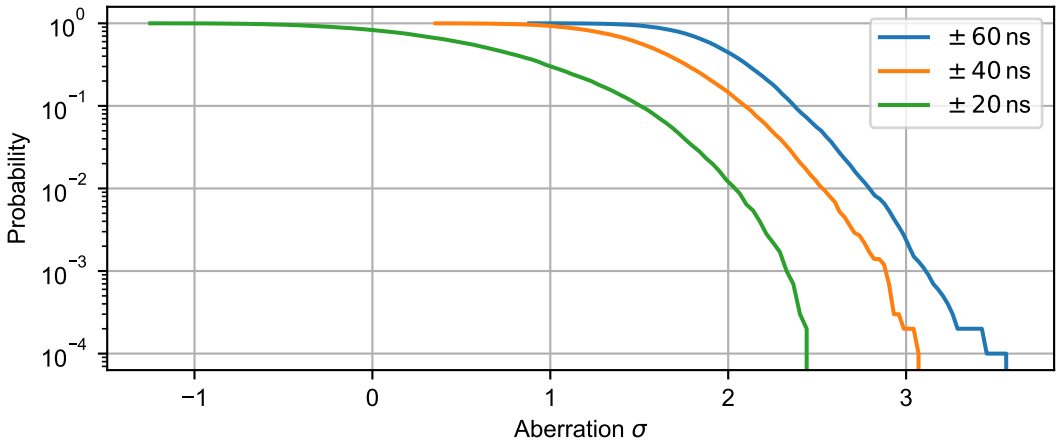

Figure 5.27: *Cumulative probability distributions for finding an outlier with an particular aberration to the mean height or higher in terms of standard deviations for different time-windows (a)* ±20 ns*, b)* ±40 ns*, c)* ±60 ns*).*

Table 5.2: *Estimation of the probability for finding a random outlier of equal or higher aberration as the potential correlation signals under investigation for different time-windows. While the outlier at about −20 ns is probably a random occurrence, the clear peak at about 7 ns very likely corresponds to a real signal.*

Peak properties		Probability per time-window		
Position	Aberration	±20 ns	±40 ns	±60 ns
(−18.8 ± 0.9) ns	1.92 ± 0.35	0.02	0.17	0.45
(7.26 ± 0.57) ns	3.51 ± 0.61	$< 1 \times 10^{-4}$	$< 1 \times 10^{-4}$	1×10^{-4}

outliers at different time delays distorting the analysis.

The data is simulated in the same manner as in the analysis with fixed bin width and evaluated like the real measurement, whereas only the mean and its standard deviation, and the maximum bin height are of interest. The weighted average of the aberration is determined and serves as the respective measurement. The process is repeated 10000 times and the aberrations are sorted into a histogram, by virtue of determining the cumulative probability distribution for finding an outlier with average aberration or higher (see Figure 5.27). We can observe the expected behavior with respect to the size of the time-window, where the cumulative probability distribution shifts towards higher aberrations for larger time-windows.

The aberration for the possible signals are extracted from the measurements as described above and the probability for finding an outlier of the same height or larger in the respective time-window is read from the distribution. The aberrations and probabilities are summarized in Table 5.2. The first outlier around the expected time delay at a mean position of about (−18.8 ± 0.9) ns has an average aberration of 1.92 ± 0.35. Compared to the former analysis at fixed bin height, the deviation from the mean reduces, since the potential correlation events become distributed over several bins. Therefore, in this analysis, the occurrence of the peak is more likely to be random, which we can expect from the ratio

between the signal-to-noise and the error on accidental coincidences. Even if the largest time-window is disregarded, in almost 20 % of the simulations for a time-window of ±40 ns a similar or higher peak can be found. Thus, the agreement with the theoretically predicted number of coincidences at the ideal bin width is probably coincidence.

The situation is different for the peak at positive time delay. Its position is determined to be (7.26 ± 0.57) ns and the mean aberration is 3.51 ± 0.61, i.e. on average, the bin height deviates by more than three standard deviations from the mean. The extracted probabilities from the cumulative probability distributions are at most 1×10^{-4} for all three time-windows under investigation. This means that, for the first two time-windows in the simulations, no peak has been observed with the same aberration. For the largest time-window of ±60 ns only one event has been recorded that shows the same characteristics as the observed signal. Even though the largest time-window probably overestimates the probability for a random appearance of an outlier in the measurement, we can conclude the probability for the signal being real to be 99.99 %.

5.3.4 Discussion

In the correlation measurement with parallel pump laser polarization, we find two potential coincidence signals for the ideal bin width of 4.6 ns, deviating by more than two standard deviations from the mean accidental coincidence background. One of the peaks appears at the expected time delay between the detector branches, whereas the significance of this approximation should not be overestimated, since it does not include the group delay of the short electronic pulses. Both outliers contain roughly the amount of coincidence events expected from the theoretical computations. At lower bin width, one of the signals vanishes and a clear peak is visible at a delay of about 7 ns, exceeding the uniform background by more than three standard deviations. In a reference measurement with cross-polarized pump beams, the creation of photon pairs is suppressed and no clear signal as in the previous measurement is observed. From this we exclude the origin of the observed correlation signal to be a systematic error, or thermal radiation, since these are not affected by the choice of pump laser polarization. The latter is additionally supported by calculations of the thermal coincidence rate. For the reference measurement, however, one outlying data point at the position of the prominent peak at 7 ns deviates by about two standard deviations at a bin width of 2.2 ns. The outlier may occur due to thermal radiation, or a slight modulation of the refractive index and indicates 7 ns being the actual delay between the detection branches.

In the simulation of the likelihood for the appearance of a random outlier deviating from the mean in terms of standard deviations, we find no definite result for the analysis at the ideal bin size of 4.6 ns. For the smallest time-window the probabilities are 0.5 % and less than 0.001 % for the two signals, respectively, and a few percent for the time-window of ±40 ns. At a time-window of ±60 ns the probabilities are a few ten percent, whereby the time-window possibly overestimates a random occurrence. Neglecting the latter, the simulation hints towards real, instead of random signals for both outlying data points.

However, repeating the simulation for varying bin widths leads to a different and definite conclusion. In this case, aberrations, like the outlier at the negative time delay, occur with a probability of 2 %, 17 % and 45 % for the respective time-window. From this analysis we can deduce a random occurrence of the signal. The peak at positive time-delay, however, is a real signal with a probability of at least 99.99 % at the largest time-window. We have therefore strong arguments for a successful measurement of photon pairs due to the changing effective cavity length by the pump laser modulation. The

amount of coincidence events contained in the peak is in agreement with the estimated value from the theoretical calculations. We exclude thermal radiation and systematic errors as an origin for the observed signal in a reference measurement and determine the probability for the correlation peak being real to be at least 99.99 %.

5.4 Summary

In this chapter, I demonstrated the formal equivalence of spontaneous four-wave mixing and the dynamical Casimir effect, in which a time-dependent boundary condition for the electromagnetic field leads to the creation of correlated photon pairs. While in spontaneous four-wave mixing two incident pump photons are annihilated and a photon pair is created, the process can be interpreted in terms of an oscillating refractive index changing the mode structure inside a cavity. Therefore, both SFWM and DCE have the same characteristics and can be interpreted as the parametric excitation of vacuum modes via a driven physical or effective cavity length. I have described and conducted an experiment where the refractive index modulation is obtained with a travelling intensity pattern due to the superposition of two high power continuous-wave lasers, incident from the side of the cavity. This process modulates the refractive index of one of the cavity mirrors at the difference frequency of the pump lasers and, thereby, changes the boundary conditions of the field mode at twice the cavity resonance frequency. The underlying mechanism in the photon picture is the annihilation of a green pump photon, creation of an infrared photon, stimulated by the infrared pump field, with the excess creating the photon pair inside the cavity. On a single photon level, the process is, therefore, distinctive from the SFWM experiments conducted in the previous chapters, since three photons are created, while only one photon is annihilated. The mechanism can, thus, be interpreted as an inelastic scattering, instead of the elastic scattering usually attributed to SFWM [7, 66].

Furthermore, I have calculated the estimated photon-pair rate and described the experimental setup, which is almost completely automated, since long integration times are necessary, in order to gain a statistically representative amount of coincidence events. I have presented and discussed measurements indicating a successful observation of the desired photon pairs, however, due to a small amount of statistics, the correlation distribution cannot be resolved. A peak at reasonable time delay is observed and the corresponding photon-pair rate matches the analytically and numerically estimated prediction in fair agreement. Thermal bunching and systematic errors as an origin for the coincidence signal are excluded by a reference measurement, where experimental conditions are similar, but the creation of photon pairs is suppressed due to the birefringence of the cavity. The exclusion of thermal radiation is additionally supported by calculations approximating the expected coincidence rate from the thermal occupation in the cavity. Even though the detection efficiency is increased by almost a factor of two, only a uniform background of accidental coincidences can be obtained in the reference measurement.

Finally, a possible random occurrence of the peak is analyzed, by virtue of simulating random correlation signals matching the measurement parameters. The cumulative probability function for finding an outlying bin deviating from the mean bin height in terms of standard deviations is obtained. From this distribution, the probability for a random occurrence of the observed signal is determined. The signal deviates from the mean height by more than three standard deviations on average. A comparison to the simulated data gives the probability for a real signal to be at least 99.99 %. The probability is found at the largest time-interval observed, which may even overestimate the probability

for a random occurrence of deviating data points.

After all, a more precise result and a characterization of the photon-pair production rate can be achieved by extending the integration time from about 12 h to several days, in order to gain more correlation events for a clear resolution of the distribution and less noise in the accidental background coincidences. In addition, besides the measurements at various combinations of the pump laser polarizations and cavity polarization modes, the measurement can be repeated at a detuning of the pump frequency by several cavity linewidths, in order to ultimately exclude thermal bunching as origin for the observed correlation signal. Furthermore, the detection setup needs to be characterized, with purpose of finding and verifying the exact time delay between the detector branches.

All in all, even though the amount of coincidence events does not allow to resolve the correlation distribution, we have found strong arguments for a successful measurement. Thermal radiation and systematic errors as an origin of the observed correlation signal have been eliminated by a reference measurement, the likelihood for a random occurrence has been estimated, and we have found a good agreement between the measurement and the theoretically predicted photon-pair rate, even though a more precise analysis is prevented by the limited measurement time. However, the observed signal clearly stems from the modulation of the refractive index and thus, from the oscillating effective cavity length. The experiment, thus, serves as an optical analogue experiment to the dynamical Casimir effect. However, whether the generalization of the dynamical Casimir effect from the mechanical modulation of the boundary conditions to the modulation of any system parameter determining the mode properties of the electromagnetic field is a unification due to similar underlying processes, is beyond the scope of this thesis. Anyway, due to the limitations of mechanical excitation frequencies only analogue experiments like shown in this chapter can gain insights to the fundamental processes.

CHAPTER 6

Summary and Outlook

In this thesis, I have studied and observed the generation of correlated photon pairs in optical high-finesse micro-resonators by driving the third-order nonlinear dielectric polarization in a sub-wavelength thick medium, and a liquid.

We have utilized the dielectric mirror coating of a micro-cavity as third-order nonlinear medium and have observed correlated photon pairs due to spontaneous four-wave mixing. In this setup, the penetration of the electric field of the cavity mode into the first few layers of the dielectric coating stack forms the nonlinear medium. Therefore, the interaction length is less than one micrometer. In the process, two incident pump photons are annihilated and a pair of signal and idler photons is created. The signal and idler modes are shifted by one free spectral range (4.5 THz) up- and downwards with respect to the dispersion-compensated cavity pump mode ($\lambda = 790\,\mathrm{nm}$). The expected quadratic dependence on pump power has been obtained and the measured photon-pair production rate is $\Gamma_{\mathrm{exp}} = (0.22 \pm 0.01)\,\mathrm{s}^{-1}\,\mathrm{W}^{-2}$. This value is in fair agreement with the theoretically estimated rate, derived by calculating the system's Hamiltonian and solving the master equation. The experiment shows that, in principle, every cavity using dielectric mirror coatings can act as a photon-pair source. Furthermore, we have shown that the Kerr effect, i.e. the response of the refractive index to the intensity of an applied electric field, can follow the oscillating intensity of the standing wave at optical frequencies.

By filling the resonator with a liquid, the nonlinear medium has been extended from the sub-wavelength scales inside the dielectric mirror coating to the whole cavity length. The liquid has a very low absorption and does not alter the finesse of the cavity. We have measured an increased rate of $\Gamma_{\mathrm{exp}} = (330 \pm 30)\,\mathrm{s}^{-1}\,\mathrm{W}^{-2}$ at the second-order signal and idler pair. The frequencies are shifted by two free spectral ranges ($2 \times 2.5\,\mathrm{THz}$) up- and downwards with respect to the pump mode ($\lambda = 784\,\mathrm{nm}$). The photon-pair production rate has increased by more than three orders of magnitude as compared to the empty cavity. Moreover, the quantum nature of the photon-pair source has been verified by a coincidence to accidental ratio of 3.1 ± 0.1, surpassing the classical limit of 2 for a thermal light source. The spectral brightness of the photon-pair source referring to the incident power is $(44 \pm 8)\,\mathrm{mW}^{-2}\,\mathrm{s}^{-1}\,\mathrm{MHz}^{-1}$, showing the narrow-band properties due to the cavity linewidth. We also measure photon pairs in the third spectral order and determine the nonlinear refractive index of the synthetic silicone oil (DC704) to $n_2 = (5.6 \pm 0.3) \times 10^{-20}\,\mathrm{m}^2\,\mathrm{W}^{-1}$ by using the earlier derived formalism for the expected photon-pair production rate.

The two experiments demonstrate the possible tunability of the photon-pair frequencies by either

using higher-order modes, or changing the cavity length, where utilizing a liquid as nonlinear medium is beneficial due to the absence of additional boundary conditions as imposed by solids. Consequently, the spectral properties of the photon-pair source can be tailored to the desired characteristics. Both experiments employ common low-power continuous-wave diode lasers and reach the high intensities required for the nonlinear process by resonant amplification inside the optical cavities. Using micro-cavities makes the apparatus easy to integrate and increases the nonlinear effects by virtue of a reduced mode volume. The experimental setups are simple due to the self-alignment of the pump laser with respect to the nonlinear media because of the the already established cavity alignment. In addition to the weak requirements for phase matching, and the tunability of the photon-pair frequencies, the scheme is an attractive candidate for photon-pair sources for usage in hybrid quantum systems. Here, the apparatus can bridge wavelength gaps in dissimilar quantum systems and, thus, interconnect remote quantum network nodes. The photon-pair generation in the liquid-filled cavity can be further increased by changing the nonlinear medium to carbon disulfide, which shows the largest nonlinearity in liquids.

The analysis of the quantum state of the correlated photon pairs is an interesting investigation, whereas it should be possible to produce polarization entangled states by either applying quantum interferometric techniques [131], or inducing a slight birefringence in the cavity [132]. The generation of photons not only on neighboring cavity modes, but one in the telecom band and one in the visible regime, is a compelling extension of the experiment. If the photon pair is entangled and the visible photon frequency is adjusted to an atomic transition, a matter qubit can be entangled with a flying qubit for quantum information purposes. With the flying qubit on a telecom band, conversion processes of visible photons for communication are not necessary. Obviously, the properties of the dielectric coatings of the cavity mirrors need to be changed to have a high finesse for the pump, signal and idler modes simultaneously. Furthermore, the creation of photon pairs not only on one, but several pairs of signal and idler modes can yield in a multiplexed photon-pair source [15]. This may be achievable by compensating dispersion at certain pump power levels. Moreover, in this context, the creation of a Kerr-frequency comb can be investigated, where light on multiple cavity modes is coherently generated by four-wave mixing, when the resonator is driven above parametric threshold [110]. Here, newly generated fields can mix with the already existent modes, to create fields on further cavity modes. The output spectrum would, thus, show lines separated by the free spectral range and with the line width of the cavity.

The underlying process of the experiments, spontaneous four-wave mixing, can be interpreted in multiple ways, such as the annihilation of two pump photons and the creation of the signal and idler photon pair, or an elastic scattering of the pump photons into the signal and idler modes. I have presented a third possible interpretation in terms of the dynamical Casimir effect. In the experiments, the effective cavity length is modulated due to the refractive index change of the dielectric mirror coating, or the liquid by the Kerr effect. In the dynamical Casimir effect, the modulation of a boundary condition to the electromagnetic field, like the periodic changing length of a cavity, leads to the creation of photon pairs by parametric excitation of the quantum vacuum. Here, the mechanical energy is converted into a pair of photons. The periodic modulation of the refractive index, due to the oscillating intensity of the standing wave at twice the pump frequency, can be seen as an analogue to the physically changing cavity length. I have investigated and shown the equivalence of both formalisms, for the dynamical Casimir effect and for the driven refractive index. Therefore, the changing effective cavity length alters the fundamental resonance frequency, likewise the oscillating physical resonator length.

Consequently, the spontaneous four-wave mixing in cavities can be interpreted as the parametric excitation of the unoccupied cavity modes due to the oscillating effective cavity length.

I have introduced an experiment, where two dissimilar high-intensity laser beams modulate the refractive index of the dielectric coating of one mirror in a high-finesse micro-cavity via the Kerr effect. Compared to the previous experiments, the material polarization is not driven by the standing wave of the cavity pump mode, but by the intensity pattern formed by the superimposed pump beams incident from the side of the resonator. The cavity, however, does not contain photons on the mode where the modulation couples to. If the angles of incidence are chosen accordingly, i.e. the wavevector component transversal to the cavity axis of both lasers is equal, the intensity pattern is parallel to the mirror surface and moves along the cavity axis. The refractive index is then modulated at the difference frequency of the pump lasers, which is chosen to be twice the cavity resonance frequency. Consequently, the resonance frequency of the unoccupied cavity mode is periodically changed and the electromagnetic vacuum is parametrically driven. This is possible, since the Kerr effect in the dielectric coating can follow the changing intensity at optical frequencies, as observed in the previous experiments.

I have calculated the Hamiltonian of the system in a similar manner to the theoretical estimations for the previous experiments. Based on the Hamiltonian, I could explain the underlying process in the single photon picture. A higher frequency pump photon (green, 581.9 THz) is annihilated and a lower frequency pump photon (infrared, 281.7 THz) is created due to stimulated emission on the virtual level. The excess creates a photon pair on the cavity mode, resonant to half of the difference frequency (infrared, 150.1 THz). The process is, thus, different from the common spontaneous four-wave mixing and is not explainable in the context of elastic scattering, but can rather be interpreted as an inelastic scattering.

We measure photon correlations between the two output directions of the cavity, where the amount of statistics was limited due to an unfortunate destruction of the cavity during measurements. Nevertheless, we have observed a coincidence signal containing the amount of photon pairs expected from initial computations, and surpassing the mean background of accidental coincidences by more than three standard deviations. We can exclude systematical errors and thermal bunching as origin for the correlation signal by a reference measurement, where the creation of photon pairs is prohibited by the polarization settings of the pump lasers and the birefringent cavity. Furthermore, the likelihood of a random appearance of the observed signal has been estimated via a simulation, resulting in a probability for a real coincidence signal of more than 99.99 %. This value is a lower margin limited by the number of simulation runs.

However, further measurements are necessary to find the correlation distribution and the bandwidth of the photon pairs. A measurement with the pump frequency detuned from the parametric resonance frequency can exclude thermal bunching as cause for the coincidence signal, and verify the dependence of the photon-pair rate on the frequency mismatch of the pump, and signal and idler frequencies. In addition, the thermal coincidence rate can be measured. Finally, correlation measurements should be repeated at several pump power levels to recover the expected quadratic dependence of the photon-pair rate on the pump power, predicted by the theoretical model. Even though the limitations of a small sample size, we have been able to clearly show the creation of correlated photon pairs due to the modulation of the refractive index and, thus, because of the oscillating effective cavity length.

In order to improve the photon-pair production rate, a first factor for enhancement is the detection efficiency and, especially, the detector efficiencies. Possibly the angles of incidence for the two pump lasers can be increased, an the cavity length can be decreased. Resultingly, a higher cavity finesse due

to reduction of clipping losses on the mirror is achieved. Moreover, the extraction efficiency of photons is enhanced due to the larger mode overlap of cavity and fiber mode. Exchanging one of the lasers to a pulsed laser, increases the peak intensity of the modulation and reduces the background of accidental coincidences, since the measurement intervals can be precisely selected from the synchronization with the laser pulses. Here, the cavity linewidth is the upper limit for the spectral, and the temporal width of the pulse. An increased photon-pair rate makes measurements of the quantum state of the photon pair, e.g. entanglement [133], possible.

In conclusion, the experiment shows the close relation between the parametric driving of vacuum modes via a third-order nonlinearity and the modulation of the physical cavity length, and serves as an optical analogue experiment to the dynamical Casimir effect. The equivalence of both system dynamics is evident in the similarity of the Hamiltonians. The experiment rather belongs to the class of simulating experiments, if the dynamical Casimir effect is considered in a more narrow sense being solely the generation of photon pairs via mechanical excitation [134]. However, the experiment shows characteristics of the dynamical Casimir effect in a wider sense, since the dielectric properties of the mirror coating are periodically modulated and, hence, the effective cavity length [134]. If the deep connection between the mechanical oscillation and optical analogue experiments, such as the modulation in a second- [27], or third-order nonlinearity [28, 114], as presented in this thesis, have a similar fundamental origin, needs to be further investigated. The coupling from electromagnetic fields to the quantum vacuum via parametric driving of vacuum modes and the mechanical excitation may be two sides of the same medal and only distinctive due to different historic approaches and interpretations. Nevertheless, observation of photon pairs from mechanical excitations of the quantum vacuum may never be possible and only analogue experiments, as shown in this thesis, can gain insights of the underlying physics.

CHAPTER 7

Acknowledgements

This work is the end of my ten years of academic education at the university of Bonn and many people accompanied me on this path. First of all, I would like to thank Prof. Dr. Michael Köhl for getting me in touch with this fascinating topic. You gave me a lot of freedom working on these exciting experiments and in trying out my ideas. I learned so much during our discussions and by working in the lab. Thank you for giving me this opportunity.

Thanks to our former postdoc Dr. Hendrik-Marten Meyer. You taught me the basic lab-skills and we were all very sad when you left the group. I still think academic research lost one of its upcoming stars to the industry.

A special thanks goes to—I think when people read this you are already—Dr. Pascal Kobel. I'm still very happy that you couldn't open that door on our first day of the pre-courses. From the moment you copied my work in this ungraded exam on that day, we had a very fruitful and competitive friendship, which brought us so far, I think. I'm glad that we went this path together and could even work in the same work group. Thanks for all your help, my friend.

Many thanks to my guys from the (Ober-) Bergische Boys, Jonas Schmitz and Felix Rönchen. Felix, it was much fun working on the liquid cavity project together. Jonas, I think without your computer skills it probably would have taken me another year for setting up my experiment. Discussing about our experiments, even though we were working on quite different topics, was always fun and I'm looking forward to see some nice results from your strontium experiment, my friends.

Thanks to Dr. Marcell Gall and Dr. Martin Link for joyful lunch, cigarette (It's good that we don't do that anymore, Marcell) and coffee breaks. I'm still not convinced of this IPA and craft-beer stuff, but I really enjoyed our after-work chill-sessions in the office, especially during corona times when no bars were open.

Nicola Wurz, thank you for entertaining discussions and dancing sessions. It was always much fun hanging out with you and, especially, kicking your butt at racket sports. I'm sorry, we never found time playing crossminton so you could kick my butt.

Thanks to Santhosh Surendra for asking me an infinite amount of questions on experiments I was not working on. You always show me that I know a lot more than I think I do. Never stop asking your questions my friend. I think you are made for research.

Thanks to Dr. Alexandra Behrle for your company, when I was sitting alone in the office. I enjoyed our Friday ritual, which I, unfortunately, did not keep up after you left the group.

Thanks to Dr. Andrea Bergschneider, the new postdoc in town, for your very helpful input to my

thesis and ordering my thoughts.

Thanks to all of the other colleagues I had throughout my time in the work group. I think we had a lot of fun at all the parties, coffee and lunch breaks, celebrating Karneval (I mean you two, Moritz and Andreas) and playing football. I enjoyed working with you people and I will miss the good discussions during breaks and in the group meeting. I'm glad that I found a lot of friends, instead of only colleagues.

A special thanks goes to Tina Naggert, our former secretary, for handling the orders, organization and bureaucracy stuff, and always having time for listening to problems. I had a lot of fun at our cigarette breaks and I'm sad that we never managed to play tennis together.

Thanks to Dr. Frank Vewinger for always having an open door and helping with problems in fruitful discussions, since you supervised my bachelor thesis a long time ago.

Thanks to Dr. Akos Hoffmann for all your help with electronics and building devices necessary for the experiments.

Last but not least, I'm very grateful for the never ending support of my family. Mom, Dad, without your emotional and financial support I would never have gotten so far. Thanks for everything.

Bibliography

[1] Max Planck, *Ueber das Gesetz der Energieverteilung im Normalspectrum*, Annalen der Physik **309** (1901) 553.

[2] Max Planck, *Über die Begründung des Gesetzes der schwarzen Strahlung*, Annalen der Physik **342** (1912) 642.

[3] P.W. Milonni, *The Quantum Vacuum: An Introduction to Quantum Electrodynamics*, Elsevier Science, 2013, ISBN: 9780080571492.

[4] Willis E. Lamb and Robert C. Retherford, *Fine Structure of the Hydrogen Atom by a Microwave Method*, Phys. Rev. **72** (3 1947) 241.

[5] Victor F. Weisskopf, *The development of field theory in the last 50 years*, Physics Today **34** (1981) 69.

[6] P. W. Milonni, *Different ways of looking at the electromagnetic vacuum*, Physica Scripta T (1988) 102, ISSN: 0281-1847.

[7] Lucia Caspani et al., *Integrated sources of photon quantum states based on nonlinear optics*, Light: Science & Applications **6** (2017) e17100, ISSN: 2047-7538.

[8] Changjia Chen et al., *Broadband fiber-based entangled photon-pair source at telecom O-band*, Opt. Lett. **46** (2021) 1261.

[9] J. Fan, A. Migdall and L. J. Wang, *Efficient generation of correlated photon pairs in a microstructure fiber*, Opt. Lett. **30** (2005) 3368.

[10] Y. J. Lu and Z. Y. Ou, *Optical parametric oscillator far below threshold: Experiment versus theory*, Phys. Rev. A **62** (3 2000) 033804.

[11] P. Hariharan and B. C. Sanders, *Cavity-enhanced parametric down-conversion as a source of correlated photons*, Journal of Modern Optics **47** (2000) 1739.

[12] L. Koch et al., "Photon Pairs from Cavity-Enhanced Parametric Down-Conversion with Tunable Bandwidth for Quantum Interfaces", *Research in Optical Sciences*, Optical Society of America, 2012 QT3A.3.

[13] C. K. Hong, Z. Y. Ou and L. Mandel, *Measurement of subpicosecond time intervals between two photons by interference*, Phys. Rev. Lett. **59** (18 1987) 2044.

[14] Dik Bouwmeester et al., *Experimental quantum teleportation*, Nature **390** (1997) 575.

[15] Siddarth Koduru Joshi et al., *A trusted node-free eight-user metropolitan quantum communication network*, eng, Science advances **6** (2020) eaba0959, ISSN: 2375-2548.

[16] Sergei Slussarenko and Geoff J. Pryde, *Photonic quantum information processing: A concise review*, Applied Physics Reviews **6** (2019) 041303.

[17] H. J. Kimble, *The quantum internet*, Nature **453** (2008) 1023.

[18] H. M. Meyer et al., *Direct Photonic Coupling of a Semiconductor Quantum Dot and a Trapped Ion*, Phys. Rev. Lett. **114** (12 2015) 123001.

[19] Petr Siyushev et al., *Molecular photons interfaced with alkali atoms*, Nature **509** (2014) 66, ISSN: 1476-4687.

[20] S. K. Lamoreaux, *Demonstration of the Casimir Force in the 0.6 to 6μm Range*, Phys. Rev. Lett. **78** (1 1997) 5.

[21] Gerald T. Moore, *Quantum Theory of the Electromagnetic Field in a Variable-Length One-Dimensional Cavity*, Journal of Mathematical Physics **11** (1970) 2679.

[22] S. A. Fulling, P. C. W. Davies and Roger Penrose, *Radiation from a moving mirror in two dimensional space-time: conformal anomaly*, Proceedings of the Royal Society of London. A. Mathematical and Physical Sciences **348** (1976) 393.

[23] C. M. Wilson et al., *Observation of the dynamical Casimir effect in a superconducting circuit*, Nature **479** (2011) 376, ISSN: 1476-4687.

[24] Tao Gong et al., *Recent progress in engineering the Casimir effect – applications to nanophotonics, nanomechanics, and chemistry*, Nanophotonics **10** (2021) 523.

[25] Markus Aspelmeyer, Tobias J. Kippenberg and Florian Marquardt, *Cavity optomechanics*, Rev. Mod. Phys. **86** (4 2014) 1391.

[26] Pasi Lähteenmäki et al., *Dynamical Casimir effect in a Josephson metamaterial*, Proceedings of the National Academy of Sciences **110** (2013) 4234, ISSN: 0027-8424.

[27] F. X. Dezael and A. Lambrecht, *Analogue Casimir radiation using an optical parametric oscillator*, EPL (Europhysics Letters) **89** (2010) 14001.

[28] D. Faccio and I. Carusotto, *Dynamical Casimir Effect in optically modulated cavities*, EPL (Europhysics Letters) **96** (2011) 24006.

[29] Diego A. R. Dalvit, Paulo A. Maia Neto and Francisco Diego Mazzitelli, "Fluctuations, Dissipation and the Dynamical Casimir Effect", *Casimir Physics*, ed. by Diego Dalvit et al., Springer Berlin Heidelberg, 2011 419, ISBN: 978-3-642-20288-9.

[30] E. Yablonovitch, *Accelerating reference frame for electromagnetic waves in a rapidly growing plasma: Unruh-Davies-Fulling-DeWitt radiation and the nonadiabatic Casimir effect*, Phys. Rev. Lett. **62** (15 1989) 1742.

[31] Maximilian P E Lock and Ivette Fuentes, *Dynamical Casimir effect in curved spacetime*, New Journal of Physics **19** (2017) 073005.

[32] Mikołaj Zaborowski et al., *Ultrahigh finesse cavity-enhanced spectroscopy for accurate tests of quantum electrodynamics for molecules*, Opt. Lett. **45** (2020) 1603.

[33] A. Ejlli et al., *The PVLAS experiment: A 25 year effort to measure vacuum magnetic birefringence*, Physics Reports **871** (2020) 1, The PVLAS experiment: A 25 year effort to measure vacuum magnetic birefringence, ISSN: 0370-1573.

[34] Pascal Kobel, Moritz Breyer and Michael Köhl, *Deterministic spin-photon entanglement from a trapped ion in a fiber Fabry–Perot cavity*, npj Quantum Information **7** (2021) 6, ISSN: 2056-6387.

[35] Matthias Steiner et al., *Single Ion Coupled to an Optical Fiber Cavity*, Phys. Rev. Lett. **110** (4 2013) 043003.

[36] Shinya Kato and Takao Aoki, *Strong Coupling between a Trapped Single Atom and an All-Fiber Cavity*, Phys. Rev. Lett. **115** (9 2015) 093603.

[37] Wataru Yoshiki and Takasumi Tanabe, *All-optical switching using Kerr effect in a silica toroid microcavity*, Opt. Express **22** (2014) 24332.

[38] Bahaa E A Saleh and Malvin Carl Teich, *Fundamentals of photonics; 2nd ed.* Wiley series in pure and applied optics, Wiley, 2007.

[39] Nur Ismail et al., *Fabry-Pérot resonator: spectral line shapes, generic and related Airy distributions, linewidths, finesses, and performance at low or frequency-dependent reflectivity*, Opt. Express **24** (2016) 16366.

[40] Christina J. Hood, H. J. Kimble and Jun Ye, *Characterization of high-finesse mirrors: Loss, phase shifts, and mode structure in an optical cavity*, Phys. Rev. A **64** (3 2001) 033804.

[41] Anthony E. Siegman, *Lasers*, University Science Books, 1986, ISBN: 0-935702-11-3.

[42] D Hunger et al., *A fiber Fabry–Perot cavity with high finesse*, New Journal of Physics **12** (2010) 065038.

[43] Gurpreet Kaur Gulati et al., *Fiber cavities with integrated mode matching optics*, Scientific Reports **7** (2017) 5556, ISSN: 2045-2322.

[44] Wolfgang Demtröder, *Experimentalphysik 2: Elektrizität und Optik; 3rd ed.* Springer, 2004.

[45] Steven J. Byrnes, *Multilayer optical calculations*, 2020, arXiv: `1603.02720 [physics.comp-ph]`.

[46] Lihong Gao, Fabien Lemarchand and Michel Lequime, *Exploitation of multiple incidences spectrometric measurements for thin film reverse engineering*, Opt. Express **20** (2012) 15734.

[47] Robert W. Boyd, *Nonlinear Optics, Third Edition*, 3rd, Academic Press, Inc., 2008, ISBN: 0123694701.

[48] Vesselin Dimitrov and Sumio Sakka, *Linear and nonlinear optical properties of simple oxides. II*, Journal of Applied Physics **79** (1996) 1741.

[49] A. Sommer et al., *Attosecond nonlinear polarization and light-matter energy transfer in solids*, Nature **534** (2016) 86.

[50] Roberto Righini, *Ultrafast Optical Kerr Effect in Liquids and Solids*, Science **262** (1993) 1386, ISSN: 0036-8075.

[51] S. Zahedpour, J. K. Wahlstrand and H. M. Milchberg, *Measurement of the nonlinear refractive index of air constituents at mid-infrared wavelengths*, Opt. Lett. **40** (2015) 5794.

[52] Sean J. Bentley et al., *Measurement of the thermal contribution to the nonlinear refractive index of air at 1064 nm*, Opt. Lett. **25** (2000) 1192.

[53] P. L. Kelley, *Self-Focusing of Optical Beams*, Phys. Rev. Lett. **15** (26 1965) 1005.

[54] Ruby Verma and Pankaj Garg, *Comparative analysis of self phase modulation (SPM) and cross phase modulation (CPM)*, International Journal of Advanced Research in Computer Science and Electronics Engineering **1** (2012).

[55] M. N. Islam et al., *Cross-phase modulation in optical fibers*, Opt Lett **12** (1987) 625.

[56] J. E. Bjorkholm and A. A. Ashkin, *CW Self-Focusing and Self-Trapping of Light in Sodium Vapor*, Phys. Rev. Lett. **32** (4 1974) 129.

[57] Matthew Mitchell and Mordechai Segev, *Self-trapping of incoherent white light*, Nature **387** (1997) 880, ISSN: 1476-4687.

[58] Cristina Rodríguez et al., *Frequency tripling mirror*, Opt. Express **23** (2015) 31594.

[59] F. Kajzar and J. Messier, *Third-harmonic generation in liquids*, Phys. Rev. A **32** (4 1985) 2352.

[60] Toshiaki Hattori, Akira Terasaki and Takayoshi Kobayashi, *Coherent Stokes Raman scattering with incoherent light for vibrational-dephasing-time measurement*, Phys. Rev. A **35** (2 1987) 715.

[61] Andreas Zumbusch, Gary R. Holtom and X. Sunney Xie, *Three-Dimensional Vibrational Imaging by Coherent Anti-Stokes Raman Scattering*, Phys. Rev. Lett. **82** (20 1999) 4142.

[62] K.-J. Boller, A. Imamoglu and S. E. Harris, *Observation of electromagnetically induced transparency*, Phys. Rev. Lett. **66** (20 1991) 2593.

[63] Michael Fleischhauer, Atac Imamoglu and Jonathan P. Marangos, *Electromagnetically induced transparency: Optics in coherent media*, Rev. Mod. Phys. **77** (2 2005) 633.

[64] K. An et al., *Optical bistability induced by mirror absorption: measurement of absorption coefficients at the sub-ppm level*, Optics Letters **22** (1997) 1433.

[65] Z. Vernon and J. E. Sipe, *Spontaneous four-wave mixing in lossy microring resonators*, Phys. Rev. A **91** (5 2015) 053802.

[66] M. Fiorentino et al., *All-fiber photon-pair source for quantum communications*, IEEE Photonics Technology Letters **14** (2002) 983.

[67] R. E. Slusher et al., *Observation of Squeezed States Generated by Four-Wave Mixing in an Optical Cavity*, Phys. Rev. Lett. **55** (22 1985) 2409.

[68] R. M. Shelby et al., *Broad-Band Parametric Deamplification of Quantum Noise in an Optical Fiber*, Phys. Rev. Lett. **57** (6 1986) 691.

[69] R. E. Slusher et al., *Squeezed-light generation by four-wave mixing near an atomic resonance*, J. Opt. Soc. Am. B **4** (1987) 1453.

[70] Rodney Loudon, *The Quantum Theory of Light*, Clarendon Press, 1973.

[71] Peter D. Drummond and Mark Hillery, *The Quantum Theory of Nonlinear Optics*, Cambridge University Press, 2014.

[72] A. Paredes and J. Récamier, *Study of the combined effects of a Kerr nonlinearity and a two-level atom upon a single nonstationary cavity mode*, J. Opt. Soc. Am. B **36** (2019) 1538.

[73] Jun John Sakurai, *Modern quantum mechanics; rev. ed.* Addison-Wesley, 1994.

[74] C. K. Law, *Effective Hamiltonian for the radiation in a cavity with a moving mirror and a time-varying dielectric medium*, Phys. Rev. A **49** (1 1994) 433.

[75] Horace P. Yuen, *Two-photon coherent states of the radiation field*, Phys. Rev. A **13** (6 1976) 2226.

[76] Murray Sargent Pierre Meystre, *Elements of Quantum Optics*, Springer-Verlag Berlin Heidelberg, 2007, ISBN: 978-3-540-74209-8.

[77] O Alibart et al., *Photon pair generation using four-wave mixing in a microstructured fibre: theory versus experiment*, New Journal of Physics **8** (2006) 67.

[78] J. Fan and A. Migdall, *A broadband high spectral brightness fiber-based two-photon source*, Opt. Express **15** (2007) 2915.

[79] Stephen C. Rand, *Lectures on Light: Nonlinear and Quantum Optics Using the density Matrix*, Oxford University Press Inc., 2010, ISBN: 978-0199574872.

[80] M. Steiner et al., *Photon Emission and Absorption of a Single Ion Coupled to an Optical-Fiber Cavity*, Phys. Rev. Lett. **113** (26 2014) 263003.

[81] David Press et al., *Photon Antibunching from a Single Quantum-Dot-Microcavity System in the Strong Coupling Regime*, Phys. Rev. Lett. **98** (11 2007) 117402.

[82] Q. Lin, F. Yaman and Govind P. Agrawal, *Photon-pair generation by four-wave mixing in optical fibers*, Opt. Lett. **31** (2006) 1286.

[83] Friedrich König et al., *Efficient and spectrally bright source of polarization-entangled photons*, Phys. Rev. A **71** (3 2005) 033805.

[84] M. Fiorentino et al., *All-fiber photon-pair source for quantum communications*, IEEE Photonics Technology Letters **14** (2002) 983.

[85] Albrecht Haase et al., *Tunable narrowband entangled photon pair source for resonant single-photon single-atom interaction*, Opt. Lett. **34** (2009) 55.

[86] Elena Fedulova et al., *Kerr effect in multilayer dielectric coatings*, Opt. Express **24** (2016) 21802.

[87] Thorsten F. Langerfeld, Hendrik M. Meyer and Michael Köhl, *Correlated photon-pair emission from a cw-pumped Fabry-Perot microcavity*, Phys. Rev. A **97** (2 2018) 023822.

[88] Thorsten F. Langerfeld, *Observation of correlated photon pairs using an optical parametric oscillator*, MA thesis: Rheinische Friedrich Wilhelms Universität Bonn, 2017.

[89] R. W. P. Drever et al., *Laser phase and frequency stabilization using an optical resonator*, Applied Physics B **31** (1983) 97, ISSN: 1432-0649.

[90] Leonard Mandel and Emil Wolf, *Optical Coherence and Quantum Optics*, Cambridge University Press, 1995.

[91] Wilmer Souder and Peter Hidnert, *Measurements of the thermal expansion of fused silica*, Scientific Papers of the Bureau of Standards **21** (1926).

[92] M.O. Scully and M.S. Zubairy, *Quantum Optics*, Cambridge University Press, 1997, ISBN: 9780521435956.

[93] Chih-Sung Chuu and S. E. Harris, *Ultrabright backward-wave biphoton source*, Phys. Rev. A **83** (6 2011) 061803.

[94] M Barbier, I Zaquine and P Delaye, *Spontaneous four-wave mixing in liquid-core fibers: towards fibered Raman-free correlated photon sources*, New Journal of Physics **17** (2015) 053031.

[95] Felix Rönchen, Thorsten F Langerfeld and Michael Köhl, *Correlated photon-pair generation in a liquid-filled microcavity*, New Journal of Physics **21** (2019) 123037.

[96] Felix Rönchen, *Correlated photon-pair generation in liquid-filled fibre-resonators*, MA thesis: Rheinische Friedrich Wilhelms Universität Bonn, 2019.

[97] Á. Börzsönyi et al., *Measurement of pressure dependent nonlinear refractive index of inert gases*, Opt. Express **18** (2010) 25847.

[98] Matthew Reichert et al., *Temporal, spectral, and polarization dependence of the nonlinear optical response of carbon disulfide*, Optica **1** (2014) 436.

[99] National Center for Biotechnology Information, *PubChem Compound Summary for CID 6348, Carbon disulfide*, `https://pubchem.ncbi.nlm.nih.gov/compound/Carbon-disulfide`, Accessed 1 June, 2021.

[100] Stefan Kedenburg et al., *Nonlinear refractive indices of nonlinear liquids: wavelength dependence and influence of retarded response*, Applied Physics B **117** (2014) 803, ISSN: 1432-0649.

[101] National Center for Biotechnology Information, *PubChem Compound Summary for CID 7416, Nitrobenzene*, `https://pubchem.ncbi.nlm.nih.gov/compound/Nitrobenzene`, Accessed 1 June, 2021.

[102] National Center for Biotechnology Information, *PubChem Compound Summary for CID 1140, Toluene*, `https://pubchem.ncbi.nlm.nih.gov/compound/Toluene`, Accessed 1 June, 2021.

[103] John G. Cramer et al., *Production of optically thin free-standing oil films from the edge of a rotating disc*, Nuclear Instruments and Methods in Physics Research **185** (1981) 29, ISSN: 0167-5087.

[104] R Ledzion et al., *Kerr constants of some mineral and silicone oils*, Quantum Electronics **29** (1999) 739.

[105] Peng Zhao et al., *Temporal and polarization dependence of the nonlinear optical response of solvents*, Optica **5** (2018) 583.

[106] K F Poulter and P J Nash, *An interferometric oil micromanometer*, Journal of Physics E: Scientific Instruments **12** (1979) 931.

[107] T. L. Van Raalte, *Measurement of the Refractive Index of Silicone Oils for the U.K.A.E.A.*, J. Opt. Soc. Am. **50** (1960) 85.

[108] S. D. McGrane et al., *Quantitative tradeoffs between spatial, temporal, and thermometric resolution of nonresonant Raman thermometry for dynamic experiments*, Appl Spectrosc **68** (2014) 1279.

[109] Hojoong Jung et al., *Tantala Kerr nonlinear integrated photonics*, Optica **8** (2021) 811.

[110] Yanne K. Chembo, *Kerr optical frequency combs: theory, applications and perspectives:* Nanophotonics **5** (2016) 214.

[111] U. Peschel, D. Michaelis and C.O. Weiss, *Spatial solitons in optical cavities*, IEEE Journal of Quantum Electronics **39** (2003) 51.

[112] A.J Scroggie et al., *Pattern formation in a passive Kerr cavity*, Chaos, Solitons, Fractals **4** (1994) 1323, Special Issue: Nonlinear Optical Structures, Patterns, Chaos, ISSN: 0960-0779.

[113] C Braggio et al., *A novel experimental approach for the detection of the dynamical Casimir effect*, Europhysics Letters (EPL) **70** (2005) 754.

[114] Stefano Vezzoli et al., *Optical analogue of the dynamical Casimir effect in a dispersion-oscillating fibre*, Communications Physics **2** (2019) 84, ISSN: 2399-3650.

[115] Mohammed F. Saleh, *Modelling spontaneous four-wave mixing in periodically tapered waveguides*, Opt. Express **27** (2019) 11979.

[116] Astrid Lambrecht, *Electromagnetic pulses from an oscillating high-finesse cavity: possible signatures for dynamic Casimir effect experiments*, Journal of Optics B: Quantum and Semiclassical Optics **7** (2005) S3.

[117] B. W. Shore, P. Meystre and S. Stenholm, *Is a quantum standing wave composed of two traveling waves?*, J. Opt. Soc. Am. B **8** (1991) 903.

[118] Reinaldo de Melo e Souza, Fran çois Impens and Paulo A. Maia Neto, *Microscopic dynamical Casimir effect*, Phys. Rev. A **97** (3 2018) 032514.

[119] Lezhi Lo, P. T. Fong and C. K. Law, *Dynamical Casimir effect in resonance fluorescence*, Phys. Rev. A **102** (3 2020) 033703.

[120] Chao-Yi Tai et al., *Determination of nonlinear refractive index in a Ta2O5 rib waveguide using self-phase modulation*, Opt. Express **12** (2004) 5110.

[121] Chung-Lun Wu et al., *Four-wave-mixing in the loss low submicrometer Ta2O5 channel waveguide*, Opt. Lett. **40** (2015) 4528.

[122] Yuan-Yao Lin et al., *Self-phase modulation in highly confined submicron Ta2O5 channel waveguides*, Opt. Express **24** (2016) 21633.

[123] Manuel Uphoff et al., *Frequency splitting of polarization eigenmodes in microscopic Fabry–Perot cavities*, New Journal of Physics **17** (2015) 013053.

[124] Thomas Begou and Julien Lumeau, *Accurate analysis of mechanical stress in dielectric multilayers*, Opt. Lett. **42** (2017) 3217.

[125] R. M. Waxler and A. Napolitano, *Relative stress-optical coefficients of some National Bureau of Standards optical glasses*, Journal of research of the National Bureau of Standards **59** (1957) 121.

[126] Chandra M Natarajan, Michael G Tanner and Robert H Hadfield, *Superconducting nanowire single-photon detectors: physics and applications*, Superconductor Science and Technology **25** (2012) 063001.

[127] Viacheslav Burenkov et al., *Investigations of afterpulsing and detection efficiency recovery in superconducting nanowire single-photon detectors*, Journal of Applied Physics **113** (2013) 213102.

[128] Claire Autebert et al., *Direct measurement of the recovery time of superconducting nanowire single-photon detectors*, Journal of Applied Physics **128** (2020) 074504.

[129] G. Kirchhoff, *Ueber das Verhältniss zwischen dem Emissionsvermögen und dem Absorptionsvermögen der Körper für Wärme und Licht*, Annalen der Physik **185** (1860) 275.

[130] Chao-Wei Liu et al., "Measurements of Thermo-Optic Coefficients in Ta2O5 based micro-ring cavity", *JSAP-OSA Joint Symposia 2017 Abstracts*, Optical Society of America, 2017.

[131] Haruka Terashima et al., *Quantum interferometric generation of polarization entangled photons*, Scientific Reports **8** (2018) 15733, ISSN: 2045-2322.

[132] Pisek Kultavewuti et al., *Polarization-entangled photon pair sources based on spontaneous four wave mixing assisted by polarization mode dispersion*, Scientific Reports **7** (2017) 5785, ISSN: 2045-2322.

[133] J. R. Johansson et al., *Nonclassical microwave radiation from the dynamical Casimir effect*, Phys. Rev. A **87** (4 2013) 043804.

[134] Viktor Dodonov, *Fifty Years of the Dynamical Casimir Effect*, Physics **2** (2020) 67, ISSN: 2624-8174.

APPENDIX A

Parametric excitation of a cavity mode by a travelling intensity wave

The nonlinear Hamiltonian derived in subsection 2.2.3 couples a cavity pump mode to adjacent, unoccupied signal and idler modes, describing the dynamics of spontaneous four-wave mixing in a third-order nonlinear material. A similar calculation is done in the following, where two superimposed coherent electromagnetic waves couple to a single cavity mode. The electromagnetic energy for a nonmagnetic medium is [70]

$$H = \frac{1}{2}\int_V \mathrm{d}^3 r \, \frac{1}{\mu_0}\mathbf{B}\cdot\mathbf{B} + \mathbf{E}\cdot\mathbf{D}\,, \tag{A.1}$$

where V is the quantization volume of the cavity mode, μ_0 is the vacuum permeability, $\mathbf{B}$ the magnetic field, $\mathbf{E}$ the electric field and $\mathbf{D}$ is the displacement field as defined in Equation 2.19. For simplicity, we drop the vector notation in the following by assuming that all fields are equally linearly polarized. Inserting the definition for the displacement field into the electromagnetic energy in Equation 2.29, we find the nonlinear term

$$H_{\mathrm{nl}} = \frac{1}{2}\int_V \mathrm{d}^3 r \, \epsilon_0 \chi^{(3)} E^4\,, \tag{A.2}$$

where the integration volume denotes the volume of the nonlinear medium inside the cavity. The different fields contributing to the total electric field are the unoccupied cavity mode $\hat{E}_{\mathrm{c}}$, and both the pump beams E_{g} and E_{ir}. Likewise in the derivation in subsection 2.2.3, the term considered here is the one mixing the square of the cavity mode and the product of the pump beams $H_{\mathrm{nl}} = 12\chi^{(3)} E_{\mathrm{g}} E_{\mathrm{ir}} \hat{E}_{\mathrm{c}}^2$. Considering the positive and negative frequency terms in the pump fields, the product contains two terms with a dependence on the sum of the frequencies and wavevectors, and the difference, respectively. The frequencies of the fields involved are chosen such that the difference frequency of the pumps matches twice the frequency of the cavity mode. The angles of the two pump beams need to be chosen such that the difference of the wavevectors is parallel with respect to the cavity axis. The interference term of the pump lasers is given by

$$E_{\mathrm{g}} E_{\mathrm{ir}} = \frac{1}{4} E_{0,\mathrm{g}} E_{0,\mathrm{ir}} (e^{i((\mathbf{k}_{\mathrm{g}}+\mathbf{k}_{\mathrm{ir}})\mathbf{r}-(\omega_{\mathrm{g}}+\omega_{\mathrm{ir}})t)} + e^{i((\mathbf{k}_{\mathrm{g}}-\mathbf{k}_{\mathrm{ir}})\mathbf{r}-(\omega_{\mathrm{g}}-\omega_{\mathrm{ir}})t)} + \mathrm{c.c.})\,. \tag{A.3}$$

Neglecting the terms containing the frequency and wavevector sums, the Hamiltonian is comparable to the term describing the coupled cavity modes in Equation 2.36 and reads

$$\hat{H}_{\mathrm{nl}} = 6\int_V \mathrm{d}^3 r\, \epsilon_0 \chi^{(3)} (E_{\mathrm{g}}^{(-)} E_{\mathrm{ir}}^{(+)} + E_{\mathrm{g}}^{(-)} E_{\mathrm{ir}}^{(+)}) \hat{E}_{\mathrm{c}}^2 \tag{A.4}$$

$$= 6\chi^{(3)} E_{0,\mathrm{g}} E_{0,\mathrm{ir}} \frac{2\hbar\omega_{\mathrm{c}}}{\pi\sigma_{\mathrm{c}}^2 l} \eta_\perp \int_0^\infty \mathrm{d}z\, \cos(\Delta k z - \Delta\omega t) \sin^2(k_{\mathrm{c}} z) e^{-\frac{2z}{z_{\mathrm{l}}}} (\hat{a}_{\mathrm{c}} - \hat{a}_{\mathrm{c}}^\dagger)^2 \quad . \tag{A.5}$$

The coupling term $\eta_\perp$ is the integral in x and y direction over the gaussian envelopes of the cavity mode and the pump beams. The oblique angle of incidence θ of the pump beams needs to be accounted for, such that the projection onto the cavity mirror is elliptical and consequently the beam waist in one direction is increased by a factor of $\cos^{-1}(\theta)$. Furthermore, an exponential decay of the cavity mode inside the mirror coating is included (cf. Figure 5.6), with the result that the integral in z-direction can be extended to infinity, for simplicity. Expressing the trigonometric functions as exponentials, the integral contains following terms

$$\cos(\Delta k z - \Delta\omega t) \sin^2(k_{\mathrm{c}} z) \tag{A.6}$$

$$= -\frac{1}{8}((e^{i(2k_{\mathrm{c}}+\Delta k)z} + e^{i(2k_{\mathrm{c}}-\Delta k)z}) e^{-i\Delta\omega t} + c.c.) + \frac{1}{4}((e^{i(\Delta k_{\mathrm{c}} z - \Delta\omega t)} + c.c.) \tag{A.7}$$

Similar to the coupling constant in subsection 2.2.3, these terms contain the phase matching condition for the photon pair generation process and describe the multiple ways to mix the momenta of the input and output fields. The contribution of the last terms is small such that they will be neglected. The resulting dimensionless factor after integration is

$$\beta = \frac{2i}{2i + z_{\mathrm{l}}\Delta k} + \frac{i}{2i - (2k_{\mathrm{c}} + \Delta k) z_{\mathrm{l}}} + \frac{i}{2i + (2k_{\mathrm{c}} - \Delta k) z_{\mathrm{l}}} \tag{A.8}$$

and consequently the Hamiltonian is

$$\hat{H}_{\mathrm{nl}} = \hbar\eta(\beta e^{-i\Delta\omega t} + \beta^* e^{i\Delta\omega t})(\hat{a}_{\mathrm{c}} - \hat{a}_{\mathrm{c}}^\dagger)^2 \,, \tag{A.9}$$

with the coupling constant

$$\eta = \frac{\omega_{\mathrm{c}}}{\pi\sigma_{\mathrm{c}}^2 l} z_{\mathrm{l}} \eta_\perp \frac{n_0^2 n_2}{\sqrt{n_{0,\mathrm{g}} n_{0,\mathrm{ir}}}} \sqrt{I_{\mathrm{g}} I_{\mathrm{ir}}} \,. \tag{A.10}$$

The Hamiltonian shows a similar structure as the Hamiltonian for spontaneous parametric downconversion in the undepleted pump limit, i.e. when the pump wave is treated classically [71]. Changing to the interaction picture following the steps taken in subsection 2.2.3, the Hamiltonian describing the system dynamics in the rotating wave approximation is given by

$$\hat{H}_{\mathrm{1I}} = \hbar\eta(\beta(\hat{a}^\dagger)^2 e^{-i\Delta t} + \beta^* \hat{a}^2 e^{i\Delta t}) \quad , \tag{A.11}$$

with the detuning $\Delta = \Delta\omega - 2\omega_{\mathrm{c}}$. This Hamiltonian is very similar to a parametric amplifier [71], where the coherent undepleted drive β is coupled to the unoccupied mode $\hat{a}$ oscillating at half the pump frequency. In a full quantum treatment of the dynamics, the resonant terms after the rotating

wave approximation are $\hat{a}_g \hat{a}_{ir}^\dagger (\hat{a}_c^\dagger)^2$ and the hermitian conjugate. The underlying process on a single photon level is, therefore, the annihilation of a green pump photon with the stimulated emission of a infrared pump photon on the virtuell level, with the excess creating a photon-pair on the cavity mode.

Determine the photon-pair rate via solving the master equation After determining the Hamiltonian in the interaction picture, we can determine the master equation and solve for the density matrix like in subsection 2.2.3. For the system studied here, two coherent pump beams are involved and one unoccupied cavity mode. Since the interaction is weak, we assume the pump beams to be undepleted classical electromagnetic waves and the cavity mode to maximally contain two photons. The system's wavefunction expressed in photon number states is $|\Psi\rangle = c_0 |0\rangle + c_1 |1\rangle + c_2 |2\rangle$ and, therefore, the density matrix is a 3×3 matrix given in general by

$$\hat{\rho} = \sum_{mn} \rho_{mn} |m\rangle \langle n| \quad \text{with} \quad \rho_{mn} = c_m c_n^*, \tag{A.12}$$

where m and n run from 0 to 2. Inserting Equation A.11 and Equation A.12 into the master equation (Equation 2.50) we get with $\tilde{\beta} = \beta \exp(-i\Delta t)$

$$\begin{aligned}\dot{\hat{\rho}} = &-i\eta \sum_{mn} \rho_{mn} [\tilde{\beta}(\sqrt{(m+1)(m+2)} |m+2\rangle \langle n| - \sqrt{n(n-1)} |m\rangle \langle n-2|) \\ &+ \tilde{\beta}^*(\sqrt{m(m-1)} |m-2\rangle \langle n| - \sqrt{(n+1)(n+2)} |m\rangle \langle n+2|) \\ &+ \kappa(\sqrt{mn} |m-1\rangle \langle n-1| - \frac{1}{2}(m+n) |m\rangle \langle n|)] \end{aligned} \tag{A.13}$$

$$= -i\eta\sqrt{2} \begin{pmatrix} -\tilde{\beta}\rho_{02} + \tilde{\beta}^*\rho_{20} & 0 & -\tilde{\beta}^*(\rho_{00} - \rho_{22}) \\ 0 & 0 & -\rho_{10} \\ \tilde{\beta}(\rho_{00} - \rho_{22}) & \rho_{01} & \tilde{\beta}\rho_{02} - \tilde{\beta}^*\rho_{20} \end{pmatrix} + \kappa \begin{pmatrix} \rho_{11} & \sqrt{2}\rho_{12} - \frac{1}{2}\rho_{01} & -\rho_{02} \\ \sqrt{2}\rho_{21} - \frac{1}{2}\rho_{10} & 2\rho_{22} - \rho_{11} & -\frac{3}{2}\rho_{12} \\ -\rho_{20} & -\frac{3}{2}\rho_{21} & -2\rho_{22} \end{pmatrix} \tag{A.14}$$

In the steady-state $\dot{\hat{\rho}} = 0$ and at zero detuning $\Delta = 0$, the system can be easily solved analytically using $\mathrm{tr}(\hat{\rho}) = 1$ [76] and we find

$$\hat{\rho} = \frac{2\eta^2|\beta|^2 + \kappa^2}{8\eta^2|\beta|^2 + \kappa^2} \begin{pmatrix} 1 & 0 & i\sqrt{2}\frac{\eta\kappa}{2\eta^2|\beta|^2+\kappa^2}\beta^* \\ 0 & \frac{4\eta^2|\beta|^2}{2\eta^2|\beta|^2+\kappa^2} & 0 \\ -i\sqrt{2}\frac{\eta\kappa}{2\eta^2|\beta|^2+\kappa^2}\beta & 0 & \frac{2\eta^2|\beta|^2}{2\eta^2|\beta|^2+\kappa^2} \end{pmatrix}. \tag{A.15}$$

Finally, the photon-pair rate can be determined via the expectation value of the photon number operator using $\langle \hat{A} \rangle = \mathrm{tr}(\hat{\rho}\hat{A})$ [76] to be

$$\Gamma = \kappa \langle \hat{a}^\dagger \hat{a} \rangle = \frac{8\kappa\eta^2|\beta|^2}{8\kappa\eta^2|\beta|^2 + \kappa^2} \approx \frac{8\eta^2|\beta|^2}{\kappa} \tag{A.16}$$

$$\approx 16 \frac{F\Delta\omega_{\mathrm{fsr}}}{\pi^2} (k_{\mathrm{c}} z_1 n_0 n_2 \sqrt{I_{\mathrm{g}} I_{\mathrm{ir}}} |\beta| \frac{\eta_\perp}{\pi\sigma_{\mathrm{c}}^2})^2 . \tag{A.17}$$